# SYNTHESIS AND APPLICATION OF USEFUL ORGANIC BUILDING BLOCKS AND CYCLIC TETRAPEPTIDE

A Dissertation

by

HUA ZHOU

Submitted to the Office of Graduate and Professional Studies of
Texas A&M University
in partial fulfillment of the requirements for the degree of

MASTER OF SCIENCE

| | |
|---|---|
| Chair of Committee, | Kevin Burgess |
| Committee Members, | Coran M. H. Watanabe |
| | John Gladysz |
| | Susie Dai |
| Head of Department, | David H. Russell |

December 2014

Major Subject: Chemistry

Copyright 2014 Hua Zhou

## ABSTRACT

Drug designing usually encounters two major difficulties: construction of small molecules and target finding for the molecules. This is frustrating because either one requires tremendous effort. My research focused on how well-known methods such as asymmetric hydrogenation and organocatalysis can facilitate organic synthesis and how EKO aided us to find protein targets for small molecules.

Synthesis of *Z*-allylic diols was a starting project. The beauty of trisubstituted allylic diols is that it can be converted to a lot of useful building blocks of organic molecules, such as 4,5-disubstituted furanone and 2,3-disubstituted furan. The construction of the scaffold needed an undervalued intermediate, vinylaluminate, which was developed decades ago. Treated with red-aluminum, 2-butyn-1-ol can be converted to a five-membered ring vinylaluminate intermediate. The only application of this intermediate was the conversion to vinyl iodide. We found a more valued application: reaction with aldehydes to form a Z-allylic diol scaffold.

The ideal was carried on further. Combination of two well-known methodologies, asymmetric hydrogenation and organocatalysis can result in the production of particularly high-value chirons. We prepared optically pure *homo*-Roche ester by asymmetric hydrogenation of a α,β-unsaturated ester. And chlorination, fluorination and amination of the ester product formed a series of useful chirons.

The two projects, though not directly related, but conceptually guided the third project: design and synthesis of small molecules that can disrupt protein-protein interactions, because we are eager to illustrate the merits of our novel approaches, EKO and EKOS. EKO is a computational program that can overlay small molecules over tens of thousands of protein-protein interfaces and find the best fit PPIs for the molecule. We used cyclic tetrapeptide and oxopiperazine dimers as examples to illustrate how EKO and EKOS work. And we also designed an expedient large-scale synthesis of cyclic tetrapeptide as probes to illustrate the idea that using creative computational methods for molecular design will have a large impact on contemporary life science.

## ACKNOWLEDGEMENTS

I would like to express my appreciation to my advisor, Prof. Kevin Burgess, for all his guidance and support during my study.

I thank Dr. John Gladysz, Dr. Coran Watanabe, and Dr. Susie Dai for serving on my graduate advisory committee. I really appreciate them for finding time to serve on my committee and also for their timely advice.

I would like to thank Ms. Jill Powers for her help through all these years.

I would like to thank former group members, Dr. Ye Zhu, Dr. Sakunchai Khumsubdee for their valuable advice, help and sharing of the project.

I also thank all current members of Burgess' group for their companionship and help.

I would like to pay a special thank to my family for all the patience and support.

## TABLE OF CONTENTS

Page

## LIST OF FIGURES

FIGURE Page

## LIST OF TABLES

## LIST OF SCHEMES

# CHAPTER I
# INTRODUCTION

## 1.1 New Methodology For Synthetically Useful Building Blocks

Creativity in organic synthesis can be interpreted in two aspects. In one aspect, it is to find a new reaction or new synthetic route that is never reported before. In the other aspect, it is to apply well-known reactions or intermediates to improve existing synthesis. Half of my master research focuses on the second aspect.

Treated with aluminum hydride, 2-butynol can afford a 5-membered ring vinyl aluminate intermediate which can be quenched by iodine to afford a well-known useful vinyl iodide species.[1-3] It is useful because it can generate a regiospecific *Z*-allylic alcohol intermediate which can be used as building blocks in organic synthesis. However, in all reported work, this vinyl aluminate intermediate needed to be converted to vinyl iodide first. There is no precedent work showing a direct reaction with electrophiles other than iodine (Figure 1.1). Therefore, nearly half of my master research was devoted on exploring new applications of this useful vinylaluminate intermediate.

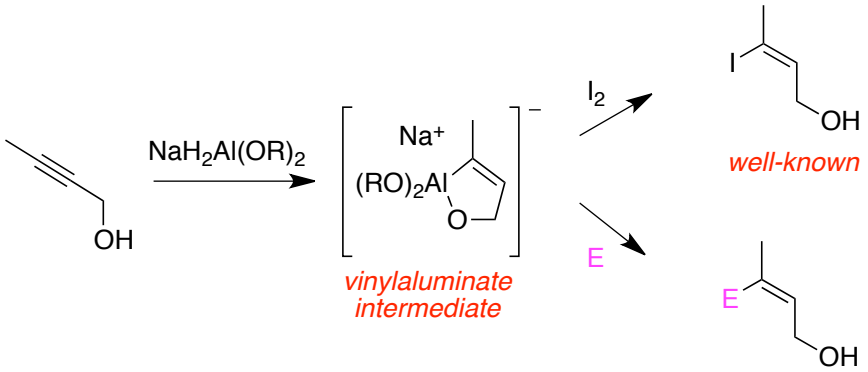


***Figure 1.1.*** Vinyl aluminate attacks electrophiles to generate *Z*-allylic alcohol.

Chiral analogs of Crabtree's catalyst, *ie N,P*-Ir complexes have been recognized as the most useful catalyst that can use for hydrogenation of olefin without coordinating functional groups.[4-6] There is even a greater deal of enamine catalyst by simple catalyst

such as proline.[7] Combination of two can lead to a methodology not reported before. Organocatalytic transformations of the *homo-Roche* aldehydes, which are obtained from asymmetric hydrogenation, are good illustrations of the idea. Asymmetric hydrogenation routes to homologs of Roche ester tend to be restricted to hydrogenations of itaconic acid derivatives, *ie* substrates that contain a relatively unhindered, 1,1-disubstituted, alkene. This is because in hydrogenations mediated by $RhP_2$ complexes, the typical catalysts, it is difficult to obtain high conversions using the alternative substrate for the same product, the isomeric *trisubstituted* alkenes (Figure 1.2). However, chemoselective modification of the identical functional groups in itaconic acid derivatives are difficult, hence it would be favorable to use the trisubstituted alkene. Trisubstituted alkene substrates *can* be hydrogenated with high conversions using chiral analogs of Crabtree's catalyst of the type *IrN(carbene)*.

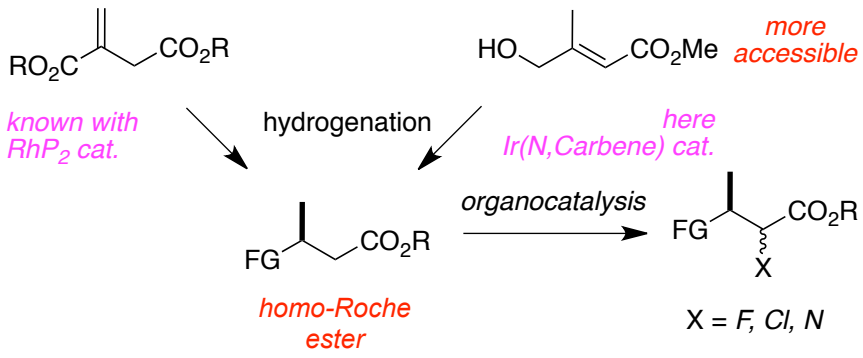


***Figure 1.2.*** Combination of asymmetric hydrogenation and organocatalysis leads to useful *homo*-Roche ester derivatives.

My work demonstrates such reactions are scalable and can be manipulated to give optically pure *homo*-Roche ester derivatives with two chiral centers and α,ω-groups that provide extensive scope for modifications. A synthesis of (*S,S*)- and (*R,S*)-γ-hydroxyvaline was performed to illustrate one application of the amination product.

## 1.2 Synthesis And Conformational Analysis Of CTPs

Cyclic tetrapeptides (CTPs) have been known for decades, mostly as natural products.[8-10] Previous syntheses of CTPs involve proline and/or glycine. Proline facilitates syntheses of CTPs because *cis*-conformations are far more thermodynamically accessible, and this "forces" the peptide to turn, so that *C*- and *N*-termini can come together for cyclization.[11-13] Glycine residues, having no side-chains, similarly allow conformations that are favorable for cyclization because a greater range of ψ and φ angles are available around Gly than for any other amino acid. Combinations of Pro-Gly in linear precursors to CTPs are particularly favorable because that motif is highly conducive to turn conformers that facilitate cyclization. For these reasons, *the overwhelming majority of synthetic CTPs reported contain Pro and/or Gly*. CTPs that have been made via peptide syntheses which do *not* contain Pro or Gly are rarely reported.[14-17]

The second half of my master research was focused on (i) developing an efficient solution phase synthesis of CTPs based upon Li's innovation and (ii) conformational analysis of CTPs. The conformations of CTPs are determined by a non-commercial program called, *quenched molecular dynamics* (QMD), devised by Dr. Monte Pettitt.[18,19]

## 1.3 Side-chain Matching And Mining On Protein-protein Interaction With EKO And EKOS

Our group published on two techniques called EKO (Exploring Key Orientations)[20] and EKOS (Exploring Key Orientations on Secondary-structures)[21] to help us to design small molecules that are semi-rigid scaffolds bearing three amino acid side-chains to resemble protein fragments. These methods enable us to explore orientations of side-chains that could result in conformations adopted by these molecules. Then data mining can match these side-chain orientations with protein fragments that fit. In this project, EKO and EKOS are performed on CTPs and oxopiperazine dimers. In EKOS, the interface regions of crystallographically characterized protein-protein interactions (PPIs) of ideal secondary structures are

targeted. EKO works in the same way as EKOS, except that the secondary structure database is replaced by one covering interface regions in crystallographically characterized PPIs.

## 1.4 Conclusion

My master degree research focused on two parts. The first was to develop simple new methods for synthesis of molecules that can be useful as synthetic building blocks and the second half was to synthesize cyclic tetrapeptides and determine their conformations, and finally explore their potential as small molecules to disrupt protein-protein interactions via computational analysis.

# CHAPTER II

# REGIO- AND STEREOSELECTIVE SYNTHESIS OF TRISUBSTITUTED (*Z*)-ALLYLIC ALCOHOLS VIA *TRANS*- HYDROALUMINATION/VINYL ADDITION

## 2.1 Introduction

Degree of difficulty in trisubstituted allylic alcohol syntheses correlates with the alkene stereochemistry. Reactions of stabilized phosphonate reagents[22,23] with aldehydes, followed by hydride reductions, to afford **A** and **B** are so generally reliable that it is usually unnecessary to look to the obvious alternatives.[24-29] Motifs C and D, however, are significantly less accessible. Preparations of these have been achieved via alkyne hydroalumination[30-34] or hydromagnesiation,[35] but if the starting material is a propagrylic alcohol, using the disconnection implied in blue, then several more steps are needed. For example, fragments **C** can be made via conversion of the hydroalumination products to aluminate anions, then to cuprates, which are eventually reacted with activated alkyl halides.[36] Synthons **D** can be made via iodine quench of the same intermediate, lithium-halide exchange, then reaction with an epoxide.[36]

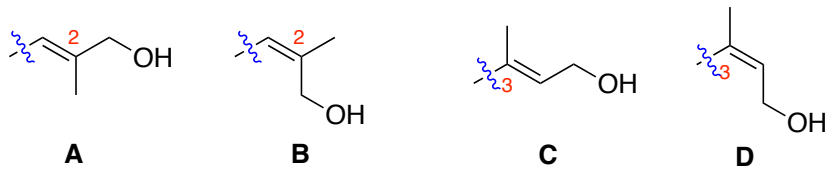


***Figure 2.1.*** Trisubstituted allylic alcohol synthons.

Other routes to **C** and **D** involve catalyzed additions of organoboranes to dienes then oxidation,[37-38] but these approaches require stereoselective syntheses of the appropriate dienes (Figure 2.1). To address some of these difficulties, a previous student Dr. Ye Zhu invented a means to synthesize compounds **F**, which represent a highly functionalized,

and therefore particularly useful, subset of the coveted motifs **D** via the simple process outlined in Scheme 2.1.

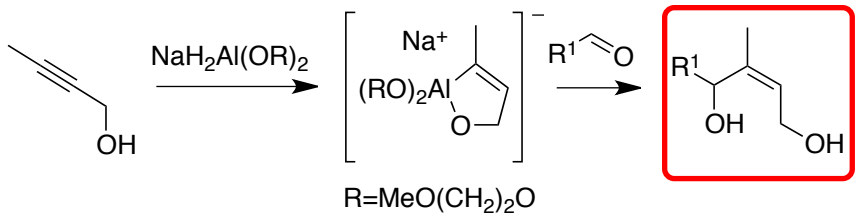


***Scheme 2.1.*** *trans*-Hydrometalation/vinyl addition reaction.

## 2.2 Results And Discussion

2-Butynol corresponds to the carbon framework of motif **D**, hence we hypothesized that the most direct way to add this fragment to an aldehyde would be via addition of its hydroalumination product with sodium bis(2-methoxyethoxy)aluminum hydride (Red-Al).[1] However, the literature on addition of this vinyl aluminate intermediate to aldehydes gave no direct indication this would work. Additions of *dialkyl*(alkenyl)alanes to aldehydes are known,[30-34] but it has often been found necessary to form the *trialkyl*(alkenyl)*aluminate anions* to induce transfer of the vinyl group.[40-41] We could find no reference to *direct* addition of propargylic alcohol hydroalumination products to aldehydes. Consequently, when we tried to react the hydroalumination products using benzaldehyde as a substrate, we were encouraged to see some product form, and delighted to optimize it to good yields (Table 2.1).

***Table 2.1.*** Optimization of *trans*-hydrometalation/vinyl addition reaction.

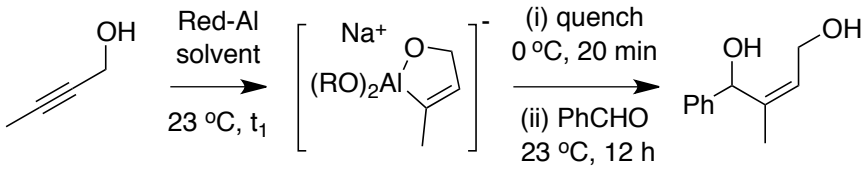

***Table 2.1.*** Continued.

| entry | solvent | Red-Al (eq.) | $t_1$ (h) | quench (eq.) | PhCHO (eq.) | yield (%)[a] |
|---|---|---|---|---|---|---|
| 1 | $CH_2Cl_2$ | 2 | 12 | EtOAc (1.0) | 2 | <5 |
| 2 | $^t$BuOMe | 2 | 12 | EtOAc (1.0) | 2 | 44 |
| 3 | THF | 2 | 12 | EtOAc (1.0) | 2 | 63 |
| 4 | $Et_2O$ | 2 | 12 | EtOAc (1.0) | 2 | 66 |
| 5 | hex. | 2 | 12 | EtOAc (1.0) | 2 | 78 |
| 6 | hex. | 2 | 4 | EtOAc (1.0) | 2 | 77 |
| 7 | hex/THF (5:1) | 2 | 4 | EtOAc (1.0) | 2 | 66 |
| 8 | hex/THF (5:1) | 1.25 | 4 | EtOAc (0.25) | 2 | 70 |
| 9 | hex/THF (5:1) | 1.25 | 4 | EtOAc (0.25) | 1.2 | 74 |
| 10 | THF | 1.25 | 4 | EtOAc (0.25) | 1.2 | 58 |
| 11 | Toluene | 1.50 | 4 | none | 2 | 88 |

[a] Determined by HPLC using 4-hydroxyphenethyl alcohol as internal standard, and based on the alcohol starting material; hex = hexane.

Entries 1 – 4 show how increased yields of **2a** approximately correlated with decreasing solvent polarities. This is consistent with literature reports that the reactivity of organoaluminum reagents is increased in apolar solvents.[41] However, the reactions in hexane tended to form gels and reproducibility problems were encountered. For this reason, a mixed solvent system with 20% THF was tested and found (entry 7) to give yields similar to the highest in pure hexane, but more consistently. Entry 10 was performed simply to check that if pure THF solvent would give better results under the

modified conditions; surprisingly, increased yield was observed when excess benzaldehdye was used without adding EtOAc (entry 11). The first ten entries were investigated by Dr. Ye Zhu and I modified the process and the optimized condition was reported in entry 11. And the preliminary studies extrapolated to other substrates as shown in Table 2.2.

***Table 2.2.*** One-pot synthesis of (*Z*)-trisubstituted allylic alcohols.[a]

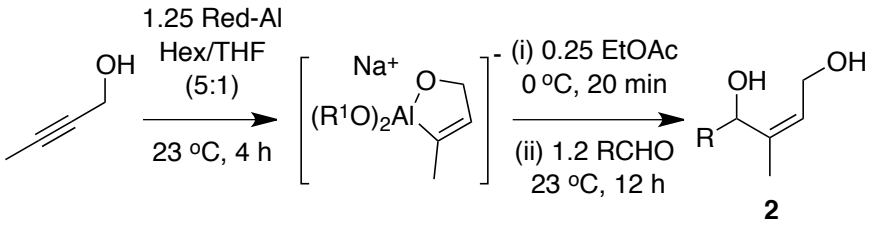


**2**

| **2** | R | isolated yield (%) | **2** | R | isolated yield (%) |
|---|---|---|---|---|---|
| **a** | 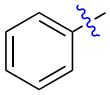 | 88[b] | **b** | 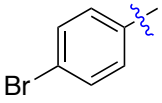 | 85[b] |
| **c** | 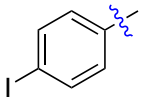 | 55 | **d** | 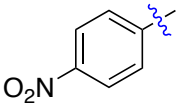 | 67 |
| **e** | 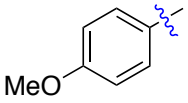 | 58 | **f** | 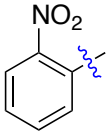 | 76 |
| **g** | 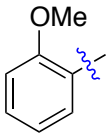 | 63 | **h** | 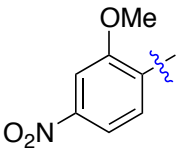 | 67 |
| **i** | 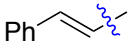 | 51 | **j** | 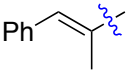 | 74 |

***Table 2.2.*** Continued.

| **2** | R | isolated yield (%) | | **2** | R | isolated yield (%) |
|---|---|---|---|---|---|---|
| **k** | 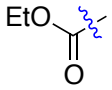 | 36 | | **l** |  | 58[c] |

[a] 2-Butyn-1-ol (2.0 mmol, 1.0 eq) was used; [b] condition of entry 11 was used; [c] the aldehyde was dissolved in hexanes and added to the reaction mixture slowly via a syringe pump.

Several trends are illustrated for application of this reaction to substrates **1**. Aryl bromide (**b**) and iodide (**c**) functionalities were tolerated, the reaction worked well for benzaldehyde derivatives with electron withdrawing (**c**) or donating (**d**) groups, even in the 2-position for which steric hinderance could have been an issue (substrates **f** - **h**). Ethyl glyoxylate (**k**) gave a somewhat reduced yield of the secondary product corresponding to spontaneous lactonization. This methodology is less robust for aliphatic aldehydes. Where there is α-branching in the substrate, and presumably slower rates of competing self-condensation processes, as for 2-methylpropanal **2l** then good yield of product could be obtained by slow addition of the aldehyde to the hydroalumination product (thus disfavoring aldehyde self condensation). Figure 2.2 illustrates two simple applications of the products **2**. The first illustrates oxidation then cyclization to the unsaturated butyrolactone **3**, and the second shows cyclization then oxidation to the 2,3-disubstitued furan **4**.

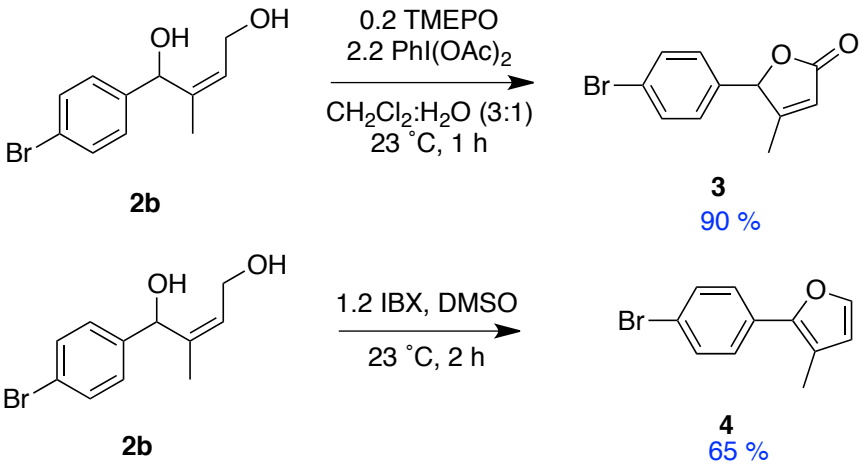


***Figure 2.2.*** One step applications of allylic alcohols **2**.

## 2.3 Conclusions

Treated with aluminum hydride, 2-butynol can afford a 5-membered ring vinyl aluminate intermediate, which can be quenched by iodine to afford a well-known useful vinyl iodide species.[1-3] It is useful as it can generate a regiospecific *Z*-allylic alcohol intermediate. We are the first group who applied the intermediate in direct synthesis to build synthetically useful trisubstituted allylic alcohols, which can be readily converted to lactones, furans and polyketides via hydrogenation.

# CHAPTER III
# HOMO-ROCHE ESTER DERIVATIVES BY ASYMMETRIC HYDROGENATION AND ORGANOCATALYSIS*

## 3.1 Introduction

Roche ester derivatives **E** are some of the most widely appreciated chirons in organic syntheses[42-45] because such compounds have both terminal functional groups that allow modification and homologation in bidirections, especially for incorporating methyl-substituted chiral centers. It seems logical that the homologous chirons **F** would be similarly useful as chirons **E** if they were more readily available. For the purposes of this study we refer to the generic class of fragments **F** as *homo-Roche ester* derivatives (Figure 3.1).

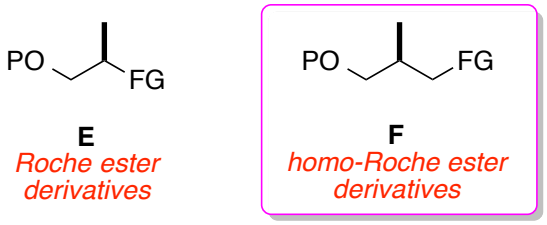


***Figure 3.1.*** Structure of Roche ester and *homo*-Roche ester derivatives.

Scalable syntheses of chirons **F** have not gained much attention in the literature. The most directing route should be a homologation of the parent chirons **E**[46] which is probably *not* the best option to obtain chirons **F**, even though they only contain one more skeletal carbon than **E** because the Roche ester is not a cheap starting material; small quantities tend to cost more than $1 per gram. Another approach is via asymmetric hydrogenations of itaconic acid or the corresponding diesters to give the $C_5$-building

* Reprinted in part with permission from "Homo-Roche Ester Derivatives by Asymmetric Hydrogenation and Organocatalysis", Sakunchai Khumsubdee, Hua Zhou and Kevin Burgess, *J. Org. Chem.* **2013**, *78*, 11948-11955. Copyright 2013 American Chemical Society.

blocks **G**.[47,48] Bidirectional homologation of chirons **G** requires efficient chemoselective modification of one of the two esters; we are aware of only one method for doing this, and it features a relatively expensive lipase in a chemoenzymatic hydrolysis to achieve a pure single monoester.[47] It is possible to instead begin with a *mono*ester of itaconic acid and hydrogenate that, but in fact the enantioselectivities for this process tend to be less than the diacid or the diester.[47,49] Alternatively it is possible to begin the syntheses with monoesters of itaconic acid, and indeed some of these are commercially available (Figure 3.2). However, these starting materials are expensive so, overall, it is better to avoid this strategy. Any strategy that uses hydrogenation of itaconic acid, in fact, is vulnerable to the types of deactivation pathways that have been documented previously.[50,51] Another route to chirons **I** is via asymmetric additions of cuprates to α,β-unsaturated thioesters.[52]

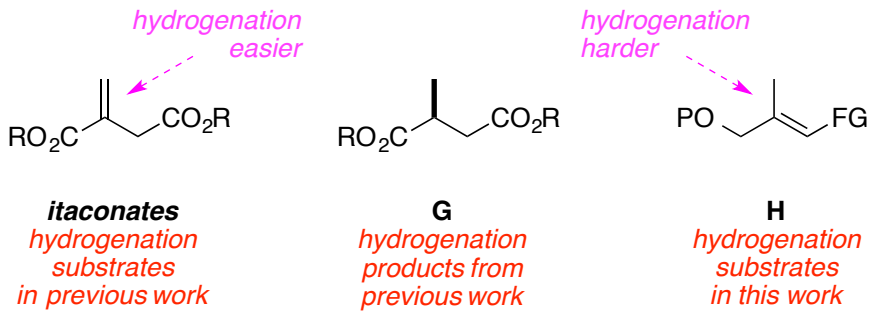


***Figure 3.2.*** Hydrogenation substrates to obtain compound **G**.

Both the hydrogenation syntheses of chirons **F** described above feature bisphosphite complexes formed from $Rh(COD)_2^+$ *in situ.* Hydrogenation of type **H** trisubstituted alkenes would give products that are chemically related to **G**, but these types of transformations tend to be difficult to achieve using $RhP_2$ complexes because the double bonds are hindered.[53] In fact, the preferred catalysts for the trisubstituted alkenes **H** tend to be *N,P*-Ir complexes, *ie* chiral analogs of Crabtree's catalyst.[53] Consequently, my work in this project was to use our particular chiral analog of Crabtree's catalyst, **(*S*)-1**,[54,55] to reduce **H** -type substrates via scalable transformations

to obtain single enantiomer of chirons **H**. The hydrogenated product was then further applied to obtain all stereoisomeric forms of the 2-substituted chirons **I** via organocatalytic modifications of the *homo-Roche* ester derivatives **F** (Figure 3.3). Similar reactions of achiral substrates via organocatalytic are well known, but finding appropriate organocatalysts to overcome the stereochemical bias exerted by the $C^3$ chiral center was an open issue.

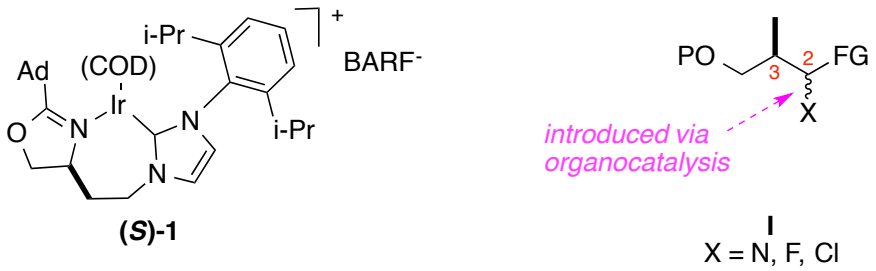


***Figure 3.3.*** Structure of catalyst **(*S*)-1** used for hydrogenation and general structure of organocatalysis product **I**.

## 3.2 Results and discussion

### 3.2.1 Synthesis of hydrogenation substrate

The synthesis of up to ester **9** was accomplished by previous graduate student, Dr. Sakunchai Khumsubdee. The synthesis is as follows. Following a literature procedure, glyoxylic acid monohydrate was converted to the α,β-unsaturated ester **J**.[56] The first new step in this work was to chemoselectively reduce the ester group of **J** in the presence of its carboxylic acid functionality[57] to give the hydroxyacid **5**[58,59] which was isolated via acid-base extraction. Subsequently, the hydroxyacid **5** was esterified to give the known[60] hydroxyester **6**. None of the steps described in Scheme 3.1 involve column chromatography, and the synthesis can give tens of grams of the product **6**.

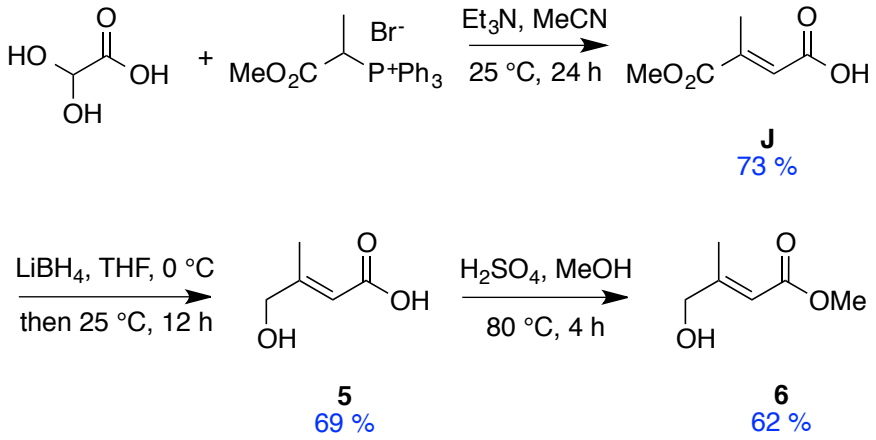


***Scheme 3.1.*** Scalable synthesis of the hydrogenation substrate **6**.

Hydrogenation of alkene **6** is the key transformation in this project (Scheme 3.2). Under the conditions shown in Scheme 3.2, approximately 15 g of the hydroxyester **6** can be hydrogenated with complete conversion to give **7** (a type **F** chiron), and the catalysts are still active at the end of this transformation. Even though the hydrogenation worked perfectly, only high, but not perfect, enantioselectivities were obtained. The acyclic product **7** was then lactonized to **8** then efficiently recrystallized under cold conditions to give optically pure material. For subsequent applications of these products (here and perhaps elsewhere), the lactone **8** was converted to two other potentially useful acyclic chirons, the alcohol **7** (now as one enantiomer) and the silyl ether **8**.

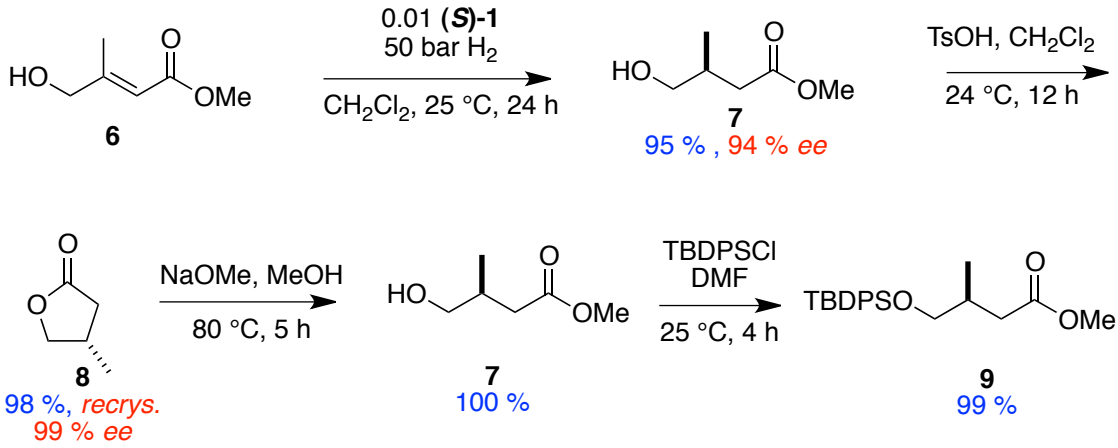


***Scheme 3.2.*** Asymmetric hydrogenation of alkene **6**, then recrystallization and TBDPS-protection to obtain ester **9**.

The ester **9** was given to me to perform the application via organocatalysis as described below in this chapter. To obtain an aldehyde **10**, the ester **9** was reduced using Brookhart's catalytic silylation/hydrolysis procedure[61] (reaction 3.1). This reduction afforded the aldehyde **10** in good yield for elaboration via organocatalytic processes involving iminium and enamine intermediates.

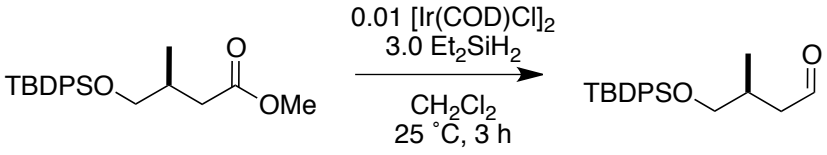


**9** **10** 75 %

*reaction 3.1*

### 3.2.2 Application With Organocatalysis

To the best of our knowledge, organocatalytic transformations of the *homo-Roche* aldehydes **10** have not been reported before. However, there is precedent for electrophilic α-substitutions of β-chiral aldehydes,[62] and, of course, a great deal of literature for the parent reactions of acyclic non-chiral aldehydes.[63] Catalysts and reagents for the organocatalytic transformation were chosen from a known literature[64-66] for each particular electrophiles then applied them to *homo*-Roche ester **9** (Figure 3.4).

*catalysts and reagents*

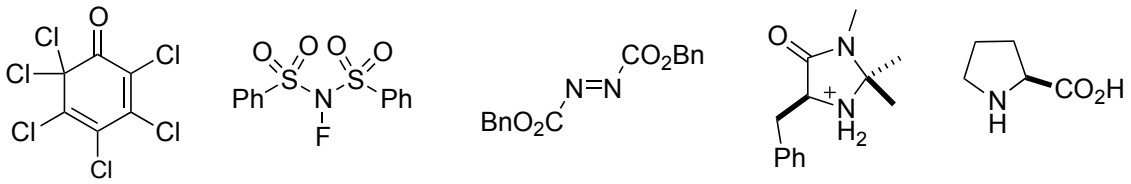


***Figure 3.4.*** Catalysts and reagents used in organocatalysis.

Scheme 3.3 shows the data accumulated for the organocatalytic transformations of aldehyde **10**. Part **a** refers to chlorinations performed using MacMillan's catalyst

**M•TFA**[67] (a commercial sample of the hydrochloride catalyst did not work in this reaction, so it was converted to the trifluoroacetate, *ie* the salt used by MacMillan's group). It emerged that the (*S*)-enantiomer of the catalyst matched[64] the substrate bias and gave an excellent stereoselectivity for the *syn*-isomer of **11** after borohydride reduction. However, in the mismatched case **(*R*)-M•TFA** overwhelmed the substrate bias hence a 10:1.0 ratio in favor of *anti*-**7** was observed. Similarly, MacMillan's fluorination procedure[65] using **(*R*)-M•$Cl_2HCCO_2^-$** gave even better matched and mismatched selectivities in catalyst-controlled reactions to give the 2-fluoroalcohols **12** after reduction. For amination reactions it was desirable to use d*ibenzyl* azocarboxylate rather than other alkyl derivatives for the reasons indicated below (Scheme 3.4), so we used List's procedure that described application of exactly that electrophile.[66] Just as in the chlorination and fluorination reactions, the aminations were catalyst-controlled. These transformations gave superb selectivity in the matched case for *syn*-**13**, and a 13:1.0 ratio for the *anti*-isomer via the mismatched process.

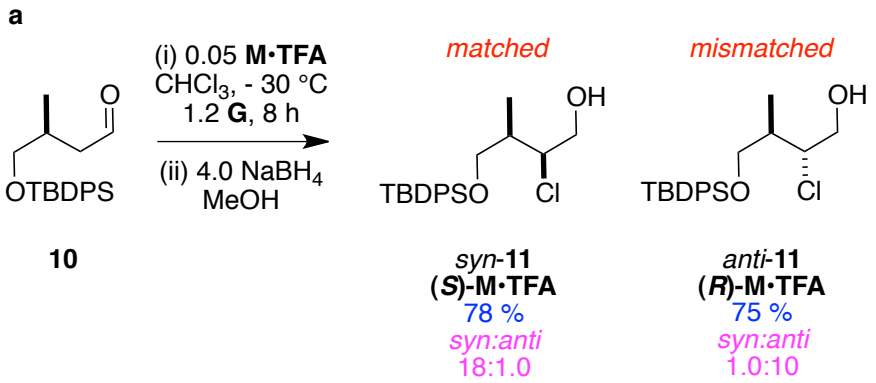


***Scheme 3.3.*** Asymmetric transformations of substrates **10**: **a** chlorination; **b** fluorination; and, **c** amination. Throughout, selectivities were determined via analytical HPLC on a Chiralcel-OD column.

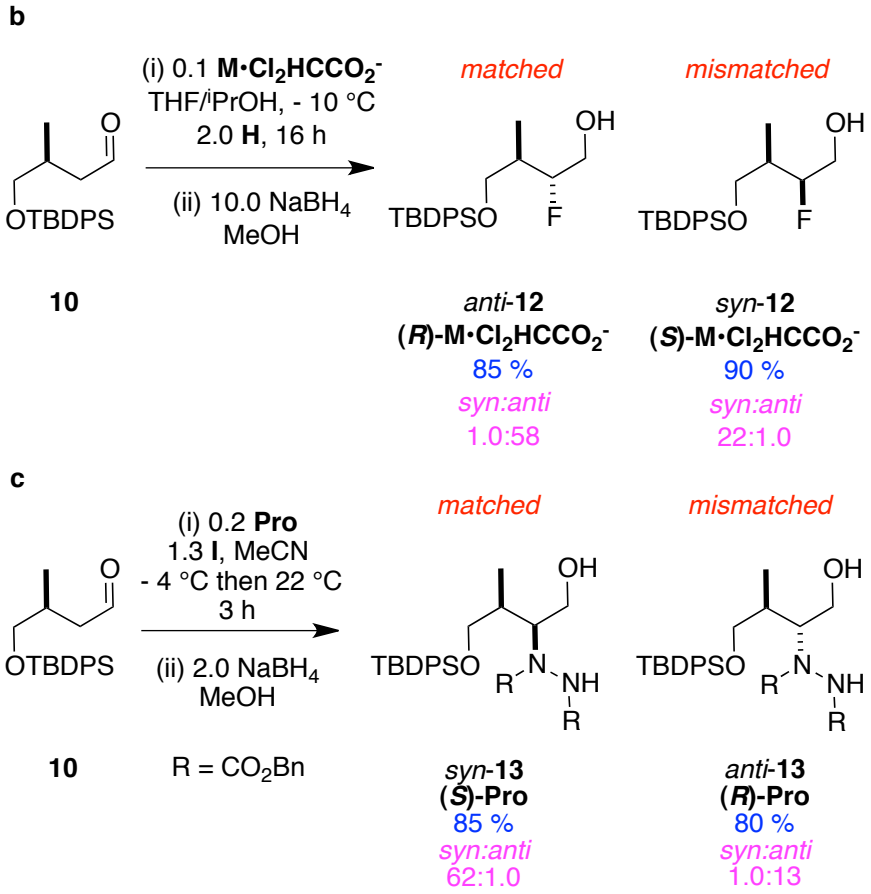


***Scheme 3.3.*** Continued.

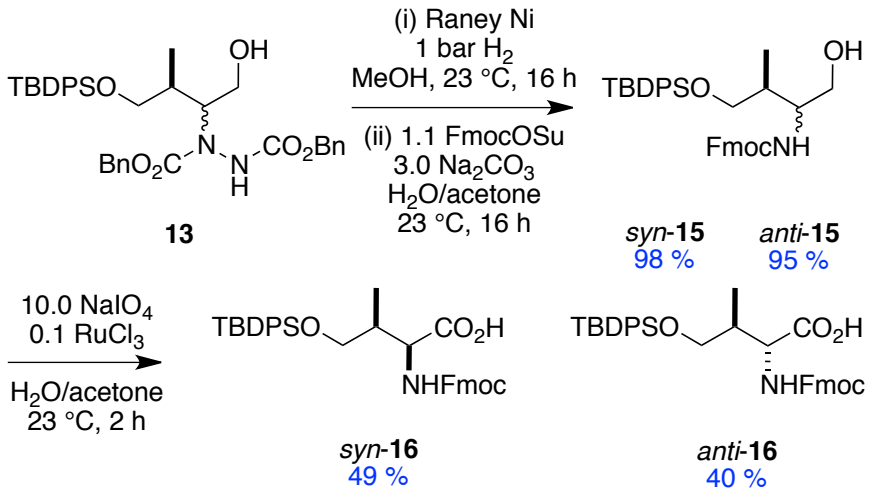


***Scheme 3.4.*** Syntheses of α-*N*-γ-*O*-protected forms of γ-hydroxyvaline.

Reactions 3.2 and 3.3 showed how the isomeric 2-chloroalcohols **11** were efficiently ring closed to the corresponding epoxides **14**. These reactions were performed because the epoxides **14** are valuable chirons, but their use has been limited by the fact that syntheses of these materials require multiple steps and some routes are only practical for one or two of the four possible stereoisomers.[68-70]

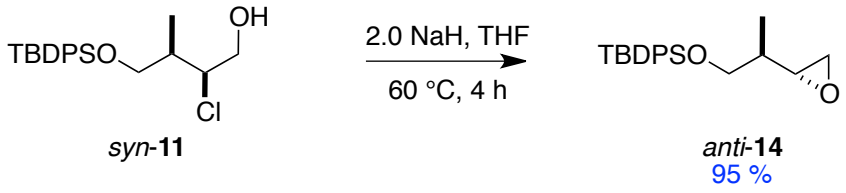


*syn*-**11** → *anti*-**14** 95 %

*reaction 3.2*

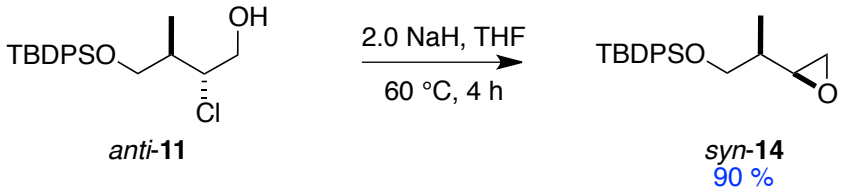


*anti*-**11** → *syn*-**14** 90 %

*reaction 3.3*

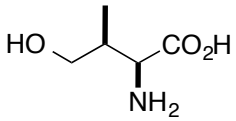


**P**

***Figure 3.5.*** Structure of γ-hydroxyvaline **P**.

Finally, derivatives of γ-hydroxyvaline **P** (Figure 3.5) were prepared to illustrate how the amination products **13** could be used in a novel short synthesis. γ-hydroxyvalines are naturally occurring amino acids that have been associated with stimulation of insulin secretion.[71] Hydrogenolysis of the benzyl protecting groups of **13** and simultaneous homolysis of the *N*-*N* bond gave the *N*-protected amino alcohols **15** after addition of Fmoc (Scheme 3.4). Catalytic oxidation of those alcohols gave the *N*-Fmoc-g-silyl protected amino acid **16**. All four stereoisomers of **16** could be obtained

using this route, and one enantiomer of each of the *syn*- and *anti*-forms was made to prove this. The final products **16** are suitably protected for many peptide synthesis strategies, so no attempt was made to obtain the corresponding g-hydroxyvalines since we have no immediate application for these. The synthesis of the 2*S*,3*S*-*syn*-isomer was performed on a large enough scale to obtain 0.42 g of product. Previous syntheses of g-hydroxyvaline derivatives required either 12 steps to obtain an enantiomer of the *N*-BOC-*O*-PMB-protected form of the reduced product (*ie* alcohol not carboxylic acid),[72] or via multistep routes to *syn*,*anti*-mixtures of various protected derivatives that were then separated (via crystallization of diastereomeric copper complexes,[73] or via column chromatography[74]).

### 3.3 Conclusions

The pivotal observation in this paper is that we may use type-**H** trisubstituted alkenes, specifically **9**, to give the same product that would be formed from hydrogenation of itaconic acid (or the diester) *and* differentiation of the two carboxylate groups (then reduction). Key to this study is the fact that chiral Crabtree's analogs like ***(S)*-1** can mediate hydrogenations of trisubstituted alkenes without suitable coordinating functional groups (CFGs) for binding Rh-centers. Fortunately, the starting material **9** is also easy to make and this facilitates the whole process.

Prior to our studies, Alexakis and Mazet elegantly combined enantioselective iridium-mediated isomerization reactions[75-78] with organocatalytic functionalization of aldehydes to form two chiral centers.[62] The work we have performed here is conceptually similar except that it is based on production of a particularly high-value chiron, the *homo*-Roche ester, and elaboration of that in distinct steps.

# CHAPTER IV
# SYNTHESIS AND CONFORMATIONAL ANALYSIS OF CYCLIC TETRAPEPTIDE

## 4.1 Introduction

Cyclic tetrapeptides (CTPs) have been known for decades, mostly as natural products.[8-10] However, to the best our knowledge, there are no applications of CTPs as probes for targeting proteins in living cells. Several reasons for this include but not limited to: inefficient synthesis, instability to hydrolysis/metabolism, and conformational heterogeneity in water.[9,79,80] Therefore, this chapter will disclose research works on molecular design and synthesis of CTPs.

### 4.1.1 Synthesis of CTPs

Previous syntheses of CTPs involve proline and/or glycine. Proline facilitates syntheses of CTPs because *cis*-conformations are far more thermodynamically accessible, and this "forces" the peptide to turn, so that *C*- and *N*-termini can come together for cyclization.[11-13] Glycine residues, having no side-chains, similarly allow conformations that are favorable for cyclization because a greater range of $\phi$ and $\psi$ angles are available around Gly than for any other amino acid. Combinations of Pro-Gly in linear precursors to CTPs are particularly favorable because that motif is highly conducive to turn conformers that facilitate cyclization. For these reasons, the overwhelming majority of synthetic CTPs reported contain Pro and/or Gly.

CTPs that have been made via conventional peptide syntheses which do *not* contain Pro or Gly, are rarely reported. Specifically, Ngu-Schwemlein prepared c{Leu-dAla-X-dAla} where X is Leu, Lys, and Glu via solution phase synthesis.[14]

In 2003, Smythe made a breakthrough in CTP synthesis by ring contraction.[15] Smythe's approach, however, had serious weaknesses and limitations. One problem was that the contraction intermediate seemed to *reform* under the conditions for photolytic

cleavage, leading to hydrolysis. It represents a step towards solving the problem of forming CTPs not containing Gly or Pro.

In 2013, there is a paper on syntheses of CTPs[17] that introduced a breakthrough synthesis. Li's innovation was to prepare tetrapeptides with *N*-terminal Ser or Thr, and *C*-terminal phenolic esters derived from salicylic aldehyde; the aldehyde can condense with *N*-terminal Ser or Thr. Subsequent *O,N*-migration, then acidolysis gives the CTPs as illustrated in Figure 4.1. A critical feature of this sequence is that the aminal formed after condensation/*O,N*-migration can, like Pro, easily access *cis*-amide conformers and this facilitates its formation. Li made *nine* cyclic tetrapeptides that do not contain Pro or Gly using this method.

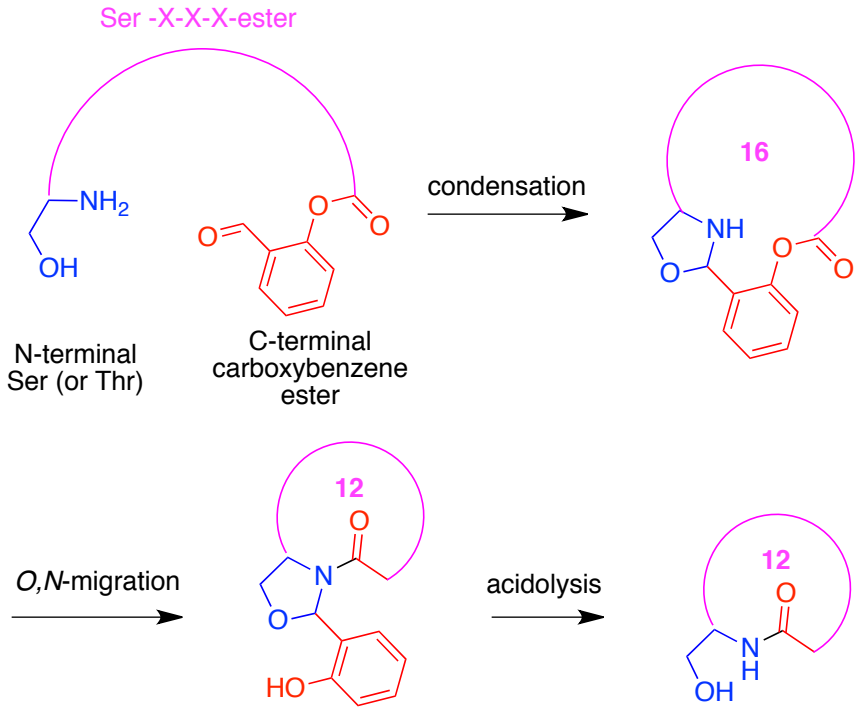


***Figure 4.1.*** Li's ligation method forms a proline like intermediate from a salicylic aldehyde ester.

Li's method is not flawless. Ozonolysis is required to cleave the intermediate molecules off the solid phase support. This step will also oxidize Trp, Cys, and Met residues. This is unfortunate because Met and Trp are common residues in PPI

interfaces,[81] and we need to include these in our probes. After cleavage via ozonolysis, the linear peptide precursor is purified via reverse phase HPLC, then rpHPLC is used again to purify the cyclized form. One rpHPLC purification is tolerable in solid phase syntheses, but two tend to give poor overall yields and slow the whole process. We therefore propose an efficient solution phase synthesis of CTPs. Our proposed *solution* phase synthesis of CTPs will also be the favored route for scaled-up (larger scale) synthesis.

### 4.1.2 Conformational Analysis Of CTP

In terms of conformational analysis, our interpretation of the literature is that CTPs which contain Gly and/or Pro *are* conformationally heterogeneous. It is supported by the work of Smythe who made 46 CTPs, all but one contained Gly and/or Pro, and only the one that did not was conformationally *homogeneous*.[16] Provided we have not missed a reference, these are the CTPs without Gly and Pro that have been prepared to date: c{Leu-dAla-X-dAla} (X = Leu, Lys, and Glu) by Ngu-Schwemlein,[14] Smythe's c{His-dArg-Phe-dTrp},[16] and nine others by Li. Of these, only c{Leu-dAla-X-dAla} (X = Leu, Lys, and Glu) and c{His-dArg-Phe-dTrp} have been studied to elucidate their conformations; Li did not comment on analyses for CTPs conformations. In other words, the only CTPs for which the conformations have been studied are the four cases listed above, and these are the ones which have alternating D- and L-amino acids.

We propose that CTPs, which do not contain Gly and/or Pro, *are* conformationally homogeneous. This chapter discloses our investigation on how stereochemistry of side-chains affects the conformation. QMD calculations[18,19] allow us to elaborate on this hypothesis, and make some predictions with a high degree of confidence. QMD can equilibrate conformations of *minimalist mimics* (semi-rigid small molecule scaffolds bearing amino acids side-chains) which can resemble several different secondary structures simultaneously.[17] QMD is ideal for simulating large numbers of conformers at a high temperature then *instant* cooling to 0 K. Typically QMD can reveal over 1000 conformers within 3 kcal/mol of the apparent global minima,

whereas other techniques might converge to just a few, or even just one, preferred conformer. The rapid cooling makes sure we can obtain thousands of accessible conformations in solution. Specifically, all diastereomers of c{Ala-Ala-Ala-Ser} were examined via QMD using a continuous dielectric medium of 80. Three Ala residues were chosen to represent the *C*α-*C*β vectors of three side chains (this is the key predictor of side-chain orientations). QMD runs for each stereoisomer to give 1500 conformations. In each case, all the conformers generated within 3 kcal•mol$^{-1}$ of the lowest energy one identified (>1000 in each case) overlaid with each other within and RMSD of 0.1 Å based on the side-chain Cα-Cβ vectors: on the basis of this observation we hypothesize, with a high degree of confidence, that each diastereomer is conformationally homogeneous.

### 4.1.3 EKO Analysis On CTPs As Small Molecules

The project will be to improve design methods for discovery of selective pharmacological probes based on CTPs for disruption of PPIs involved in cell signaling processes. We published a technique called EKO (Exploring Key Orientations), that can be used to match certain small molecule chemotypes to particular PPI interfaces. It is a strategy that uses QMD to sample a large number (*eg* 1500) of accessible conformers of a chemotype, and stores α,β-coordinates for each three side-chain set in a database, which covers interface regions in crystallographically characterized PPIs. Then in a data mining operation, an algorithm systematically overlays each set of coordinates from the accessible conformations with each set of side-chain coordinates, produces root mean square deviations (RMSD Å) for the overlays, ranks goodness of fit, and notes the relative energy of that conformation.

EKO begins with semi-rigid small scaffolds that bear at least three amino acid side-chains. Those chemotypes are not new; there are numerous reports of such *minimalist* secondary structure mimics (reviewed by us)[113] and some of them have been applied to perturb PPIs. However, we pointedly exclude ones that are too flexible (more than 4 or 5 freely rotating bonds in the scaffold is not ideal). We also exclude minimalist

mimics that cannot be prepared with side-chains corresponding to most of the genetically encoded amino acids; many of the published minimalist mimic designs are difficult to functionalize in this way. We suggested that molecules of this kind (*ie* within the limitations above) are preferred chemotypes for perturbing PPIs irrespective of the secondary structures at the interfaces.

EKO can be used in complementary ways that we call *biology- and chemistry-centered*. The biology-centered approach selects *one* PPI of particular interest, and evaluates accessible conformations for *several* mimics against the interface region(s) involved. Like high throughput screening, the target is decided first *then* researchers try to find chemistry to fit.

*Chemistry-centered* implementations of EKO compare conformations of *one* molecule with vast numbers of crystal structures of PPI interface regions. This is like affinity chromatography of cell lysates using a small molecule bait. When we reported EKO earlier this year, the database that we used contained 53,000 crystallized PPIs (those in the PDB up to the end of 2007) and a supercomputer employed to do the data mining. Due to recent developments, we are now able to evaluate over 120,000 structures involving PPIs (2012) on a desktop computer in about 6 – 10 h. Expansion of the PPI database to cover 2008-2012 is highly significant because the most interesting structures tend to be the newest ones. Additionally, now we can conveniently extract the more interesting *heterodimeric* PPI hits from the *homooligomers* whereas this was not an option before.

Our preferred mode of action is to find PPI targets using the chemistry-driven approach, then elaborate on the results using the biology-centered strategy using the hit PPIs; that means the hits follow naturally from the proposed chemotypes, and we are not trying to force the chemistry onto particular PPIs. This was the strategy used for in the current application to identify the featured PPIs. This strategy is also logical from a computational perspective. EKO in the chemistry-centered approach uses less conformers (select ones sorted for diversity) than when it is run in the biology-centered way. Our hypotheses for CTPs that will perturb TNF-TNFR2 emerged because from

chemistry-centered hits for one mimic; then we used the more thorough biology-centered strategy to evaluate all 8 diastereomers of c{Ala-Ala-Ala-dSer} as interface mimics for this PPI.

### 4.1.4 CTPs Targeting TNF-TNFR2 As Small Molecules

TNF•TNFR2 was a heterodimeric protein complex that EKO highlighted by matching conformers of the fundamental CTP scaffold with the 120,000 PPI interface database in a chemistry-centered approach. TNF, a pleiotropic cytokine, is overproduced in secretory fluids of patients with chronic inflammatory diseases, and is implicated in angiogenesis.[83,84] Most TNF-related toxicities are mediated through activation of the nuclear transcription factor, NF-κB[85-87] which regulates the expression of various genes that play critical roles in apoptosis, viral replication, tumorigenesis, autoimmune diseases, and inflammation. Activation of TNFR2 is thought to be associated with autoimmune diseases.[88] Blocking TNF induced inhibition of NF-κB is therefore a good *in vitro* model for anti-inflammation. Another good indication of anti-inflammatory activity by TNF antagonists is downregulation of *c-Jun* kinase. This is one of the mitogen-activated protein (MAP) kinases involved in a variety of cellular responses mediated by cytokines (including TNF), hormones, and stress-inducing reagents.[89] The activator protein-1 (AP-1), a transcription factor, is regulated, at least in part, by phosphorylation mediated by *c-Jun* kinase.[90] *c-Jun* also plays an important role in the regulation of cellular proliferation.[91]

CTPs can be potential small molecule probes to selectively perturb TNF-TNFR2 PPI. To the best of our knowledge, the only small molecule inhibitor of TNF-α was developed by Cunningham's group.[109] The compound composed of trifluoromethylphenyl indole and dimethyl chromone moiety linked by a dimethylamine spacer. It inhibited TNF-α binding to its receptor 1 (TNFR1) by displacing one of the subunits from the TNF-α trimer. The resulting TNF-α dimer maintained the same basic structural subunit fold as the trimer, but it lost the ability to bind to TNFR1. And to date, there is no small molecule that can inhibit TNF-a binding to TNFR2. Therefore, we are

pleased to see that CTPs have the potential to disrupt TNF-TNFR2 PPI. The biology-centered approach of EKO also suggested that CTPs not only overlays on TNF-TNFR2 interface, it can also overlay on TNF-α trimer.

## 4.2 Results And Discussion

### 4.2.1 Synthesis Of CTPs

A key feature of our strategy toward CTP synthesis is the use of methyl 3,4-diaminobenzoate **17** as *N*-terminal (Scheme 4.1). This was incorporated because conversion to the derivative **22** would afford a leaving group as described by Dawson.[82] It is encouraging to see that, the solubility characteristics of the 3,4-diaminobenzoate moieties are such that the intermediates can be precipitated from dichloromethane solution in high purity (NMR) and with good recovery; this greatly expedites the synthesis. Phenylalanine is introduced to increase the solubility of the product. Intermediate **20** therefore would not precipitate out of dichloromethane. Fortunately, these intermediates are generally insoluble in diethyl ether regardless of amino acid side chains. After work-up and removal of solvent, and the product was washed by diethyl ether. It is pure without further purification. Linear tetrapeptide **21** was converted to **23** via a 3-step one-pot reaction. Acetal **23** was purified by flash chromatography, and then global deprotection followed by ligation afforded ligated product **24**, which was converted to final CTP **25** by acidolysis.

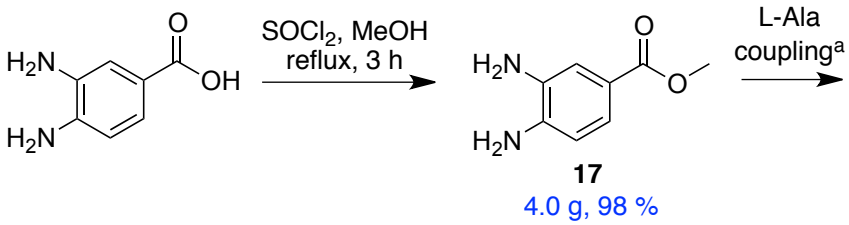


***Scheme 4.1.*** Solution phase synthesis of c{Ala-Ala-Phe-Ser}.

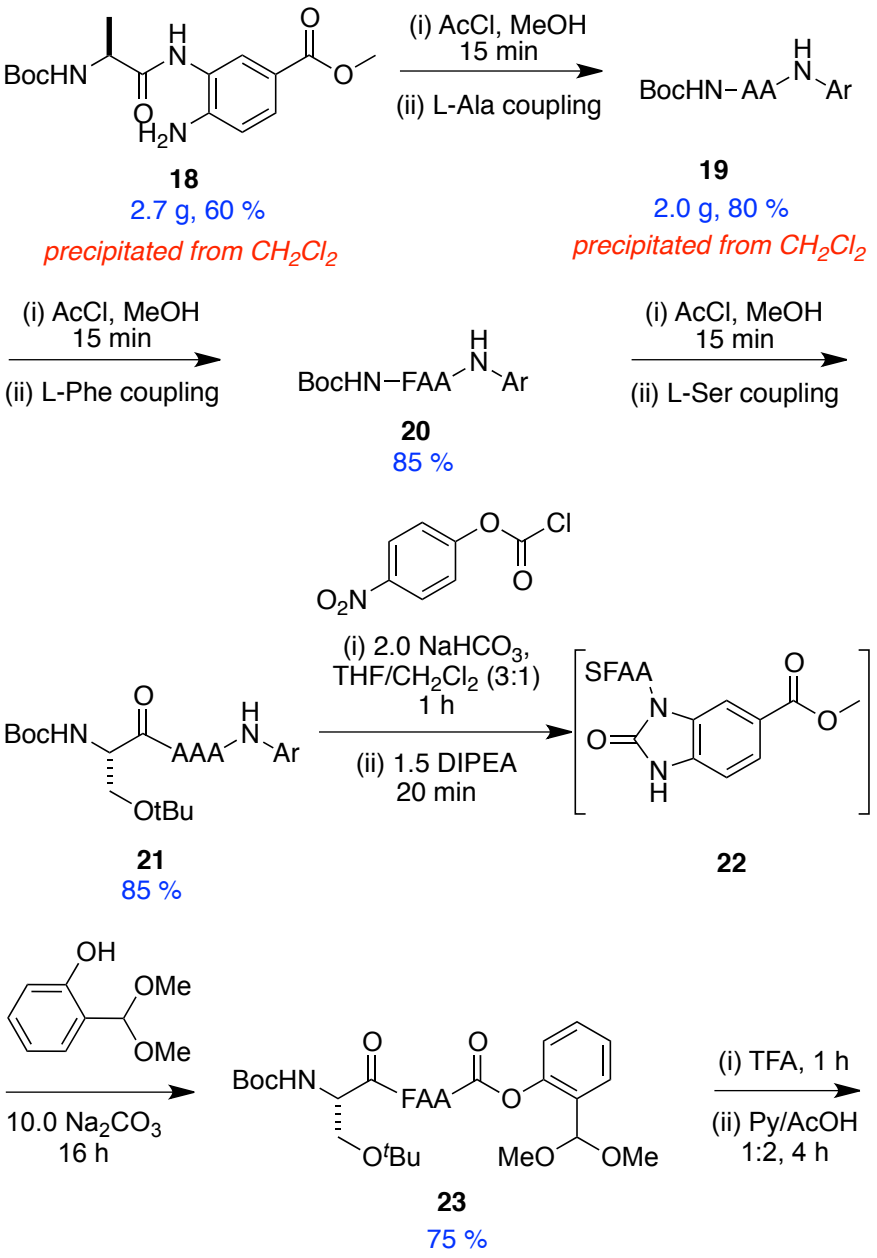


***Scheme 4.1.*** Continued.

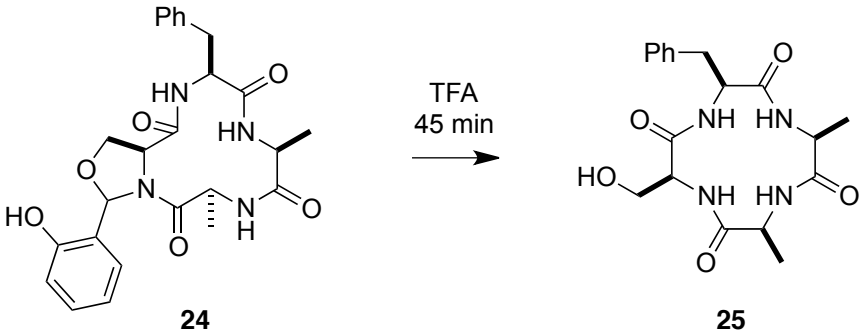


**24** **25**

10 %

a. coupling condition: 1.1 Boc protected amino acid, 1.2 HOBt, 1.2 EDCI, 5.0 $Et_3N$, $CH_2Cl_2$, 12 h.

***Scheme 4.1.*** Continued.

CTP **26** with three methyl side chains was the first targeted final product (Figure 4.2), because the same side chains are used in QMD studies. Unfortunately, due to the solubility and purification problems, CTP **26** has poor solubility in any solvent, which makes purification difficult. Li also made aldehyde **27** and proceeded to the ligation product, but no explanation was provided regarding why he did not pursue the final product.

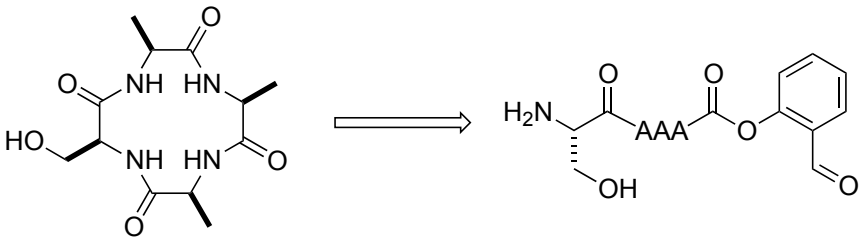


**26** **27**

***Figure 4.2.*** Preparation of c{Ala-Ala-Ala-Ser} **26**.

Several other CTPs were also attempted as shown in Figure 4.3. But most of them were stopped before the global deprotection stage. Our proposed *solution* phase synthesis of CTPs will be the favored route for scaled-up (larger scale) syntheses. It will also be used in an efficient divergent manner, as proposed in Figure 4.4 that covers

syntheses of all the isomers in one enantiomeric series of c{Ala-Ala-Phe-Ser}. These compounds are necessary for the conformational studies.

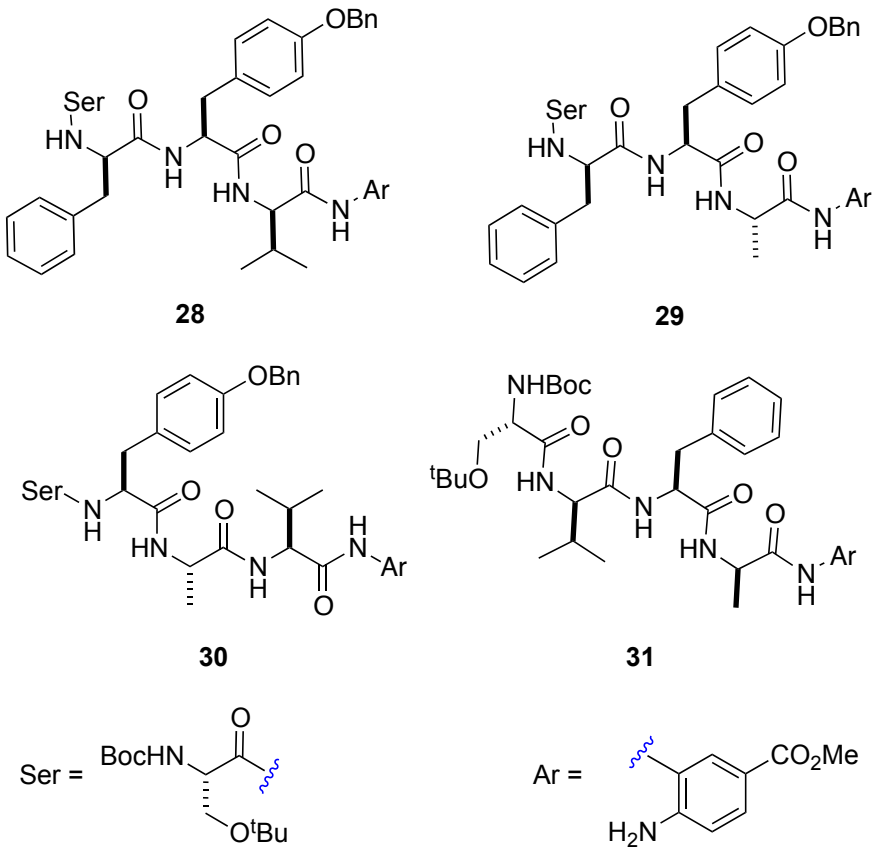


***Figure 4.3.*** Preparation of other CTP precursors.

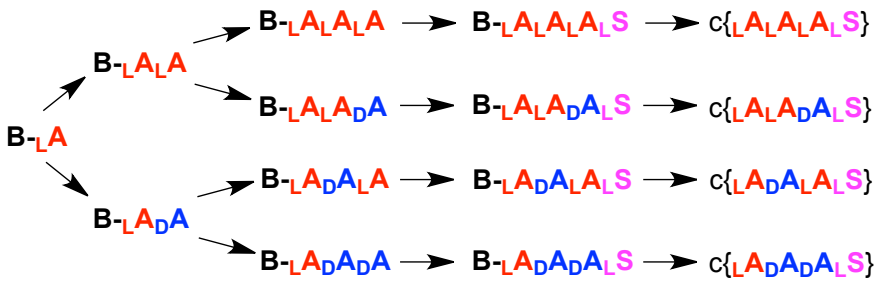


***Figure 4.4.*** Divergent synthesis of 8 diastereomers of CTPs.

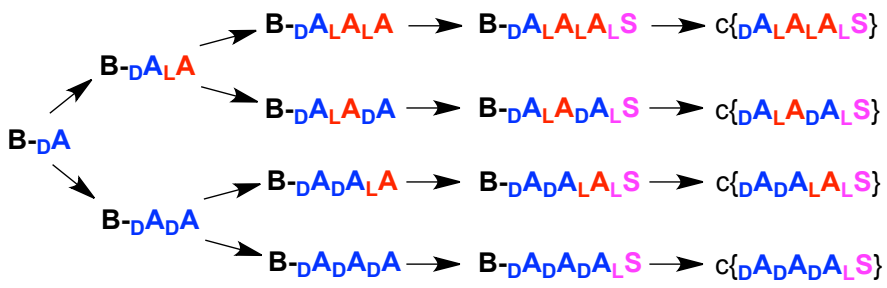


***Figure 4.4.*** Continued.

### 4.2.2 Conformational Analysis Of CTP

The divergent synthesis then motivated us to explore whether CTPs exist in one predominant conformation, and, if so, can that be correlated with the stereochemistries of the amino acids in the macrocycle.

The features of conformation of each diastereomer is as follows: off-axis-top, and equatorial side, views of the anticipated preferred conformations of each c{Ala-Ala-Ala-Ser}diastereomer are shown in Figure 4.5. Throughout, L-amino acids are colored purple, D-isomers are shown in green, and the LSer residue is oriented on the "Eastern" side of the molecule. For c{Ala-Ala-Ala-Ser} (abbreviated to LSerLLL in Figure 4.5.) all the NH atoms are pointing towards the North pole, and all the side-chains are splayed out in equatorial positions skewed towards the Northern hemisphere. In LSerLLD, the methyl group of the DAla is in an equatorial position but skewed towards the *Southern* hemisphere, and the NH atom of that amino acid now points towards the *South* pole. All the methyl groups and NH atoms for the other, L-stereochemistry, amino acids remain oriented as they are in the parent structure, LSerLLL. Careful consideration of all the other diastereomers in the series show the same trend: when the conformers are oriented with the Ser in the Eastern position and the Ser side-chain equatorial in the Northern hemisphere, then: (i) all the LAla residues have NH atoms that point towards the North pole, and methyl groups in equatorial positions over the Northern hemisphere; and, quite logically, (ii) all the DAla residues have NH atoms that point towards the South pole, and methyl groups in equatorial positions over the Southern hemisphere. This bias is true for all the diastereomers, irrespective of how many D-amino acids are incorporated.

Mathematically, that means ϕ,ψ, (Table 4.1) are uniformly *ca* -140, -18 degrees for L-amino acids, and +140, +18 for their D-isomers (within about 15° tolerance, maximum, shown in Table 4.1). The ϕ and ψ angles in the CTPs adjust so that the N-H bond vector always dissects Me-αC-CO, and the C=O vector similarly dissects Me-αC-H, irrespective of the amino acid stereochemistry.

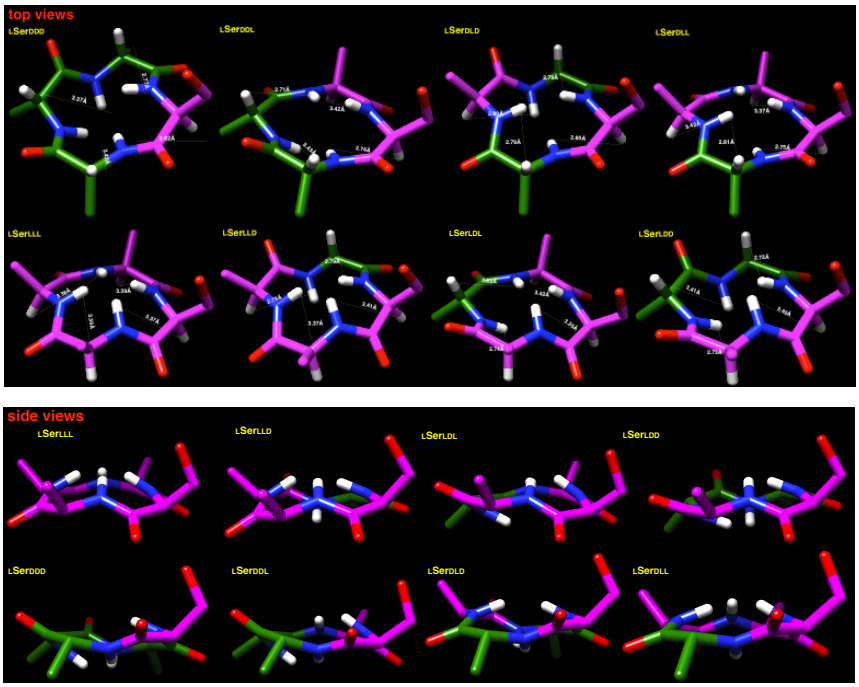


***Figure 4.5.*** Systematic stereomutation of amino acids in CTPs causes the preferred conformers to invert in logical stages from dome to basin shapes. L-amino acid is colored purple and D-amino acid is colored green.

***Table 4.1.*** Phi/Psi angle measurement of each c{Ala-Ala-Ala-dSer} diastereomer.

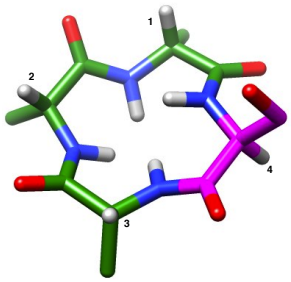

***Table 4.1.*** Continued.

| | Ha | phi (˚) | psi (˚) | NH-Ha (Å) |
|---|---|---|---|---|
| DDD | 1 | -148 | 27.8 | 2.82 |
| | 2 | 140 | 21.6 | 3.43 |
| | 3 | 136 | 12.9 | 3.37 |
| | 4 | 141 | -33 | 2.77 |
| DDL | 1 | -143 | 32 | 2.74 |
| | 2 | 144 | 20.4 | 3.43 |
| | 3 | 143 | -35.8 | 2.71 |
| | 4 | -143 | -18.6 | 3.42 |
| DLD | 1 | -142 | 29 | 2.8 |
| | 2 | 143 | -30.4 | 2.79 |
| | 3 | -143 | 29.9 | 2.8 |
| | 4 | 143 | -30 | 2.79 |
| DLL | 1 | 143 | 32.5 | 2.75 |
| | 2 | 148 | -29 | 2.81 |
| | 3 | -140 | -21.1 | 3.42 |
| | 4 | -136 | -12.5 | 3.37 |

| | Ha | phi (˚) | psi (˚) | NH-Ha (Å) |
|---|---|---|---|---|
| LDL | 1 | -136 | -11.8 | 3.35 |
| | 2 | -143 | 34.5 | 2.74 |
| | 3 | 147 | -29.9 | 2.82 |
| | 4 | -140 | -21.5 | 3.42 |
| LLD | 1 | -140 | -19.5 | 3.41 |
| | 2 | -137 | -13.9 | 3.37 |
| | 3 | -142 | -35.3 | 2.73 |
| | 4 | 147 | -29.6 | 2.79 |
| LDD | 1 | -143 | -19.3 | 3.4 |
| | 2 | -143 | 34.3 | 2.73 |
| | 3 | 142 | 19.6 | 3.41 |
| | 4 | 143 | -35.1 | 2.72 |
| LLL | 1 | -137 | -21.7 | 3.37 |
| | 2 | -138 | -15.4 | 3.39 |
| | 3 | -135 | -14.7 | 3.38 |
| | 4 | -138 | -14.5 | 3.39 |

To test our hypothesis regarding correlation of stereochemistry and preferred conformations of non-Pro/Gly CTPs, we propose to: assign all proton NMR peaks using HSQC and COSY; measure N<u>H</u> to αC<u>H</u> $^{3}$J coupling constants; measure through-space inter-residue contacts via 2D-NOESY (large N<u>H</u> to N<u>H</u> and small N<u>H</u> to αC<u>H</u> cross peaks are expected in cases where the N<u>H</u> atoms point to the same pole, but we predict N<u>H</u> to N<u>H</u> interactions will be reduced and N<u>H</u> to αC<u>H</u> interaction will be increased between amino acids of different stereochemistries).

### 4.2.3 EKO Analysis On CTPs As Small Molecules

When EKO was applied to all 8 stereomers of c{Ala-Ala-Ala-dSer} screening over 120,000 PPI interfaces, we found about 6,500 protein targets and they were further

narrowed down to about 300 heterodimeric protein targets (Appendix D). A brief summary of targets is shown in Table 4.2.

***Table 4.2.*** Summary of mining results of c{Ala-Ala-Ala-dSer} with RMSD< 0.3 Å.

| CTP | Interesting Targets | pdb ID |
|---|---|---|
| LLL | none | |
| LLD | HIV-1 reverse transcriptase | 1hys |
| LDL | Human alpha thrombin<br>Serine/threonine kinnase PAK1<br>Extracellular domain of human EGF | 1bhx<br>1f3m<br>1nql |
| LDD | CDK2/Cyclin<br>HIV-1 reverse transcriptase<br>Paf-AH Holoenzyme | 1h1q<br>1hys<br>1vyh |
| DLD | Human alpha thrombin<br>CDK2/Cyclin interface | 1bhx<br>1h1q |
| DLL | Human Angiogenin<br>IL4-IL4R-IL13Ra ternary complex<br>PCSK9 | 1h0d<br>3bpn<br>3h42 |
| DDL | Protein phosphatase 2A core enzyme<br>TNF-TNFR2 complex<br>PCSK9 | 2ie3<br>3alq<br>3h42 |
| DDD | Human alpha thrombin | 1bhx |

We find that CTPs *can* overlay with *loop* regions with *i, i* +1, *i* + 2 arrangement. Three targets are chosen as examples shown in Figure 4.6.

Interleukin-4 is a cytokine critical to the development of T cell mediated humoral immune responses, which are associated with allergy and asthma. The actions of interleukin-4 were exerted through different combinations of shared receptors.[110] Therefore, disruption of the interaction between interleukin and its receptor can inhibit activities of interleukin-4. IL4-IL4R complex was recrystallized with 2.9 Å resolution. c{dAla-Ala-Ala-dSer} overlaid on receptor IL-4Ra (light blue) at Lys-290, Leu-291 and Cyc-292 of its interface with IL4 (green).

Low-density-lipoprotein (LDL) receptor-related proteins 5 and 6 (LRP5/6) are Wnt co-receptors essential for Wnt/β-catenin signaling. Human LRP6 complexed with Dickkopf 1 (Dkk1) was recrystallized with 2.8 Å resolution. Dkk1 inhibits Wnt signaling by interacting with the extracellular domains of LRP5/6, which is a drug target for multiple diseases.[111] c{Ala-dAla-dAla-dSer} overlaid on LRP6 at Asp-191, Thr-192, and Asn 193 of its interface with Dkk1.

**i.**

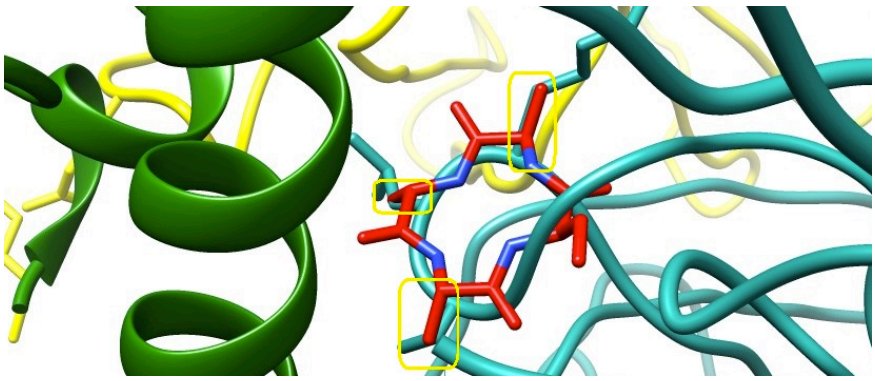

**ii.**

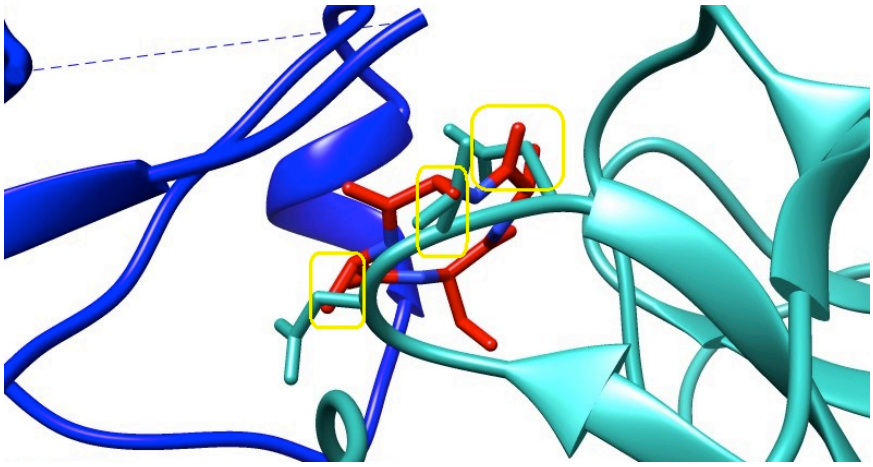

***Figure 4.6.*** **i.** c{dAla-Ala-Ala-dSer} overlaid on crystal structure of the IL4-IL4R ternary complex; **ii.** c{Ala-dAla-dAla-dSer} overlaid on crystal structure of LRP6-Dkk1 complex, it is low density lipoprotein complex; **iii-a** Target PPI interaction sites to perturb the TGF•EGFR interactions are boxed. From EKO, we hypothesize that CTPs can be made to perturb: **iii-b** the EGFR•TGF, and **iii-c** EGFR•EGFR interfaces.

**iii.**

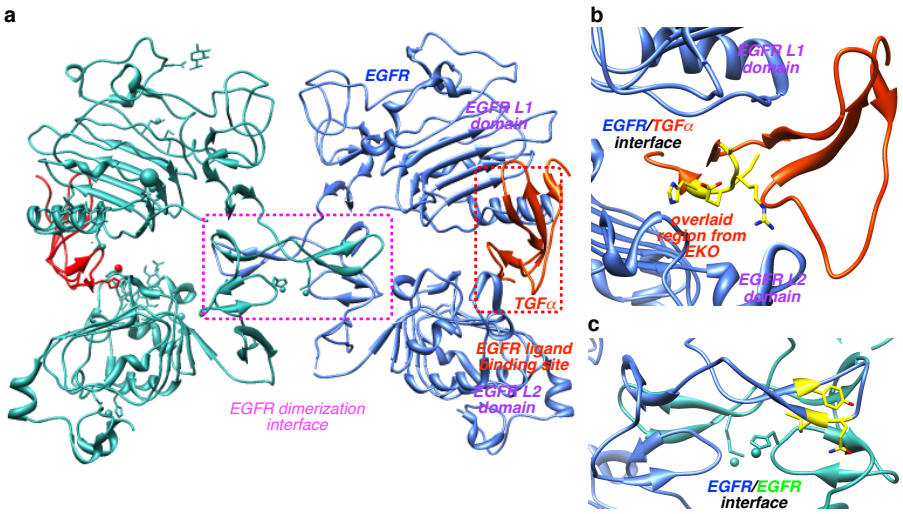


***Figure 4.6.*** Continued.

Epidermal growth factor (EGF) receptor is the prototype of the ErbB (HER) family receptor tyrosine kinases (RTKs), which regulate cell growth and differentiation and are implicated in many human cancers. The majority of small molecules designed to influence EGFR target the *kinase* domains,[99,104,105] not the PPIs.[106] When these are used as probes they can only shut down the tyrosine kinase activity, and most do this non-selectively (*ie* inhibit other kinases). Another probe class is large cyclic peptides that perturb the EGFR•EGFR interface; these have been shown to inhibit autophosphorylation of the Tyr-kinase and subsequent signaling.[107,108] The non-ligated, "inactive" form of EGFR (1IVO) rests in an autoinhibited conformation. On introduction of transforming growth factor-α (TGFα; 1MOX) (or EGF, not the focus here), the ligand binds two identical domains along the periphery of the EGFR dimer and causing conformational changes, but the EGFR•EGFR interface is maintained.[109,110] Mutagenesis studies on TGFα implicate Arg42 and Leu48 as key residues involved in binding EGFR.[111]

### 4.2.4 CTPs Targeting TNF-TNFR2 As Small Molecules

TNFR2 is one of the promising targets EKO found for CTP. Based on EKO c{dAla-dAla-Ala-dSer} overlays on TNF at the TNF-TNFR2 interface region: Phe-144, Ala-145, Glu-146 (RMSD 0.223 Å). Interestingly, TNF-TNFR2 interface has two hot-spot regions.[108] Region 1 consists of Asp54, Glu57, Glu70; Ser72 and Ser73 of TNFR2 forms H bond with Arg32 of TNF. Region 2 consists of Arg77, Lys108, Arg133; Arg113 and Arg77 of TNFR2 formed close contacts to Asp143, Gln149 and Glu23 of TNF. Loop 143-149 is believed to be a key interface region, because it is in a molecular pocket and is interesting target for TNF inhibition.[108] EKO analysis showed that CTP overlays on TNF at Phe-144, Ala-145 and Glu-146, which is located right on the loop.

We are therefore encouraged to apply EKO on TNF-TNFR2 for a thorough analysis. The results showed that the following CTPs have potential to bind at interfaces of TNF-TNFR2: c{dF-A-E-S}, c{dE-dA-F-S}, c{dY-dS-dV-S}, c{V-S-Y-S}, c{dY-dS-dV-S}, c{dE-dA-F-dS}, c{dF-A-E-dS}, c{dV-dS-dY-dS}, c{dY-dS-V-dS}, c{dV-S-Y-dS}, c{V-S-Y-dS}. It is interesting the EKOS finds pairs of hits like c{dY-dS-dV-S} and c{V-S-Y-S} where the sequence and stereochemistries are reversed as in retro-inverso peptides.[98] EKO analysis showed that c{E-dP-dL-dS} and c{dL-P-E-dS} can also overlay at the interface that forms the TNF trimer (Figure 4.7d ~ f).

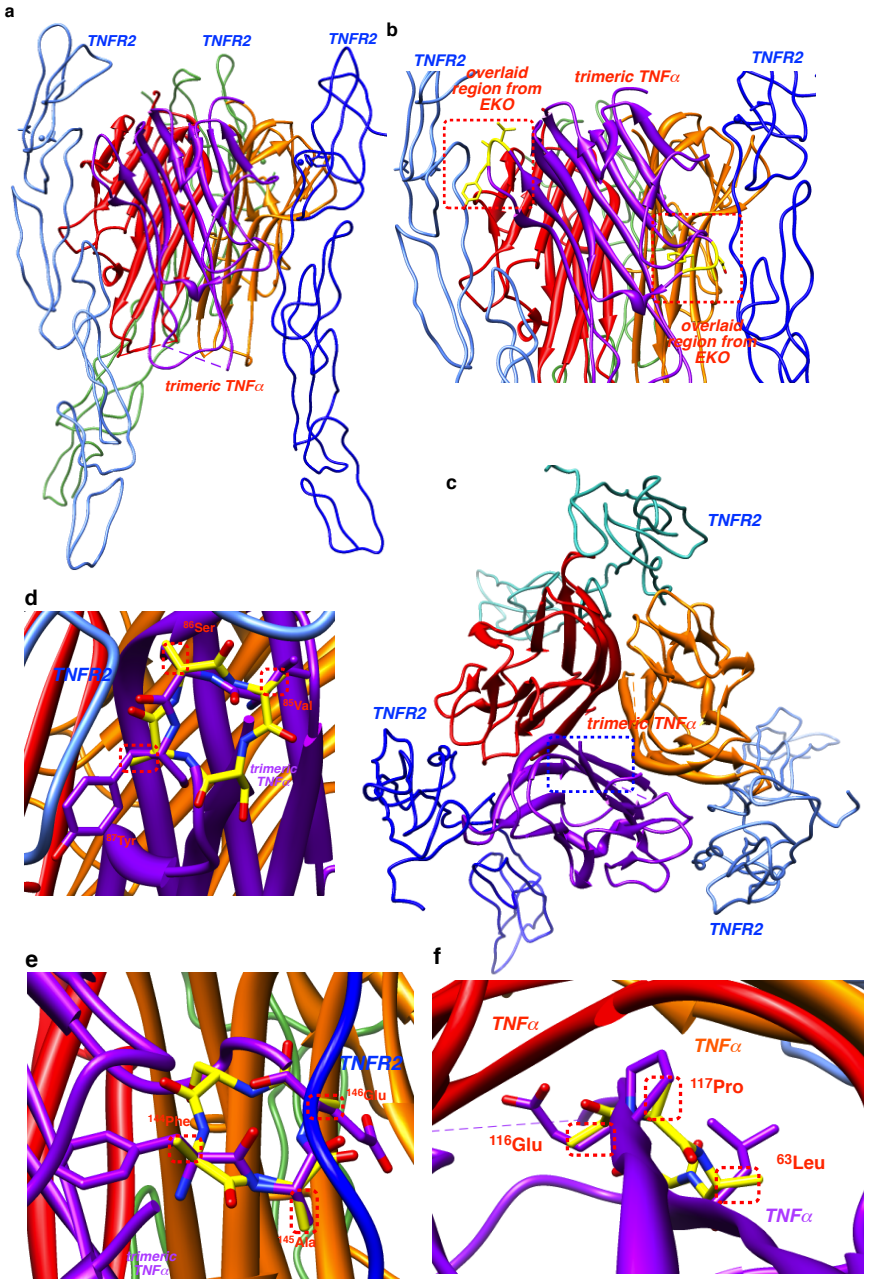


***Figure 4.7.*** **a.** Structure of TNF•TNFR2 (3ALQ);[99] **b.** Interface regions where CTPs are hypothesized to bind; **c.** Structure of the TNF trimer (top view, 3ALQ) showing where a CTP is predicted to perturb formation of the trimer; **d – f.** Expanded views of the CTPs overlaid on the relevant PPI regions.

## 4.3 Conclusions

The liquid phase reaction is a 12-step synthesis, which requires one step of flash chromatography and one prep HPLC purification process. The only drawback is that the poor solubility of cyclized intermediate in most solvent makes purification difficult. QMD study suggested that CTPs with no Pro/Gly are conformationally stable. It also provided insights on how side-chain orientations can change conformation of CTP scaffold.

CTPs are suggested to be good loop mimics by EKO analysis. EKO analysis also showed that CTP is a good interface mimic as it overlays on about 300 heterodimeric PPIs, some of which are related with cancer, obesity, HIV, etc. TNF-TNFR2 is a particularly interesting target found by EKO. Previous studies suggested that loop 143-149 on TNF is a key interaction region with TNFR2. Small molecules that overlay on this loop will be potential inhibitors of TNF-TNFR2 interaction. It is therefore encouraging to see that CTPs overlays right on this loop. The significance of this project is to show practical routes to small molecule probes that can be used to study cell signaling, and to inspire interest in design of molecules for biomedical applications.

# CHAPTER V

# EKO AND EKOS ANALYSIS ON OXOPIPERAZINE DIMERS

## 5.1 Introduction

Oxopiperazine dimers are molecules developed by Paramjit Arora as α-helical mimics.[102] He used macromodel MMFF force field to find the most stable conformations of oxopiperazine dimers and suggested they are α-helical mimics. He further suggested that a *trans*-amide bond geometry (Figure 5.1) was preferred over *cis* geometry and would place three side chains of the molecule in orientations to reproduce the arrangement of *i*, *i*+4, *i*+7 residues on an α-helix. Their molecular modeling studies of oxopiperazine dimers were supported by NOESY experiment, which showed that the *cis*-amide isomer did not exist; and the CD studies, which demonstrated that oxopiperazine dimers adopted stable α-helical conformation.

Oxopiperazine dimers were then studied by Dr. Arora as PPI inhibitors by a computational approach for peptidomimetic design called Rosetta,[112] and the oxopiperazine scaffold was first proved to be a p53/Mdm2 inhibitor. P53 activation domain targets Mdm2 with residues Phe19, Trp23, and leu26. The three residues formed key contacts between p53 and Mdm2. The modeling study suggested that if the side-chains are $R^1$=Phe, $R^2$=Trp, and $R^4$=Leu, the oxopiperazine dimers overlayed well at these three residues of Mdm2. The study was supported by binding affinity studies. If the Phe, Trp, and Leu residues at $R^1$, $R^2$, and $R^4$ were replaced by other amino acids such as alanine or lysine, it led to significant decrease in the binding affinities of the scaffold to Mdm2. The results suggested that the side chains in these positions on the oxopiperazine dimer are making substantial contact with the target interface.

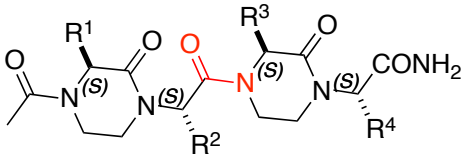


***Figure 5.1.*** Oxopiperazine dimer developed by Paramjit Arora.

Oxopiperazine derivatives were also proved to be a HIF1α/p300(CBP) inhibitor.[114] HIF1α had four helical residues (Leu818, Leu822, Asp823, and Gln824) closely contacted with p300/CBP, and Rosetta study predicted that oxopiperazine dimers could mimic three residues, Leu818, Leu822 and Gln 824. The Rosetta prediction was further proved by fluorescence-binding assay and NMR studies.

Oxopiperazine dimers were proved to be a set of molecules that are α-helix mimics and are able to mimic α-helical interfaces of PPIs. However, Dr. Arora did not consider all stereochemistry possibilities of the scaffold. When the stereochemistry varies, it is possible to result in different conformation, which leads to different secondary structure mimicry. We therefore introduce EKOS analysis to explore the full potential of oxopiperazine dimers as ideal secondary protein structure mimics.

EKOS (Exploring Key Orientations on Secondary-structures) was another technique published in our group.[21] Similar to EKO, EKOS begins with semi-rigid small scaffolds that bear at least three amino acid side-chains. EKOS also uses QMD (as described in previous chapter) to simulate a large number of accessible conformations for each minimalist mimic tested. Specifically, EKOS implements an algorithm that performs the following operations. For every secondary structure, EKOS determines α,β-coordinates for each possible combination of three side-chains (*ie* 6 coordinates), and stores them in a database. EKOS then performs a similar process on all the accessible conformers of a test chemotype, and stores them in another database (*eg* 1000 x {3 x – α,β coordinates} x {number of three side-chain combinations}, for 1000 conformers of a mimic with three side chains). Then, in a data mining operation, the algorithm systematically overlays each set of coordinates from each accessible conformation with each set of side-chain coordinates, produces a root mean square deviation (RMSD Å) for each overlay, ranks its goodness of fit, and notes the relative energy of that conformation.

EKO is also applied on oxopiperazine dimers to find potential PPIs. The three objectives of this chapter are: (i) EKOS analysis of oxopiperazine dimers to show

whether they can mimic on interfaces of other protein secondary structures besides α-helix; (ii) to show whether EKO analysis can find protein targets Mdm2 and p300/CBP that has been found by Dr. Arora, and (iii) whether EKO analysis can find other protein targets for oxopiperazine dimers.

## 5.2 Results And Discussion

### 5.2.1 QMD And EKOS Analysis On Oxopiperazine Dimers

Oxopiperazine dimers have four amino acid side chains. Dr. Arora's study showed that side-chains 1, 2, and 4 played a pivotal role in forming the helical mimic and side-chain 3 is not involved (Figure 5.2). Thus, the same three side-chains were used during QMD analysis and overlay process of EKOS analysis. The two studies were then applied to all sixteen stereomers of oxopiperazine dimers. The studies on eight diastereomers (the stereochemistry of uninvolved side-chain is *S*) are included in the thesis; the other eight (enantiomers) were accomplished by graduate student Maritess Aranallo, which is not included in the thesis.

When all three side-chains are derived from L-amino acid in the order of 1, 2, 4, the isomer is labeled as LLL; likewise when all three side-chains are derived from D-amino acid in the same order, the isomer is labeled as DDD.

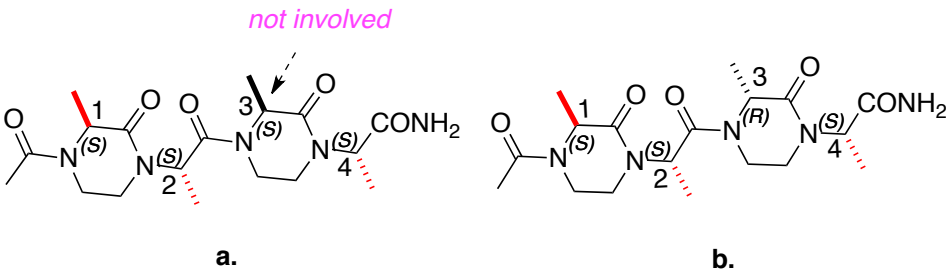


***Figure 5.2.*** Oxopiperazine dimers developed by Dr. Arora. **a.** Calculation results included in the thesis; **b**. Calculation done by Maritess Aranallo.

QMD calculations were performed with energy cutoff of 3.0 Kcal/mol and RMSD of 0.5 Å. All conformations were clustered based on Cα and Cβ coordinates of

side chain 1, 2 and 4. The number of clusters represents the number of significantly different conformations. As the QMD results suggested in Table 5.1, all stereomers of oxopiperazine dimers can adopt several conformations. For each isomer, there is at least one major cluster. The LDD isomer is the only one that has one predominant cluster (224 structures). The second cluster is considered a minor cluster as it contains 64 structures. The third cluster is insignificant as it only has 2 structures. The reason could be that the LDD isomer has four side chains with alternating stereochemistry (LDLD), if we include side chain 3. Such alternating stereochemistry may result in an extra stable conformation.

***Table 5.1.*** QMD calculation results of oxopiperazine dimers.

| Molecule ID | # of structures | # of clusters | Ratio of structure # among clusters |
|---|---|---|---|
| LLL | 540 | 6 | 134:85:240:33:37:11 |
| LLD | 621 | 8 | 129:48:34:39:211:27:131:2 |
| LDL | 389 | 7 | 155:60:42:72:41:14:5 |
| LDD | 294 | 3 | 224:68:2 |
| DLL | 625 | 6 | 261:104:10:27:24 |
| DLD | 741 | 9 | 189:122:86:101:60:53:10:10 |
| DDL | 632 | 8 | 200:173:81:18:13:13:18 |
| DDD | 325 | 3 | 104:203:18 |

QMD results clearly illustrated that oxopiperazine dimers could adopt more than one stable conformation. Change in stereochemistry of side chains also caused the change of conformations. Different conformations will cause different overlaying results on secondary protein structures. We therefore performed EKOS analysis to explore various possibilities of oxopiperazine dimers as protein secondary structure mimics.

EKOS analysis overlays oxopiperazine dimers onto seven ideal secondary structures: sheet-turn-sheet, antiparallel β-sheet, parallel β-sheet, β-strand, π-helix, α-helix, and 310-helix. Results of EKOS analysis are summarized in Figure 5.3. The middle line represents the average RMSD value. Each colored bar represents the RMSD

value of an ideal secondary structure. If the bar points to left, it means the RMSD value is better than the average; if the bar points to right, it means the RMSD value is worse than the average. For example, the average RMSD value of DLD isomer overlaying on seven ideal secondary structures is 0.49 Å. The RMSD for sheet-turn-sheet overlay (red bar) is 0.2 Å on left; that means the actual RMSD value is 0.29 Å. Likewise, the RMSD for β-strand overlay (green bar) is 0.3 Å on right; the actual RMSD value is 0.79 Å.

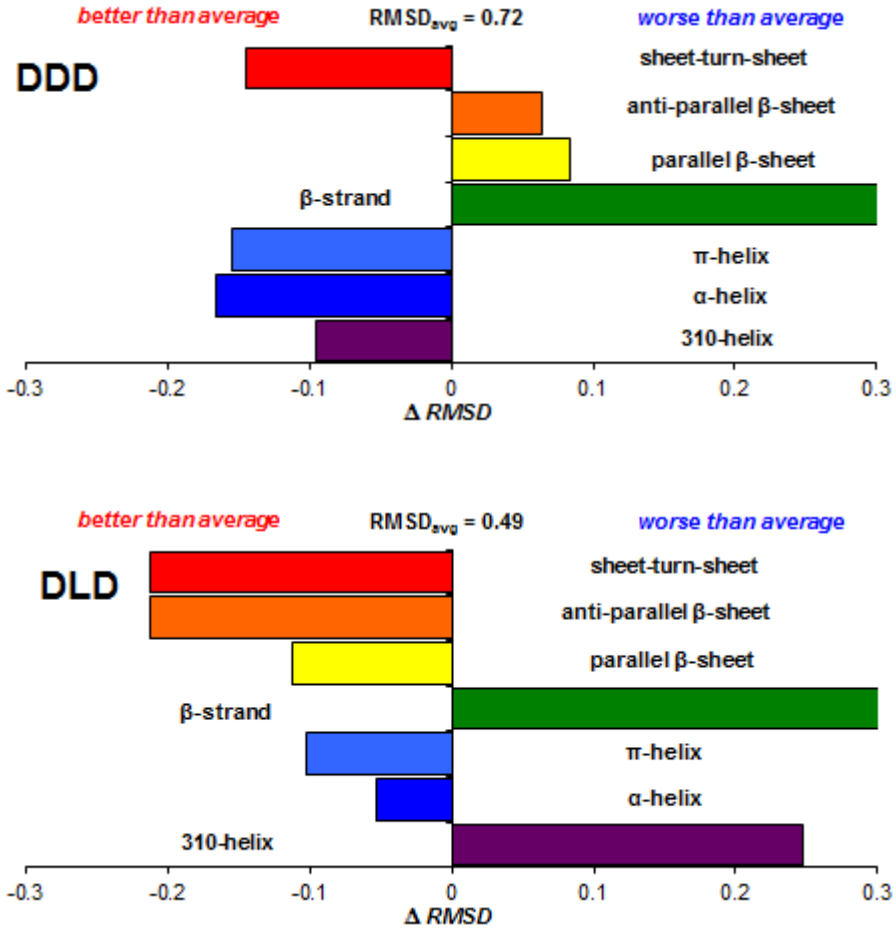


***Figure 5.3.*** Matching results of oxopiperazine dimers on ideal secondary structures calculated by EKOS.

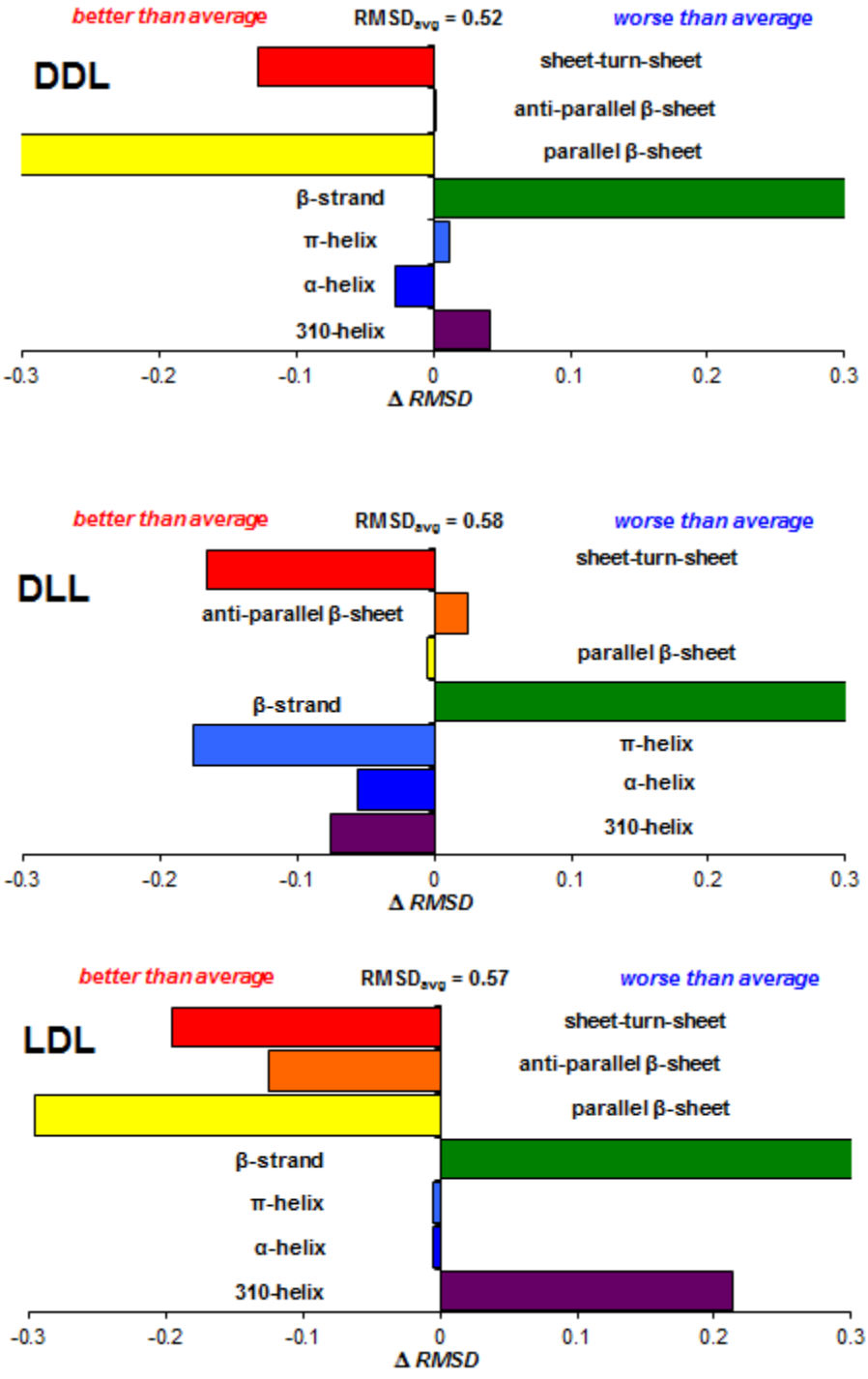


***Figure 5.3.*** Continued.

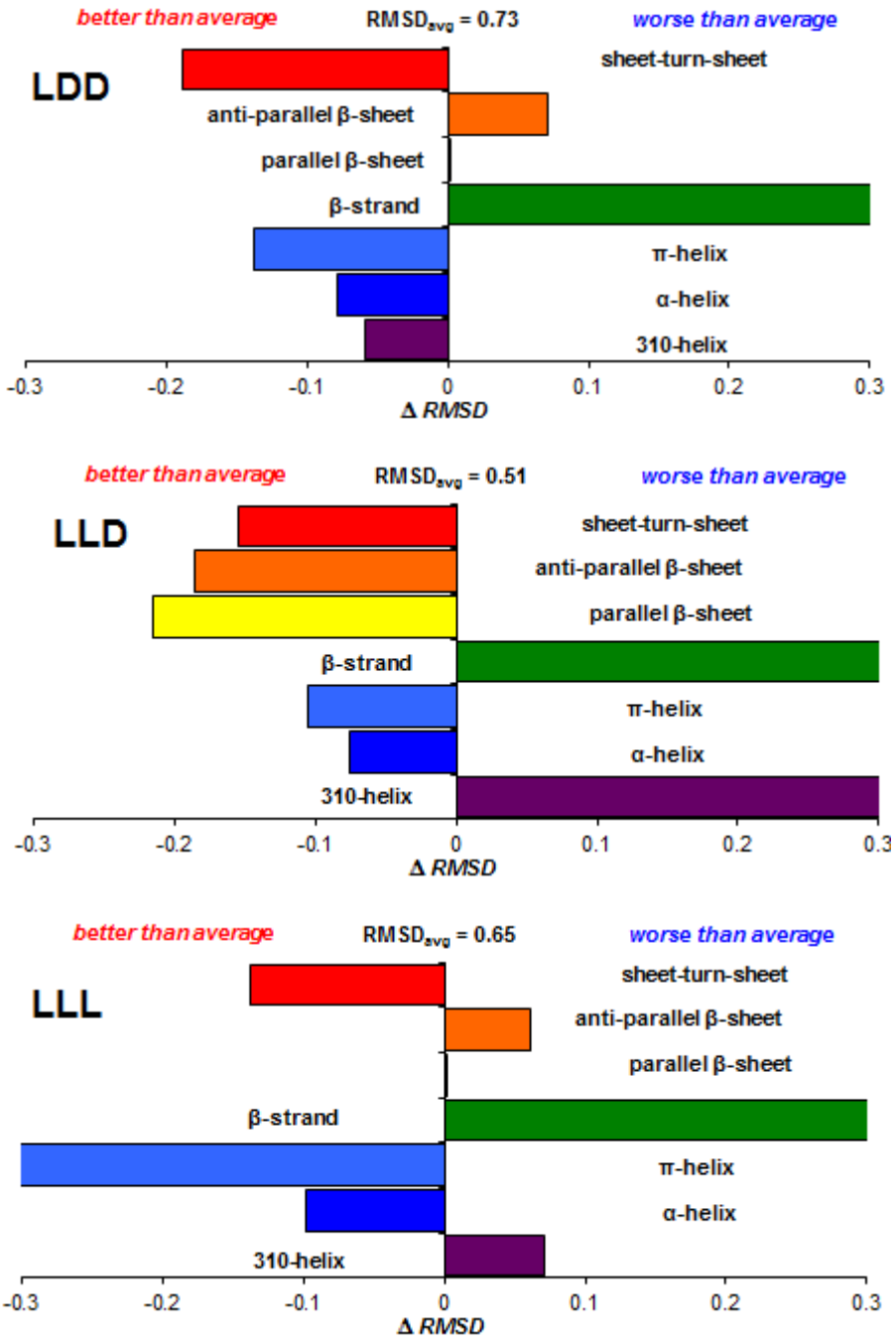


***Figure 5.3.*** Continued.

EKOS showed that the oxopiperazine dimers are good π-helical and α-helical mimics with RMSD 0.33 ~ 0.59 Å. The LLL isomer is the best π-helical mimic (RMSD

= 0.33 Å) and LLD isomer is the best α-helical mimic (RMSD = 0.44 Å). EKOS analysis revealed that when side chain 2 (Figure 5.2) is derived from L-amino acid, oxopiperazine dimers are better π-helical and α-helical mimics (RMSD 0.33 ~ 0.41 Å); when side chain 2 is derived from D-amino acid, their fitness as π-helical and α-helical mimics are lowered as RMSD values increased (RMSD 0.53 ~ 0.59 Å). For example, LLL isomer is the best π-helical mimic whereas LDL is the worst π-helical mimic. The only difference between two mimics is the stereochemistry of side chain 2. When the stereochemistry is flipped, the conformation of the scaffold changes, which results in changing the overlapping positions at interface of π-helix. Furthermore, the average RMSD for α-helical mimic is 0.53 Å. The LLL isomer is a good α-helical mimic (RMSD = 0.55 Å), but DDL, DLD, DLL, and LLD isomers are all better α-helical mimics than LLL isomers. Dr. Arora's study suggested that the LLL isomer of oxopiperazine dimers was an α-helical mimic, EKOS study showed that it is also an excellent π-helical mimic. In addition, DDL and DLL isomers are good 310-helix mimics (RMSD ~ 0.5 Å), but the rest isomers are poor 310-helix mimics.

Besides helical mimicry, DLD, DDL, LDL and LLD isomers are good parallel β-sheet and sheet-turn-sheet mimics (RMSD = 0.20 ~ 0.40 Å). DLD isomer is the only good antiparallel β-sheet mimic (RMSD = 0.28 Å). Oxopiperazine dimers are generally poor β-strand mimics (RMSD > 0.80 Å).

### 5.2.2 EKO Study On Oxopiperazine Dimers

When EKO was applied to all 8 diastereomers of oxopiperazine dimers screening over 120,000 PPI interfaces. However, EKO did not find p53/Mdm2 and HIF1α/p300(CBP) as the targets. The possible reasons are (i) the RMSD value for EKO analysis is 0.3 Å, which might exclude these two targets; and (ii) only least amount of conformers of oxopiperazine dimers were used during chemistry-centered approach of EKO analysis, which is possible to miss interactions with other conformers. And yet, we still found 10,680 protein targets and they were further narrowed down to 610 heterodimeric protein targets (Appendix E). A brief summary of targets is shown in

Table 5.2.Three protein complexes are used as examples to show how oxopiperazine dimers overlay on PPIs.

***Table 5.2.*** Brief summary of mining results of oxopiperazine dimers.

| CTP | Interesting Targets | pdb ID |
|---|---|---|
| LLL | None | |
| LLD | Human TGF-beta Type II Receptor | 1ktz |
| | Human NFAT1 and Fos-Jun on the IL-2 ARRE1 Site | 1s9k |
| | tumor-specific, MHC class II-restricted TCR | 2iam |
| LDL | YSd1 Fab bound to DR5 (TNF) | 1za3 |
| | PCSK9 | 3h42 |
| | Interleukin-1 receptor complex | 3o4o |
| LDD | eIF4A-PDCD4 complex | 2zu6 |
| DLL | CD40L in complex with TNF | 1i9r |
| | TGF-beta signaling complex | 2pjy |
| | eIF4A-PDCD4 complex | 2zu6 |
| DDL | VEGF | 1bj1 |
| | 1n0w RAD51-BRCA2 BRC (breast cancer) | 1n0w |
| | HIV-1 reverse transcriptase | 3lp0 |
| DLD | VirA-Rab1 (Ras related) | 4fmb |
| DDD | PCSK9:EGFA | 3gcx |
| | Caspase-9 | 1nw9 |
| | farnesyltransferase | 1s63 |
| | TRAIL-SDR5(apoptosis, death receptor 5) | 1du3 |

BRCA2 is a breast cancer susceptibility protein that controls the function of RAD51, a recombinase enzyme, in pathways for DNA repair by homologous recombination.[105] Mutations in the BRCA2 gene cause increased susceptibility to breast, ovarian and other cancer types. Cancer-associated mutations that affect the BRC repeat (blue) disrupt its predicted interaction with RAD51 (red), yielding structural insight into mechanisms for cancer susceptibility. RAD51-BRCA2 complex was recrystallized with 1.7 Å resolution. There are three main points of contact involving residues Phe 1524, Ala 1527, Leu 1545 and Phe 1546 (gold color in Figure 5.4). The affinity between BRC4

and RAD51 is further enhanced by hydrophobic contacts involving residues IL3 1534 in the linker region.

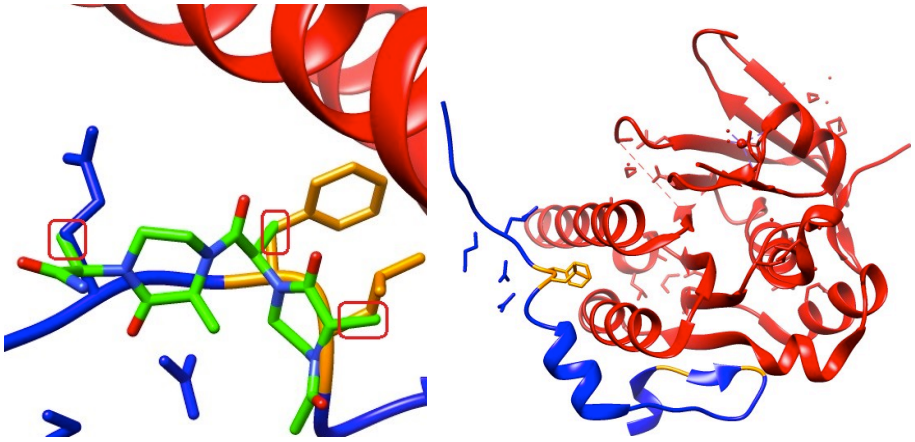

**a** **b**

***Figure 5.4.*** **a**. Crystal structure of RAD51-BRCA2 complex; **b**. Oxopiperazine dimer overlays on BRCA2.

DDL isomer of oxopiperazine dimer overlays on BRCA2 at Glu 1548, Phe 1546 and Leu 1545, which is the hot spot of the complex. Small molecules overlaying on hot spot are expected to have interesting effects on PPIs. Other parts of the oxopiperazine dimer are not folded toward the interface, and therefore will not generate undesired interactions to push oxopiperazine dimer away from the expected binding site.

Programmed cell death protein 4 (PDCD4)[106] is a translation inhibitor that suppresses neoplastic transformation in cultured cells and transgenic mice. Loss or reduced expression of PDCD4 has been implicated in the development and progression of a variety of aggressive human cancers. PDCD4 is believed to perform its tumor suppressor function primarily through interaction with eIF4A and eIF4G, which are components of mRNA-binding complex eIF4. A crystal structure of PDCD4 with elF4A complex was obtained with 2.8 Å resolution. PDCD4 has two domains: mMA3 and cMA3 domains and only cMA3 domain (green in Figure 5.5) binds to one eIF4A (red). At the center of the interface, Glu-210, Glu-249, and Asp-253 in mMA3 form an ion pair network with Arg-110 and Arg-161 from eIF4A. Glu-183 and Glu-186 of mMA3 form a

network with Thr-281 and Arg-283 of eIF4A. Glu-111 and Asn-280 in eIF4A hydrogen bonded with Gln-173 and His-178 in mMA3.

**a.**

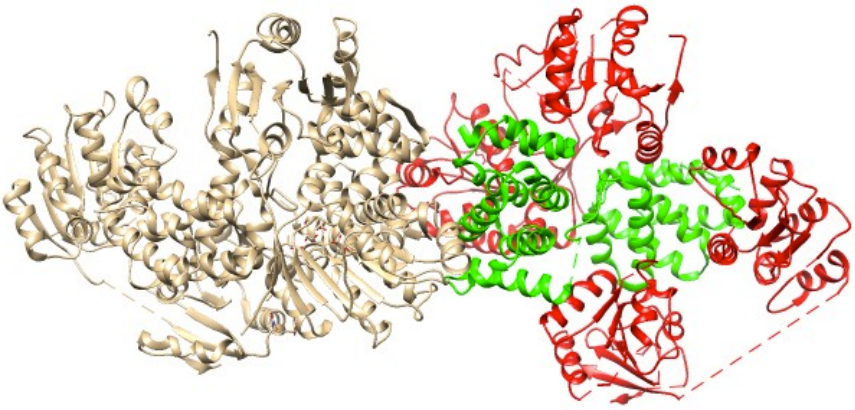

**b.**

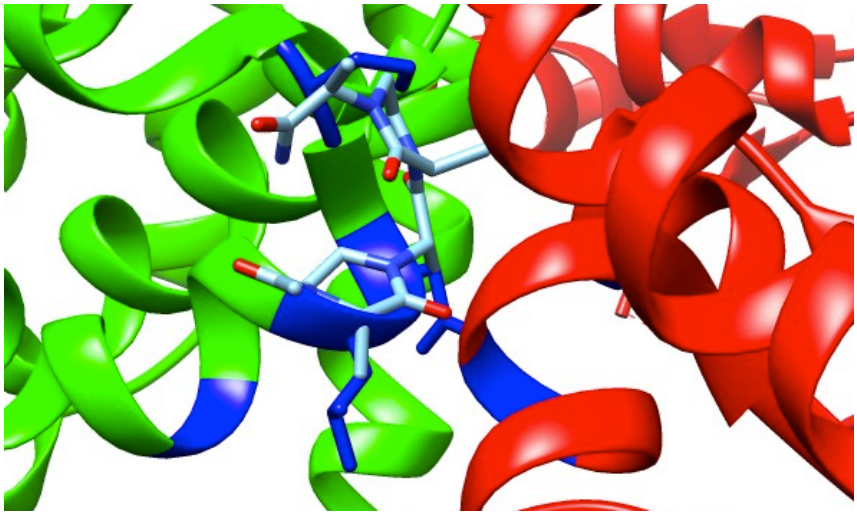

***Figure 5.5.*** **a**. Crystal structure of PDCD4 with elF4A complex; **b**. Oxopiperazine dimer overlays on cMA3 domain of PDCD4.

The interface consists of two helical structures. The DLL isomer of oxopiperazine dimer overlays on helical part of cMA3 domain at Leu-252, Asp-253 and Pro-255. Asp-253 is the hot spot on cMA3 interacting with elF4A. It is consistent with

EKOS result, which suggests oxopiperazine dimer is a helical mimic. However, the unchanged side-chain is pointing toward elF4A, which may result in unexpected interaction with elF4A. When unexpected interaction occurs, small molecules may not overlay at the expected site.

LLD isomer of oxopiperazine dimer also showed interesting interaction between TGF-beta3 (blue in Figure 5.6) and its Type II receptor (green). The crystal structure of the complex was obtained by Hinck's group with resolution of 2.1 Å.[107] The interaction at the interface is hydropholic interactions (red). There is however a key hydrogen bonding interaction between Arg-94 on TGF-beta3 and Asp-32 on Type II receptor.

**a.**

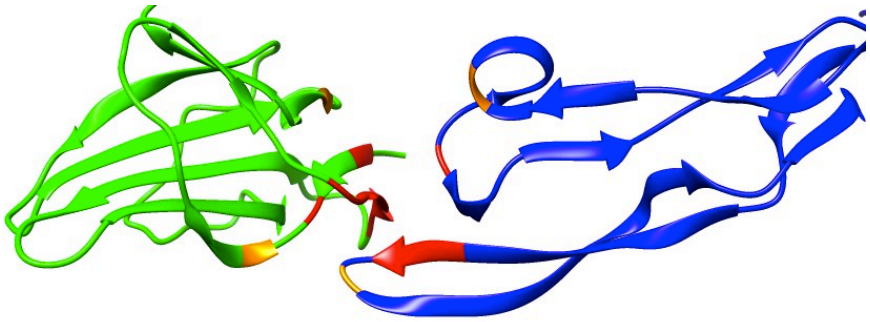

**b.**

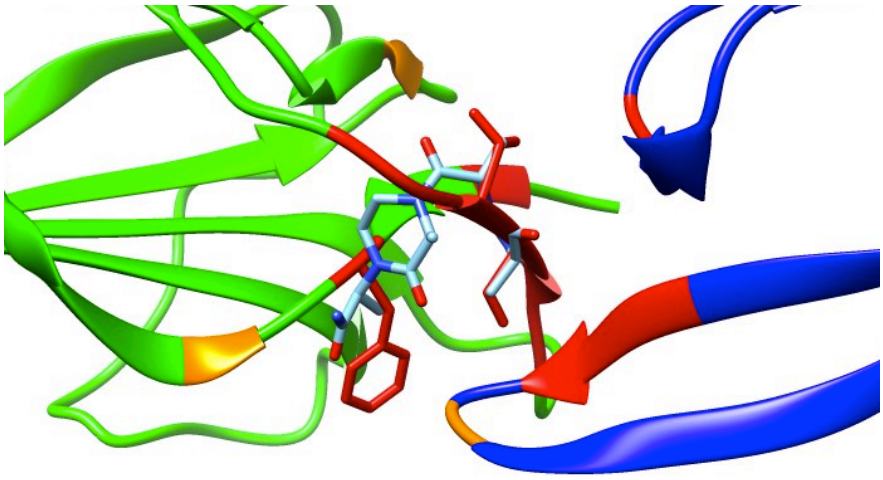

***Figure 5.6.*** **a**. Crystal structure of TGF-beta3(blue) and its Type II receptor(green); **b**. Oxopiperazine dimer overlays on Type II receptor.

LLD isomer of oxopiperazine dimer overlays on Type II receptor at Phe-30, Thr-51, and Ser-52. As shown in Figure 5.4b, oxopiperazine dimer overlays on the hydrophobic interface. There is no undesired interaction between small molecules and protein observed. Although oxopiperazine dimer is not shown to disrupt the key PPI, hydrogen bond between Arg-94 and Asp-32; it is likely that when oxopiperazine dimer interacts with Type II receptor on the hydrophobic region, it changes the conformation of the protein and therefore disrupt the key hydrogen bond interaction.

## 5.3 Conclusions

Oxopiperazine dimer is suggested to adopt one conformation and be a good α-helical mimic by Dr. Arora's work.[102] Our studies broadened the scope of oxopiperazine dimers as both protein secondary structure mimics and small molecules that target PPIs. QMD study first showed that more than one conformation of oxopiperazine dimers could exist, which provided the molecules with more possibilities to mimic the protein secondary structures. EKOS then showed that the LLL isomer can be good mimics for both π and alpha-helix whereas Dr. Arora only suggested it is an α-helical mimic. In addition, when the stereochemistry of side chains changed, oxopiperazine dimers can be good mimics for other protein secondary structures such as β-sheet and sheet-turn-sheet. EKO is also practiced on oxopiperazine dimers to demonstrate how small molecules can quickly find potential targets. EKO study showed that oxopiperazine dimer is a good universal peptidomimetic scaffold as it overlays on about 600 heterodimeric PPIs among which there are proteins related with cancer, diabetes, HIV, etc. Therefore, oxopiperazine dimers are good protein interface mimics.

# CHAPTER VI
# CONCLUSIONS AND OUTLOOK

## 6.1 Conclusions

### 6.1.1 Synthesis Of Trisubstituted Allylic Alcohols Via Hydroalumination/ Vinyl Addition

The well-known vinyl aluminate intermediate was directly applied to synthesis of trisubstituted allylic alcohols, which are synthetically useful building blocks for 2,3 disubstituted furans and 4,5 disubstituted furanones. The optimized condition was only applied to benzaldehyde and bromobenzaldehdye to obtain product **2a** and **2b** in high yield (Figure 6.1). The future work may include application of the optimized condition to the rest of substrates achieve higher yield and the reaction may also be done in low temperature with chiral catalyst to obtain optically enriched trisubstituted allylic alcohols.

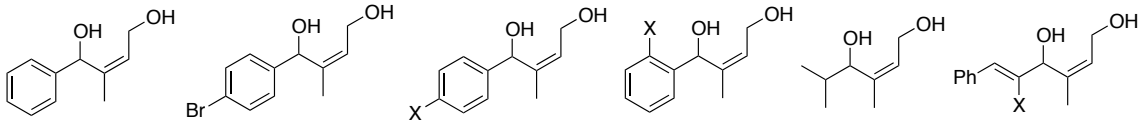


**2a** 88 %
**2b** 85 %
**2c,** X= I, 55 %
**2d,** X= $NO_2$, 67 %
**2e,** X= OMe, 58 %
**2f,** X= $NO_2$, 76 %
**2g,** X= OMe, 63 %
**2h** 58 %
**2i,** X= H, 57 %
**2j,** X= Me, 74 %

***Figure 6.1.*** Trisubstituted allylic alcohols synthesized.

### 6.1.2 *Homo*-Roche Ester Derivatives By Asymmetric Hydrogenation And Organocatalysis

Catalyst 1 was applied to large-scale synthesis of homo-Roche ester which could be readily transformed to α-substituted homo-Roche ester derivatives via organocatalysis. The combination of asymmetric hydrogenation and organocatalysis illustrated the idea that two different, but well-known, methods can be applied to synthesis of useful chirons together.

### 6.1.3 Synthesis And Conformational Analysis Of Cyclic Tetrapeptides

We invented an expedient liquid phase synthesis of cyclic tetrapeptides, which could include amino acids that are common residues in PPI interfaces such as Trp, Cyc and Met. Although there is only one final product obtained, there are several advanced intermediates synthesized in gram-scale, which can be readily converted to the final products in three steps. A thorough computational analysis (QMD) of the conformation of CTPs were also completed, which correlated the stereochemistry to the preferred conformations of non-Pro/Gly CTPs. The future work may include assigning all proton NMR peaks using HSQC and COSY and measuring N<u>H</u> to αC<u>H</u> $^{3}J$ coupling constants and through-space inter-residue contacts via 2D-NOESY.

EKO analysis also suggested that TNF-TNFR2 is a promising target for CTPs. The future work may include cellular assays which will measure inhibition or promotion of TNF-induced cell death.

### 6.1.4 EKO And EKOS Analysis On Oxopiperazine Dimers

EKOS studies suggested that the LLL isomer of oxopiperazine dimers could be good mimics for both π and a-helixes. When the stereochemistry of the scaffold changed, oxopiperazine dimers could also mimic with other protein secondary structures such as β-sheet and sheet-turn-sheet. Oxopiperazine scaffold was proved to be a p53/Mdm2 inhibitor and HIF1α/p300 (CBP) inhibitor. However, EKO did not find these two targets, even through EKO study showed that oxopiperazine dimers could overlay on about 600 heterodimeric PPIs. The future work may include performing a thorough EKO analysis via biology-centered approach on p53/Mdm2 and HIF1α/p300 (CBP).

## REFERENCES


(1) Corey, E. J.; Katzenellenbogen, J. A.; Posner, G. H. *J. Am. Chem. Soc.* **1967**, *89,* 4245.

(2) Borden, W. J. *J. Am. Chem. Soc.* **1970**, *92,* 4898.

(3) Grant, B.; Djerassi, C. *J. Org. Chem.* **1974**, *39,* 968.

(4) Cui, X.; Burgess, K. *Chem. Rev.* **2005**, *105*, 3272.

(5) Roseblade, S. J.; Pfaltz, A. *Acc. Chem. Res.* **2007**, *40*, 1402.

(6) Pfaltz, A.; Blankenstein, J.; Hilgraf, R.; Hormann, E.; McIntyre, S.; Menges, F.; Schonleber, M.; Smidt, S. P.; Wustenberg, B.; Zimmermann, N. *Adv. Synth. Catal.* **2003**, *345*, 33.

(7) Mukherjee, S.; Yang, J. W.; Hoffmann, S.; List, B. *Chem. Rev.* **2007**, *107*, 5471.

(8) Singh, S. B.; Zink, D. L.; Polishook, J. D.; Dombrowski, A. W.; Darkin-Rattray, S. J.; Schmatz, D. M.; Goetz, M. A. *Tetrahedron Lett.* **1996**, *37*, 8077.

(9) Shute, R. E.; Kawai, M.; Rich, D. H. *Tetrahedron* **1988**, *44*, 685.

(10) Hamada, Y.; Shioiri, T. *Chem. Rev.* **2005**, *105*, 4441.

(11) Takeuchi, Y.; Marshall, G. R. *J. Am. Chem. Soc.* **1998**, *120*, 5363.

(12) El Haddadi, M.; Cavelier, F.; Vives, E.; Azmani, A.; Verducci, J.; Martinez, J. *J. Pept. Sci.* **2000,** *6*, 560.

(13) Cini, E.; Botta, C. B.; Rodriquez, M.; Taddei, M. *Tetrahedron Lett.* **2009**, *50*, 7159.

(14) Ngu-Schwemlein, M.; Zhou, Z.; Bowie, T.; Eden, R. *J. Mol. Struct.* **2003**, *655*, 59.

(15) Meutermans, W. D. F.; Bourne, G. T.; Golding, S. W.; Horton, D. A.; Campitelli, M. R.; Craik, D.; Scanlon, M.; Smythe, M. L. *Org. Lett.* **2003**, *5*, 2711.

(16) Horton, D. A.; Bourne, G. T.; Coughlan, J.; Kaiser, S. M.; Jones, A.; Ruehmann, A.; Turner, J. Y.; Smythe, M. L. *Org. Biomol. Chem.* **2008**, *6*, 1386.

(17) Wong, C. T. T.; Lam, H. Y.; Song, T.; Chen, G.; Li, X. *Angew. Chem. Int. Ed.* **2013**, *52*, 10212.

(18) O'Connor, S. D.; Smith, P. E.; Al-Obeidi, F.; Pettitt, B. M. *J. Med. Chem.* **1992**, *35*, 2870.

(19) Pettitt, B. M.; Matsunaga, T.; Al-Obeidi, F.; Gehrig, C.; Hruby, V. J.; Karplus, M. *Biophys. J.* **1991**, *60*, 1540.

(20) Ko, E.; Raghuraman, A.; Perez, L. M.; Ioerger, T. R.; Burgess, K. *J. Am. Chem. Soc.* **2013**, *135*, 167.

(21) Xin, D.; Ko, E.; Perez, L. M.; Ioerger, T. R.; Burgess, K. *Org. Biomol. Chem.* **2013**, *11*, 7789.

(22) Still, W. C.; Gennari, C. *Tetrahedron Lett.* **1983**, *24,* 4405.

(23) Wadsworth, W. S. Jr. *Org. React. (N. Y.)* **1977**, 73.

(24) Sreekumar, C.; Darst, K. P.; Still, W. C. *J. Org. Chem.* **1980**, *47,* 4260.

(25) Garner, P.; Ramakanth, S. *J. Org. Chem.* **1987**, *54,* 2629.

(26) Hodgson, D. M.; Arif, T. *Org. Lett.* **2010**, *12,* 4204.

(27) Chen, Y. K.; Walsh, P. J. *J. Am. Chem. Soc.* **2004**, *126,* 3702.

(28) Kerrigan, M. H.; Jeon, S.; Chen, Y. K.; Salvi, L.; Carroll, P. J.; Walsh, P. J. *J. Am. Chem. Soc.* **2009**, *131,* 8434.

(29) Fehr, C.; Magpantay, I.; Vuagnoux, M.; Dupau, P. *Chem. Eur. J.* **2011**, *17,* 1257.

(30) Newman, H. *Tetrahedron Lett.* **1971**, *12,* 4571.

(31) Tsuda, T.; Yoshida, T.; Saegusa, T. *J. Org. Chem.* **1988**, *55,* 1037.

(32) Spino, C.; Beaulieu, C. *Angew. Chem. Int. Ed.* **2000**, *39*, 1930.

(33) Spino, C.; Granger, M. C.; Boisvert, L.; Beaulieu, C. *Tetrahedron Lett.* **2002**, *43,* 4183.

(34) Ramachandran, P. V.; Rudd, M. T.; Burghardt, T. E.; Reddy, M. V. R. *J. Org. Chem.* **2003**, *71,* 9310.

(35) Sato, F. *J. Organomet. Chem.* **1985**, *285*, 53.

(36) Langille, N. F.; Jamison, T. F. *Org. Lett.* **2006**, *8,* 3761.

(37) Zurwerra, D.; Gertsch, J.; Altmann, K. H. *Org. Lett.* **2010**, *12,* 2302.

(38) Ely, R. J.; Morken, J. P. *Org. Lett.* **2010**, *12,* 4348.

(39) Wu, J. Y.; Moreau, B.; Ritter, T. *J. Am. Chem. Soc.* **2009**, *131,* 12915.

(40) Zweifel, G.; Whitney, C. C. *J. Am. Chem. Soc.* **1967**, 89, 2753.

(41) Zweifel, G.; Steele, R. B. *J. Am. Chem. Soc.* **1967**, *89,* 2754.

(42) Herrmann, J. L. Schlessinger, R. H. *Tetrahedron Lett.* **1973**, *14*, 2429.

(43) Jeulin, S.; Ayad, T.; Ratovelomanana-Vidal, V.; Genet, J.-P. *Adv. Synth. Catal.* **2007**, *349*, 1592.

(44) Pautigny, C.; Jeulin, S.; Ayad, T.; Zhang, Z.; Genet, J. P.; Ratovelomanana-Vidal, V. *Adv. Synth. Catal.* **2008**, *350*, 2525.

(45) Qiu, M.; Wang, D. Y.; Hu, X. P.; Huang, J. D.; Yu, S. B.; Deng, J.; Duan, Z. C.; Zheng, Z. *Tetrahedron: Asymmetry* **2009**, *20*, 210.

(46) Zhao, J.; Burgess, K. *Org. Lett.* **2009**, *11*, 2053.

(47) Ostermeier, M.; Brunner, B.; Korff, C.; Helmchen, G. *Eur. J. Org. Chem.* **2003**, *9*, 3453.

(48) Hekking, K. F. W.; Lefort, L.; de Vries, A. H. M.; van Delft, F. L.; Schoemaker, H. E.; de Vries, J. G.; Rutjes, F. P. J. T. *Adv. Synth. Catal.* **2008**, *350*, 85.

(49) Abo, M.; Mori, K. *Biosci., Biotechnol., Biochem.* **1993**, *57*, 265.

(50) Christopfel, W. C.; Vineyard, B. D. *J. Am. Chem. Soc.* **1979**, *101*, 4406.

(51) Schmidt, T.; Baumann, W.; Drexler, H. J.; Heller, D. *J. Organomet. Chem.* **2011**, *696*, 1760.

(52) Howell, G. P.; Fletcher, S. P.; Geurts, K.; ter Horst, B.; Feringa, B. L. *J. Am. Chem. Soc.* **2006**, *128*, 14977.

(53) Khumsubdee, S.; Burgess, K. *ACS Catal.* **2013**, *3*, 237.

(54) Powell, M. T.; Hou, D. R.; Perry, M. C.; Cui, X.; Burgess, K. *J. Am. Chem. Soc.* **2001**, *123*, 8878.

(55) Perry, M. C.; Cui, X.; Powell, M. T.; Hou, D. R.; Reibenspies, J. H.; Burgess, K. *J. Am. Chem. Soc.* **2003**, *125*, 113.

(56) Wolff, M.; Seemann, M.; Grosdemange-Billiard, C.; Tritsch, D.; Campos, N.; Rodriguez-Concepcion, M.; Boronat, A.; Rohmer, M. *Tetrahedron Lett.* **2002**, *43*, 2555.

(57) Huang, F. C.; Lee, L. F. H.; Mittal, R. S. D.; Ravikumar, P. R.; Chan, J. A.; Sih, C. J.; Caspi, E.; Eck, C. R. *J. Am. Chem. Soc.* **1975**, *97*, 4144.

(58) Krohn, K.; Riaz, M.; Floerke, U. *Eur. J. Org. Chem.* **2004**, *2004*. 1261.

(59) Krohn, K.; Riaz, M. *Tetrahedron Lett.* **2004**, *45*, 293.

(60) Fontana, A. *J. Org. Chem.* **2001**, *66*, 2506.

(61) Cheng, C.; Brookhart, M. *Angew. Chem. Int. Ed.* **2012**, *51*, 9422.

(62) Quintard, A.; Alexakis, A.; Mazet, C. *Angew. Chem. Int. Ed.* **2011**, *50*, 2354.

(63) Mukherjee, S.; Yang, J. W.; Hoffmann, S.; List, B. *Chem. Rev.* **2007**, *107*, 5471.

(64) Masamune, S.; Choy, W.; Peterson, J. S.; Sita, L. R. *Angew. Chem. Int. Ed.* **1985**, *24*, 1.

(65) Beeson, T. D.; MacMillan, D. W. C. *J. Am. Chem. Soc.* **2005**, *127*, 8826.

(66) List, B. *J. Am. Chem. Soc.* **2002**, *124*, 5656.

(67) Brochu, M. P.; Brown, S. P.; MacMillan, D. W. C. *J. Am. Chem. Soc.* **2004**, *126*, 4108.

(68) Yadav, J. S.; Sengupta, S. *Eur. J. Org. Chem.* **2013**, *2013*, 376.

(69) Sawada, D.; Katayama, T.; Tsukuda, Y.; Saito, N.; Saito, H.; Takagi, K. I.; Ochiai, E.; Ishizuka, S.; Takenouchi, K.; Kittaka, A. *Tetrahedron* **2010**, *66*, 5407.

(70) Mori, K.; Kyota, H.; Malosse, C.; Rochat, D. *Liebigs Ann. Chem.* **1993**, *1993*, 1201.

(71) Broca, C.; Manteghetti, M.; Gross, R.; Baissac, Y.; Jacob, M.; Petit, P.; Sauvaire, Y.; Ribes, G. *Eur. J. Pharmacol.* **2000**, *390*, 339.

(72) Bauer, S. M.; Armstrong, R. W. *J. Am. Chem. Soc.* **1999**, *121*, 6355.

(73) Cudic, M.; Mari, F.; Fields, G. B. *J. Org. Chem.* **2007**, *72*, 5581.

(74) Adrian Meredith, J.; Wallberg, H.; Vrang, L.; Oscarson, S.; Parkes, K.; Hallberg, A.; Samuelsson, B. *Eur. J. Med. Chem.* **2010**, *45*, 160.

(75) Mantilli, L.; Gerard, D.; Torche, S.; Besnard, C.; Mazet, C. *Angew. Chem., Int. Ed.* **2009**, *48*, 5143.

(76) Mantilli, L.; Mazet, C. *Tetrahedron Lett.* **2009**, *50*, 4141.

(77) Mantilli, L.; Gerard, D.; Torche, S.; Besnard, C.; Mazet, C. *Chem. Eur. J.* **2010**, *16*, 12736.

(78) Mantilli, L.; Mazet, C. *Chem. Commun.* **2010**, *46*, 445.

(79) Glenn, M.; Kelso, M.; Tyndall, J.; Fairlie, D. *J. Am. Chem. Soc.* **2003**, *125,* 640.

(80) Cavelier-Frontin, F.; Achmad, S.; Verducci, J.; Jacquier, R.; Pepe, G. *J. Mol. Struct.: THEOCHEM* **1993**, *105*, 125.

(81) Conte, L. L.; Chothia, C.; Janin, J. *J. Mol. Biol.* **1999**, *285,* 2177.

(82) Blanco-Canosa, J, B.; Dawson, P. E. *Angew. Chem. Int. Ed.* 2**008**, *47,* 6851.

(83) Wong, M.; Ziring, D.; Korin, Y.; Desai, S.; Braun, J.; Reed, E.; Singh, R. R. *Clin. Immunol.* **2008**, *126*, 121.

(84) Feldmann, M. *Nat. Rev. Immunol.* **2002**, *2,* 364.

(85) Baldwin, A. S. Jr. *Annu. Rev. Immunol.* **1996**, *14,* 649.

(86) Baeuerle, P. A.; Baichwal, V. R. *Adv. Immunol.* **1997**, *65,* 111.

(87) Baichwal, V. R.; Baeuerle, P. A. *Curr. Biol.* **1997**, *7,* R94.

(88) Faustman, D.; Davis, M. *Nat. Rev. Drug Discovery* **2010**, *9,* 482.

(89) Blenis, J. *Proc. Nat'l Acad. Sci. USA* **1993**, *90,* 5889.

(90) Karin, M.; Delhase, M. *Proc. Nat'l Acad. Sci. USA* **1998**, *95,* 9067.

(91) Karin, M.; Liu, Z. Zandi, E. *Curr. Opin. Cell Biol.* **1997**, *9,* 240.

(92) He, M. M.; Smith, A. S.; Oslob, J. D.; Flanagan, W. M.; Braisted, A. C.; Whitty, A.; Cancilla, M. T.; Wang, J.; Lugovskoy, A. A.; Yoburn, J. C.; Day, E. S.; Cruz, L. A.; Cachero, T. G.; Miller, S. K.; Friedman, J. E.; Choong, I. C.; Cunningham, B. C. *Science* **2005**, *310,* 1022.

(93) Byla, P.; Andersen, M. H.; Holtet, T. L.; Jacobsen, H.; Munch, M.; Gad, H. H.; Thogersen, H. C.; Hartmann, R. *J. Biol. Chem.* **2010**, *285,* 12096.

(94) Leung, C. H.; Zhong, H. J.; Yang, H.; Cheng, Z.; Victor, M.; Abagyan, R.; Wong, C. Y.; Ma, D. L. *Angew. Chem. Int. Ed.* **2012**, *51*, 9010.

(95) Carter, P. A.; Scherle, J. A.; Muckelbauer, M. E.; Voss, R. Q.; Liu, L. A.; Thompson, A. J.; Tebben, K. A.; Solomon, Y. C.; Lo, Z.; Li, P.; Strzemienski, G.; Yang, N.; Falahatpisheh, M.; Xu, Z.; Wu, N. A.; Farrow, K.; Ramnarayan, J.; Wang, D.; Rideout, V.; Yalamorri, P.; Domaille, D. J.; Underwood, J. M.; Trzaskos, S. M.; Friedman, R. C.; Decicco, C. P. *Proc. Nat'l. Acad. Sci. USA* **2001**, *98,* 11879.

(96) Jackson, R. W.; Tabone, J. C.; Howbert, J. J. *Bioorg. Med. Chem. Lett.* **2003**, *13*, 205.

(97) Jackson, R. W.; Gelinas, R.; Baughman, T. A.; Cox, T.; Howbert, J. J.; Kucera, K. A.; Latham, J. A.; Ramsdell, F.; Singh, D.; Darwish, I. S. *Bioorg. Med. Chem. Lett.* **2002**, *12,* 1093.

(98) Chorev, M.; Goodman, M. *Acc. Chem. Res.* **1993**, *26*, 266.

(99) Mukai, Y.; Nakamura, T.; Yoshikawa, M.; Yoshioka, Y.; Tsunoda, S.; Nakagawa, S.; Yamagata, Y.; Tsutsumi, Y. *Sci. Signaling* **2010**, *3*, ra83.

(100) Tully, S. E.; Rawat, M.; Hsieh-Wilson, L. C. *J. Am. Chem. Soc.* **2006**, *128,* 7740.

(101) Chakrabarti, S.; Davidge, S. T. *J. Vasc. Res.* **2013**, *50*, 21.

(102) Tosovska, P.; Arora, P. S. *Org. Lett.* **2010**, *12*, 1588.

(103) Panek, J. S.; Beresis, R. T. *J. Org. Chem.* **1996**, *61*, 6496.

(104) Diez, S.; Navarro, G.; Tros de Ilarduya, C. *J. Gene Med.* **2009**, *11*, 38.

(105) Pellegrin, L.; Yu, D. S.; Lo, T.; Anand, S.; Lee, M.; Blundell, T. L.; Venkitaraman, A. R. *Nature* **2002**, *420*, 287.

(106) Chang, J. H.; Cho, Y. H.; Sohn, S. Y.; Choi, J. M.; Kim, A.; Kim, Y.; C.; Jang, S. K.; Cho, Y. *Proc. Nat'l Acad. Sci. USA* **2009**, *102,* 3148.

(107) Hart, P. J.; Deep, S.; Taylor, A. B.; Shu, Z.; Hinck, C. S.; Hinck, A. P. *Nature Structural Biology* **2002**, *9*, 203.

(108) Mukai, Y.; Nakamura, T.; Yoshikawa, M.; Yoshioka, Y.; Tsunoda, S. Nakagawa, S.; Yamagata, Y.; Tsutsumi, Y. *Science Signaling* **2010**, *3*, ra83.

(109) He, M. M.; Smith, A. S.; Oslob, J. D.; Flanagan, W. M.; Braisted, A. C.; Whitty, A.; Cancilla, M. T.; Wang, J.; Lugovskoy, A. A.; Yoburn, J. C.; Fung, A. D.; Farrington, G.; Eldredge, J. K.; Day, E. S.; Cruz, L. A.; Cachero, T. G.; Miller, S. K.; Friedman, J. E.; Choong, I, C.; Cunningham, B. C. *Science* **2005**, *210*, 1022.

(110) LaPorte, S. L.; Juo, Z, S.; Vaclavikova, J.; Colf, L. A.; Qi, X.; Heller, N. M.; Keegan, A. D.; Carcia, K. G. *Cell* **2008**, *132*, 259.

(111) Cheng, Z.; Biechele, T.; Wei, Z.; Morrone, S.; Moon, R. T.; Wang, L.; Xu, W. *Nat. Struct. Mol. Biol.* **2011**, *18*, 1204.

(112) Lao, B. B.; Drew, K.; Guarracino, D. A.; Brewer, T. F.; Heindel, D. W.; Bonneau, R.; Arora, P, S. *J. Am. Chem. Soc.* **2014,** *136,* 7877.

(113) Ko, E.; Liu, J.; Burgess, K. *Chem. Soc. Rev*. **2011**, *40*, 4411.

(114) Lao, B. B.; Grishagin, I.; Mesallati, H.; Brewer, T. F.; Olenyuk, B. Z.; Arora, P. S. *Proc. Nat'l Acad. Sci. USA* **2014**, *111*, 7531.

# APPENDIX A
# GENERAL EXPERIMENTAL PROCEDURES

All reactions were carried out under an atmosphere of dry nitrogen or argon. Glassware was oven-dried prior to use. Unless otherwise indicted, common reagents or materials were obtained from commercial source and used without further purification. All the solvents were used after appropriate distillation or purification.

Flash column chromatography was performed using silica gel 60 (230-400 mesh). Analytical thin layer chromatography (TLC) was carried out on Merck silica gel plates with QF-254 indicator and visualized by UV. IR spectra were recorded on a Bruker Tensor 27 spectrometer. Optical rotations were measured on Jasco DIP-360 digital polarimeter. $^{1}H$ and $^{13}C$ spectra were recorded on Varian 300 (300 MHz $^{1}H$; 75 MHz $^{13}C$), Avance 400 (400 MHz $^{1}H$; 100 MHz $^{13}C$) or Varian 500 (500 MHz $^{1}H$; 125 MHz $^{13}C$) spectrometer at room temperature. Chemical shifts were reported in ppm relative to the residual $CDCl_3$ (δ 7.28 ppm $^{1}H$; δ 77.0 ppm $^{13}C$), $CD_3OD$ (δ 3.31 ppm $^{1}H$; δ 49.0 ppm $^{13}C$) or $d^6$-DMSO (δ 2.49 ppm $^{1}H$; δ 39.5 ppm $^{13}C$). Coupling constants (J) were reported in Hertz (Hz). The following abbreviations were used to explain the multiplicities: s = singlet, d = doublet, t = triplet, q = quartet, dd = double doublet, dq = double quartet, m = multiplet, br = broad.

## APPENDIX B
## EXPERIMENTAL FOR CHAPTER II

### A. Preparation of compounds 2a-2l

**General Procedure for (*Z*)-Allylic Diol Synthesis**

A Red-Al solution (3M in toluene) (7.5 mL, 2.5 mmol) was dissolved in 2 mL of hexanes/THF (5:1) mix-solvent. The solution was stirred at 0 ºC for 5 min, followed by slow addition of 2-butyn-1-ol (140 mg, 2.0 mmol). The solution was stirred at 23 ºC for 4 h. EtOAc (0.98 mL, 1.0 mmol) was then added to the solution at 0 ºC. The solution was stirred for 1 min at room temperature, and the aldehydes (2.5 mmol) were added. The solution was stirred at 23 ºC for 12 h before quenched with 5 mL of HCl (*1N*). The mixture was diluted with EtOAc, and the organic layer was separated. The aqueous layer was extracted with EtOAc for 3 times. The combined organic layers were dried with $MgSO_4$, and concentrated *in vacuo*. The residue was purified via flash chromatography (30% - 50% EtOAc/hexanes).

**(*Z*)-2-methyl-1-phenylbut-2-ene-1,4-diol (2a).** Product was obtained as a white solid (260 mg, 1.48 mmol, 74%). $^1$H NMR (300 MHz, $CDCl_3$) δ 7.40-7.26 (5H, m), 5.72 (1H, s), 5.70-5.65 (1H, m), 4.48-4.38 (1H, m), 4.38-4.30 (1H, m), 2.38 (1H, br), 1.76 (1H, br), 1.68 (3H, s); $^{13}$C NMR (75 MHz, $CDCl_3$) δ 141.7, 141.4, 128.3, 127.2, 126.2, 125.7, 71.4, 58.1, 18.4. HRMS (ESI, TOF): Exact mass calcd for $C_{11}H_{14}LiO_2[M+Li]^+$ 185.1154. Found 185.1146.

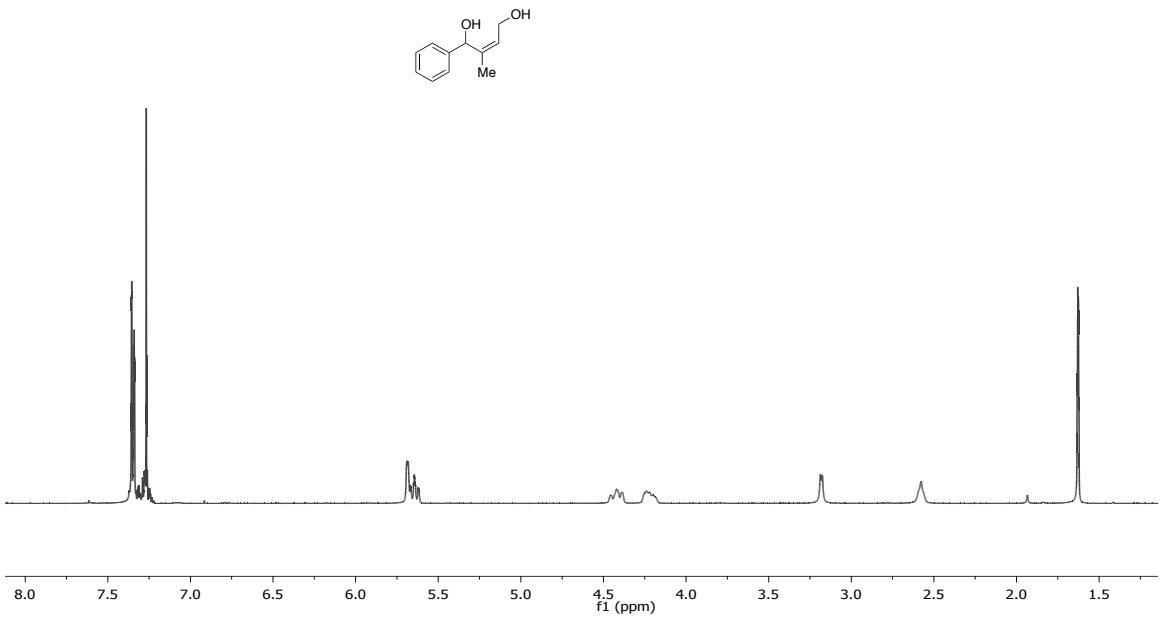
OH
OH
Me
8.0
7.5
7.0
6.5
6.0
5.5
5.0
4.5
4.0
3.5
3.0
2.5
2.0
1.5
f1 (ppm)

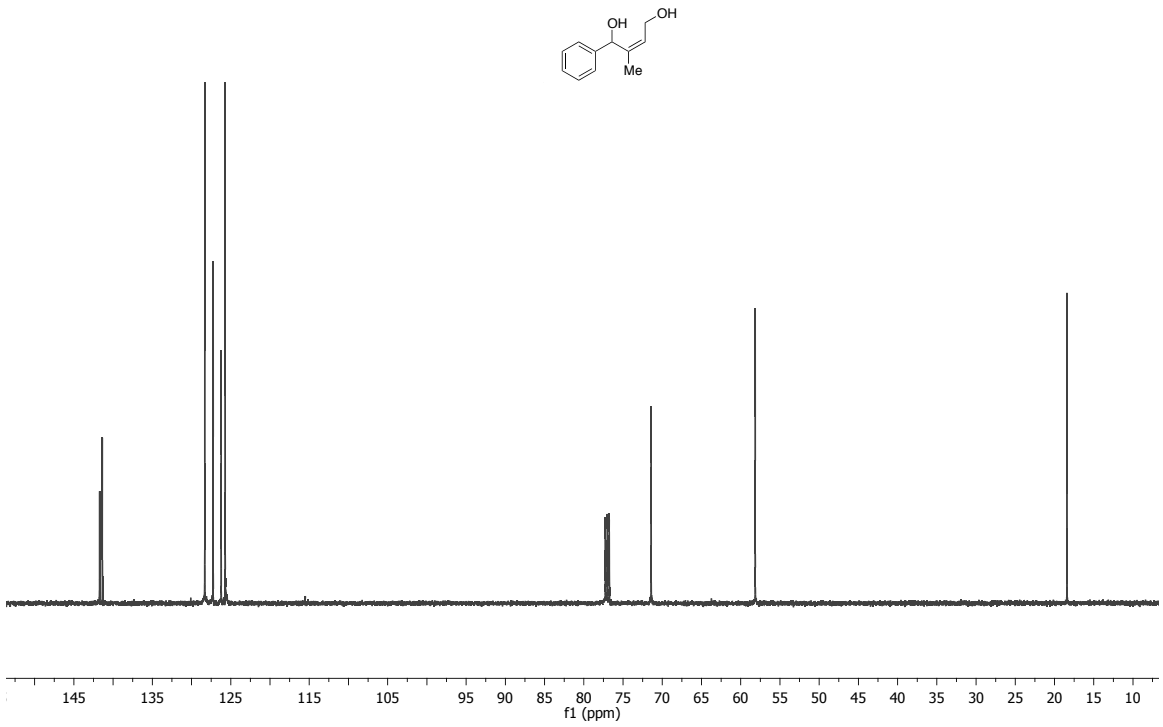
OH
OH
Me
145
135
125
115
105
95
90
85
80
75
70
65
60
55
50
45
40
35
30
25
20
15
10
f1 (ppm)

**(*Z*)-1-(4-bromophenyl)-2-methylbut-2-ene-1,4-diol (2b).** Product was obtained as a white solid (370 mg, 1.44 mmol, 72%). $^{1}$H NMR (300 MHz, $CDCl_3$) δ 7.46 (2H, d, *J* = 6.0 Hz), 7.24 (2H, d, *J* = 12.0 Hz), 5.65 (2H, m), 4.44-4.36 (1H, dd, *J* =12.5, 7.8 Hz), 4.28-4.24 (1H, dd, *J* =12.5, 7.5 Hz), 3.65 (2H, br), 1.60 (3H, s); $^{13}$C NMR (75 MHz, $CDCl_3$) δ 141.1, 140.8, 131.4, 127.5, 126.6, 121.1, 71.0, 58.3, 18.3. HRMS (ESI, TOF): Exact mass calcd for $C_{11}H_{13}BrLiO_2[M+Li]^+$ 263.0259. Found 263.0251.

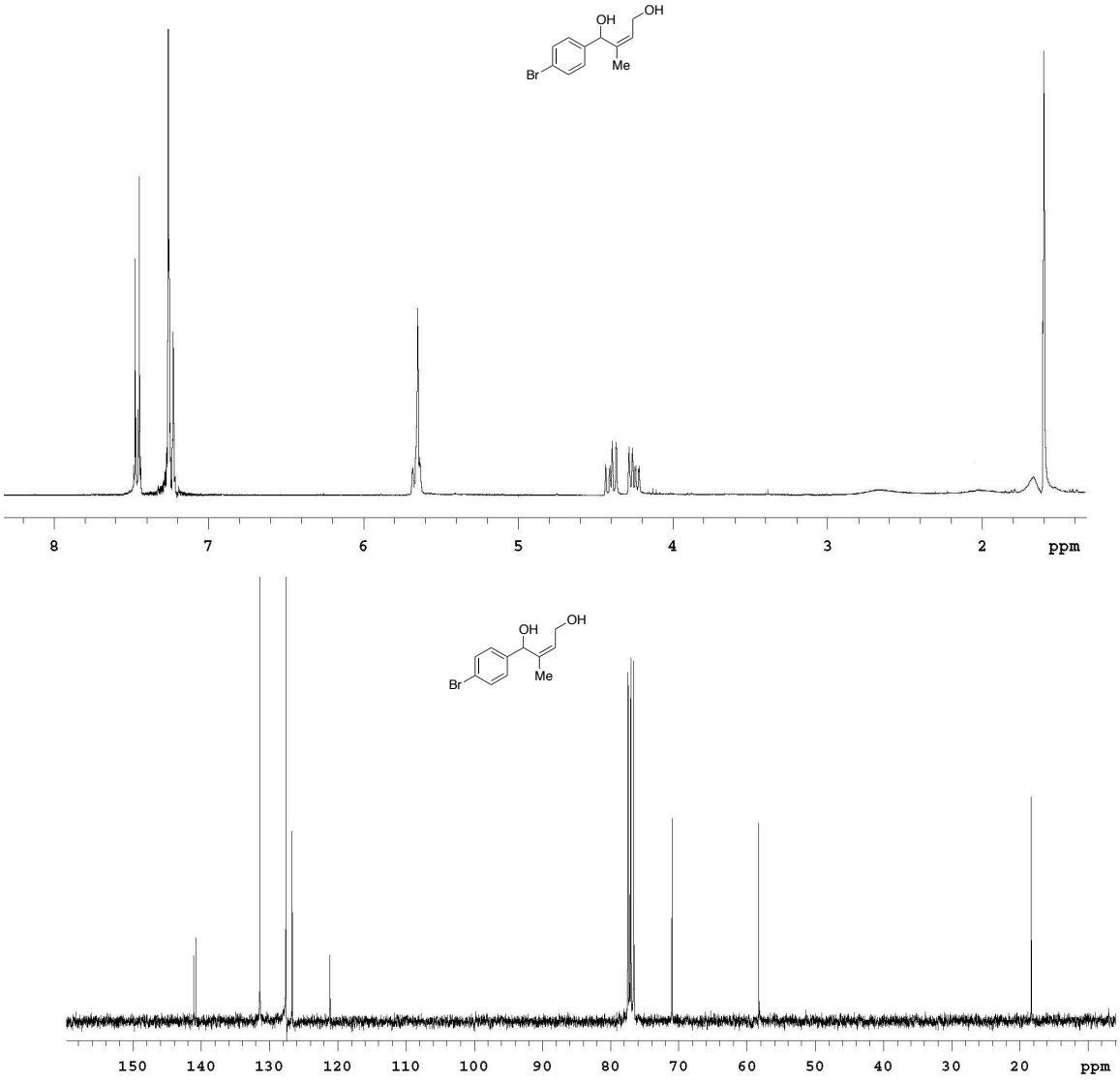

**(*Z*)-1-(4-iodophenyl)-2-methylbut-2-ene-1,4-diol (2c).** Product was obtained as a yellow solid (330 mg, 1.10 mmol, 55%). $^{1}$H NMR (300 MHz, $CDCl_3$) δ 7.66 (2H, d, *J* = 9.0 Hz), 7.08 (2H, d, *J* = 12.0 Hz), 5.63 (2H, m), 4.44-4.35 (1H, dd, *J* = 12.5, 7.5 Hz), 4.23-4.17 (1H, dd, *J* = 12.5, 6.8 Hz), 3.10 (1H, br), 2.43 (1H, br), 1.58 (3H, s); $^{13}$C NMR (75 MHz, $CDCl_3$) δ 141.5, 141.2, 137.3, 127.8, 126.5, 92.7, 70.9, 58.1, 18.3. HRMS (ESI, TOF): Exact mass calcd for $C_{11}H_{15}O_2[M+H]^+$ 179.1072. Found 179.1069.

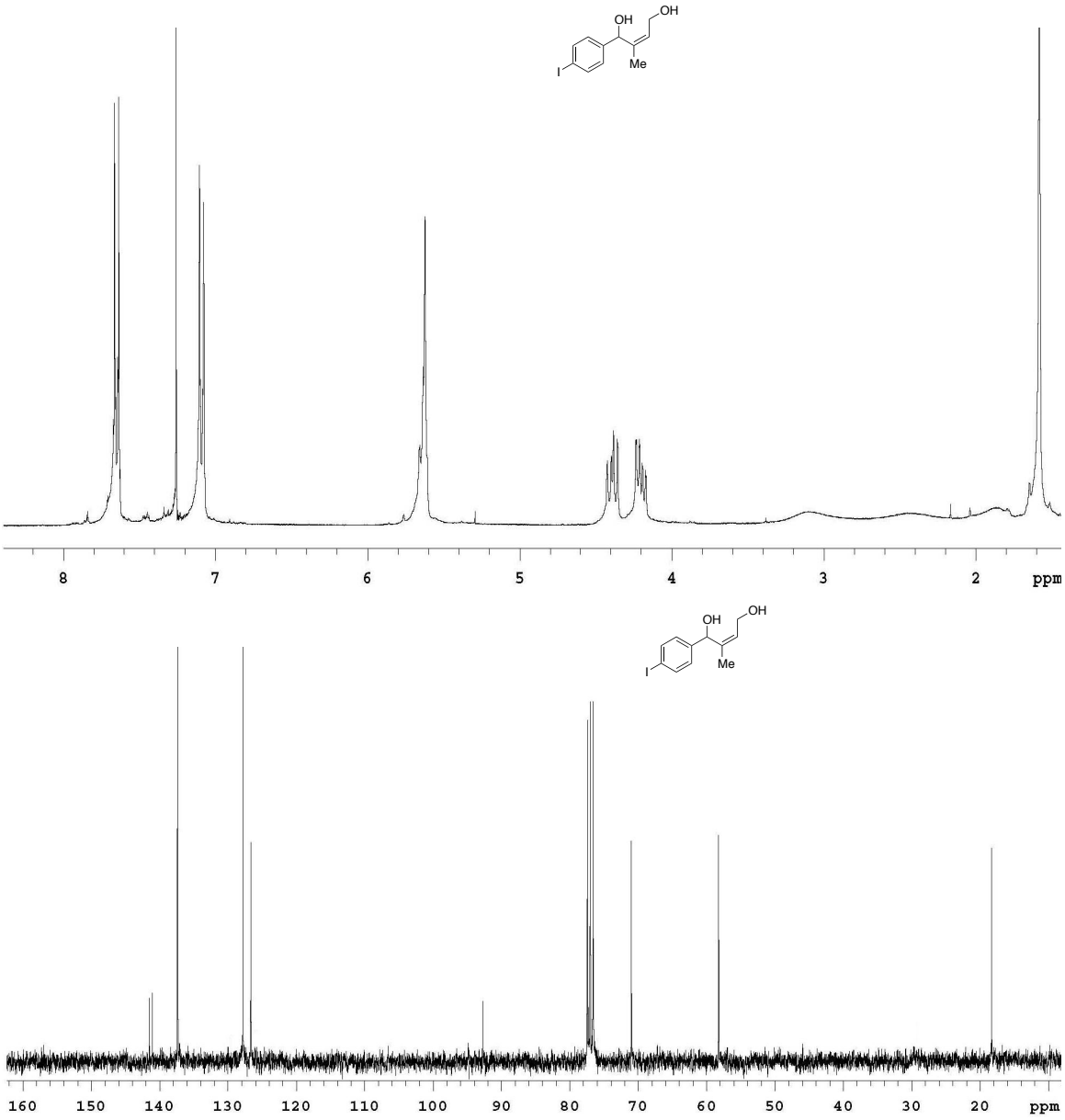

**(*Z*)-2-methyl-1-(4-nitrophenyl)but-2-ene-1,4-diol (2d).** Product was obtained as a yellow solid (300 mg, 1.34 mmol, 67%). $^{1}$H NMR (500 MHz, $CDCl_3$) δ 8.23 (2H, d, *J* = 10.0 Hz), 7.59 (2H, d, *J* = 10.0 Hz), 5.85 (1H, s), 5.75 (1H, t, *J* = 5.0 Hz), 4.46 (1H, dd, *J* = 10.0, 15.0 Hz), 4.33 (1H, dd, *J* = 5.0, 10.0 Hz), 2.77 (1H, br), 1.89 (1H, br), 1.61 (3H, s); $^{13}$C NMR (125 MHz, $CDCl_3$) δ 149.1, 147.1, 140.8, 127.4, 126.6, 123.6, 70.6, 58.2, 18.1. HRMS (ESI, TOF): Exact mass calcd for $C_{11}H_{13}LiNO_4[M+Li]^+$ 230.1005. Found 230.0999.

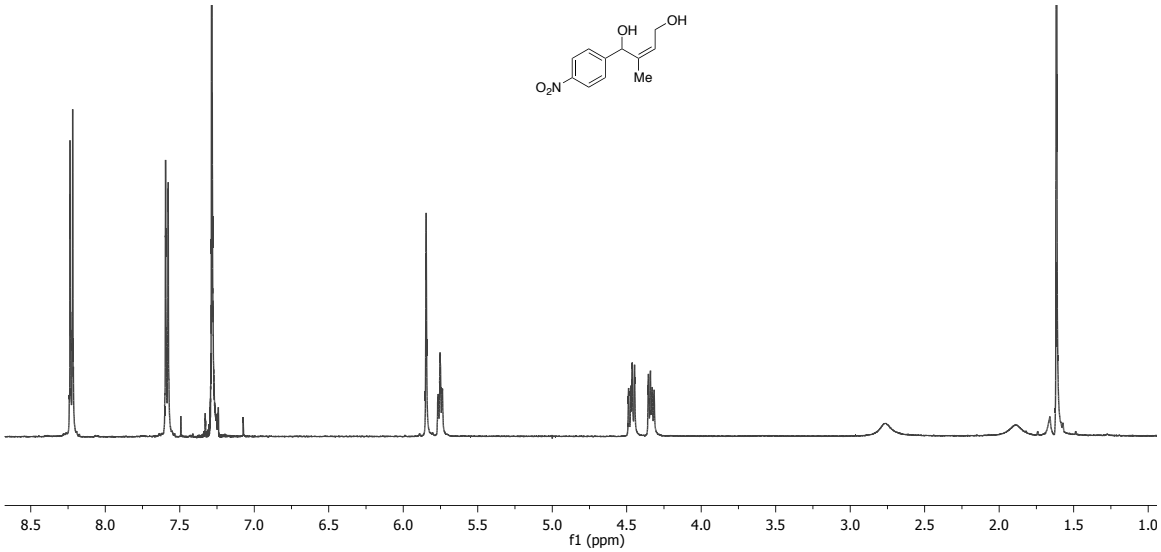


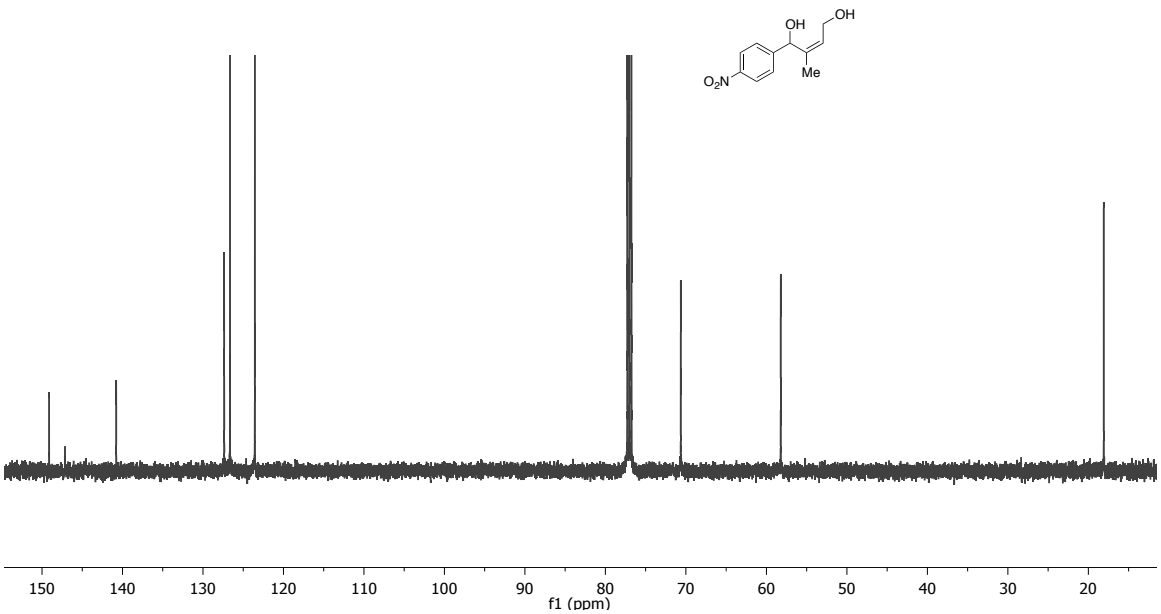

**(*Z*)-1-(4-methoxyphenyl)-2-methylbut-2-ene-1,4-diol (2e).** Product was a white solid (240 mg, 1.16 mmol, 58%). $^{1}$H NMR (300 MHz, $CDCl_3$) δ 7.27-7.24 (2H, m), 6.87-6.85 (2H, m), 5.60 (2H, m), 4.37 (1H, dd, *J* =12.4, 7.8 Hz), 4.21 (1H, dd, *J* = 12.5, 6.5 Hz), 3.78 (3H, s), 2.83 (1H, br), 2.33 (1H, br), 1.62 (3H, s); $^{13}$C NMR (75 MHz, $CDCl_3$) δ 158.8, 141.4, 134.0, 127.0, 126.1, 113.7, 71.5, 58.3, 55.3, 18.6. HRMS (ESI, TOF): Exact mass calcd for $C_{12}H_{16}LiO_3[M+Li]^+$ 215.1259. Found 215.1256.

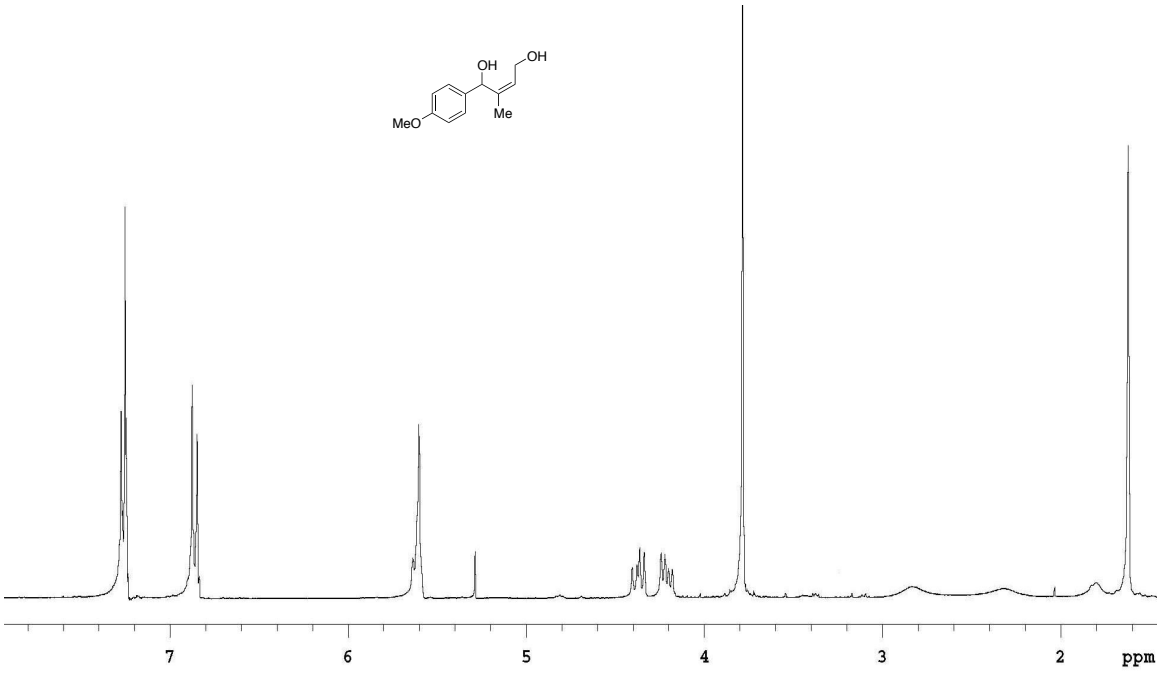


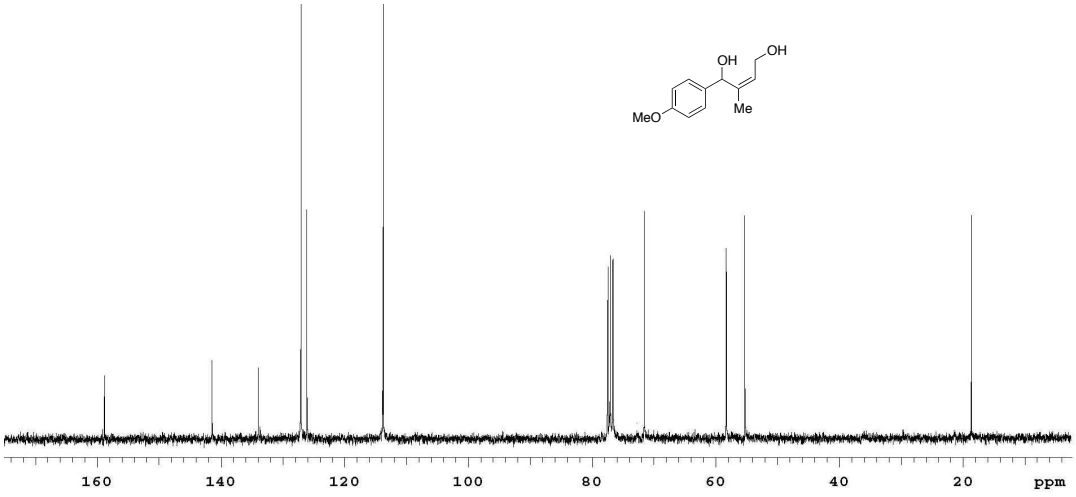

**(*Z*)-2-methyl-1-(2-nitrophenyl)but-2-ene-1,4-diol (2f).** Product was obtained as a white solid (340 mg, 1.52 mmol, 76%). $^{1}$H NMR (300 MHz, $CDCl_3$) δ 7.91 (2H, dd, *J* = 9.0, 15.0 Hz), 7.66 (2H, t, *J* = 9.0 Hz), 7.44 (1H, t, *J* = 9.0 Hz), 6.23 (1H, s), 5.74-5.66 (1H, m), 4.40-4.19 (2H, m), 3.31 (1H, br), 2.33 (1H, br), 1.48 (3H, s). $^{13}$C NMR (75 MHz, $CDCl_3$) δ 148.0, 138.5, 136.5, 133.2, 128.7, 128.5, 128.2, 124.5, 67.4, 58.4, 19.4. HRMS (ESI, TOF): Exact mass calcd for $C_{11}H_{13}LiNO_4$[M+Li]$^+$ 230.1005. Found 230.1016.

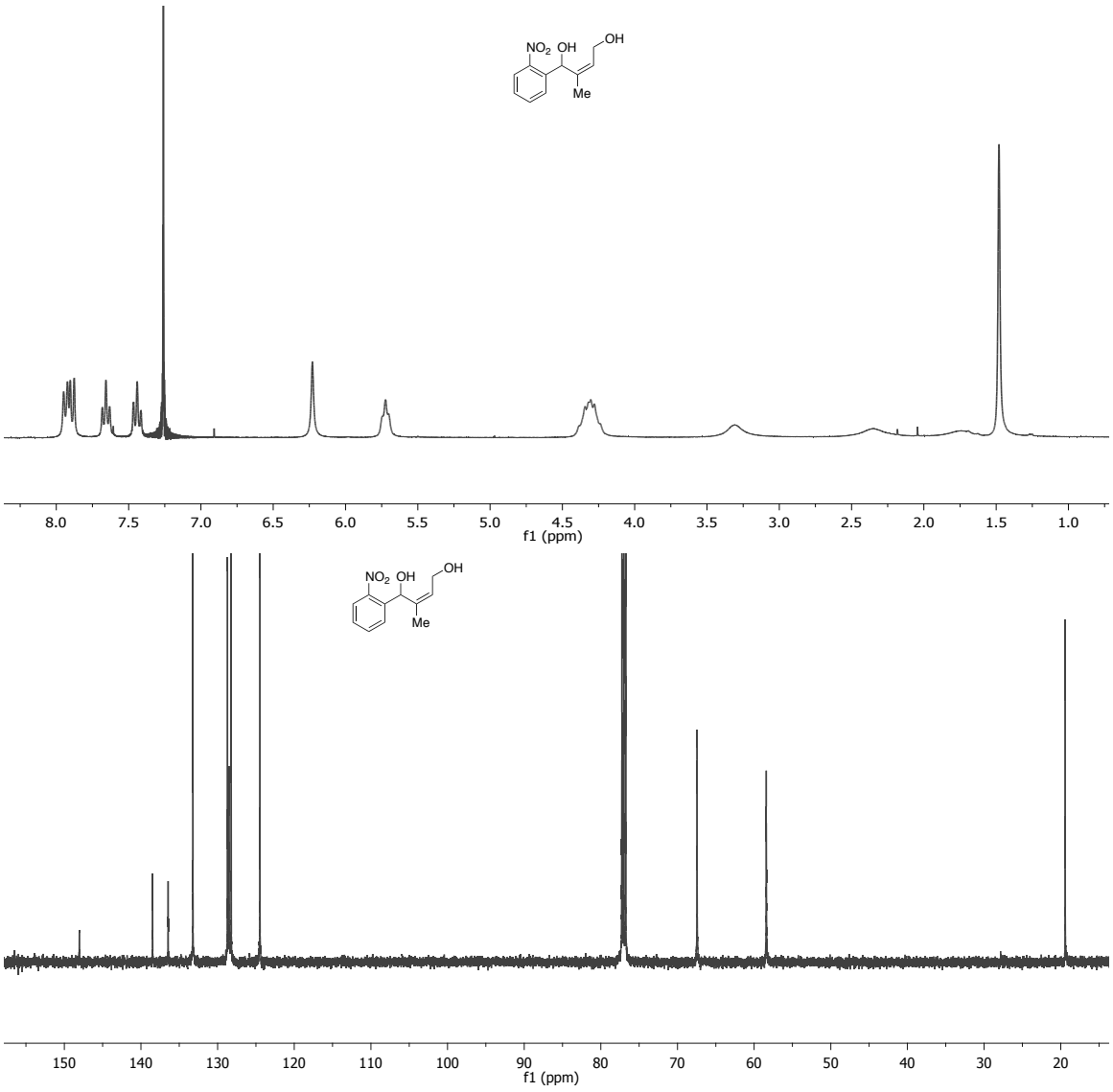

**(*Z*)-1-(2-methoxyphenyl)-2-methylbut-2-ene-1,4-diol (2g).** Product was obtained as a white solid (260 mg, 1.26 mmol, 63%). $^{1}$H NMR (300 MHz, $CDCl_3$) δ 7.50-7.47 (1H, m), 7.27-7.21 (1H, dt, *J* = 4.3, 2.8 Hz), 6.98 (1H, td, *J* = 7.5, 1.0 Hz), 6.84 (1H, d, *J* = 8.2), 5.94 (1H, s), 5.62-5.60 (1H, m), 4.39 (1H, dd, *J* = 12.5, 8.1), 4.21-4.14 (1H, m), 3.79 (3H, s), 3.36 (1H, br), 1.63 (3H, s); $^{13}$C NMR (75 MHz, $CDCl_3$) δ 156.1, 139.7, 129.9, 128.3, 127.1, 126.6, 120.7, 110.4, 66.8, 58.1, 55.3, 18.5. HRMS (ESI, TOF): Exact mass calcd for $C_{12}H_{16}LiO_3[M+Li]^+$ 215.1259. Found 215.1256.

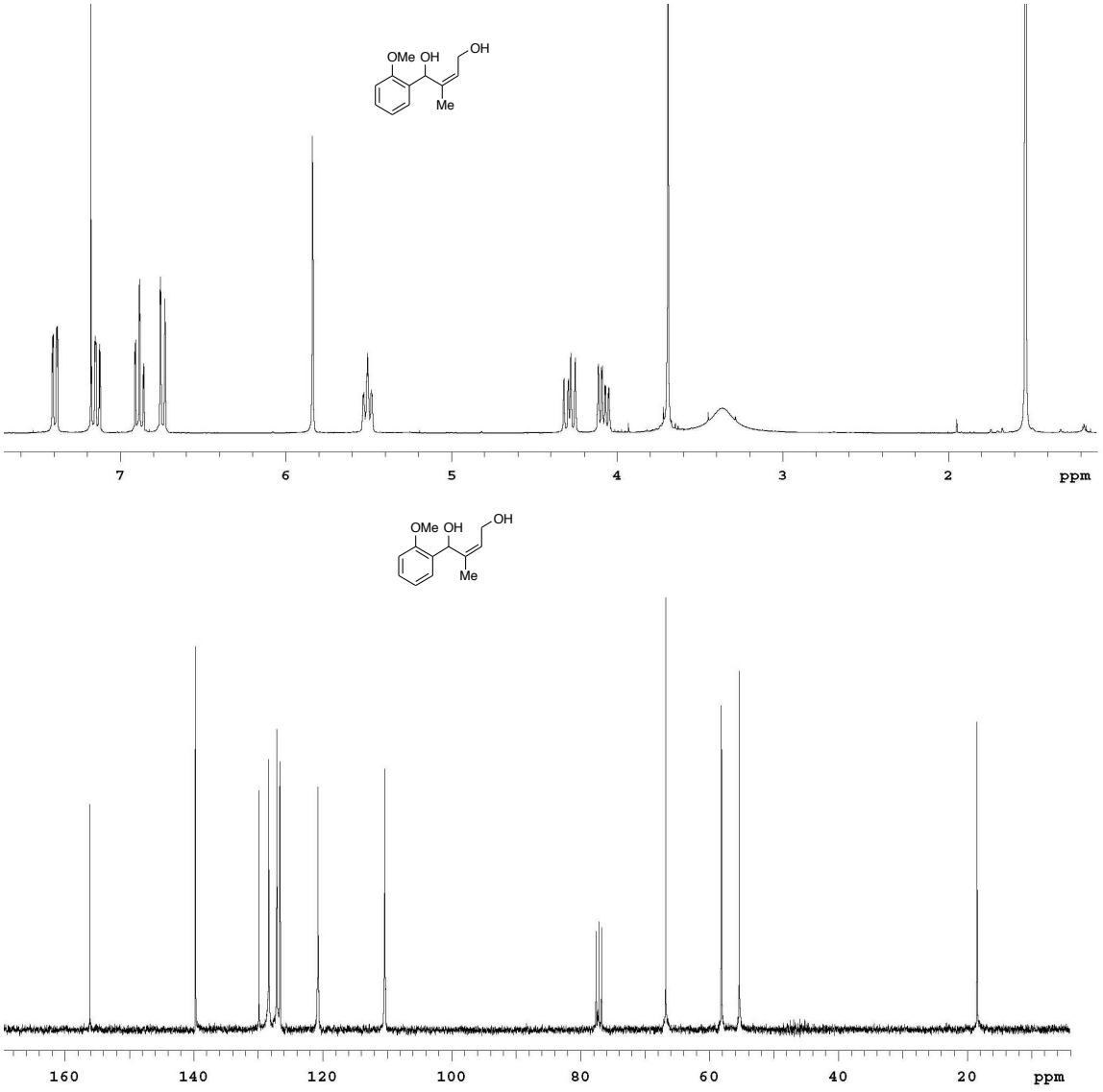

**(*Z*)-1-(2-methoxy-4-nitrophenyl)-2-methylbut-2-ene-1,4-diol (2h).** Product was obtained as a white solid (340 mg, 1.34 mmol, 67%) $^{1}$H NMR (300 MHz, $CDCl_3$) δ 7.90-7.87 (1H, m), 7.73-7.67 (2H, m), 5.95 (1H, s), 5.65 (1H, t, *J* = 7.1 Hz), 4.52-4.40 (1H, m), 4.29-4.19 (1H, m), 3.91 (3H, s), 3.32 (1H, br), 2.07 (1H, br), 1.58 (3H, s); $^{13}$C NMR (75 MHz, $CDCl_3$) δ 156.2, 148.1, 138.9, 137.4, 127.5, 127.4, 115.9, 105.2, 66.4, 58.2, 56.0, 18.2. HRMS (ESI, TOF): Exact mass calcd for $C_{12}H_{15}LiNO_5[M+Li]^+$ 260.1110. Found 260.1107.

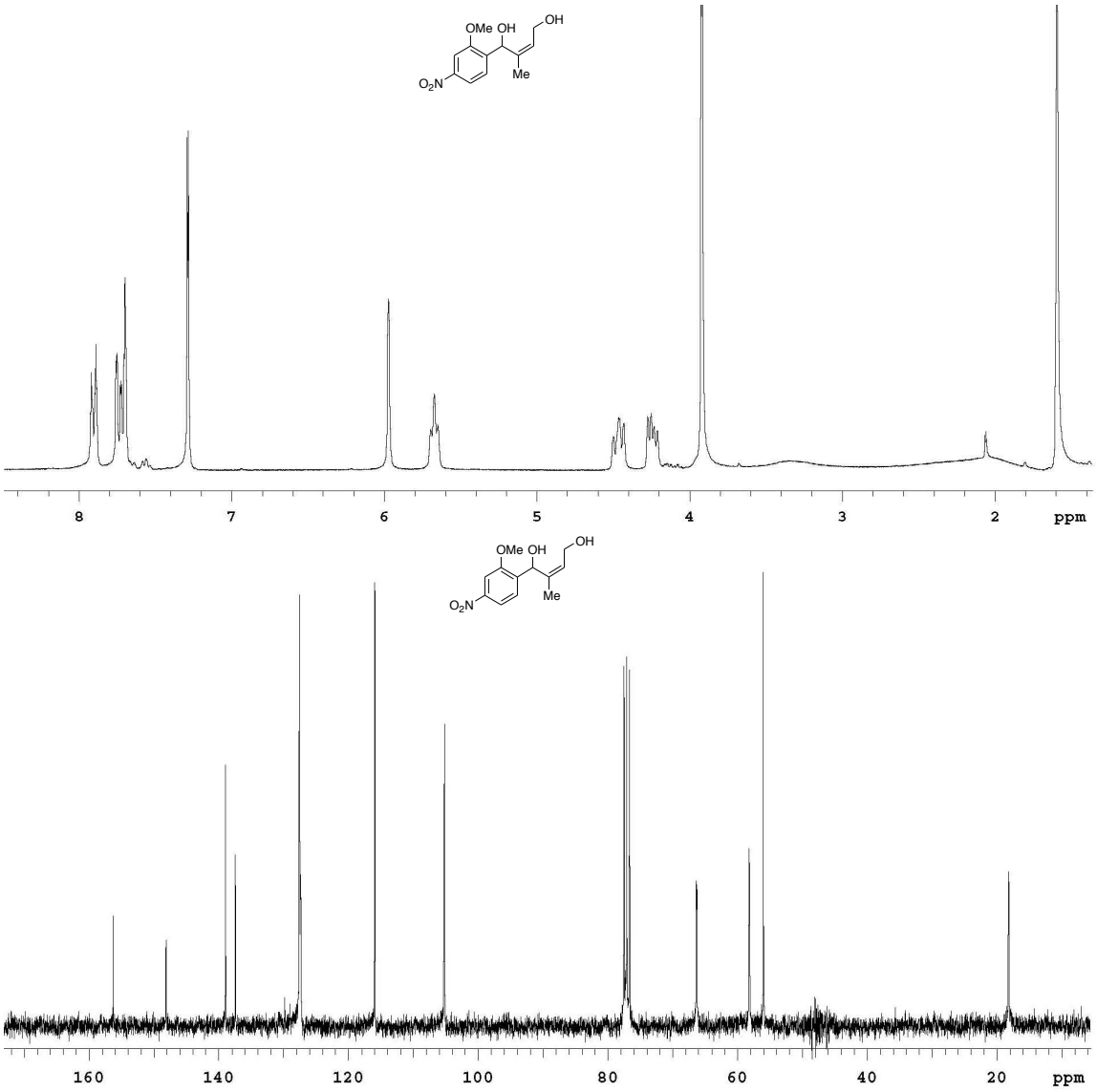

**(2*Z*,5*E*)-3-methyl-6-phenylhexa-2,5-diene-1,4-diol (2i).** Product was obtained as a white solid (210 mg, 1.02 mmol, 51%) $^{1}$H NMR (300 MHz, $CDCl_3$) δ 7.61-7.40 (2H, m), 7.34-7.21 (3H, m), 7.01 (1H, dd, *J* = 9.0, 15.0 Hz), 6.58 (1H, d, *J* = 15.0 Hz), 6.33 (1H, d, *J* = 12.0 Hz), 4.30-4.23 (1H, m), 3.77-3.67 (1H, m), 3.65-3.54 (1H, m), 2.21 (1H, br), 1.92 (1H, br), 1.88 (3H, s); $^{13}$C NMR (75 MHz, $CDCl_3$) δ 137.4, 136.8, 132.9, 128.6,126.4, 126.3, 124.2, 65.3, 13.7. HRMS (ESI, TOF): Exact mass calcd for $C_{13}H_{16}LiO_2$ $[M+Li]^+$ 211.1310. Found 211.1300.

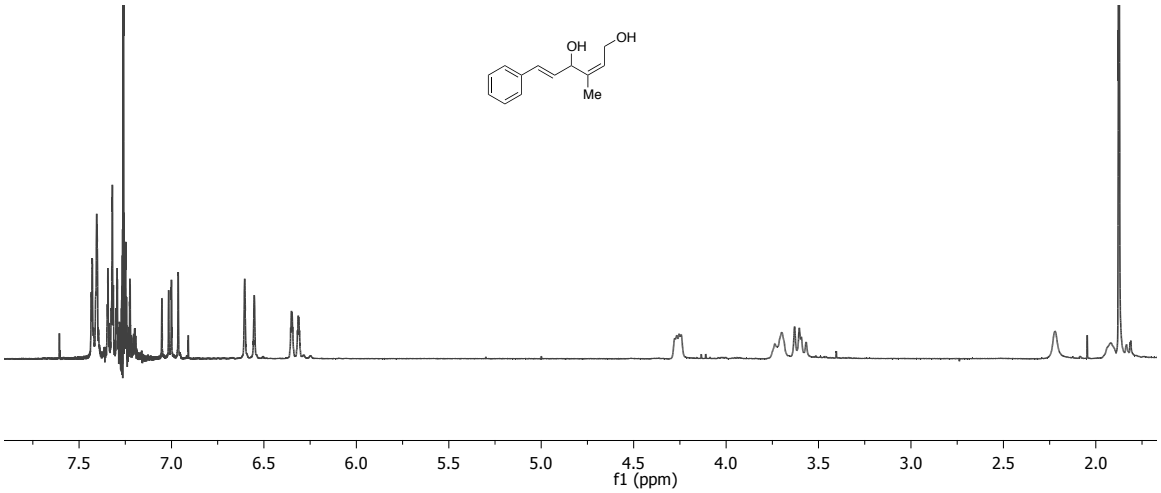


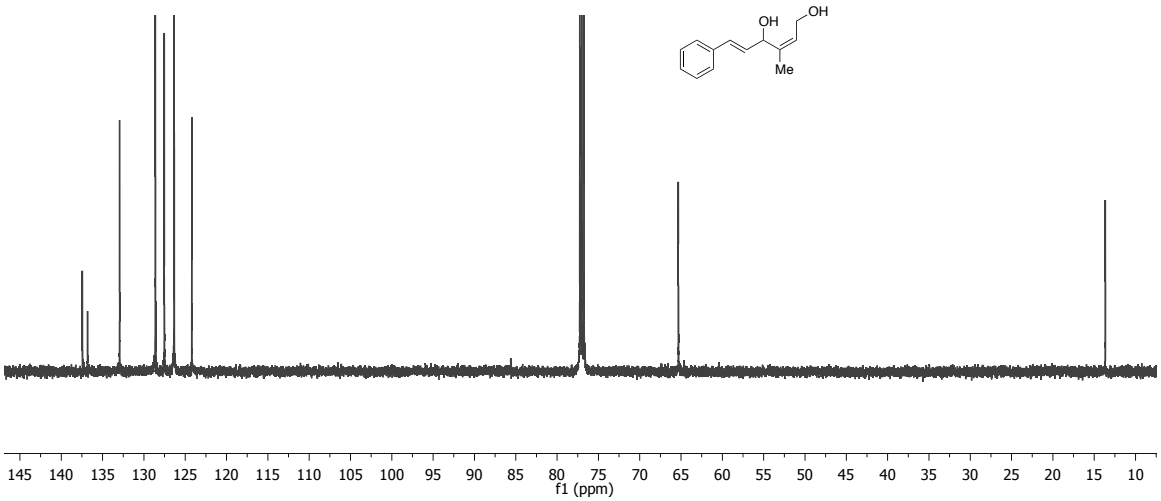

**(2*Z*,5*E*)-3,5-dimethyl-6-phenylhexa-2,5-diene-1,4-diol (2j).** Product was obtained as a white solid (320 mg, 1.48 mmol, 74%). $^{1}$H NMR (300 MHz, $CDCl_3$) δ 7.40-7.22 (5H, m), 6.72 (1H, s), 5.74 (1H, t, *J* = 6.0 Hz), 5.06 (1H, s), 4.39 (1H, dd, *J* = 6.0, 15.0 Hz), 4.29 (1H, dd, *J* = 6.0, 15.0 Hz), 2.77 (1H, br), 1.81 (3H, s), 1.76 (3H, s), 1.63 (1H, s); $^{13}$C NMR (75 MHz, $CDCl_3$) δ 139.5, 137.6, 128.9, 128.1, 127.6, 126.4, 125.0, 124.9, 74.8, 58.5, 18.7, 14.9. HRMS (ESI, TOF): Exact mass calcd for $C_{14}H_{18}LiO_2$ $[M+Li]^+$ 225.1467. Found 225.1476.

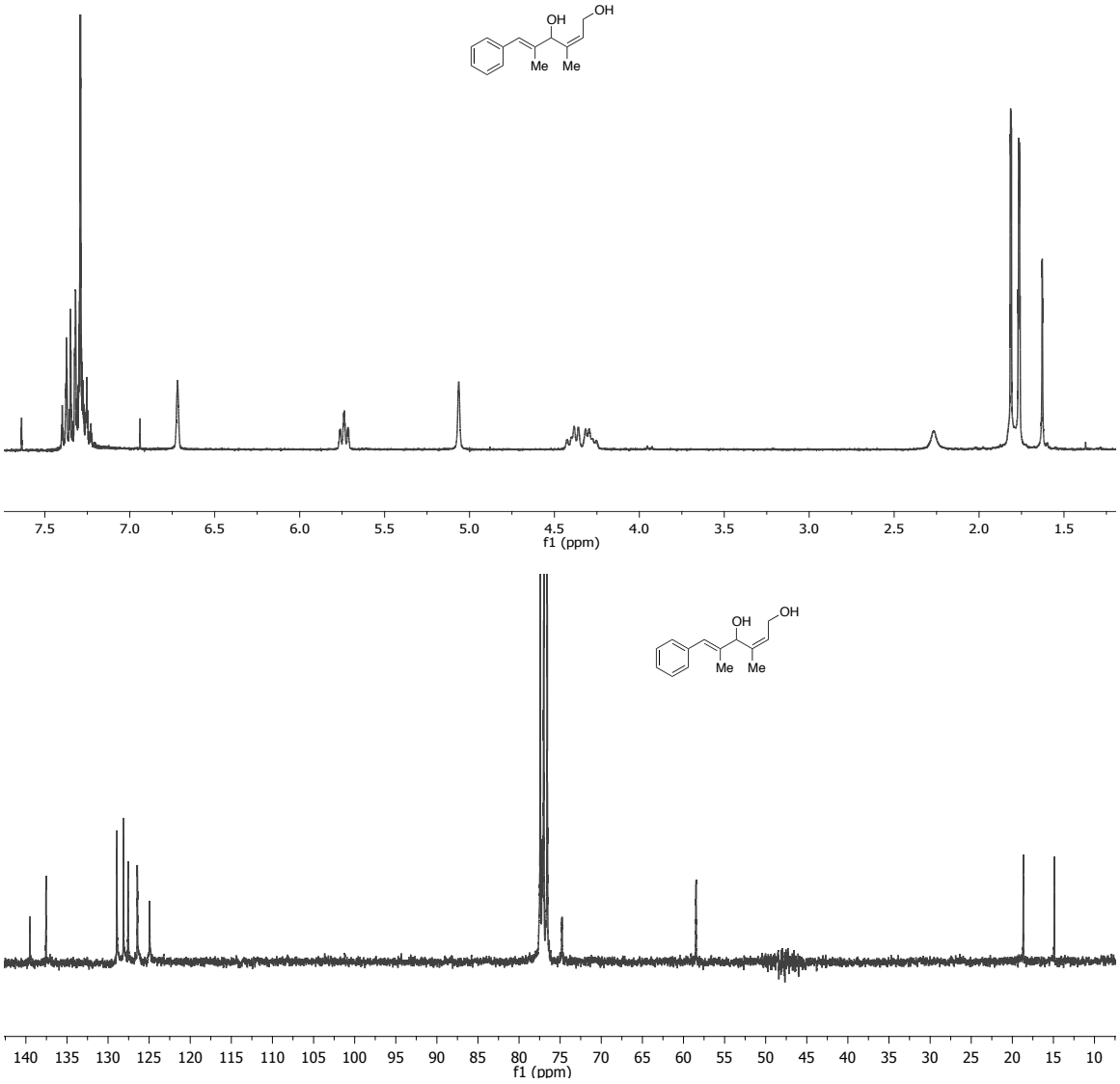

**3-hydroxy-4-methyl-3,6-dihydro-2H-pyran-2-one (2k').** Product was obtained as a colorless oil (92mg, 0.72 mmol, 36%). $^{1}$H NMR (300 MHz, $CDCl_3$) δ 6.80-6.76 (1H, m), 5.17 (1H, s), 4.68-4.58 (1H, m), 4.42-4.32 (1H, m), 4.23 (1H, br), 1.85 (3H, s); $^{13}$C NMR (75 MHz, $CDCl_3$) δ 192.4, 143.0, 131.6, 92.5, 61.5, 14.7. HRMS (ESI, TOF): Exact mass calcd for $C_6H_8LiO_3$ $[M+Li]^+$ 135.0634. Found 135.0629.

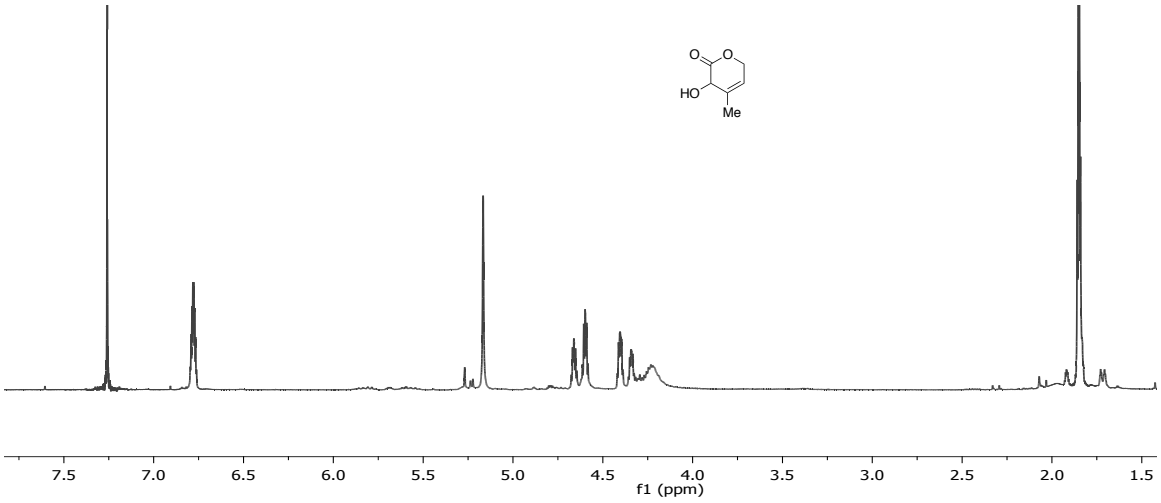


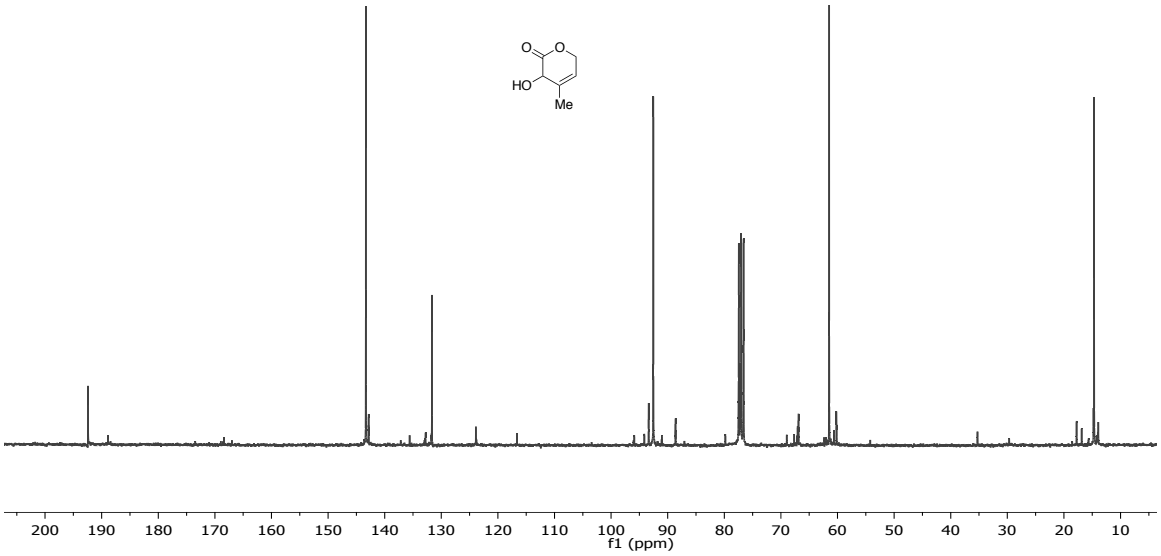

**(*Z*)-3,5-dimethylhex-2-ene-1,4-diol (2l).** Product was obtained as a colorless oil (170mg, 1.16 mmol, 58%). $^{1}$H NMR (300 MHz, $CDCl_3$) δ 5.53 (1H, m), 4.30-4.22 (1H, m), 4.04-3.92 (2H, m), 3.20 (2H, s), 1.79-1.70 (4H, m), 1.05-1.01 (3H, d), 0.73-0.70 (3H, d); $^{13}$C NMR (75 MHz, $CDCl_3$) δ 140.7, 126.5, 75.3, 57.6, 31.1, 19.3, 18.8, 18.0. HRMS (ESI, TOF): Exact mass calcd for $C_8H_{16}LiO_2[M+Li]^+$ 151.1310. Found 151.1303.

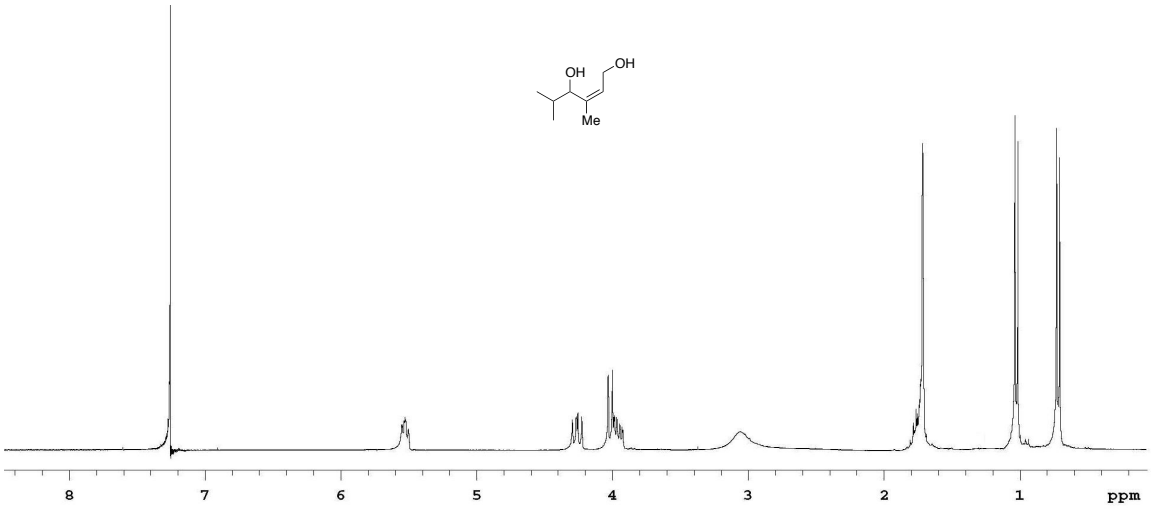


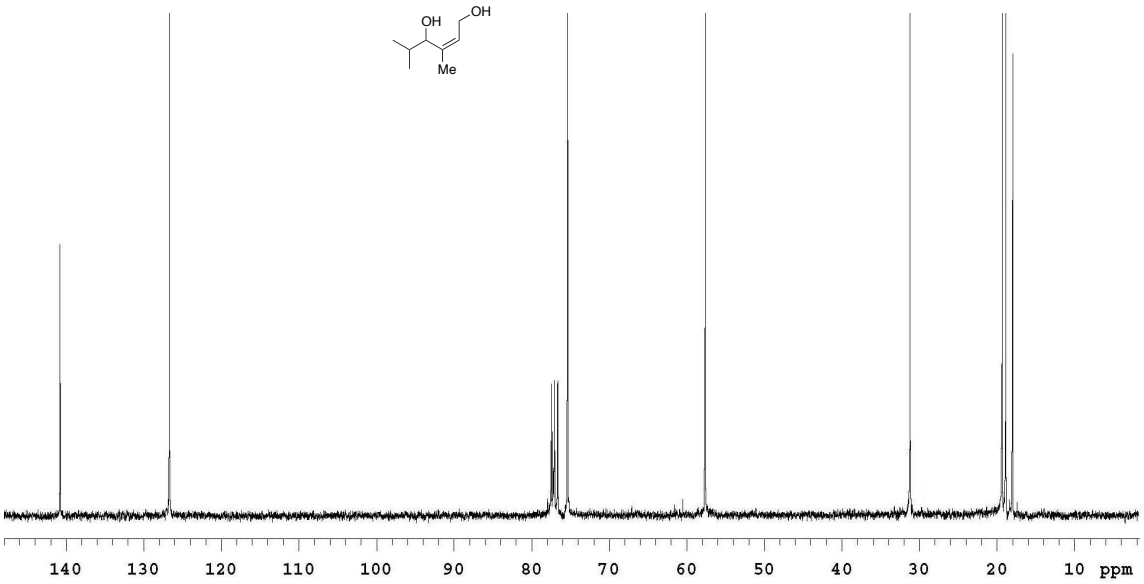

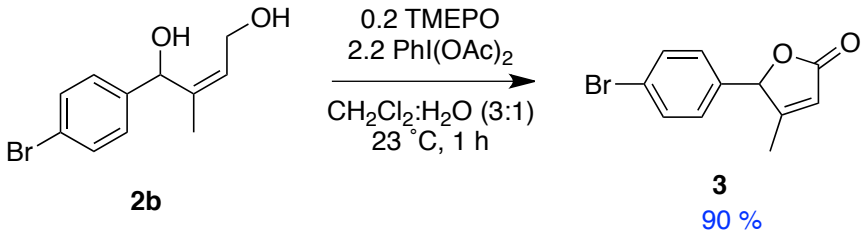


**2b** **3**

90 %

To a solution of **2b** (307 mg, 1.20 mmol) in 7.5 mL of $CH_2Cl_2$ and 1.5 mL of $H_2O$ were added TEMPO (40 mg, 0.20 mmol) and $PhI(OAc)_2$ (850 mg, 2.6 mmol). The reaction mixture was stirred for 1 h at 25 °C, and then was quenched with saturated aqueous $NaHCO_3$, extracted with $CH_2Cl_2$, washed with brine, dried over $MgSO_4$, and concentrated. Purification by column chromatography (5% - 20% EtOAc-Hexane) afforded the desired lactone **3** (273 mg, 1.08 mmol, 90%) of as a colorless oil. $^1$H NMR (300 MHz, $CDCl_3$) δ 7.54 (2H, d, $J$ = 9.0 Hz), 7.12 (2H, d, $J$ = 9.0 Hz), 5.95-5.93 (1H, m), 5.67 (1H, s), 1.92 (3H, s); $^{13}$C NMR (75 MHz, $CDCl_3$) δ 173.0, 168.0, 133.4, 132.3, 128.4, 123.5, 116.5, 85.7, 14.0. HRMS (ESI, TOF): Exact mass calcd for $C_{11}H_{10}BrNO_2[M+H]^+$ 252.9864. Found 252.9861.

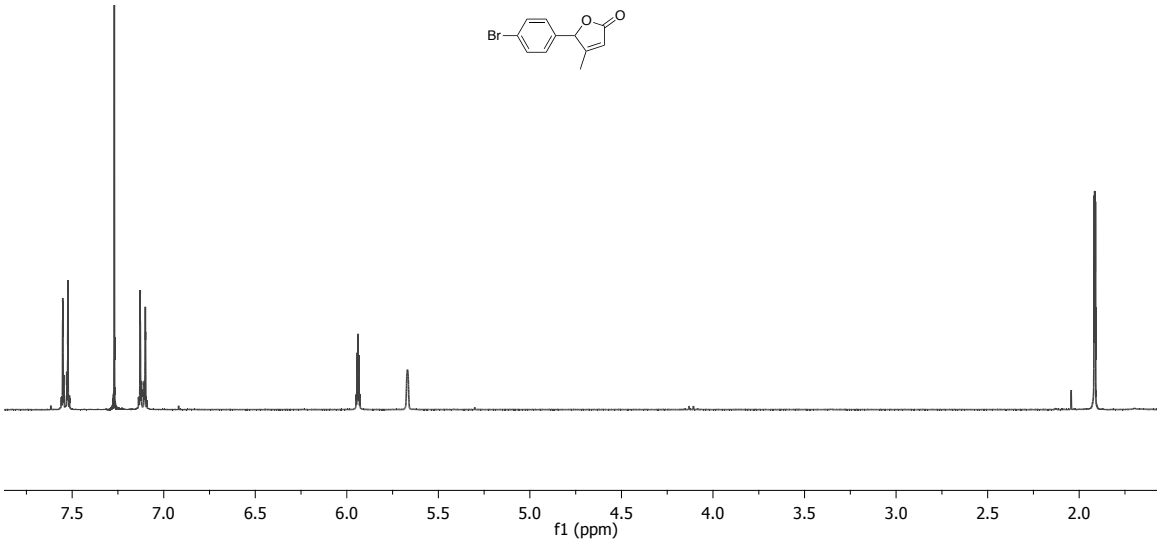
Br
O
O
7.5
7.0
6.5
6.0
5.5
5.0
4.5
4.0
3.5
3.0
2.5
2.0
f1 (ppm)

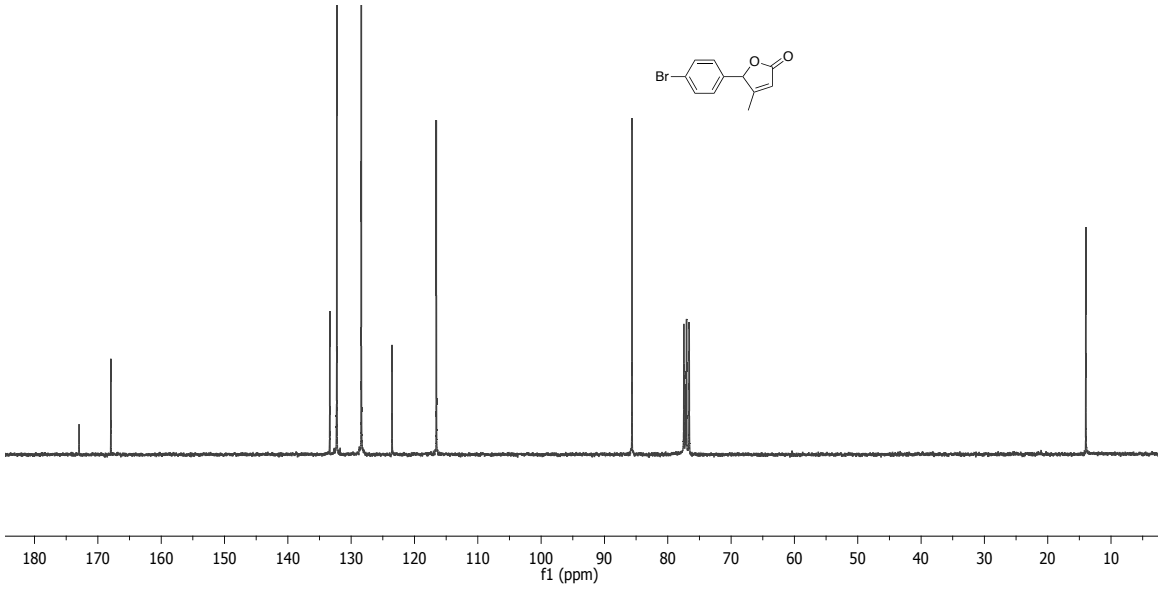
Br
O
O
180
170
160
150
140
130
120
110
100
90
80
70
60
50
40
30
20
10
f1 (ppm)


**2b** **4**
65 %

To a solution of **2b** (307 mg, 1.20 mmol) in 5 mL anhydrous DMSO was added IBX (403 mg, 1.44 mmol). The reaction mixture was stirred for 2 h at 23 °C and then quenched with $H_2O$ (10 mL). The mixture was filtered through Celite and the filter cake was washed with $CH_2Cl_2$ and $H_2O$. The layers were separated and the aquous phase was extracted with $CH_2Cl_2$. The combined organic phase was dried ($Na_2SO_4$) and concentrated. The residue was purified by column chromatography and the desired furan **4** (180 mg, 0.780 mmol, 65%) was obtained as a colorless oil; $^1$H NMR (300 MHz, $CDCl_3$) δ 7.56-7.50 (4H, m), 7.41 (1H, s), 6.36 (1H, s), 2.30 (1H, s); $^{13}$C NMR (75 MHz, $CDCl_3$) δ 147.6, 140.9, 131.6, 130.2, 126.7, 120.4, 116.9, 115.3. HRMS (ESI, TOF): Exact mass calcd for $C_{11}H_{10}BrO[M+H]^+$ 236.9915. Found 236. 9910.

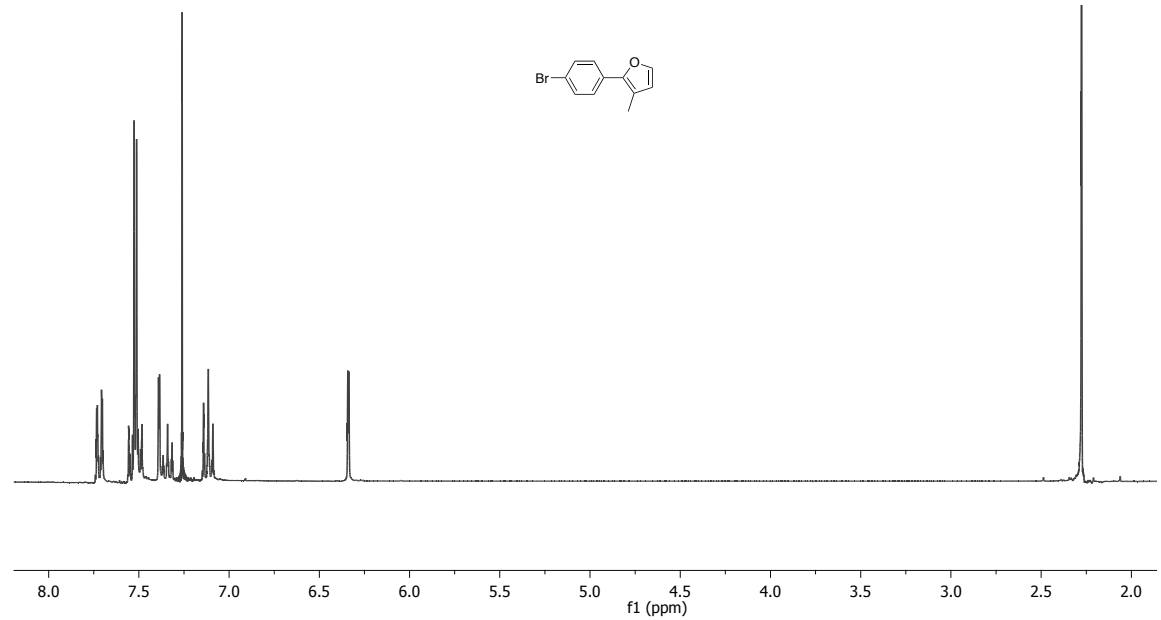
Br
O
8.0
7.5
7.0
6.5
6.0
5.5
5.0
4.5
4.0
3.5
3.0
2.5
2.0
f1 (ppm)

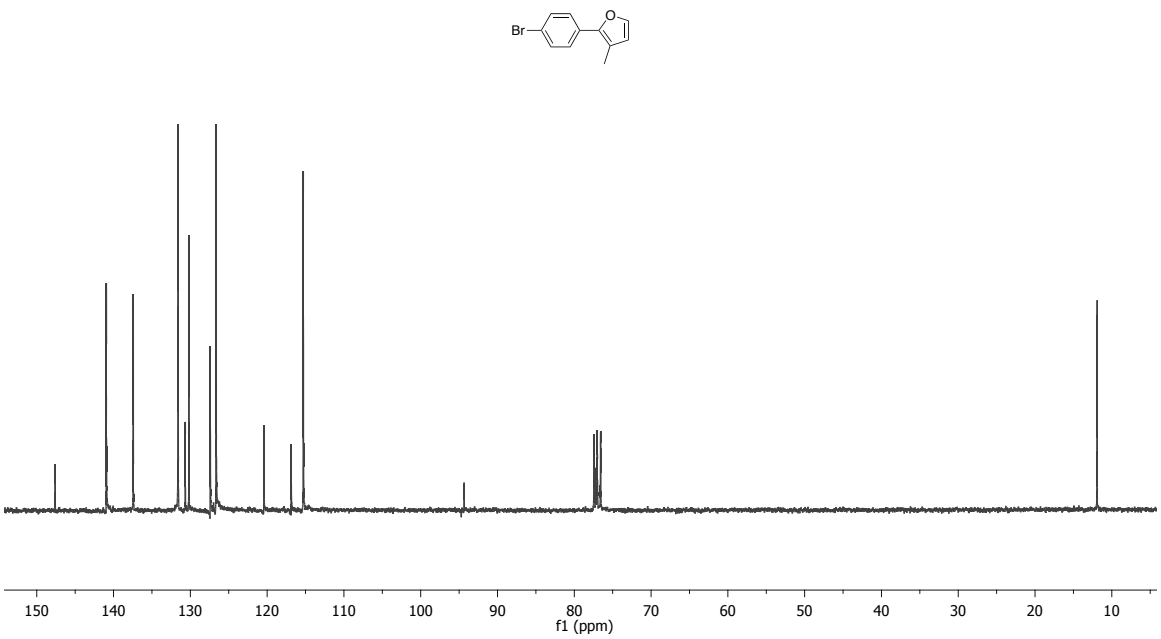
Br
O
150
140
130
120
110
100
90
80
70
60
50
40
30
20
10
f1 (ppm)

## APPENDIX C
## EXPERIMENTAL FOR CHAPTER III

### A. Preparation of compound 6

**Preparation of (*E*)-Methyl 4-Hydroxy-3-methylbut-2-enoate 6**

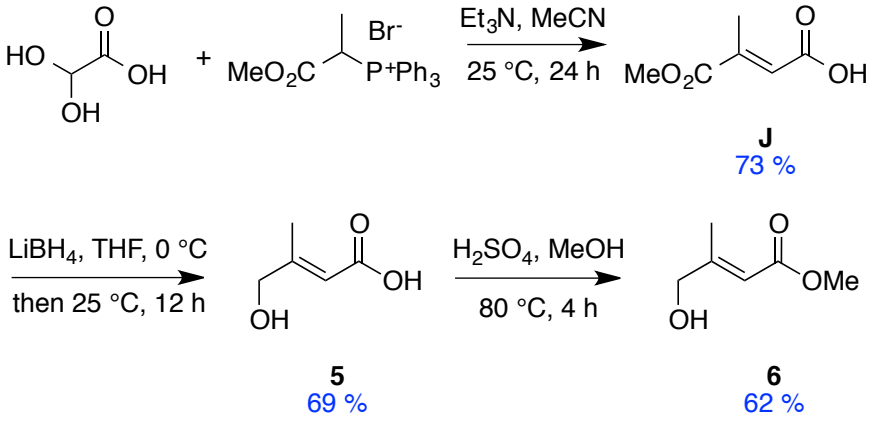


**(*E*)-4-Methoxy-3-methyl-4-oxobut-2-enoic acid (J).**

To a solution of (1-methoxy-1-oxopropan-2-yl)triphenylphosphonium bromide (42.9 g, 100 mmol) in dry MeCN (300 mL) was added triethylamine (13.2 mL, 95 mmol) and glyoxylic acid monohydrate (8.74 g, 95 mmol) at 0 °C. The solution was further stirred at 0 °C for 2 h and at room temperature overnight. Half of the solvent was removed under reduced pressure, and ethyl acetate (100 mL) was added. The resulting solution was washed with saturated aqueous $NaHCO_3$ (3 × 50 mL). The combined aqueous layers were extracted with ethyl acetate (2 × 50 mL), acidified (pH 1 - 2) at 0 °C with concentrated HCl (50 mL) and extracted with ethyl acetate (3 × 50 mL). The combined organic layers were evaporated to dryness, yielding a clear oil **J** (10.5 g, 73%) which was used for the next reaction without further purification.

**(*E*)-4-Hydroxy-3-methylbut-2-enoic acid (5).**

$LiBH_4$ (400 mmol) was added to (*E*)-4-methoxy-3-methyl-4-oxobut-2-enoic acid **J** (200 mmol) in THF (200 mL) at 0 °C. The reaction mixture was then allowed to

ambient temperature and stirred for 12 h. The mixture was poured into 1N HCl and extracted with ethyl acetate (3 × 50 mL). The combined organic layers were dried over $Na_2SO_4$ and solvent was removed under reduced pressure to yield the product **5** as a white solid (16 g, 69%) which was used for the next reaction without further purification.

**(*E*)-Methyl 4-Hydroxy-3-methylbut-2-enoate (6).**

To a solution of $H_2SO_4$ in 50 mL of MeOH, (*E*)-4-hydroxy-3-methylbut-2-enoic acid **5** (150 mmol) was added at room temperature. The mixture was stirred and refluxed for 4 h. After cooling to ambient temperature, solvent was removed under reduced pressure. The residue was dissolved in $CH_2Cl_2$. The organic layer was washed with $NaHCO_3$, brine and dried over $Na_2SO_4$. Solvent was removed under reduced pressure to obtain product **6** as a clear oil (12 g, 93 mmol, 62 %). $^1$H NMR (400 MHz, $CDCl_3$) δ 6.48 (1H, d, $J$ = 4.7 Hz), 3.96 (2H, s), 3.63 (3H, s), 1.89 (3H, d, $J$ = 6.6 Hz); $^{13}$C NMR (100 MHz, $CDCl_3$) δ 167.2, 132.3, 119.7, 67.2, 58.3, 26.2. HRMS (ESI, TOF): Exact mass calcd for $C_6H_{11}O_3$ $[M+H]^+$ 131.0708. Found 131.0711.

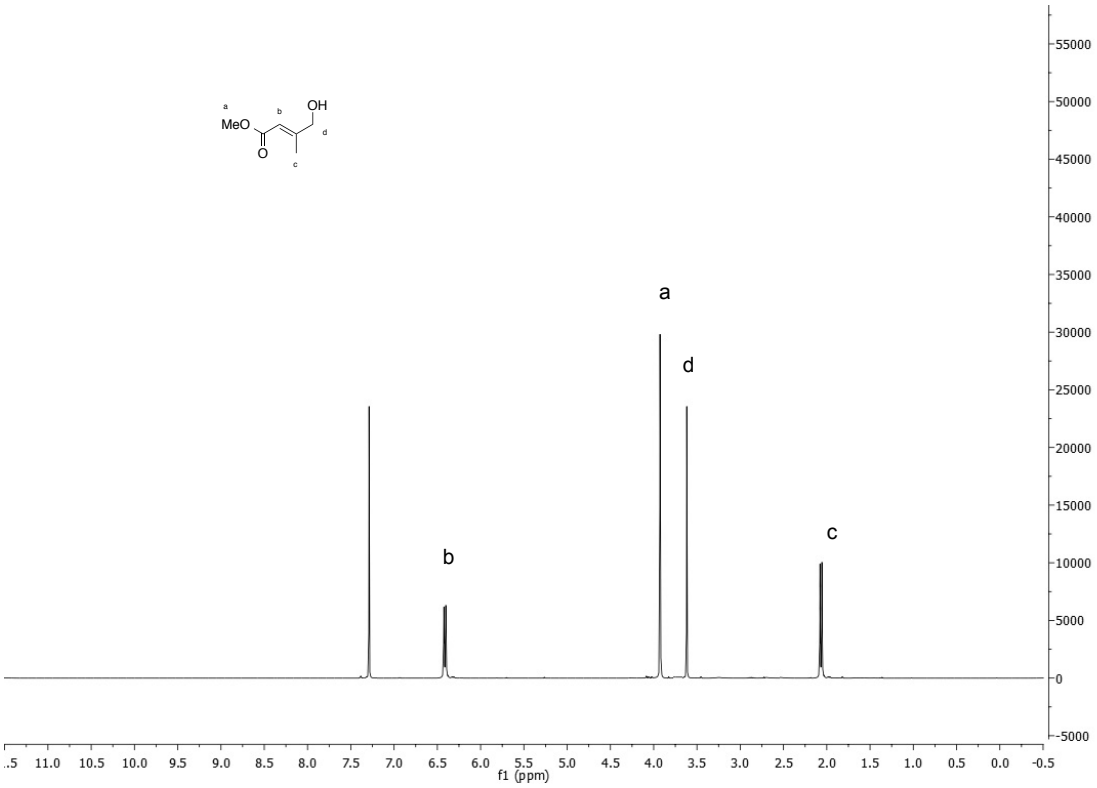
a
MeO
b
OH
d
O
c
a
d
b
c
55000
50000
45000
40000
35000
30000
25000
20000
15000
10000
5000
0
-5000
11.0 10.5 10.0 9.5 9.0 8.5 8.0 7.5 7.0 6.5 6.0 5.5 5.0 4.5 4.0 3.5 3.0 2.5 2.0 1.5 1.0 0.5 0.0 -0.5
f1 (ppm)

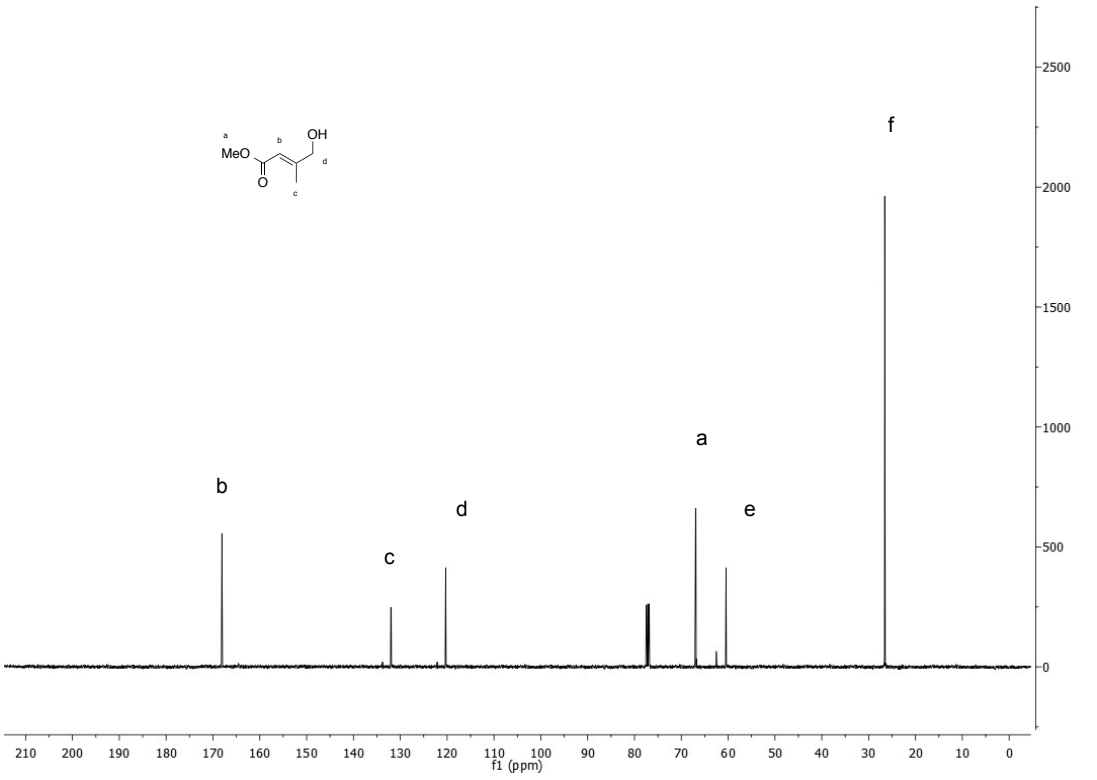
a
MeO
b
OH
d
O
c
f
b
c
d
a
e
2500
2000
1500
1000
500
0
210 200 190 180 170 160 150 140 130 120 110 100 90 80 70 60 50 40 30 20 10 0
f1 (ppm)

**B. Catalytic Hydrogenation Conditions**

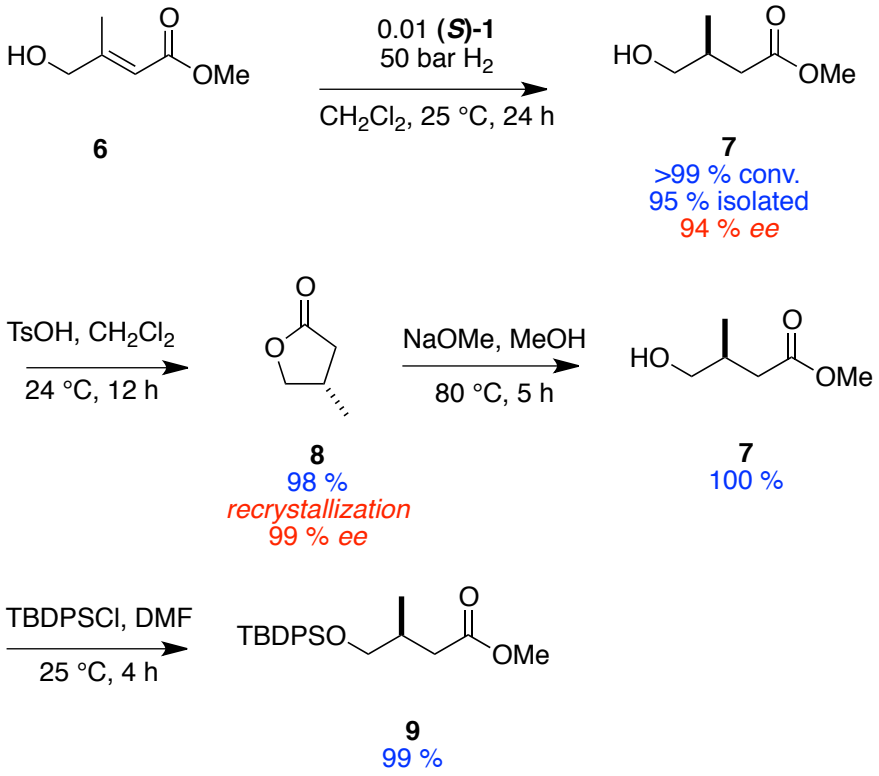


(*E*)-Methyl 4-hydroxy-3-methylbut-2-enoate **6** (120 mmol) and **(*S*)-1** (1 mol %) were dissolved in $CH_2Cl_2$ (0.5 M). The resulting mixture was degassed by three cycles of freeze-pump-thaw and then transferred to a Parr Bomb. The bomb was pressurized to 50 bar with hydrogen and the mixture was stirred at 300 rpm for 24 h. The bomb was then vented and solvent was evaporated. The crude product was passed through a short silica plug using 10-30% EtOAc/hexanes as the eluent. The enantiomeric ratio was then measured through chiral GC analysis.

**Methyl (*S*)-4-Hydroxy-3-methylbutanoate (7).**

Colorless oil, 15.2 g, 114 mmol (95% isolated yield); $^1$H NMR (400 MHz, $CDCl_3$) δ 4.05 (3H, s), 3.35 (2H, dd, $J$ = 6.6, 12 Hz), 2.48 (2H, m), 2.07 (1H, m), 0.92 (3H, d, $J$ = 6.6 Hz); $^{13}$C NMR (100 MHz, $CDCl_3$) δ 171.0, 68.5, 62,1, 37.8, 32.5, 14.7. HRMS (ESI, TOF): Exact mass calcd for $C_6H_{13}O_3$ $[M+H]^+$ 133.0865. Found 133.0864.

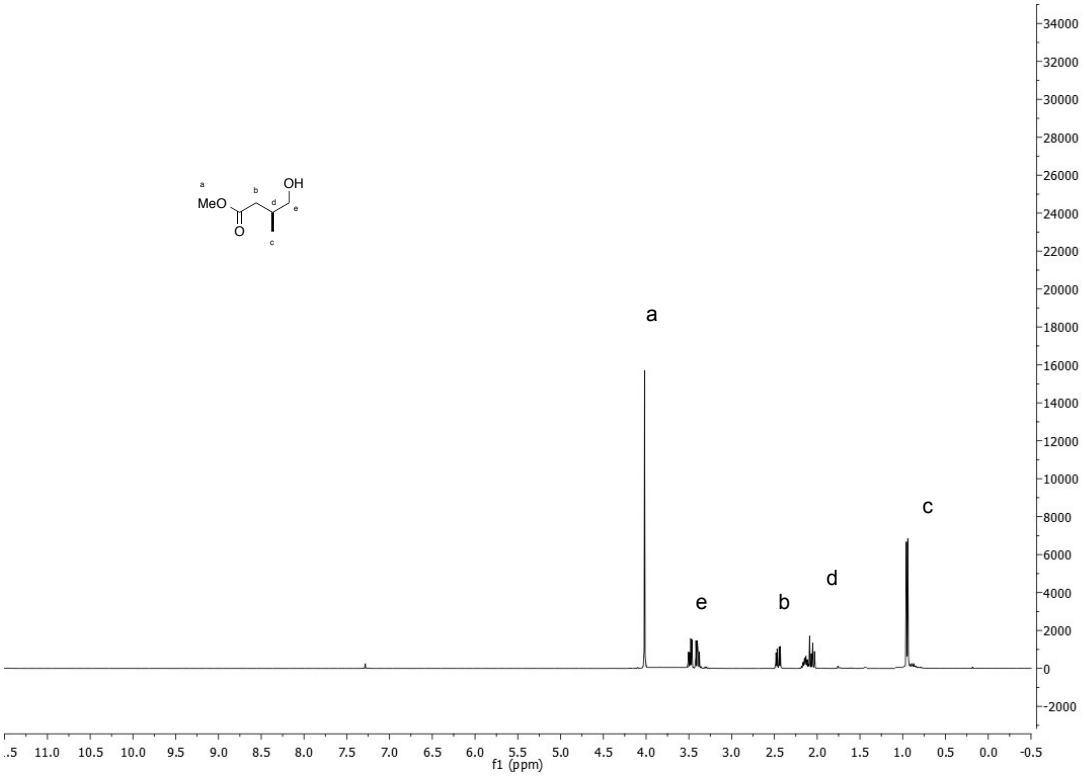
a
MeO
OH
O
a
b
c
d
e
f1 (ppm)

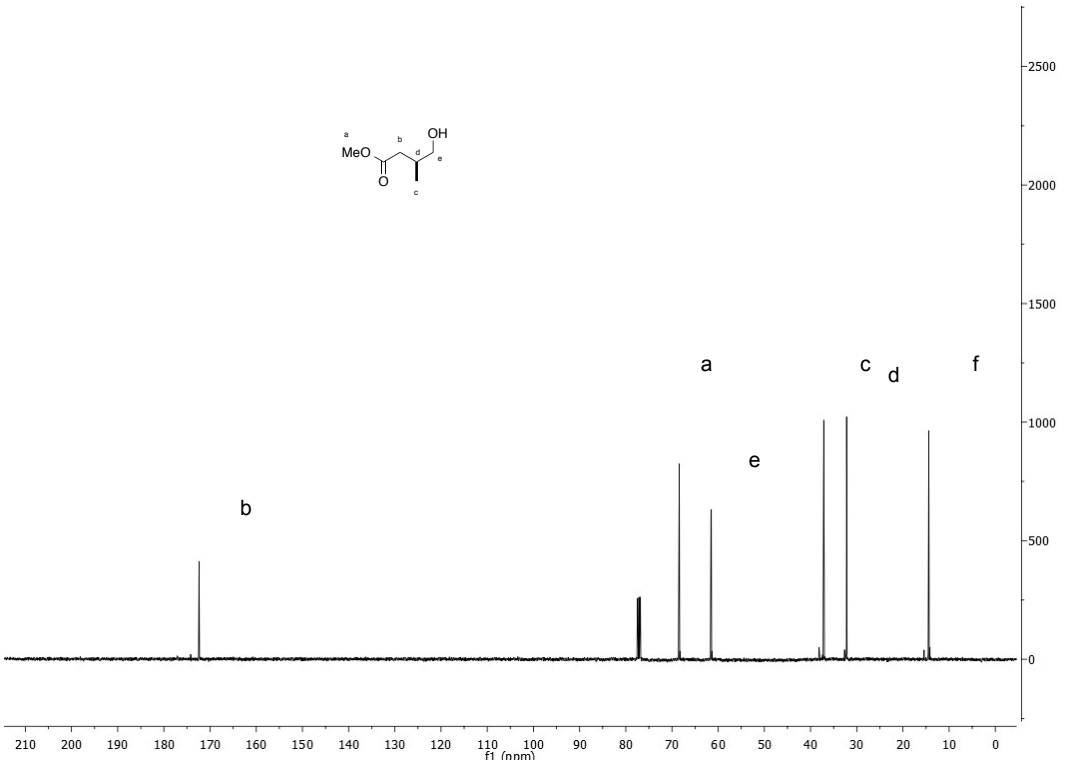
a
MeO
OH
O
a
b
c
d
e
f
f1 (ppm)

**C. Preparation of (*S*)-4-Methyldihydrofuran-2(3*H*)-one (8)**

To a solution of methyl (*S*)-4-hydroxy-3-methylbutanoate **7** (12 g, 90 mmol) in 30 mL of $CH_2Cl_2$, TsOH (0.95 equiv) was added at room temperature. The mixture was stirred for 6 h, then the organic layer was washed with $H_2O$ (3 × 30 mL), brine and dried over $Na_2SO_4$. Solvent was removed under reduced pressure to yield product as colorless oil (9.8 g, 98%).

**D. Recrystallization conditions**

(*S*)-4-Methyldihydrofuran-2(3*H*)-one **8** was dissolved in EtOAc and hexane and the mixture was cooled to -20 °C. After getting precipitation, solvent was decanted in low temperature and washed with cold hexane.

**E. Preparation of compound 9**

**Preparation of Methyl (*S*)-4-((*tert*-Butyldiphenylsilyl)oxy)-3-methylbutanoate (9).**

To a solution of methyl (*S*)-4-hydroxy-3-methylbutanoate **7** (5.5g, 42 mmol) in 30 mL of DMF, TBDPSCl (0.95 equiv) was added at room temperature. The mixture was stirred for 4 h, then solvent was removed under reduced pressure. The residue was dissolved in $CH_2Cl_2$. The organic layer was washed with $H_2O$ (3 × 30 mL), brine and dried over $Na_2SO_4$. Solvent was removed under reduced pressure and the crude was purified by chromatography using 5% EtOAc/hexane as eluent to obtain product **9** as a clear oil (15 g, 42 mmol, 99%). $^1$H NMR (400 MHz, $CDCl_3$) δ 7.79-7.30 (10H, m), 3.69 (3H, s), 3.59 (2H, dd, $J$ = 3.3, 12 Hz), 2.63-2.60 (2H, m), 2.32-2.20 (1H, m), 1.09 (9H, s), 1.02 (3H, d, $J$ = 6.6 Hz); $^{13}$C NMR (100 MHz, $CDCl_3$) δ 173.5, 137.8, 133.8, 129.7, 126.9, 68.7, 51.9, 38.7, 26.8, 19.7, 16.1. HRMS (ESI, TOF): Exact mass calcd for $C_{22}H_{31}O_3Si$ $[M+H]^+$ 371.0242. Found 371.0222.

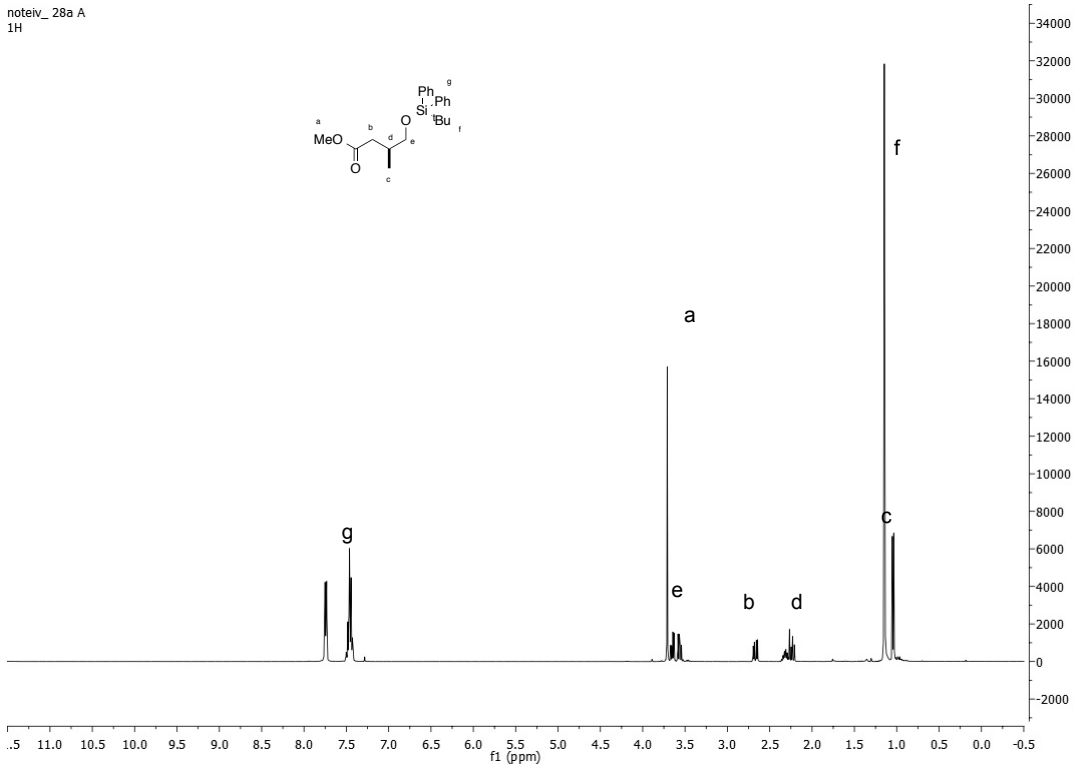
noteiv_ 28a A
1H
MeO
O
Si
Ph
Ph
tBu
a
b
c
d
e
f
g
f1 (ppm)

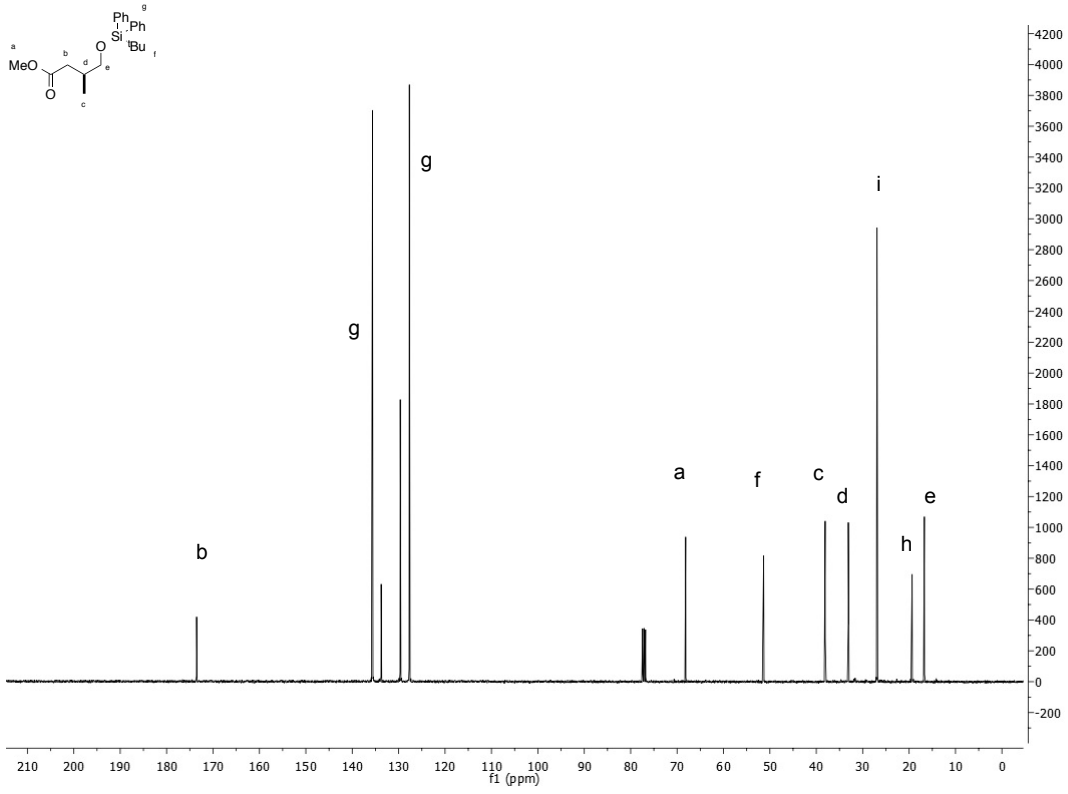
MeO
O
Si
Ph
Ph
tBu
a
b
c
d
e
f
g
h
i
f1 (ppm)

**F. Preparation of (*S*)-4-*(tert*-Butyldiphenylsilyloxy)-3-methylbutanal (10).**

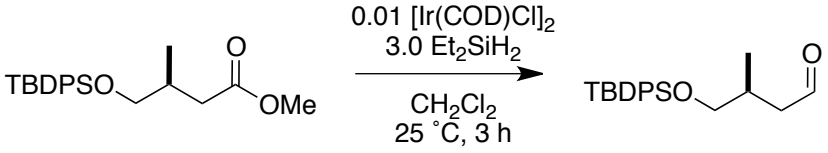


**9** **10**
75 %

A modification of reported procedure[61] was used. Under an atmosphere of argon, to an oven dried flask was added $[Ir(COD)Cl]_2$ (10 mg, 0.015 mmol) and 1.5 mL of $CH_2Cl_2$. Then diethyl silane (529 mg, 6.0 mmol) was added and the resulting mixture was stirred at 23 °C for 1 minute. After addition of methyl (*S*)-4-((*tert*-butyldiphenylsilyl)oxy)-3-methylbutanoate **9** (3.0 mmol), the mixture was stirred at 23 °C for 1 h. Then add another portion of $[Ir(COD)Cl]_2$ (10 mg, 0.015 mmol) and diethyl silane (265 mg, 3.00 mmol) to the mixture and allow it to stir 23 °C for 2 h. The reaction was diluted with diethyl ether and quenched by 0.1 M HCl. After stirring for 20 minutes, the layers were separated and the aqueous layer was extracted with $CH_2Cl_2$. The combined organic layers were dried with $MgSO_4$, and concentrated under vacuum. Purification of the residue by flash chromatography on silica gel using ~10%-15% $CH_2Cl_2$/hexanes as eluents gave the desired aldehyde **10** as colorless oil (766 mg, 2.25 mmol, 75%). $^1$H NMR (400 MHz, $CDCl_3$) δ 9.86 (1H, t, *J* = 2.1 Hz), 7.81-7.74 (4H, m), 7.54-7.47 (6H, m), 3.70 (1H, dd, *J* = 9.9, 5.1 Hz), 3.57 (1H, dd, *J* = 9.9, 6.9 Hz), 2.69 (1H, ddd, *J* = 15.9, 5.7, 2.1 Hz), 2.48-2.39 (1H, m), 2.35 (1H, ddd, *J* = 15.9, 7.2, 2.1 Hz), 1.18 (9H, s), 1.05 (3H, d, *J* = 6.7 Hz); $^{13}$C NMR (100 MHz, $CDCl_3$) δ 202.5, 135.6, 135.6, 133.6, 133.5 129.8, 127.8, 68.5, 48.2, 31.3, 27.0, 19.3, 16.9. IR ($CH_2Cl_2$) n ($cm^{-1}$) 3070, 2931, 2858, 2360, 1724, 1469, 1427, 1111, 806.3, 740.7, 702.1. HRMS (ESI, TOF): Exact mass calcd for $C_{21}H_{28}O_2SiLi$ $[M+Li]^+$ 347.2019. Found 347.2021.

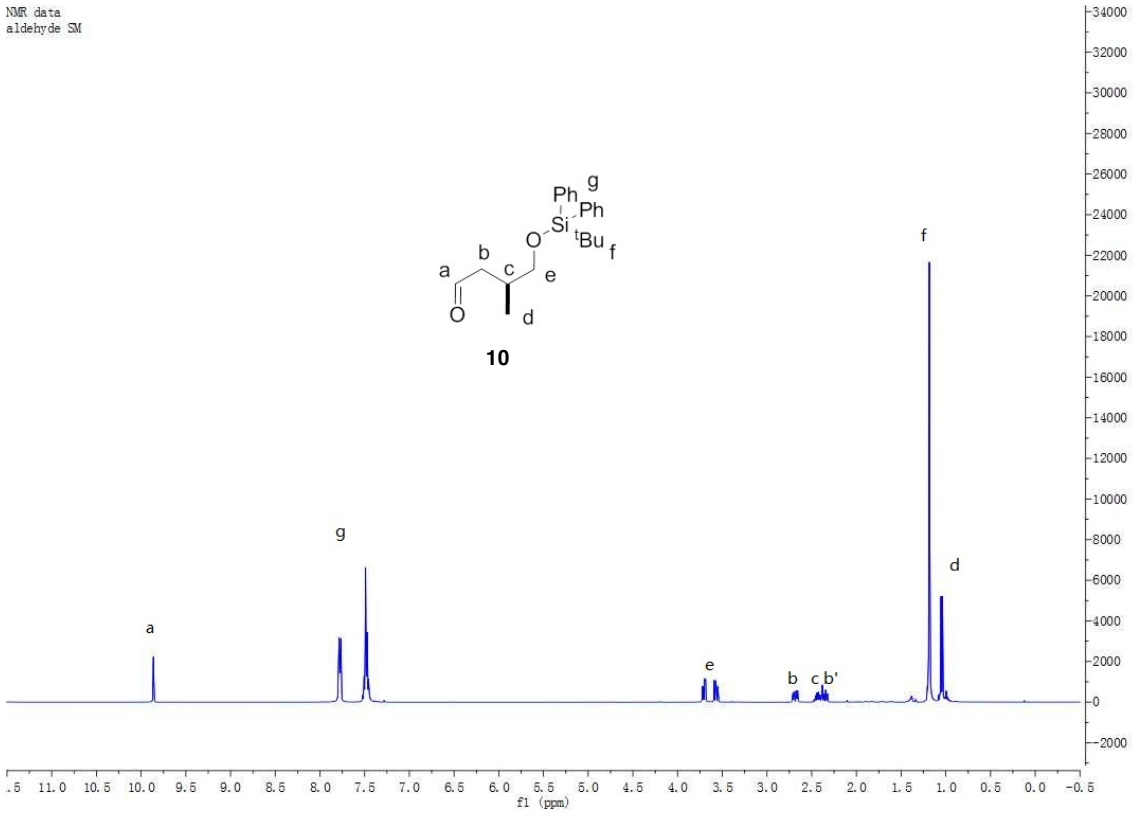
NMR data
aldehyde SM
Ph
g
Ph
Si
tBu
f
O
a
b
c
e
O
d
10
f
g
d
a
e
b
c
b'
f1 (ppm)

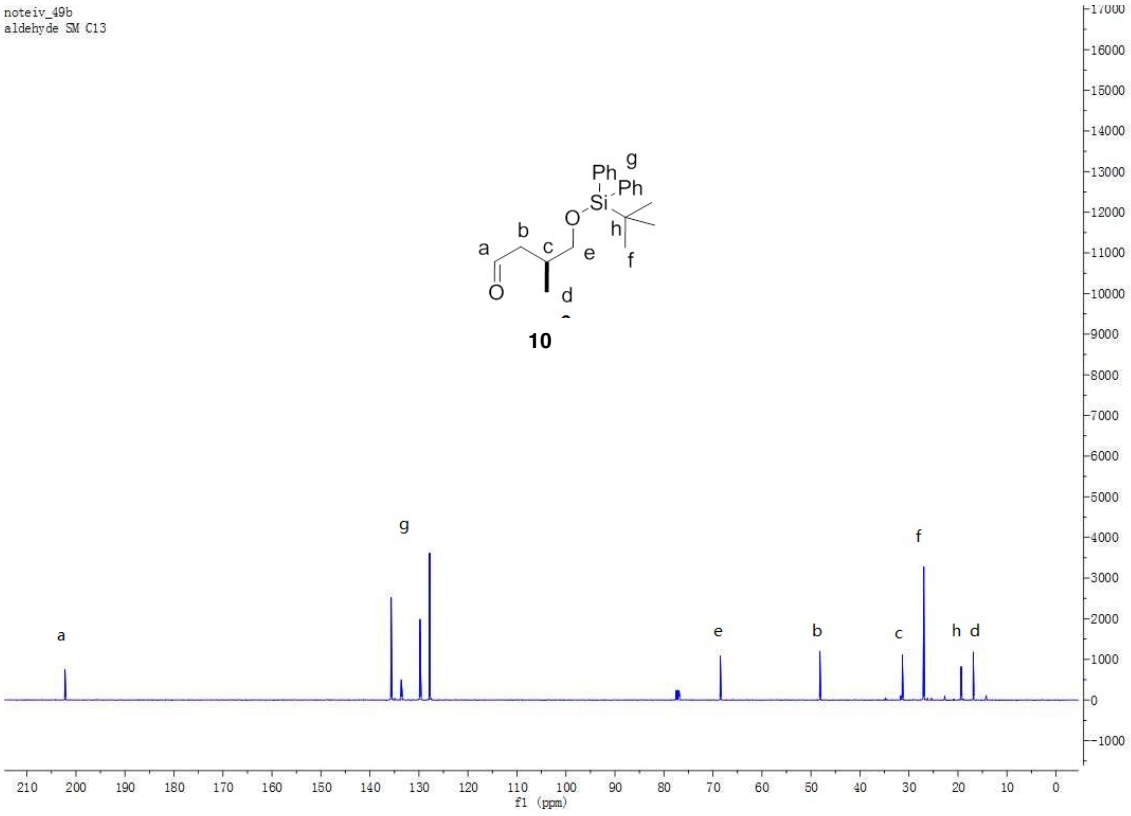
noteiv_49b
aldehyde SM C13
Ph
Ph
Si
O
a
b
c
d
e
f
g
h
10
a
g
e
b
c
f
h d
f1 (ppm)

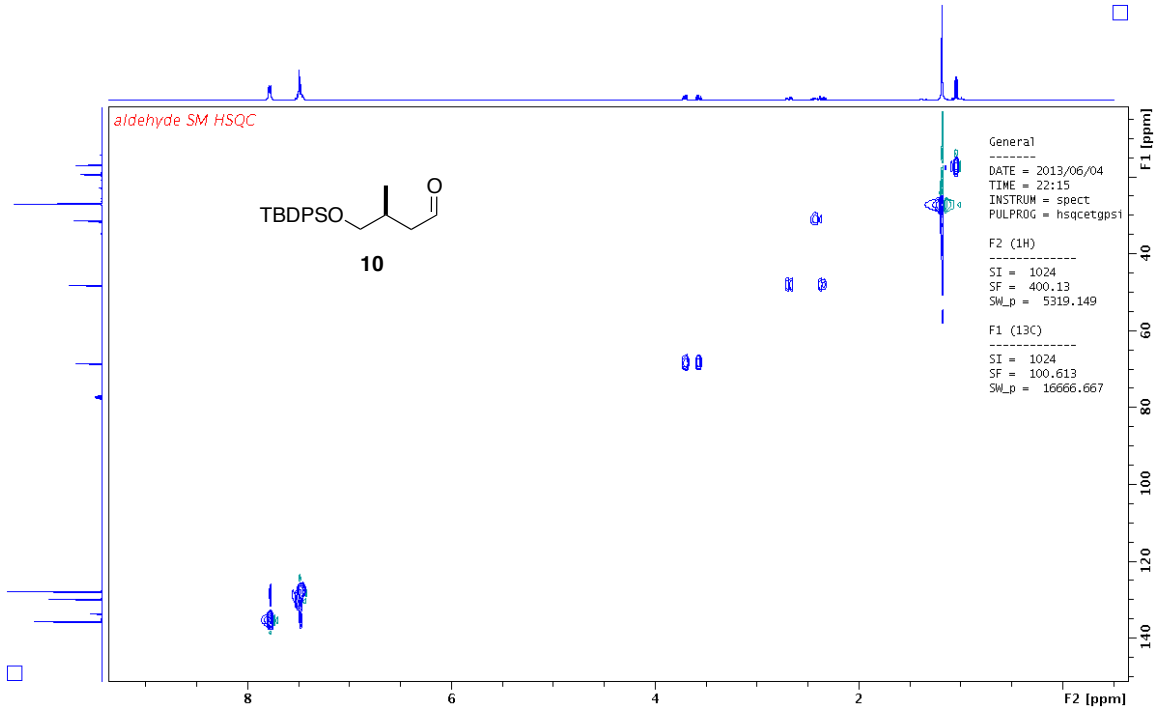
aldehyde SM HSQC
TBDPSO
O
10
General
DATE = 2013/06/04
TIME = 22:15
INSTRUM = spect
PULPROG = hsqcetgpsi
F2 (1H)
SI = 1024
SF = 400.13
SW_p = 5319.149
F1 (13C)
SI = 1024
SF = 100.613
SW_p = 16666.667
F1 [ppm]
F2 [ppm]

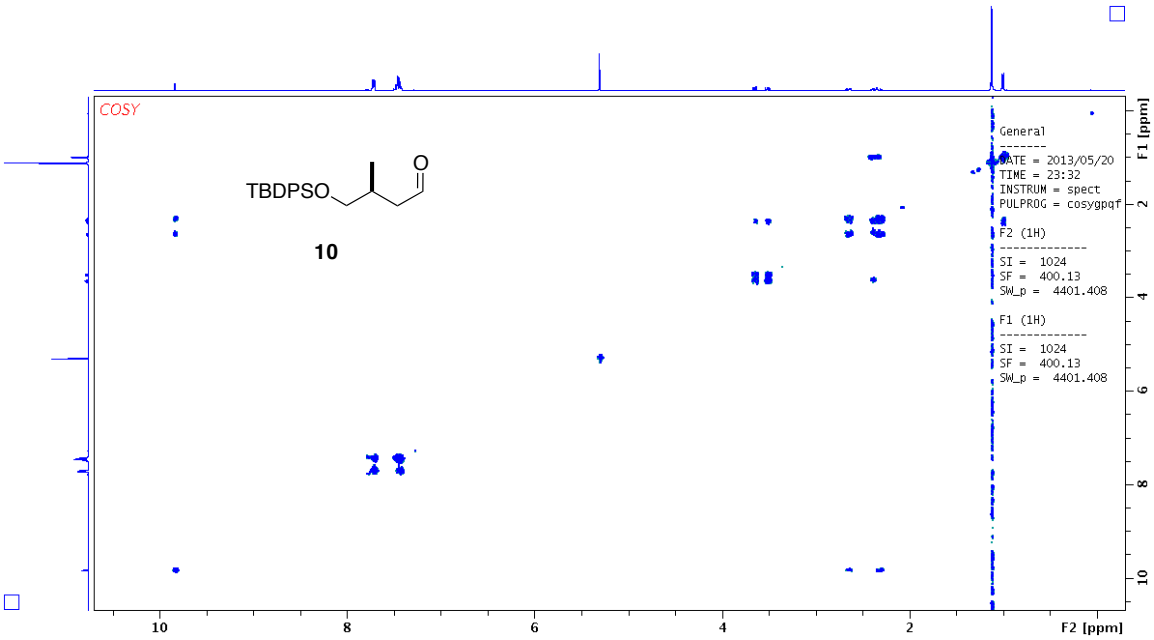


## G. Typical Procedure for a-Chlorination of the Aldehyde

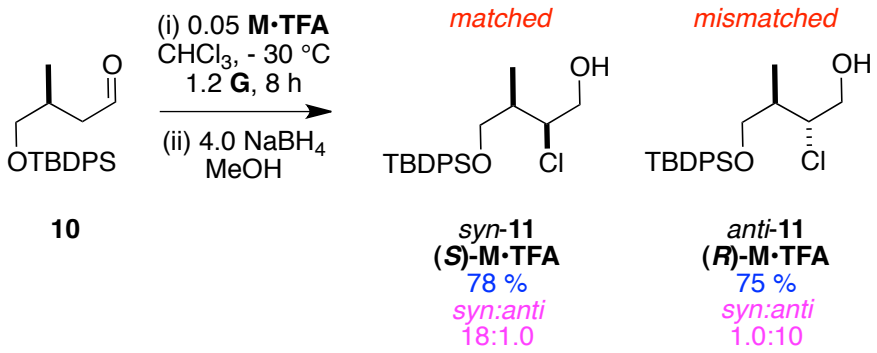


**10**

*syn*-**11**
(***S***)-**M·TFA**
78 %
*syn:anti*
18:1.0

*anti*-**11**
(***R***)-**M·TFA**
75 %
*syn:anti*
1.0:10

A modification of reported procedure[67] was used. 5-Benzyl-2,2,3,-trimethylimidazolidin-4-one trifluoroacetic acid salt (13.5 mg, 0.050 mmol) in chloroform (1 mL) is cooled to -30 °C for five minutes prior to addition of 2,3,4,5,6,6-hexachloro-2,4-cyclohexadien-1-one (181 mg, 0.60 mmol). The aldehyde **10** (170 mg, 0.50 mmol) was added to the yellow mixture. The resulting mixture was stirred at -30 °C for 8 h. The reaction was then warmed to 0 °C and MeOH (1 mL) was added to the mixture, followed by $NaBH_4$ (80 mg, 2 mmol). After stirring at 0 °C for 5 minutes, the reaction was quenched by 1 M $KHSO_4$. The aqueous solution was extracted with EtOAc three times. The combined organic layers were dried with $MgSO_4$, and concentrated *in*

*vacuo*. Purification of the residue by flash chromatography on silica gel, eluting with 2.5%-5.0% EtOAc/hexanes gave the desired alcohol as colorless oil.

**H. Typical Procedure for Preparation Epoxides**

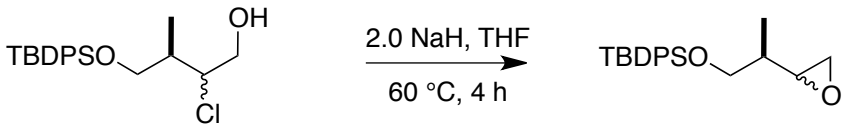


**11** **14**
95 %

Under Ar, to a solution of **11** (75 mg, 0.20 mmol) in anhydrous THF was added NaH (10 mg, 0.40 mmol) and the mixture was stirred at 60 °C for 4 h. The reaction was quenched by 1 M KHSO4. The aqueous solution was extracted with $CH_2Cl_2$ three times. The combined organic layers were dried with $MgSO_4$, and concentrated in vacuo. Purification of the residue by flash chromatography on silica gel, eluting with $CH_2Cl_2$/hexanes (20%) gave the desired epoxide as a colorless oil.

**(2*S*,3*R*)-4-((*tert*-Butyldiphenylsilyl)oxy)-2-chloro-3-methylbutan-1-ol (*syn*-11).**

The compound was prepared according to the typical a-chlorination procedure catalysed by (*S*)-5-benzyl-2,2,3,-trimethylimidazolidin-4-one trifluoroacetic acid salt. Purification by flash chromatography afforded *syn*-**11** as a colorless oil (147 mg, 0.390 mmol, 78% isolated yield). $^1$H NMR (400 MHz, $CDCl_3$) δ 7.81-7.75 (4H, m), 7.54-7.44 (6H, m), 4.49-4.45 (1H, m), 3.88-3.86 (2H, m), 3.71-3.62 (2H, m), 2.34 (1H, br), 2.22-2.16 (1H, m), 1.12 (9H, s), 1.05 (3H, d, $J$ = 6.7 Hz); $^{13}$C NMR (100 MHz, $CDCl_3$) δ 135.6, 135.6, 133.2, 129.8, 127.8, 66.5, 65.7, 65.7, 38.8, 26.9, 19.3, 11.8. IR ($CH_2Cl_2$) n ($cm^{-1}$) 3356, 3071, 2932, 2859, 2361, 1470, 1427, 1377, 1111, 822. HRMS (ESI, TOF): Exact mass calcd for $C_{21}H_{30}ClO_2Si$ $[M+H]^+$ 377.1704. Found 377.1718. The diastereoselectivity was 18:1.0, determined by Chiral HPLC (Chiralcel OD, Hex/iPrOH 99:1, 1 mL/min, 25 °C), $t_r$ 11.7 min (major diastereomer), $t_r$ 12.7 min (minor diastereomer).

The product was converted to the epoxide according to the typical epoxidation procedure. Purification by flash chromatography afforded (2*R*,3*R*)-4-*tert*-

butyldiphenylsilyloxy-1,3-epoxy-3-methylbutane (*anti*-**14**) as a colorless oil (67 mg, 0.19 mmol, 95% isolated yield). $^{1}$H NMR (400 MHz, $CDCl_3$) δ 7.70-7.67 (4H, m), 7.49-7.38 (6H, m), 3.66 (2H, dd, *J* = 6.3, 1.6 Hz), 2.90-2.87 (1H, m), 2.79 (1H, dd, *J* = 4.9, 4.1 Hz), 2.63 (1H, dd, *J* = 5.0, 2.8 Hz), 1.65-1.56 (1H, m), 1.09 (9H, s), 1.03 (3H, d, *J* = 6.8 Hz); $^{13}$C NMR (100 MHz, $CDCl_3$) δ 135.6, 133.6, 129.7, 127.7, 66.4, 55.1, 46.8, 39.1, 26.8, 19.2, 13.3. IR ($CH_2Cl_2$) n ($cm^{-1}$) 3070, 2927, 2859, 2338, 1462, 1427, 1389, 1362, 1111, 933.6, 887.3, 821.7. HRMS (ESI, TOF): Exact mass calcd for $C_{21}H_{28}O_2SiLi$ $[M+Li]^+$ 347.2019. Found 347.2020.

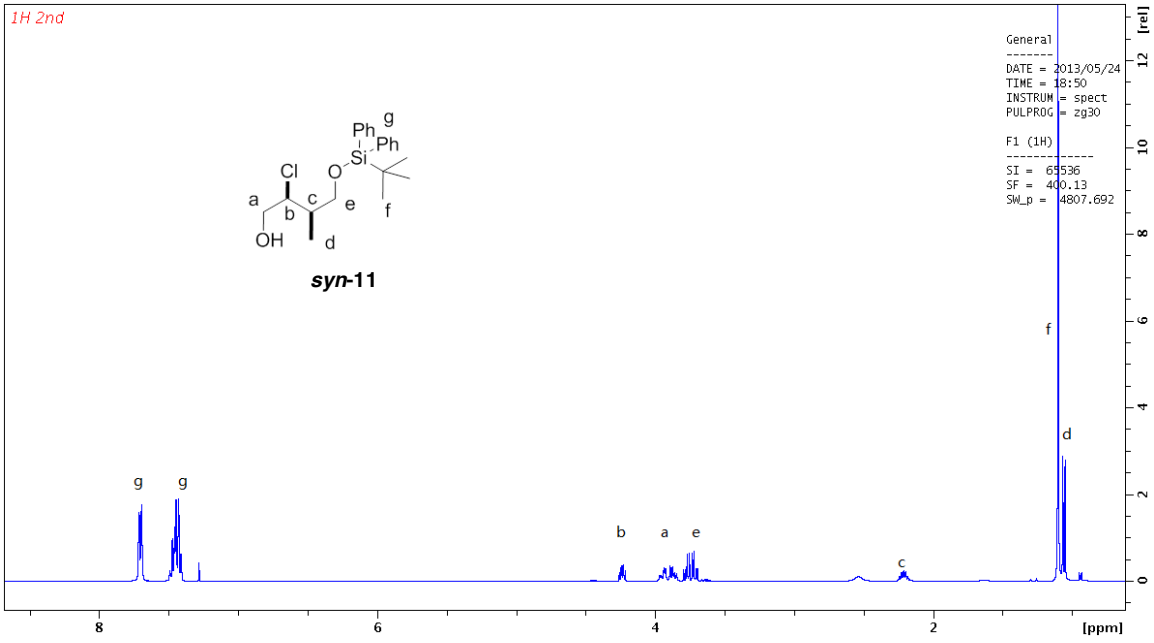

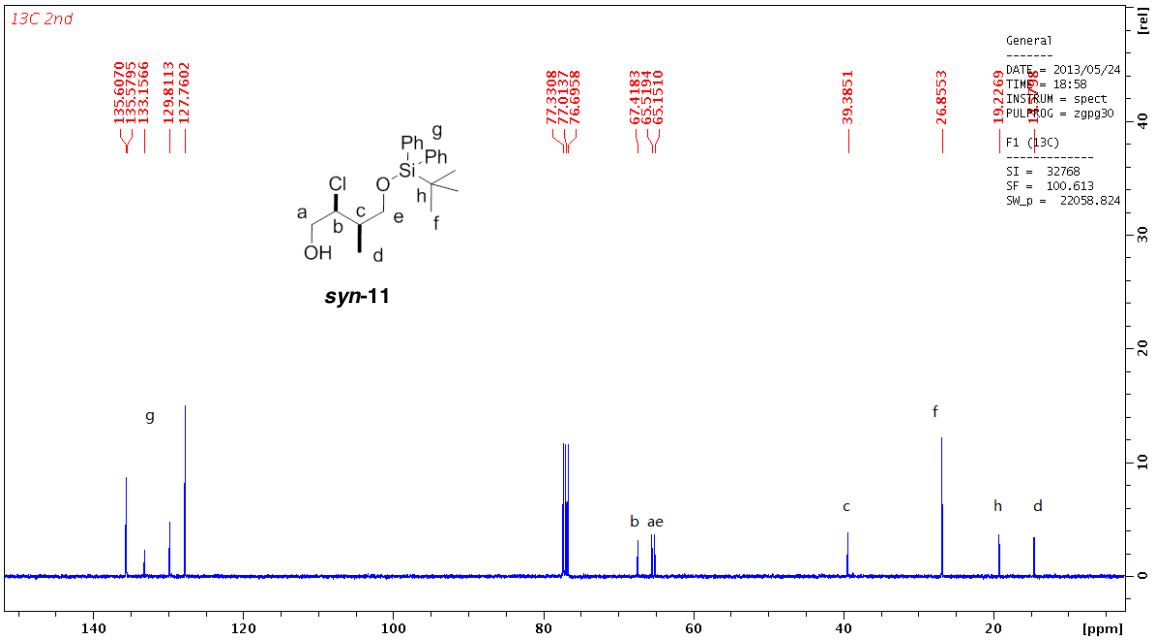
13C 2nd
135.6070
135.5795
133.1566
129.8113
127.7602
77.3308
77.0137
76.6958
67.4183
65.5194
65.1510
39.3851
26.8553
19.2269
17.7455
General
DATE = 2013/05/24
TIME = 18:58
INSTRUM = spect
PULPROG = zgpg30
F1 (13C)
SI = 32768
SF = 100.613
SW_p = 22058.824
Ph
Ph
Si
g
Cl
O
h
a
b
c
e
f
OH
d
syn-11
g
b ae
c
f
h
d
[rel]
[ppm]

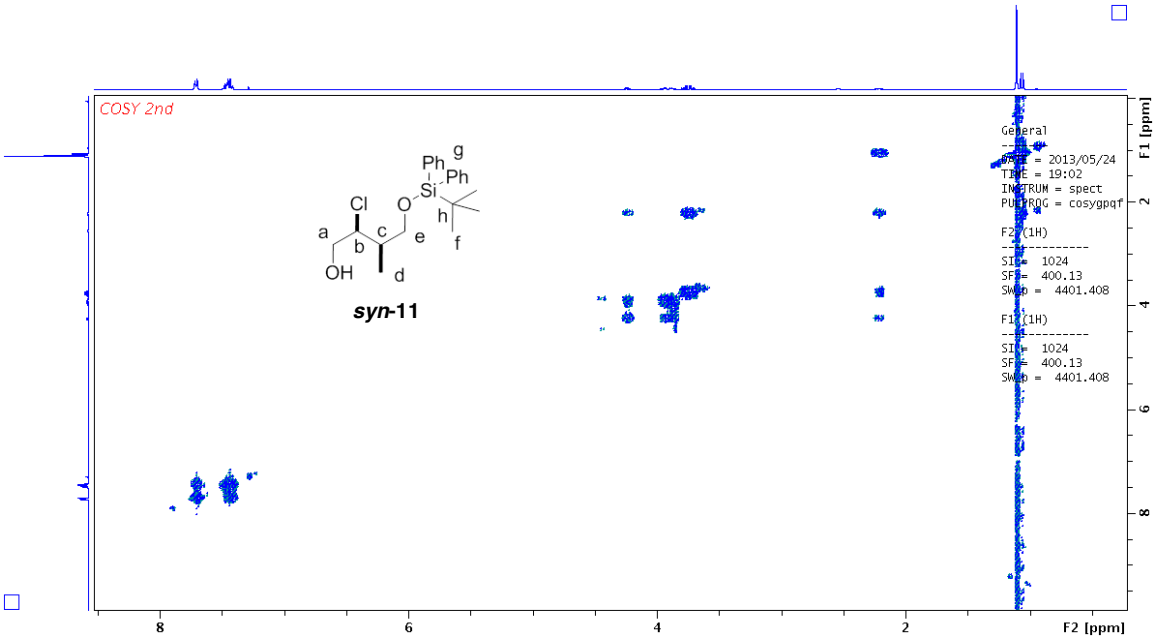
COSY 2nd
General
DATE = 2013/05/24
TIME = 19:02
INSTRUM = spect
PULPROG = cosygpqf
F2 (1H)
SI = 1024
SF = 400.13
SWp = 4401.408
F1 (1H)
SI = 1024
SF = 400.13
SWp = 4401.408
Ph
Ph
Si
g
Cl
O
h
a
b
c
e
f
OH
d
syn-11
F1 [ppm]
F2 [ppm]

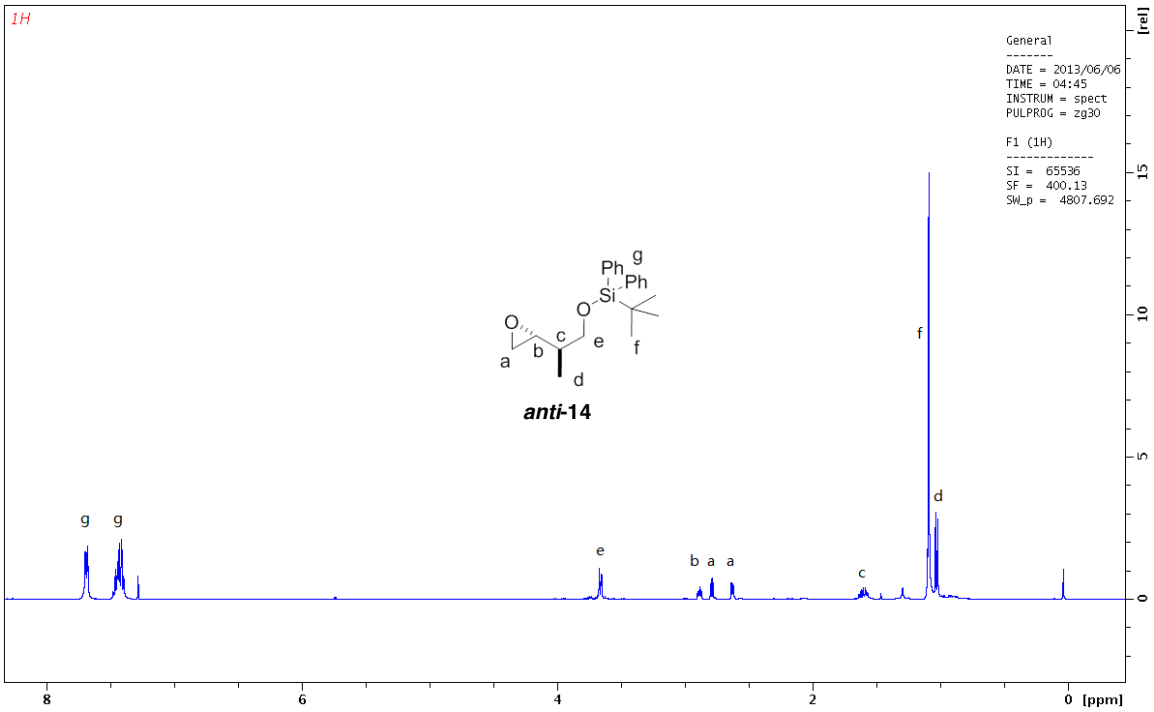
1H
General
DATE = 2013/06/06
TIME = 04:45
INSTRUM = spect
PULPROG = zg30
F1 (1H)
SI = 65536
SF = 400.13
SW_p = 4807.692
[rel]
[ppm]
anti-14

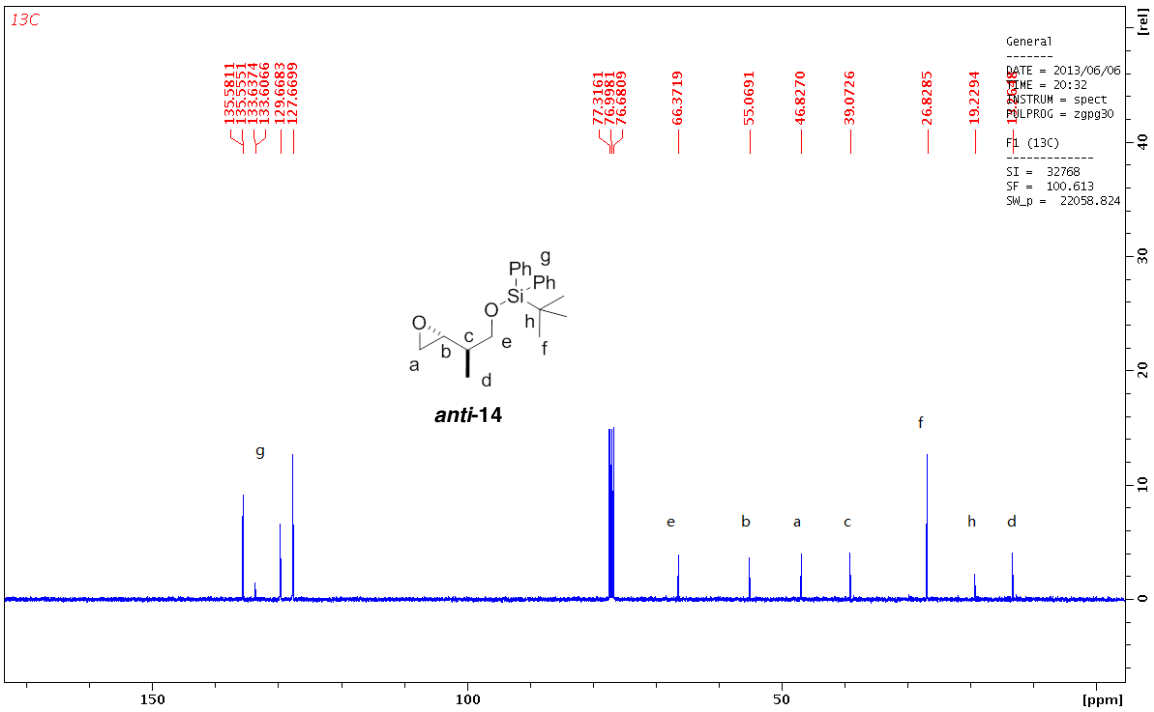
13C
General
DATE = 2013/06/06
TIME = 20:32
INSTRUM = spect
PULPROG = zgpg30
F1 (13C)
SI = 32768
SF = 100.613
SW_p = 22058.824
[rel]
[ppm]
anti-14

**(2*R*,3*R*)-4-((*tert*-Butyldiphenylsilyl)oxy)-2-chloro-3-methylbutan-1-ol (*anti*-11).**

The compound was prepared according to the typical chlorination procedure catalysed by (*R*)-5-benzyl-2,2,3,-trimethylimidazolidin-4-one trifluoroacetic acid salt. Purification by flash chromatography afforded *anti*-**11** as a colorless oil (141 mg, 0.374 mmol, 75% isolated yield). $^{1}$H NMR (400 MHz, $CDCl_3$) δ 7.74-7.68 (4H, m), 7.51-7.39 (6H, m), 4.26-4.22 (1H, m), 3.95 (1H, dd, *J* = 12.2, 4.5 Hz), 3.87 (1H, dd, *J* = 12.2, 6.5 Hz), 3.78 (1H, dd, *J* = 10.4, 5.9 Hz), 3.72 (1H, dd, *J* = 10.4, 4.3 Hz), 2.54 (1H, br), 2.27-2.16 (1H, m), 1.10 (2H, s), 1.06 (1H, d, *J* = 7.0 Hz); $^{13}$C NMR (100 MHz, $CDCl_3$) δ 135.6, 133.1, 129.8, 127.8, 67.4, 65.5, 65.1, 39.4, 26.9, 19.2, 14.6. IR ($CH_2Cl_2$) n ($cm^{-1}$) 3383, 3071, 2932, 2859, 2361, 1470, 1427, 1389, 1111. HRMS (ESI, TOF): Exact mass calcd for $C_{21}H_{30}ClO_2Si$ $[M+H]^+$ 377.1704. Found 377.1710. The diastereoselectivity was 1.0:10 determined by Chiral HPLC (Chiralcel OD, Hex/iPrOH 99:1, 1 mL/min, 25 °C), $t_r$ 11.8 min (minor diastereomer), $t_r$ 12.8 min (major diastereomer).

The product was then converted to the epoxide according to the typical epoxidation procedure. Purification by flash chromatography afforded (2*S*,3*R*)-4-*tert*-butyldiphenylsilyloxy-1,3-epoxy-3-methylbutane (*syn*-**14**) as a colorless oil (61 mg, 0.18 mmol, 90% isolated yield). The relative stereochemistry was determined by comparing with a known epoxide, which was reported previously.[153] $^{1}$H NMR (400 MHz, $CDCl_3$) δ 7.74-7.66 (4H, m), 7.48-7.38 (6H, m), 3.75 (2H, qd, *J* = 9.9, 5.1 Hz), 3.02-2.99 (1H, m), 2.81-2.75 (1H, m), 2.57 (1H, dd, *J* = 5.0, 2.8 Hz), 1.68-1.60 (1H, m), 1.10 (9H, s), 1.03 (3H, d, *J* = 7.0 Hz); $^{13}$C NMR (100 MHz, $CDCl_3$) δ 135.6, 133.8, 129.6, 127.6, 66.2, 54.0, 45.6, 38.5, 26.9, 19.3, 12.6. IR ($CH_2Cl_2$) n ($cm^{-1}$) 3071, 2928, 2859, 1470, 1427, 1389, 1362, 1111, 933.6, 875.7, 821.7. HRMS (ESI, TOF): Exact mass calcd for $C_{21}H_{28}O_2SiLi$ $[M+Li]^+$ 347.2019. Found 347.2003.

Relative stereochemistry determination of **11**: the $^{1}$H NMR data of *syn*-**14** matched with reported data[70] and differs from that of *anti*-**14**. Therefore, the relative stereochemistry assignment was confirmed.

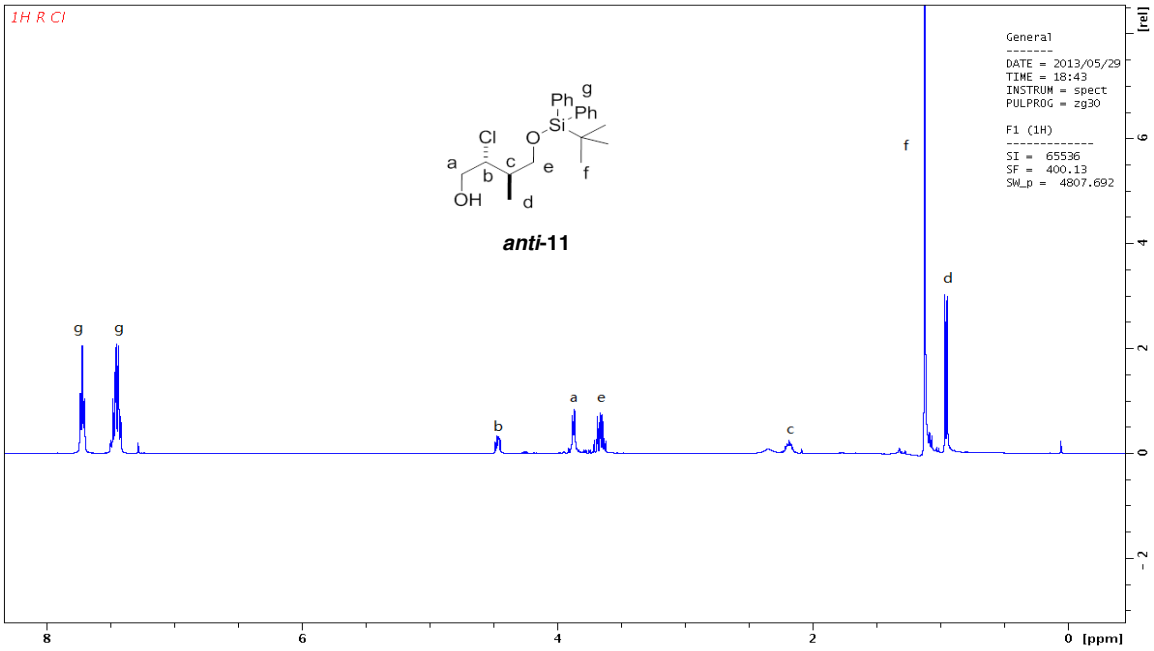
1H R Cl
General
DATE = 2013/05/29
TIME = 18:43
INSTRUM = spect
PULPROG = zg30
F1 (1H)
SI = 65536
SF = 400.13
SW_p = 4807.692
anti-11
[rel]
[ppm]

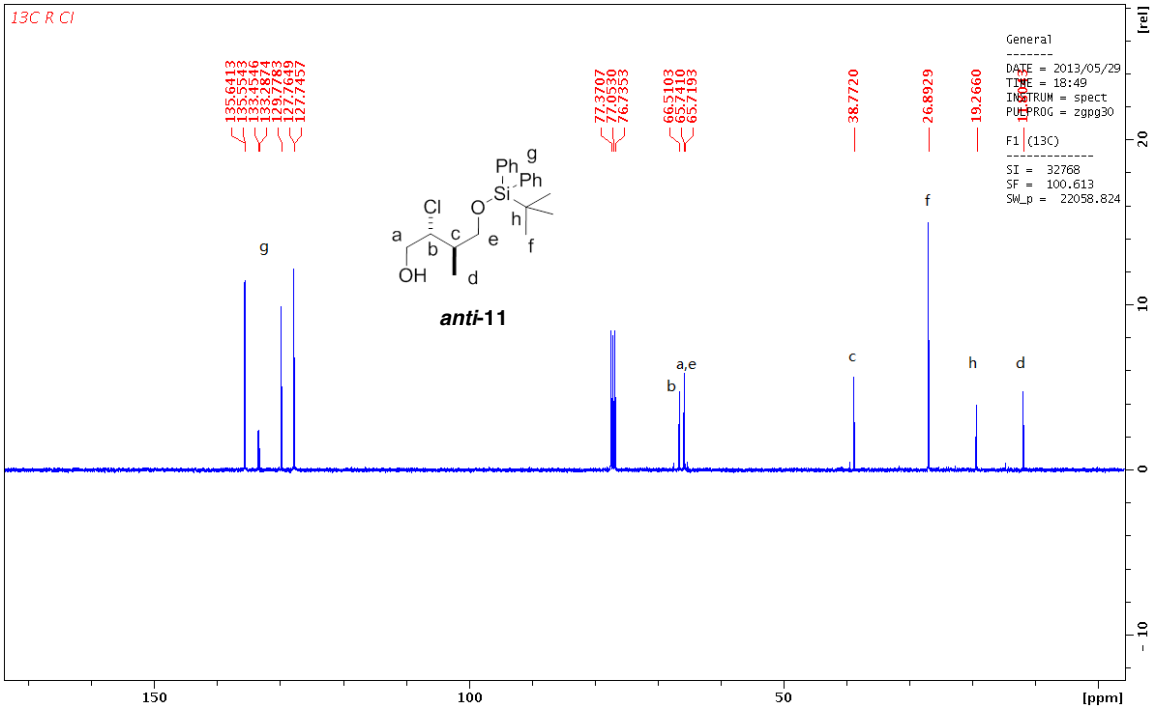
13C R Cl
General
DATE = 2013/05/29
TIME = 18:49
INSTRUM = spect
PULPROG = zgpg30
F1 (13C)
SI = 32768
SF = 100.613
SW_p = 22058.824
anti-11
[rel]
[ppm]

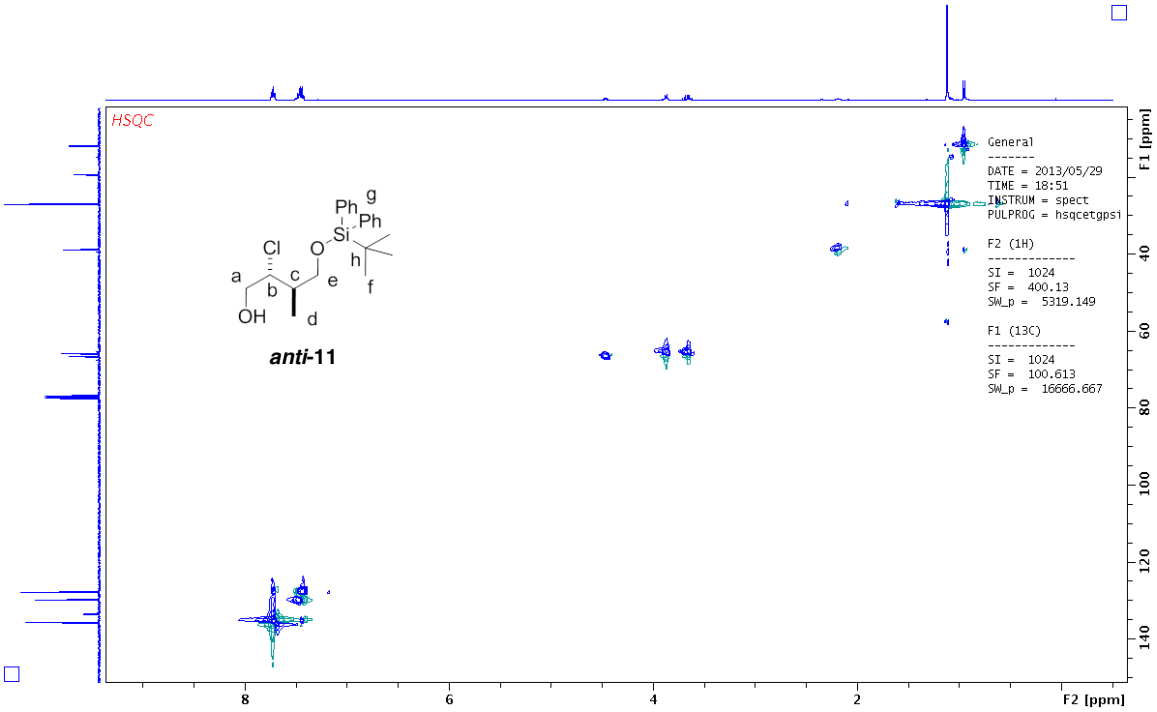
HSQC
Ph
g
Ph
Si
O
Cl
h
a
c
e
f
b
OH
d
anti-11
General
DATE = 2013/05/29
TIME = 18:51
INSTRUM = spect
PULPROG = hsqcetgpsi
F2 (1H)
SI = 1024
SF = 400.13
SW_p = 5319.149
F1 (13C)
SI = 1024
SF = 100.613
SW_p = 16666.667
F1 [ppm]
40
60
80
100
120
140
8
6
4
2
F2 [ppm]

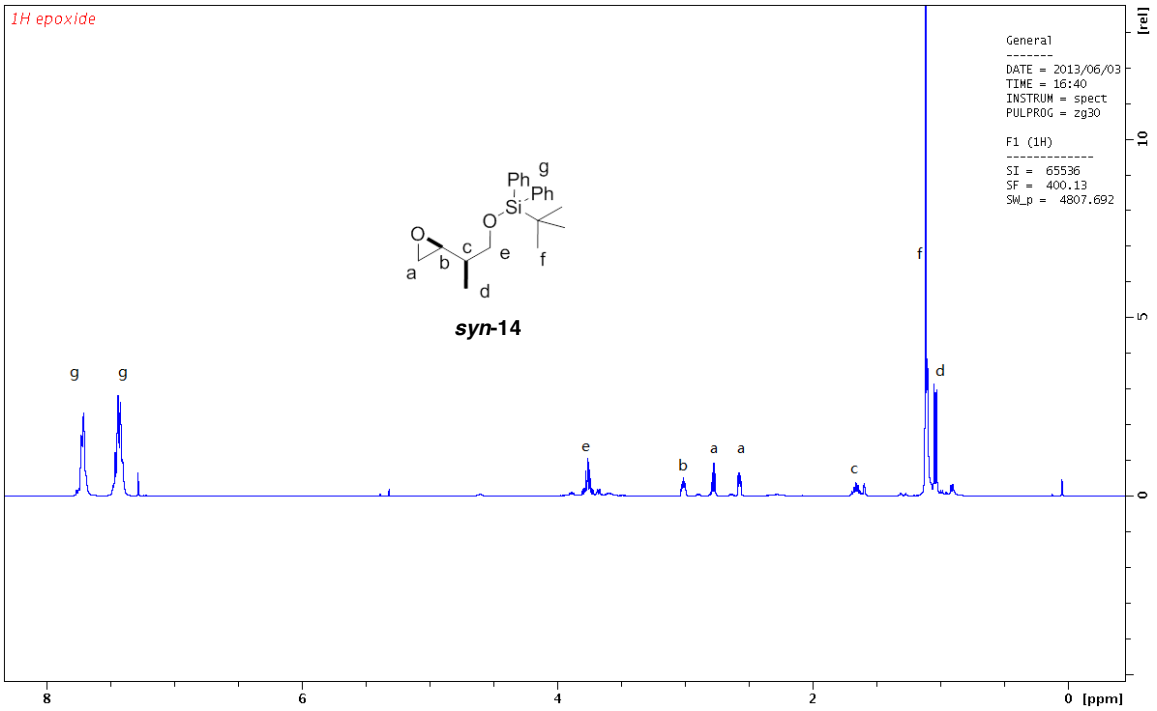
1H epoxide
Ph
g
Ph
Si
O
O
a
b
c
e
f
d
syn-14
General
DATE = 2013/06/03
TIME = 16:40
INSTRUM = spect
PULPROG = zg30
F1 (1H)
SI = 65536
SF = 400.13
SW_p = 4807.692
[rel]
10
5
0
g
g
e
b
a
a
c
f
d
8
6
4
2
0 [ppm]

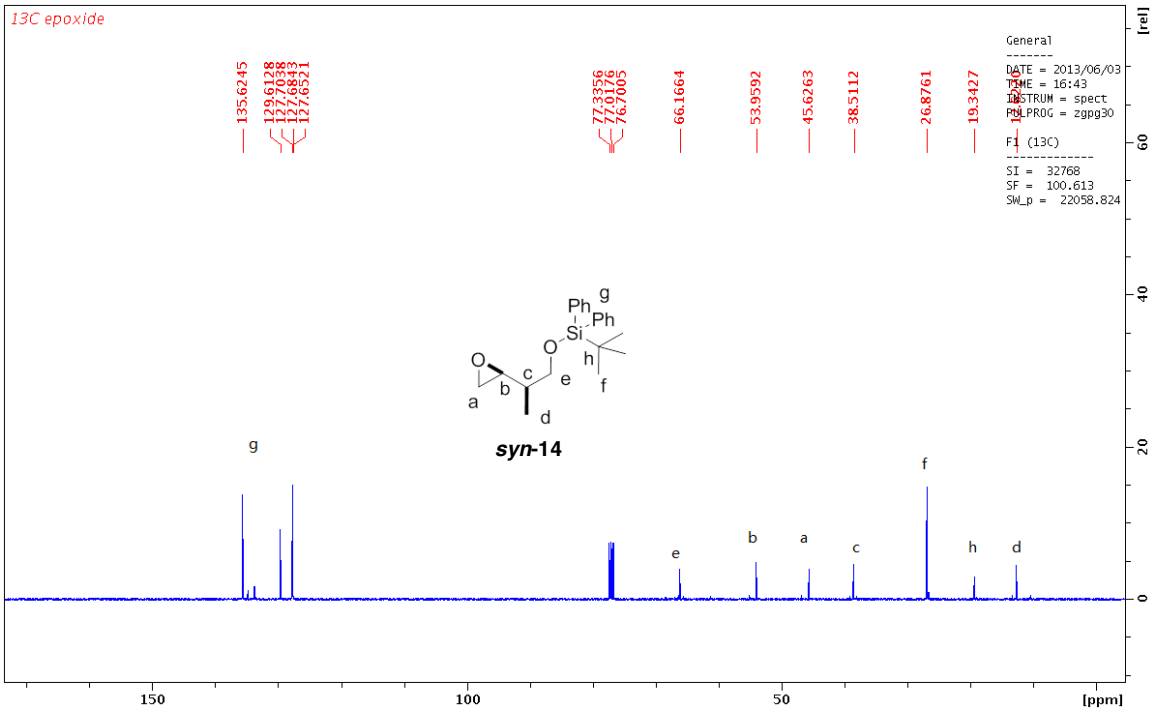


## I. Typical Procedure for a-Fluorination of the Aldehyde.

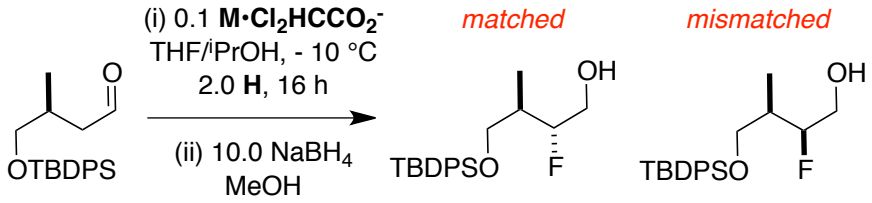


**10**

*anti*-**12**
(***R***)-M·$Cl_2HCCO_2^-$
85 %
*syn:anti*
1.0:58

*syn*-**12**
(***S***)-M·$Cl_2HCCO_2^-$
90 %
*syn:anti*
22:1.0

A modification of reported procedure[65] was used. 5-Benzyl-2,2,3,-trimethylimidazolidin-4-one dichloroacetic acid salt (38 mg, 0.10 mmol) and *N*-fluorobenzenesulfonimide (315 mg, 1.0 mmol) was dissolved in THF (4.5 mL) and $^{i}$PrOH (0.5 mL). The mixture was cooled to -10 °C prior to addition of the aldehyde (170 mg, 0.50 mmol). The resulting mixture was stirred at -10 °C for 16 h and was then warmed to 0 °C. To the mixture at 0°C was added 1 mL MeOH and $NaBH_4$ (200 mg, 5 mmol). After stirring at 0 °C for 5 minutes, the reaction was quenched by 1 M $KHSO_4$.

The mixture was diluted with water and the aqueous solution was extracted with EtOAc three times. The combined organic layers were dried with $MgSO_4$, and concentrated *in vacuo*. The residue was redissolved in dichloromethane and the solid was filtered off on a small silica pad. The mixture was concentrated again *in vacuo*. Purification of the residue by flash chromatography on silica gel, eluting with ~5%-10% EtOAc/hexanes gave the desired alcohol as colorless oil.

**(2*S*,3*R*)-4-((*tert*-Butyldiphenylsilyl)oxy)-2-fluoro-3-methylbutan-1-ol (*syn*-12).**

The compound was prepared according to the typical a-fluorination procedure catalysed by (*S*)-5-benzyl-2,2,3,-trimethylimidazolidin-4-one dichloroacetic acid salt. Purification by flash chromatography afforded *syn*-**12** as a colorless oil (162 mg, 0.449 mmol, 90% isolated yield). $^1$H NMR (400 MHz, $CDCl_3$) δ 7.72-7.69 (4H, m), 7.51-7.39 (6H, m), 4.75-4.59 (1H, m), 3.96-3.68 (4H, m), 2.22-2.01 (2H, m), 1.11 (9H, s), 1.04 (3H, d, $J$ = 7.0 Hz); $^{13}$C NMR (100 MHz, $CDCl_3$) δ 135.6 (d, $J$ = 2.3 Hz), 133.5 (d, $J$ = 3.1 Hz), 129.7 (d, $J$ = 1.3 Hz), 127.7 (s), 95.4 (d, $J$ = 170.3 Hz), 64.5 (d, $J$ = 6.1 Hz), 63.3 (d, $J$ = 22.2 Hz), 37.1 (d, $J$ = 18.9 Hz), 26.9 (s), 19.3 (s), 13.0 (d, $J$ = 6.8 Hz); $^{19}$F NMR (282 MHz, $CDCl_3$) δ -194.48 (dtd, $J$ = 40.0, 25.3, 14.5 Hz). IR ($CH_2Cl_2$) n ($cm^{-1}$) 3364, 3071, 2928, 2855, 2361, 1470, 1427, 1393, 1362, 1111, 1049. HRMS (ESI, TOF): Exact mass calcd for $C_{21}H_{30}FO_2Si$ $[M+H]^+$ 361.1999. Found 361.2021. The diastereoselectivity was 22:1.0 determined by Chiral HPLC (Chiralcel OD, Hex/iPrOH 99:1, 1 mL/min, 25 °C), $t_r$ 16.05 min (major diastereomer), $t_r$ 23.68 min (minor diastereomer).

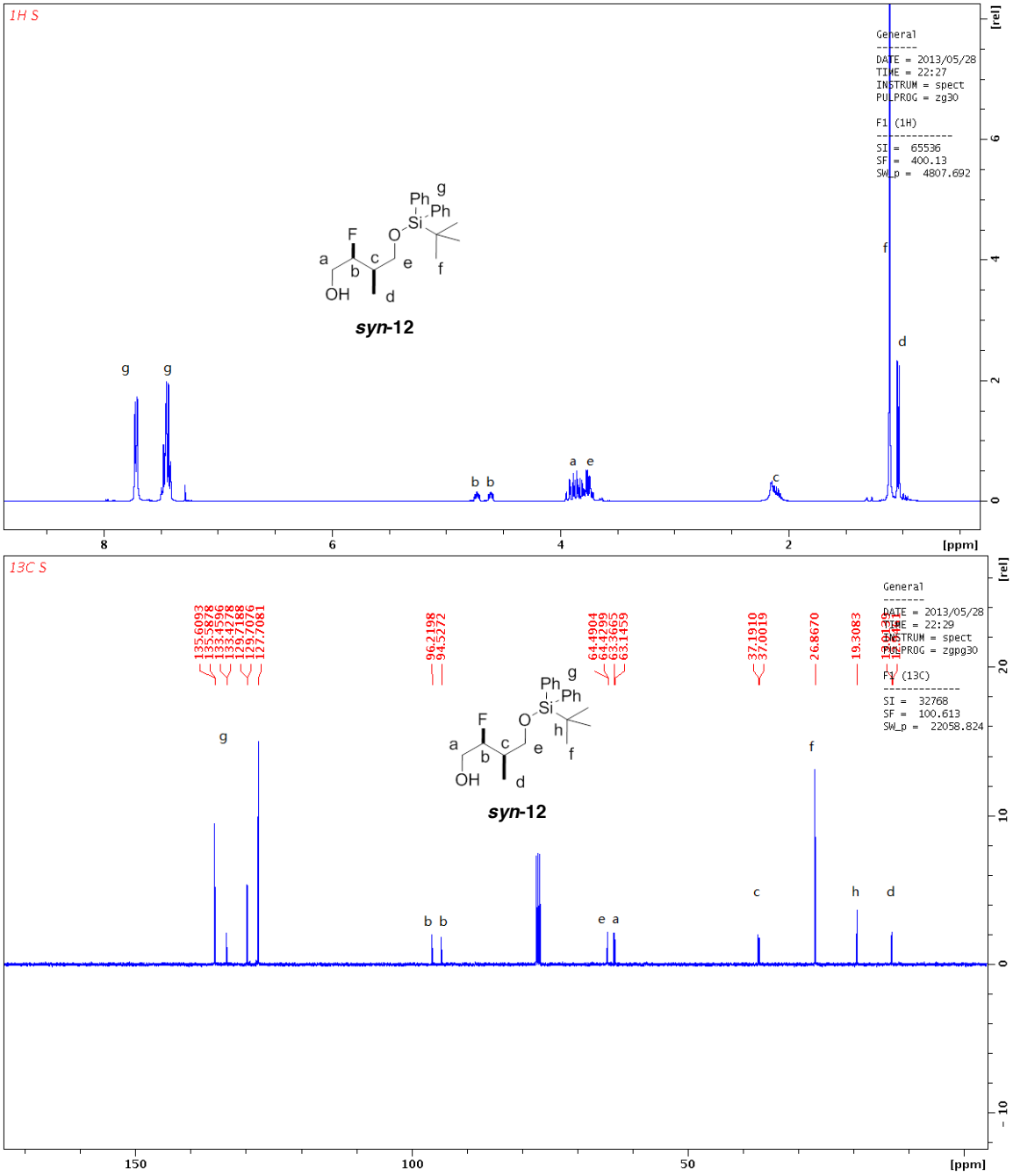
1H S
General
DATE = 2013/05/28
TIME = 22:27
INSTRUM = spect
PULPROG = zg30
F1 (1H)
SI = 65536
SF = 400.13
SW_p = 4807.692
[rel]
[ppm]
syn-12
13C S
General
DATE = 2013/05/28
TIME = 22:29
INSTRUM = spect
PULPROG = zgpg30
F1 (13C)
SI = 32768
SF = 100.613
SW_p = 22058.824
135.6093
133.4278
133.3596
133.4278
129.7188
129.7076
127.7081
96.2198
94.5272
64.4904
64.4269
63.4655
63.1459
37.1910
37.0019
26.8670
19.3083
[rel]
[ppm]
syn-12

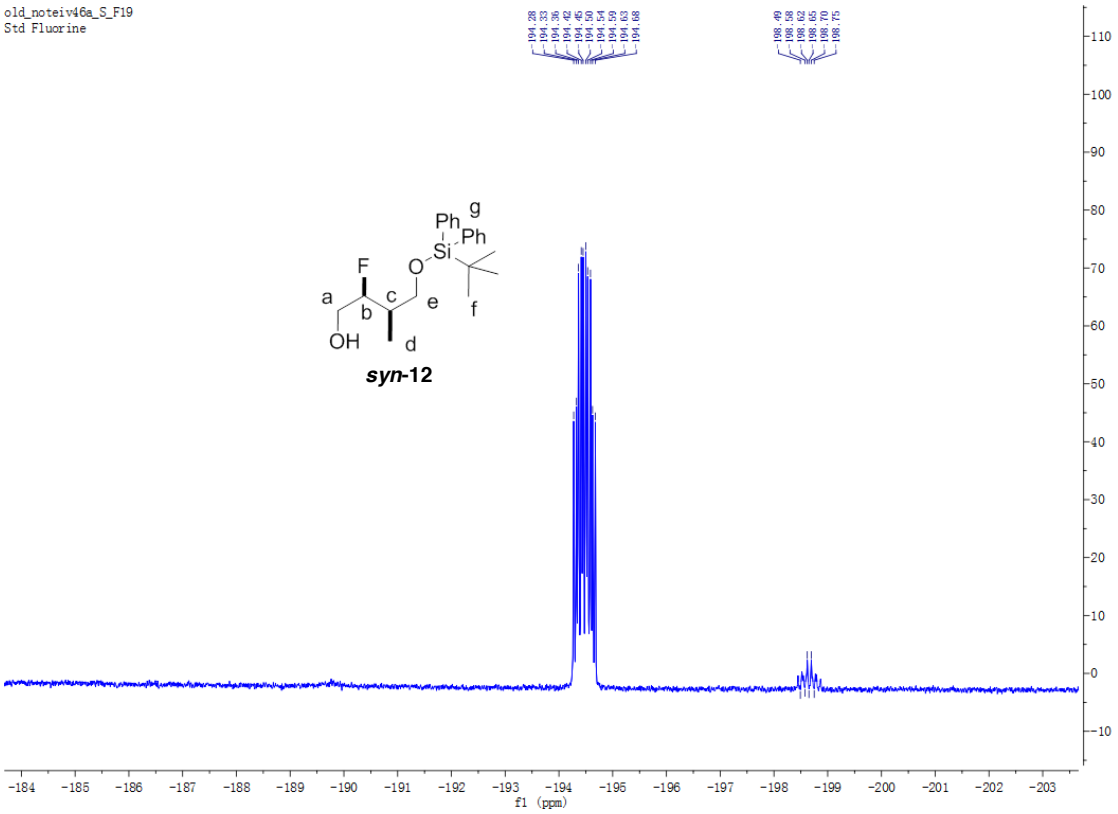
old_noteiv46a_S_F19
Std Fluorine
194.28
194.33
194.36
194.42
194.45
194.50
194.54
194.59
194.63
194.68
198.49
198.58
198.62
198.65
198.70
198.75
Ph
Ph
g
Si
O
F
a
b
c
d
e
f
OH
syn-12
f1 (ppm)

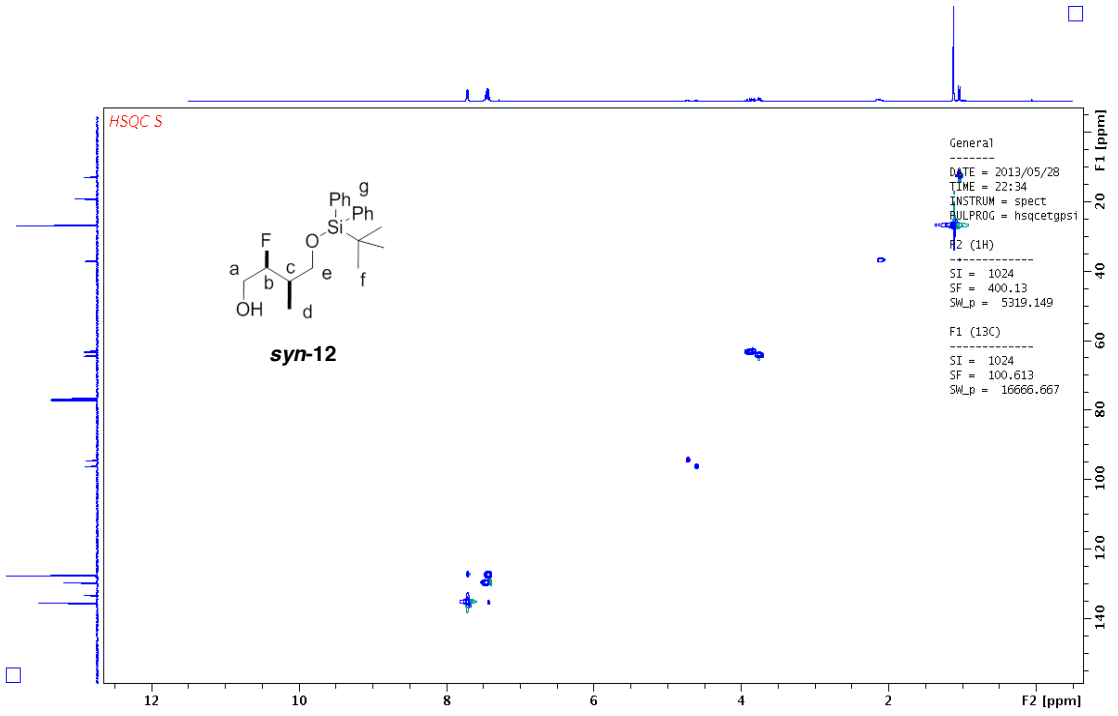
HSQC S
Ph
Ph
g
Si
O
F
a
b
c
d
e
f
OH
syn-12
General
DATE = 2013/05/28
TIME = 22:34
INSTRUM = spect
PULPROG = hsqcetgpsi
F2 (1H)
SI = 1024
SF = 400.13
SW_p = 5319.149
F1 (13C)
SI = 1024
SF = 100.613
SW_p = 16666.667
F2 [ppm]
F1 [ppm]

**(2*R*,3*R*)-4-((*tert*-Butyldiphenylsilyl)oxy)-2-fluoro-3-methylbutan-1-ol (*anti*-12).**

The compound was prepared according to the typical a-fluorination procedure catalysed by (*R*)-5-benzyl-2,2,3,-trimethylimidazolidin-4-one dichloroacetic acid salt. Purification by flash chromatography afforded *anti*-**12** as a colorless oil (153 mg, 0.424 mmol, 85% isolated yield). $^{1}$H NMR (400 MHz, $CDCl_3$) δ 7.74-7.69 (4H, m), 7.51-7.41 (6H, m), 4.82-4.63 (1H, m), 3.97-3.75 (2H, m), 3.67-3.64 (2H, m), 2.28 (1H, br), 2.11–2.00 (1H, m), 1.12 (9H, s), 0.99 (3H, dd, $J$ = 7.0, 0.8 Hz); $^{13}$C NMR (100 MHz, $CDCl_3$) δ 135.6 (d, $J$ = 4.5 Hz), 133.3 (d, $J$ = 8.2 Hz), 129.8 (s), 127.8 (d, $J$ = 1.6 Hz), 95.4 (d, $J$ = 171.0 Hz), 65.2 (d, $J$ = 6.0 Hz), 63.7 (d, $J$ = 22.6 Hz), 37.4 (d, $J$ = 19.6 Hz), 26.9 (s), 11.7 (d, $J$ = 5.8 Hz); $^{19}$F NMR (282 MHz, $CDCl_3$) δ -198.46 to -198.93 (m). IR ($CH_2Cl_2$) n ($cm^{-1}$) 3356, 3071, 2932, 2859, 2361, 1470, 1427, 1389, 1362, 1111, 1034. HRMS (ESI, TOF): Exact mass calcd for $C_{21}H_{30}FO_2Si$ $[M+H]^+$ 361.1999. Found 361.2035. The diastereoselectivity was 1.0:58, determined by Chiral HPLC (Chiralcel OD, Hex/iPrOH 99:1, 1 mL/min, 25 °C), $t_r$ 16.05 min (minor diastereomer), $t_r$ 23.68 min (major diastereomer).

Relative stereochemistry determination of **12**: since both catalyst and reaction condition are identical to what has been reported, and the reaction is catalyst controlled; the stereochemistry was assigned according to MacMillan's fluorinated product. The product cannot be easily converted to any known structure.

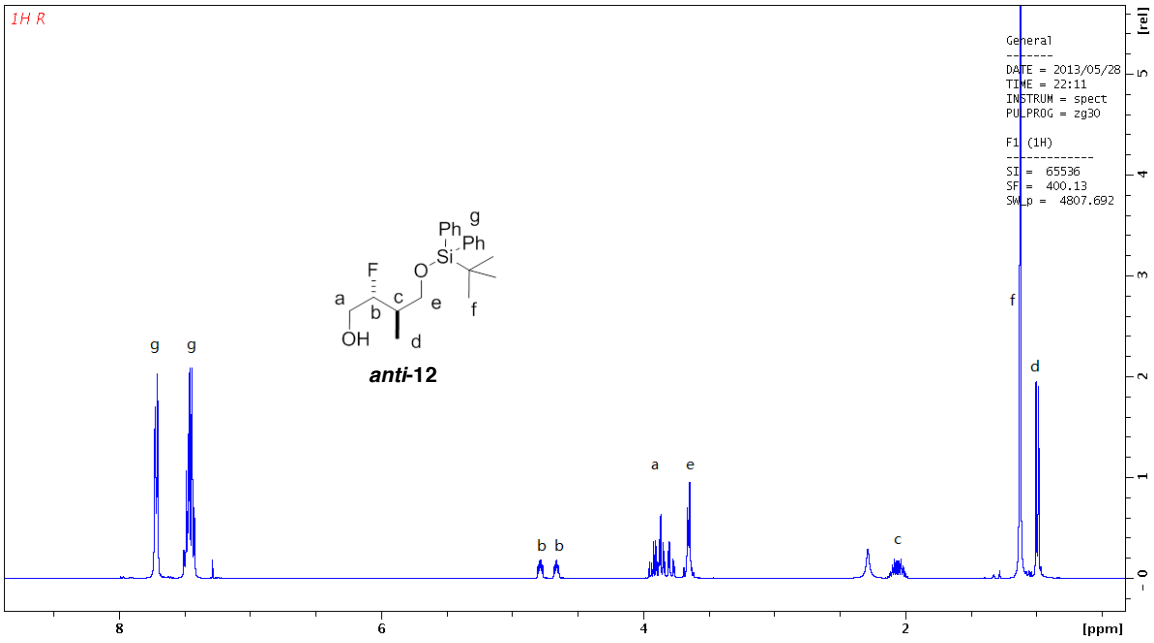
1H R
General
DATE = 2013/05/28
TIME = 22:11
INSTRUM = spect
PULPROG = zg30
F1 (1H)
SI = 65536
SF = 400.13
SW_p = 4807.692
[rel]
[ppm]
anti-12

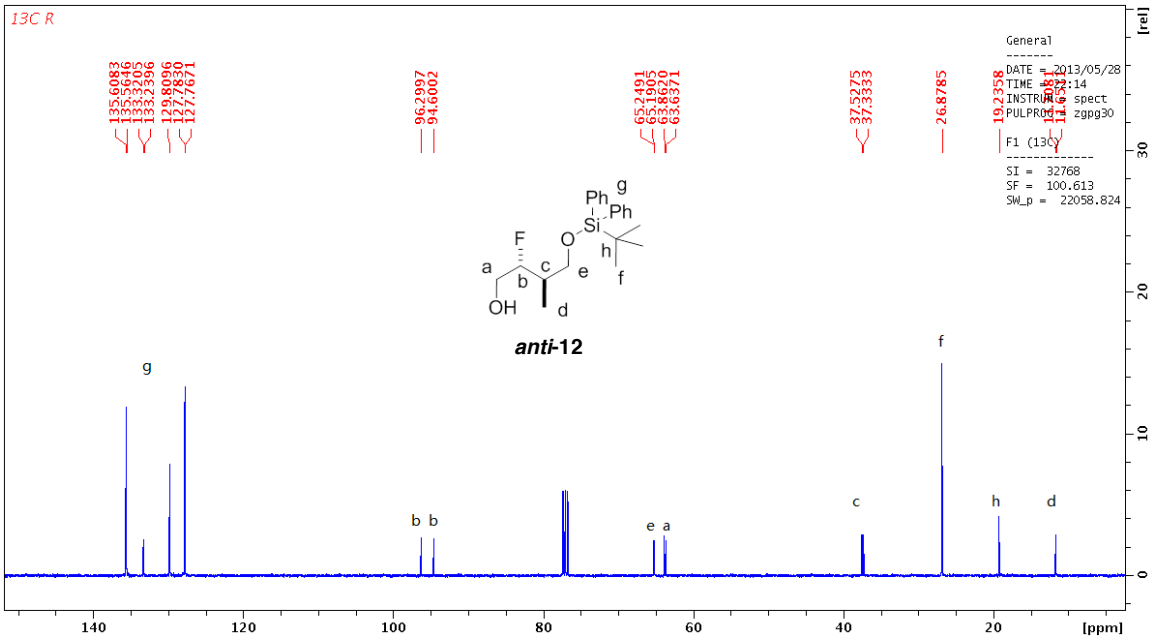
13C R
135.6083
133.6446
133.3205
133.2396
129.8096
127.7830
127.7671
96.2097
94.6002
65.2491
65.1905
63.8620
63.6371
37.5275
37.3333
26.8785
19.2358
General
DATE = 2013/05/28
TIME = 22:14
INSTRUM = spect
PULPROG = zgpg30
F1 (13C)
SI = 32768
SF = 100.613
SW_p = 22058.824
[rel]
[ppm]
anti-12

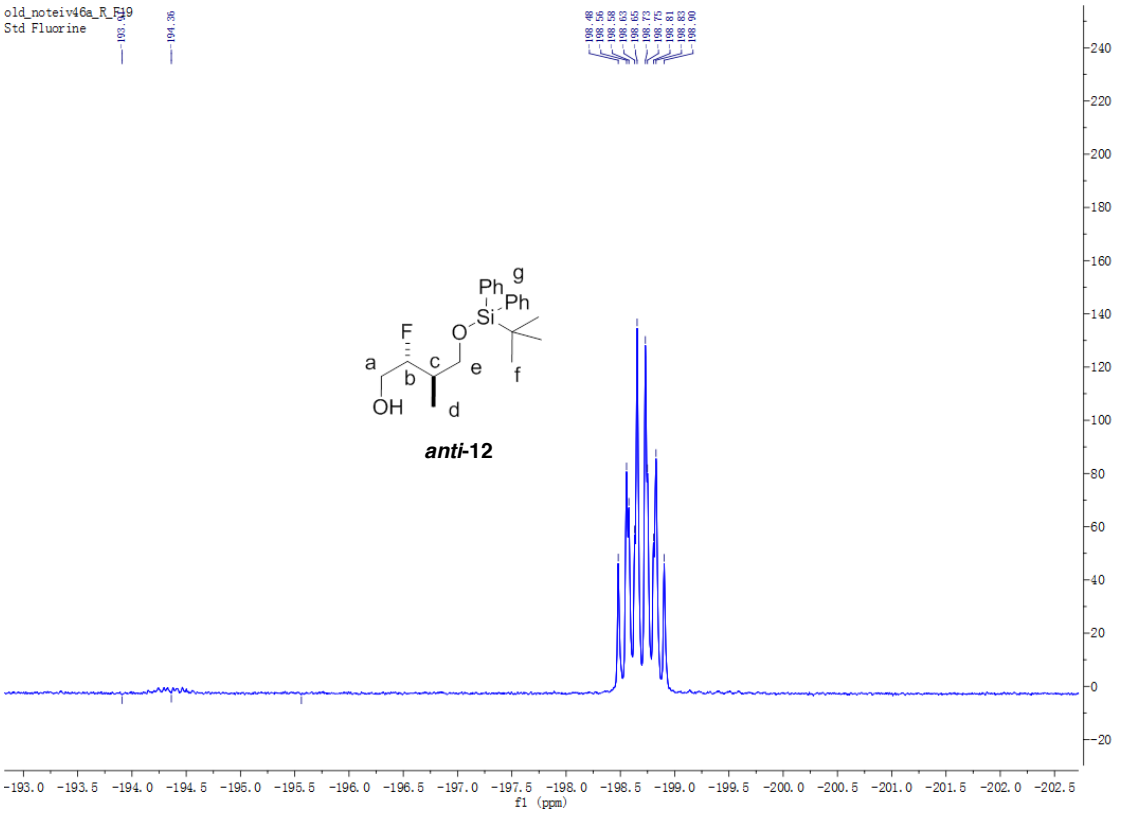


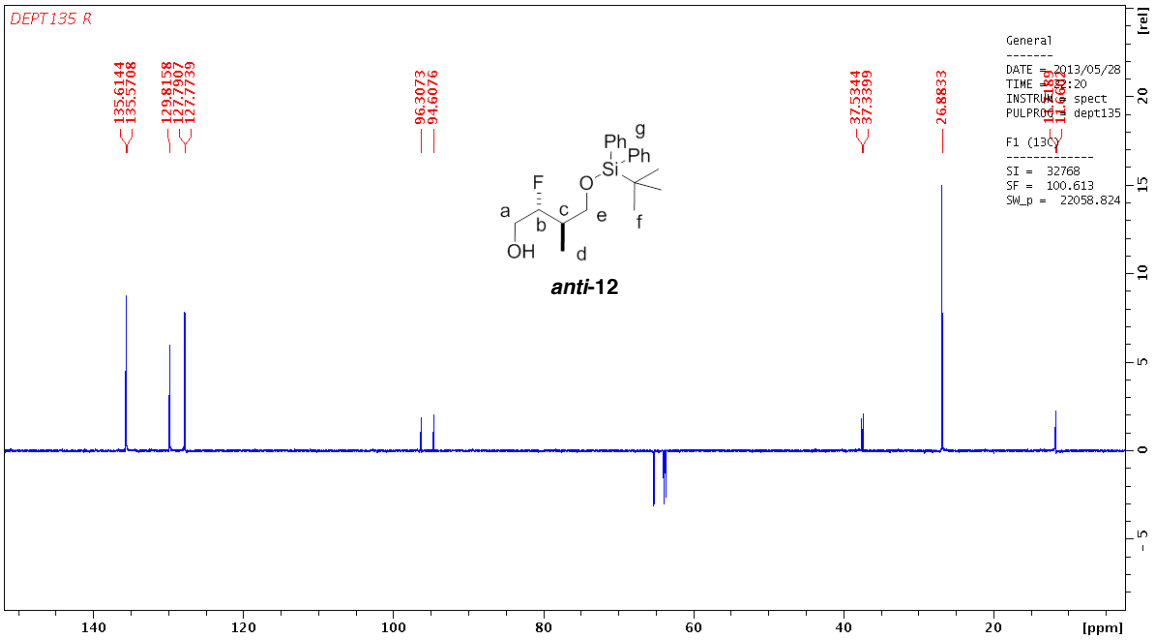


## J. Typical Procedure for the a-Amination of the Aldehyde

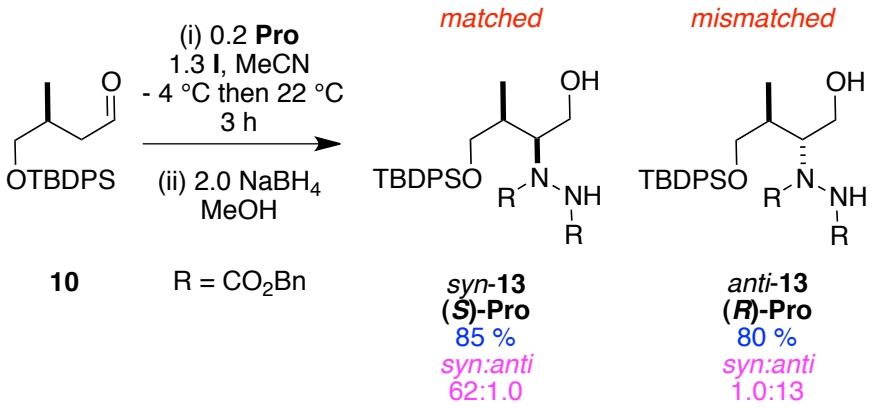


A modification of reported procedure[104] was used. Dibenzyl azodicarboxylate (90%, 1.29 g, 3.9 mmol) and proline (70 mg, 0.6 mmol) in MeCN (10 mL) were cooled down to -3 °C. The aldehyde (1.02 g 3.00 mmol) was then added and the mixture was stirred at -3 °C for 2 h. The reaction was gradually warmed to 20 °C within *ca.* 1 h. The mixture was then cooled to 0 °C, treated with MeOH (3 mL) and $NaBH_4$ (240 mg, 6 mmol) and was stirred for 5 min at 0 °C. The reaction was quenched by 1 M $KHSO_4$. The aqueous solution was extracted with EtOAc three times. The combined organic layers were dried with $MgSO_4$, and concentrated *in vacuo*. Purification of the residue by flash chromatography on silica gel, eluting with 15% EtOAc/hexanes gave the desired alcohol as white foamy solid.

**Dibenzyl 1-((2*R*,3*S*)-4-((*tert*-Butyldiphenylsilyl)oxy)-1-hydroxy-3-methylbutan-2-yl)hydrazine-1,2-dicarboxylate (*anti*-13).**

The compound was prepared according to the typical a-amination procedure catalysed by (*R*)-Proline. Purification by flash chromatography afforded *anti*-**13** as a white foamy solid (1.54 g, 2.40 mmol, 80% isolated yield). $^1$H NMR (400 MHz, $CDCl_3$) δ 7.70-7.67 (4H, m), 7.50-7.27 (16H, m), 6.85 (1H, d, $J$ = 31.1 Hz), 5.37-5.10 (4H, m), 4.45-4.12 (2H, m), 3.80-3.41 (4H, m), 1.95-1.66 (1H, m), 1.12-1.09 (9H, m), 0.99-0.88 (3H, m); $^{13}$C NMR (100 MHz, $CDCl_3$) δ 159.1, 157.4, 135.6, 133.3, 133.2, 129.6, 129.8, 128.7, 128.6, 128.2, 127.9, 127.8, 127.7, 68.6, 65.9, 65.6, 60.4, 35.6, 26.9, 19.3, 15.1. IR ($CH_2Cl_2$) n ($cm^{-1}$) 3356, 3032, 2928, 1717, 1454, 1408, 1265, 1227, 1111, 1057. HRMS (ESI, TOF): Exact mass calcd for $C_{37}H_{45}N_2O_6Si$ $[M+H]^+$ 641.3047. Found 641.3078.

The diastereoselectivity was 1.0:13, determined by Chiral HPLC (Chiralcel OD, Hex/iPrOH 93:7, 1 mL/min, 25 °C), $t_r$ 10.3 min (minor diastereomer), $t_r$ 14.4 min (major diastereomer).

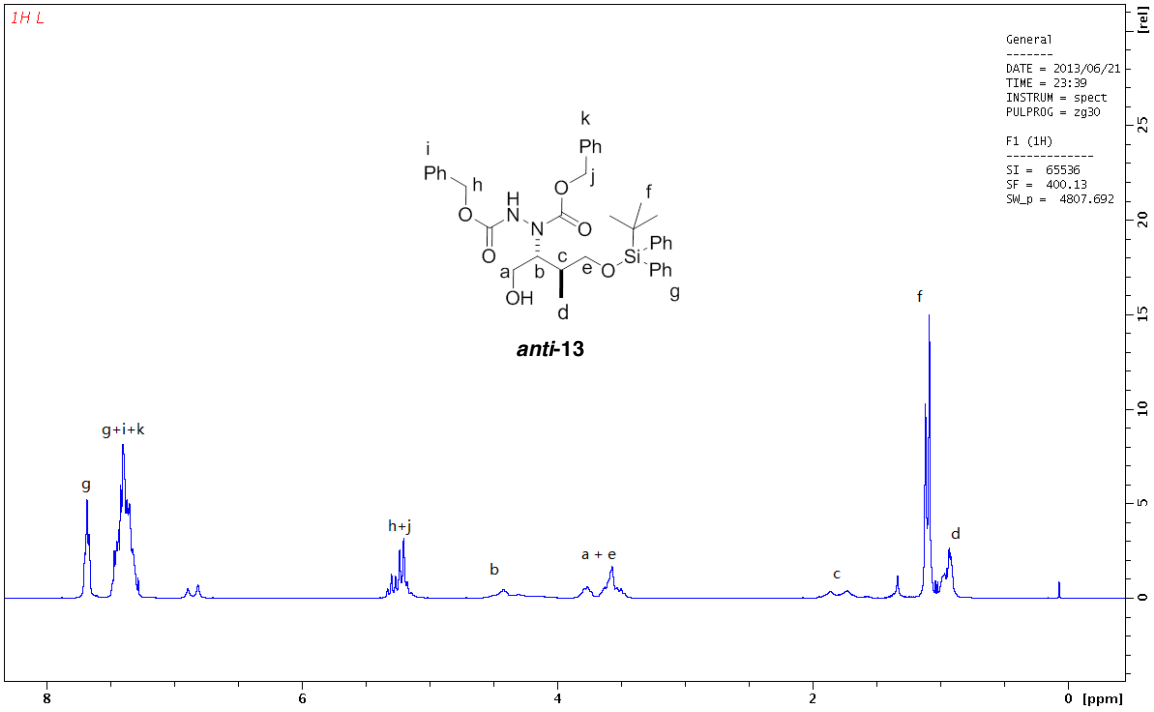

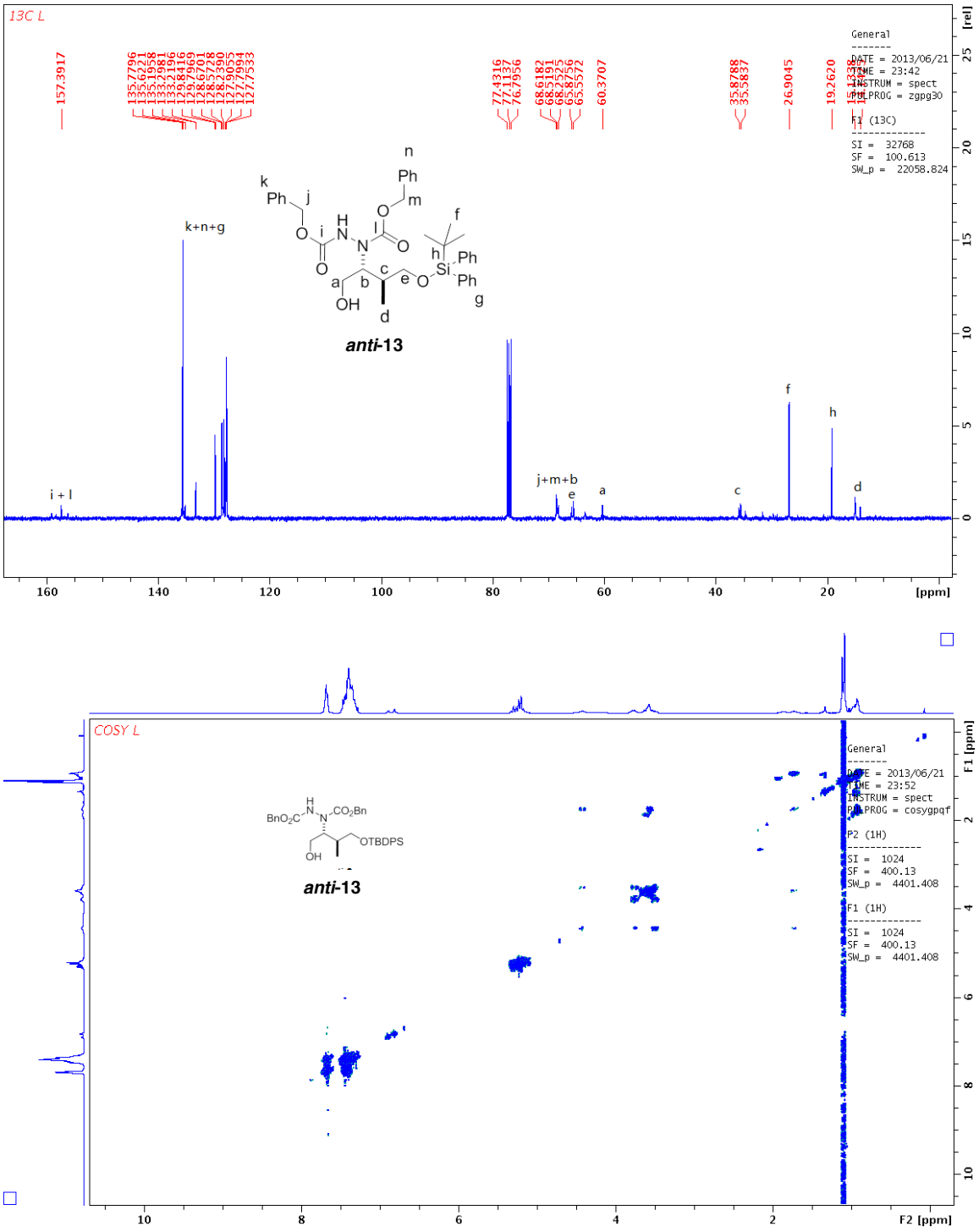


**Dibenzyl 1-((2*S*,3*S*)-4-((*tert*-Butyldiphenylsilyl)oxy)-1-hydroxy-3-methylbutan-2-yl)hydrazine-1,2-dicarboxylate (*syn*-13).**

The compound was prepared according to the typical a-amidation procedure catalysed by (*S*)-Proline. Purification by flash chromatography afforded *syn*-**13** as a white foamy solid (1.63 g, 2.54 mmol, 85% isolated yield). $^{1}$H NMR (400 MHz, $CDCl_3$) δ 7.69-7.62 (4H, m, *J* = 13.5, 6.6 Hz), 7.50-7.24 (16H, m), 6.96 (1H, s), 5.30-5.22 (3H, m), 5.13 (1H, dd, *J* = 12.1, 9.6 Hz), 4.36-4.16 (2H, m), 3.86-3.70 (2H, m), 3.59-3.44 (2H, m), 1.80 (1H, br), 1.11-1.08 (9H, m), 0.93-0.90 (3H, m); $^{13}$C NMR (100 MHz, $CDCl_3$) δ 158.6 (d, *J* = 65.9 Hz), 156.6 (d, *J* = 27.3 Hz), 135.8, 135.6, 135.5, 135.4, 133.0, 130.1, 129.9, 128.6, 128.5, 128.1, 127.9, 127.8, 68.3, 64.0, 63.2, 60.6, 35.5, 27.0, 19.2, 14.9. IR ($CH_2Cl_2$) n ($cm^{-1}$) 3356, 3032, 2959, 1724, 1470, 1408, 1261, 1223, 1111, 1053. HRMS (ESI, TOF): Exact mass calcd for $C_{37}H_{45}N_2O_6Si$ $[M+H]^+$ 641.3047. Found 641.3063. The diastereoselectivity was 62:1.0, determined by Chiral HPLC (Chiralcel OD, Hex/iPrOH 93:7, 1 mL/min, 25 °C), $t_r$ 10.2 min (minor diastereomer), $t_r$ 14.3 min (major diastereomer).

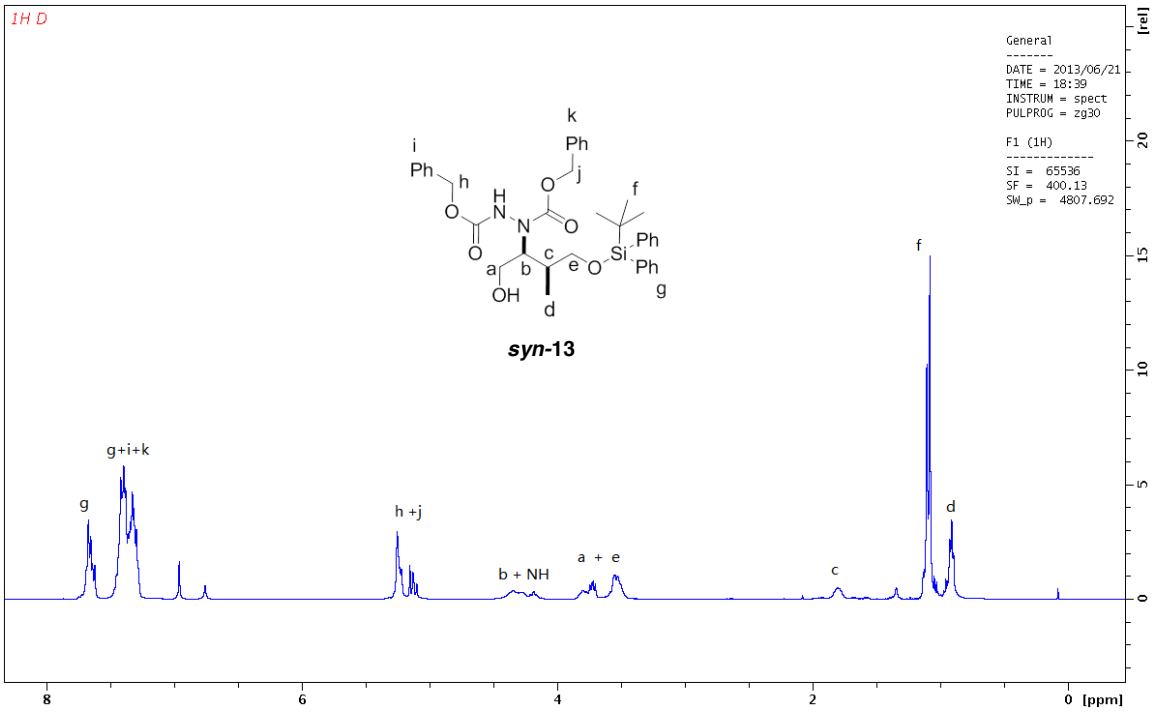

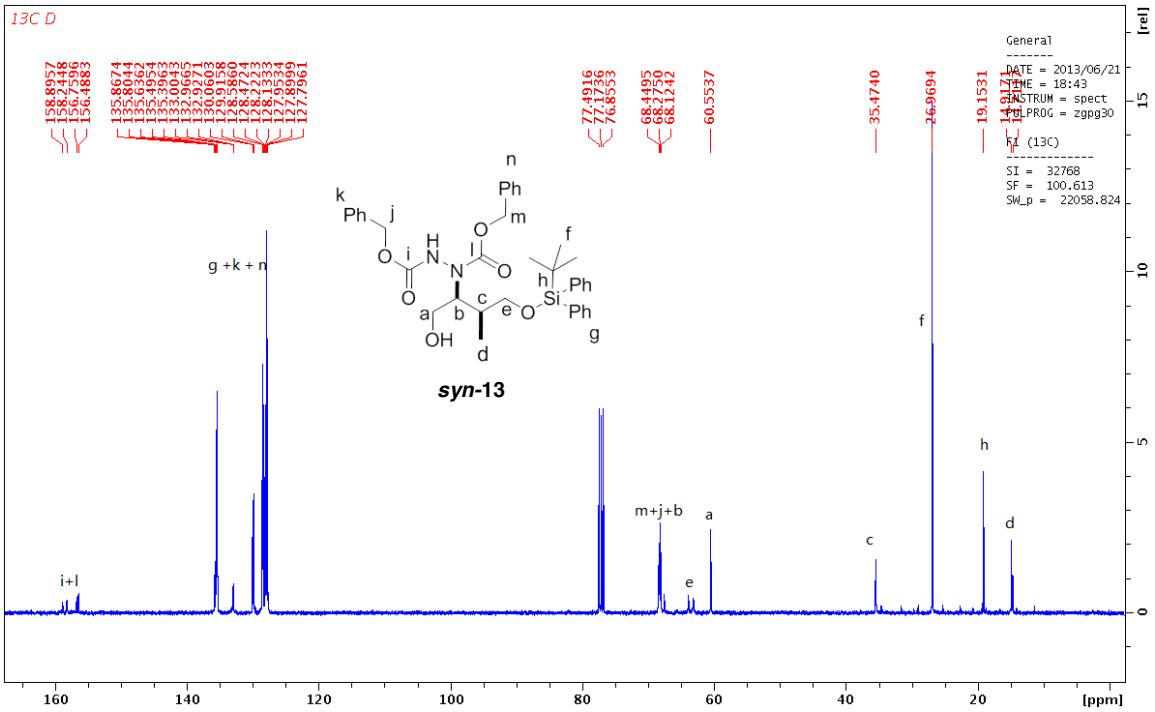


**K. Typical Procedure for the Hydrogenolysis and Benzylation of the Alcohol.**

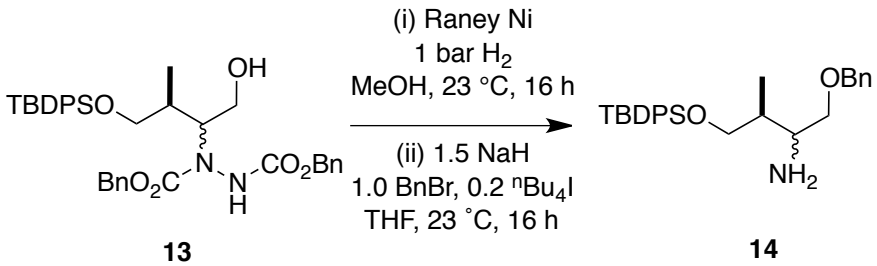


To Raney–Nickel (~0.3 g, prewashed with dry MeOH) in MeOH (1 mL), was added AcOH (0.3 mL) and a solution of **13** (64 mg, 0.10 mmol) in MeOH (1 mL). The solution was degassed and stirred under a slightly positive pressure of hydrogen (balloon) at 23 °C for 16 h. The reaction was then filtered through a short pad of Celite, and washed with $CH_2Cl_2$. The mixture was concentrated *in vacuo* and the residue was redissolved in $CH_2Cl_2$ and was neutralized by anhydrous $Na_2CO_3$. The solvent was removed by vacuum and the crude product was subjected to benzyl protection without further purification. Under Ar atmosphere, to a solution of the hydrogenated crude product (0.15 mmol) in anhydrous THF was added NaH (4.8 mg, 0.4 mmol). After

stirring for 5 min, BnBr (19 mL, 0.15 mmol) and $^{n}Bu_4NI$ (11.1 mg, 0.03 mmol) was added and the mixture was stirred at 23 °C for 16 h. The reaction was quenched by 1 M $KHSO_4$. The aqueous solution was extracted with EtOAc (three times). The combined organic layers were dried with $MgSO_4$, and concentrated *in vacuo*. Purification of the residue by flash chromatography on silica gel, eluting with ~1.0% - 2.5% MeOH/$CH_2Cl_2$ gave the desired product as a white foamy solid.

**(2*S*,3*S*)-1-(Benzyloxy)-4-((*tert*-butyldiphenylsilyl)oxy)-3-methylbutan-2-amine (*syn*-14).**

The compound was prepared according to the typical hydrogenolysis and benzylation procedure. Purification by flash chromatography afforded *syn*-**14** as a white foamy solid (22 mg, 0.050 mmol, 50% yield in two steps). $^1$H NMR (400 MHz, $CDCl_3$) δ 7.71-7.65 (4H, m), 7.48-7.28 (11H, m), 4.55 (2H, d, *J* = 4.8 Hz), 3.77-3.60 (3H, m), 3.47 (1H, dd, *J* = 9.3, 7.6 Hz), 3.18 (1H, td, *J* = 7.2, 3.4 Hz), 2.80 (2H, br), 1.90-1.79 (1H, m), 1.08 (9H, s), 0.94 (3H, d, *J* = 7.0 Hz); $^{13}$C NMR (100 MHz, $CDCl_3$) δ 138.1, 135.6, 133.4, 133.3, 129.7, 128.4, 127.8, 127.7, 73.3, 72.8, 66.8, 53.9, 38.1, 27.0, 19.2, 13.9.

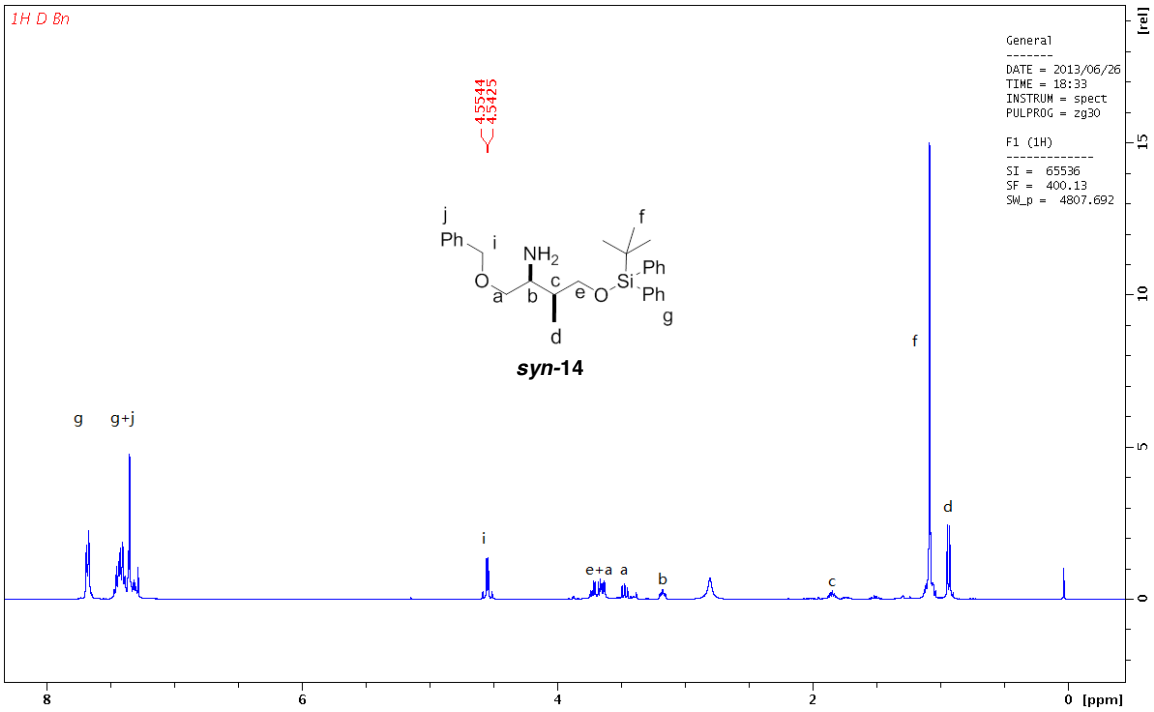
1H D Bn
General
DATE = 2013/06/26
TIME = 18:33
INSTRUM = spect
PULPROG = zg30
F1 (1H)
SI = 65536
SF = 400.13
SW_p = 4807.692
4.5514
4.5425
syn-14
g
g+j
i
e+a
a
b
c
f
d
[rel]
[ppm]

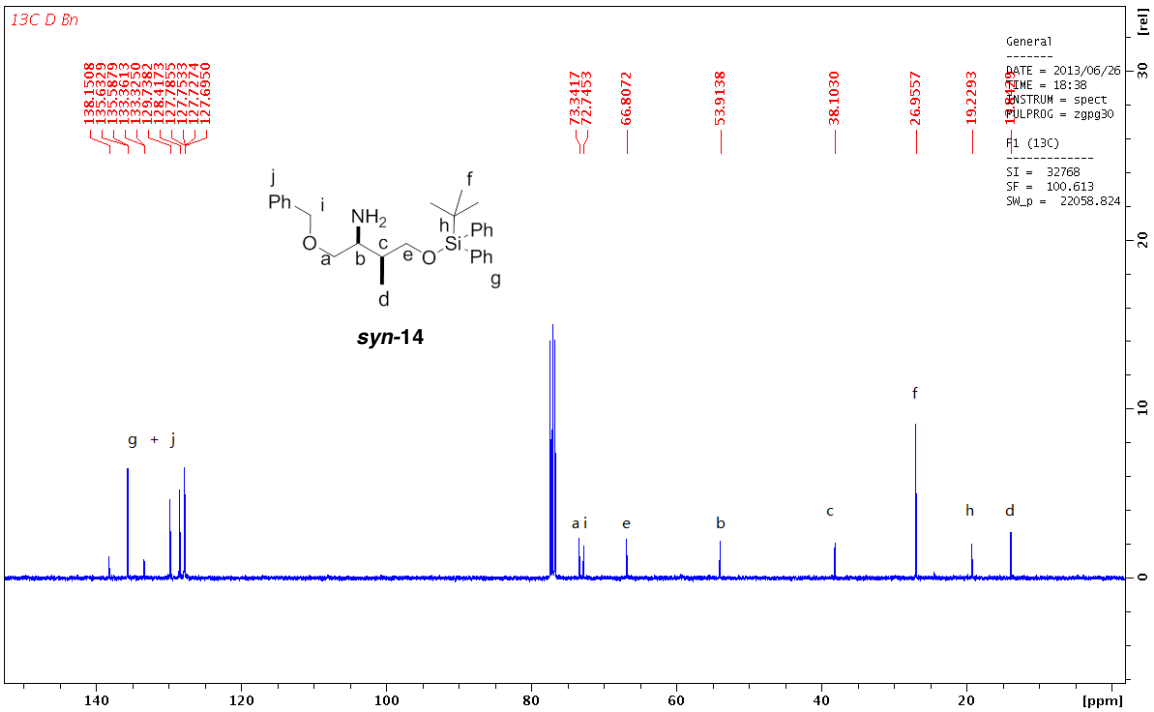
13C D Bn
General
DATE = 2013/06/26
TIME = 18:38
INSTRUM = spect
PULPROG = zgpg30
F1 (13C)
SI = 32768
SF = 100.613
SW_p = 22058.824
138.1508
135.6329
135.5673
133.3613
133.3250
129.7382
128.4173
127.7855
127.7723
127.7274
127.6950
73.3417
72.7453
66.8072
53.9138
38.1030
26.9557
19.2293
syn-14
g + j
a i
e
b
c
f
h
d
[rel]
[ppm]

**(2*R*,3*S*)-1-(Benzyloxy)-4-((*tert*-butyldiphenylsilyl)oxy)-3-methylbutan-2-amine (*anti*-14).**

The compound was prepared according to the typical hydrogenolysis and benzylation procedure. Purification by flash chromatography afforded *anti*-**14** as a white foamy solid (22 mg, 0.050 mmol, 50 % yield in two steps). $^{1}$H NMR (400 MHz, $CDCl_3$) δ 7.70-7.67 (4H, m), 7.49-7.28 (11H, m), 4.54 (2H, s), 3.68-3.58 (2H, m), 3.56-3.49 (1H, m), 3.38 (1H, dd, $J$ = 10.2, 6.5 Hz), 3.26 (1H, br), 1.83 (1H, br), 1.51 (2H, br), 1.08 (9H, s), 0.92 (3H, d, $J$ = 6.9 Hz); $^{13}$C NMR (100 MHz, $CDCl_3$) δ 138.5, 135.6, 133.8, 133.7, 129.6, 128.4, 127.7, 127.6, 74.3, 73.2, 66.8, 29.7, 26.9, 19.3, 11.7.

Relative stereochemistry determination of **13**: the $^{13}$C NMR data of *syn*-**14** matched with reported data[103] and differ from that of *anti*-**14**. Therefore, the relative stereochemistry assignment was confirmed.

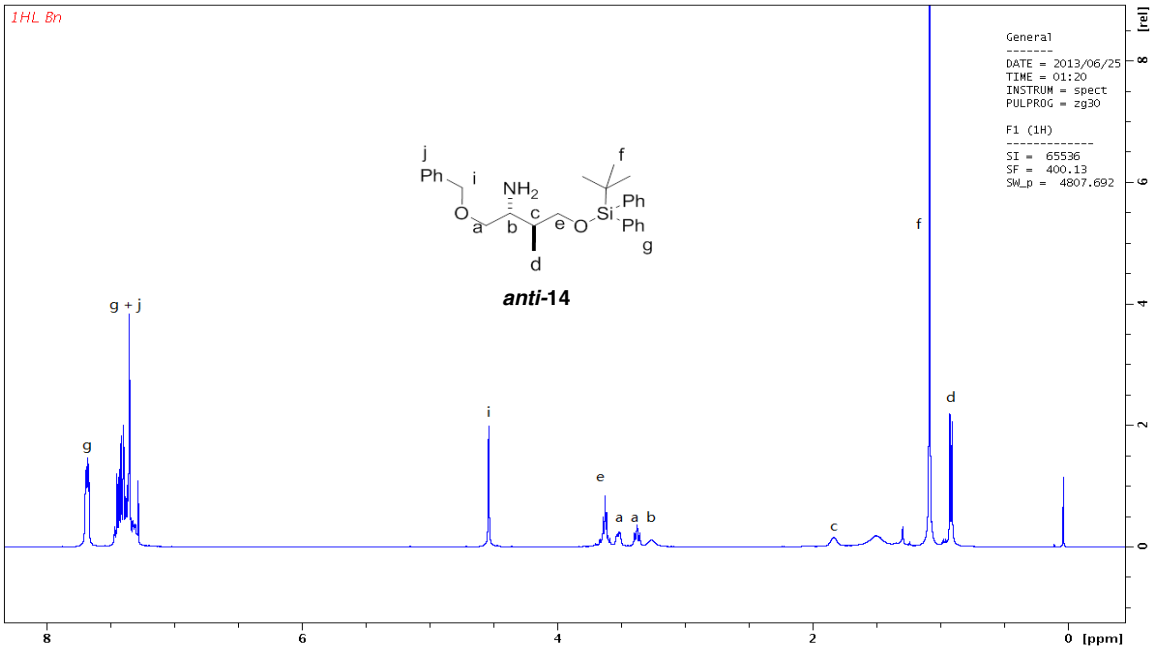

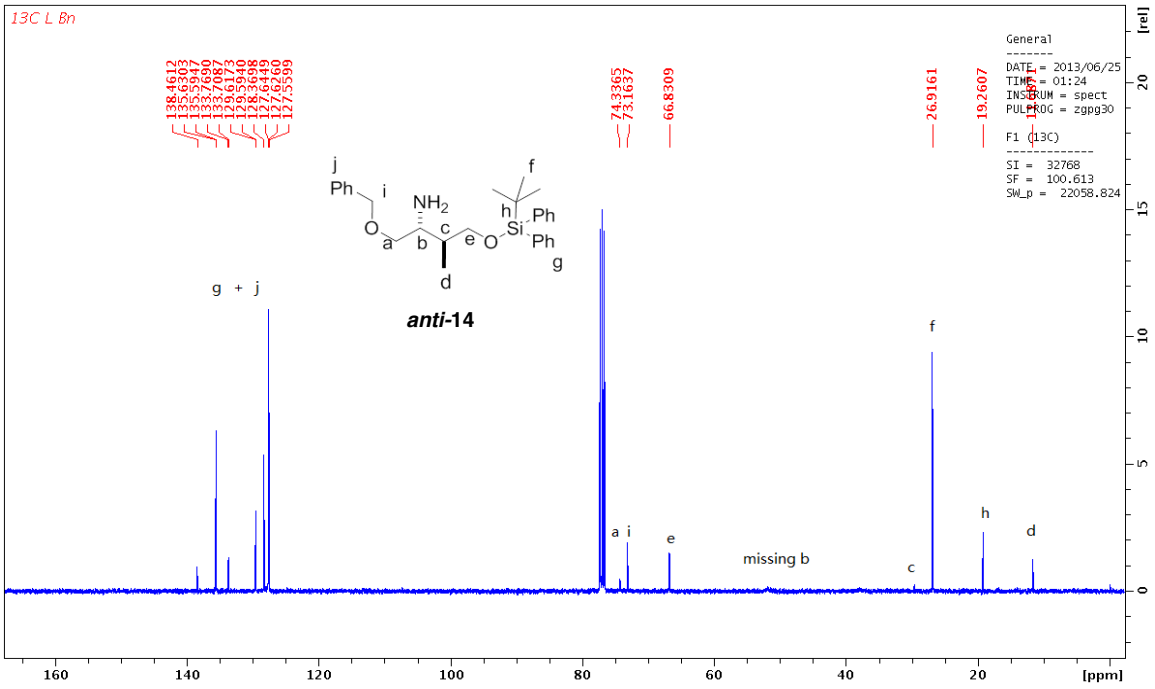
13C L Bn
138.4612
135.6303
133.9947
133.7690
133.7087
129.6173
129.5940
128.5498
127.6449
127.6260
127.5599
74.3365
73.1637
66.8309
26.9161
19.2607
14.1587
General
DATE = 2013/06/25
TIME = 01:24
INSTRUM = spect
PULPROG = zgpg30
F1 (13C)
SI = 32768
SF = 100.613
SW_p = 22058.824
anti-14
g + j
a i
e
missing b
c
f
h
d
[ppm]
[rel]

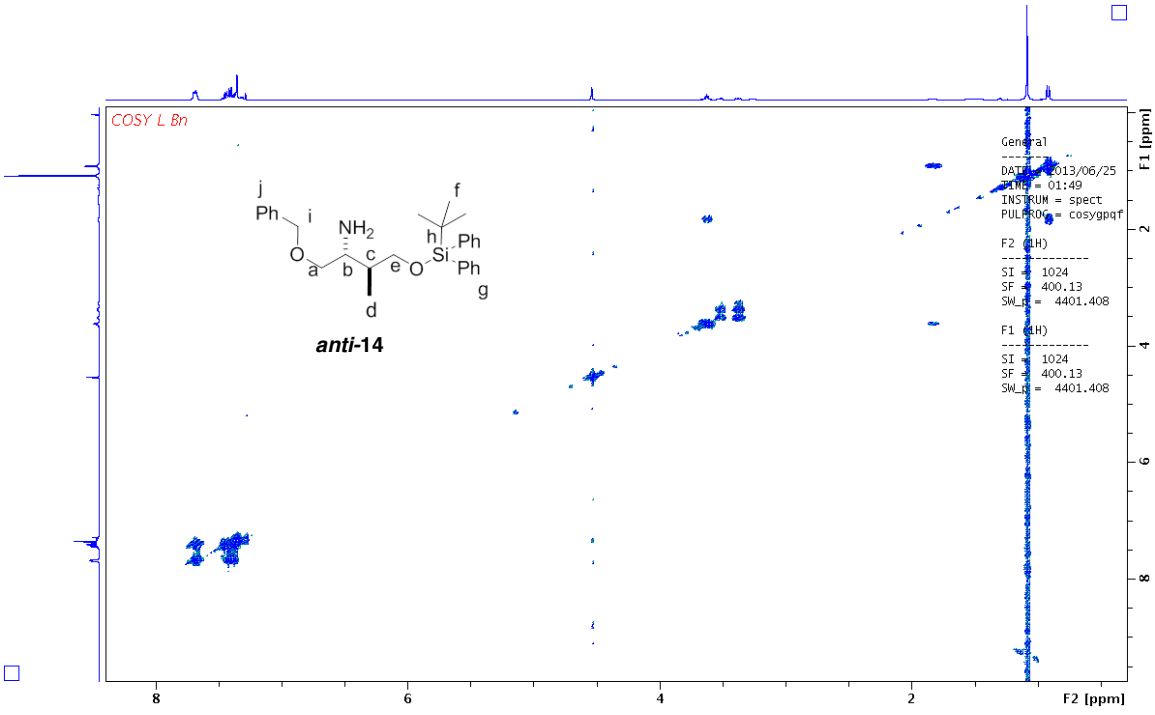
COSY L Bn
anti-14
General
DATE = 2013/06/25
TIME = 01:49
INSTRUM = spect
PULPROG = cosygpqf
F2 (1H)
SI = 1024
SF = 400.13
SW_p = 4401.408
F1 (1H)
SI = 1024
SF = 400.13
SW_p = 4401.408
F2 [ppm]
F1 [ppm]

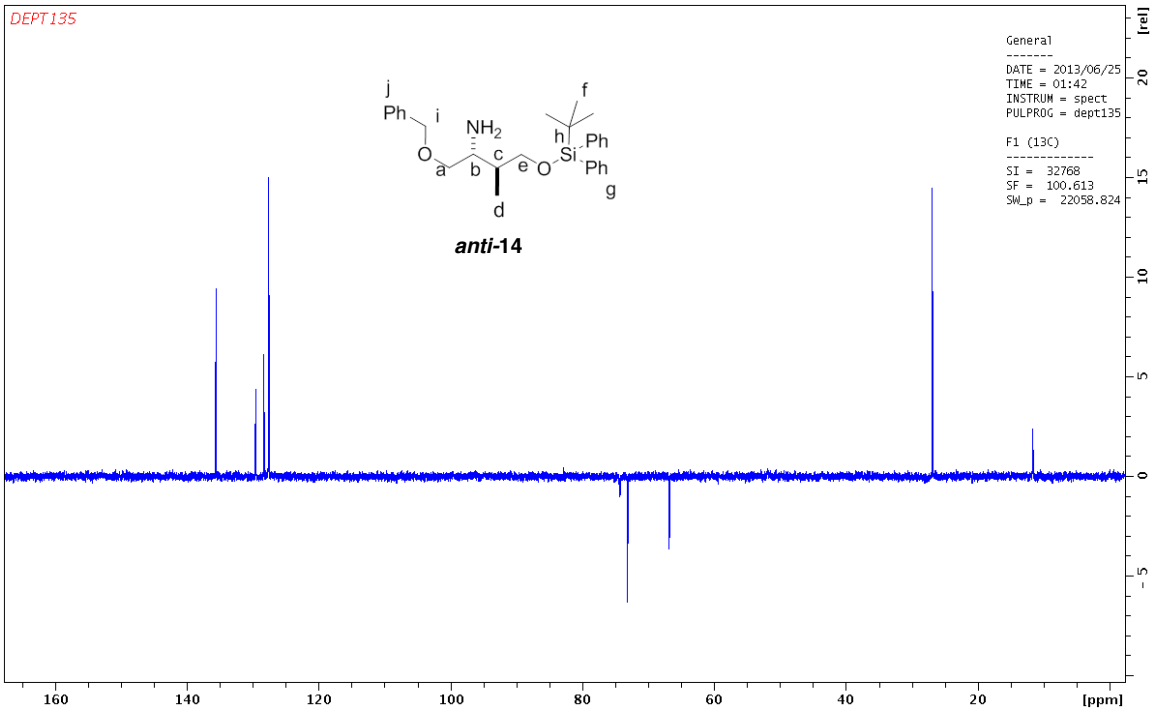


**L. Typical Procedure for the Preparation of a-Amino Acid.**

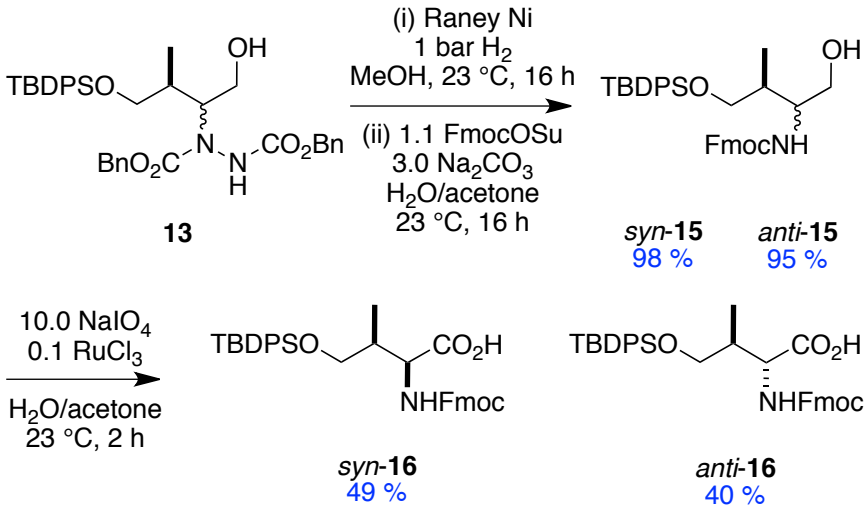


To Raney–Nickel (~1.5 g, prewashed with dry MeOH) in MeOH (10 mL), was added AcOH (3 mL) and a solution of **13** (1.44 g, 2.25 mmol) in MeOH (10 mL). The solution was degassed and stirred under a slightly positive pressure of hydrogen (balloon) at 23 °C for 16 h. The reaction was then filtered through a short pad of Celite, and

washed with $CH_2Cl_2$. The mixture was concentrated *in vacuo* and the residue was redissolved in $CH_2Cl_2$ and was neutralized by anhydrous $Na_2CO_3$. The solvent was removed by vacuum and the crude product was subjected to Fmoc-protection without further purification. To a solution of the above crude product in $H_2O$ (10 mL) and acetone (10 mL) was added FmocOSu (830 mg, 2.5 mmol) and $Na_2CO_3$ (715 mg, 6.7 mmol). The reaction was stirred at 23 °C for 16 h. The mixture was extracted with EtOAc three times. The combined organic layers were dried with $MgSO_4$, and concentrated *in vacuo*. Purification of the residue by flash chromatography on silica gel, eluting with ~10% - 20% EtOAc/hexanes gave **15** as a white foamy solid. To a solution of $RuCl_3$ (29 mg, 0.14 mmol) and $NaIO_4$ (2.95 g, 13.8 mmol) in water was added **12** (800 mg, 1.4 mmol). The mixture was stirred at 23 °C for 2 h, and then added MeOH (2 mL). The reaction was stirred until solid precipitation occurred. The solid was filtered on Celite and washed it with EtOAc. 1 M $KHSO_4$ (3 mL) was added to the filtrate. Then, the aqueous phase was extracted by EtOAc. The combined organic layers were dried with $MgSO_4$, and concentrated *in vacuo*. Purification of the residue by flash chromatography on silica gel, eluting with ~15% - 50% EtOAc/hexanes gave the desired acid as a white foamy solid.

**(9*H*-Fluoren-9-yl)methyl ((2*S*,3*S*)-4-((*tert*-Butyldiphenylsilyl)oxy)-1-hydroxy-3-methylbutan-2-yl)carbamate (*syn*-15).**

Purification by flash chromatography afforded *syn*-**15** as a white foamy solid (1.28 g, 2.20 mmol, 98 % yield in two steps). $^1$H NMR (400 MHz, $CDCl_3$) δ 7.86-7.74 (6H, m), 7.66 (2H, dd, *J* = 7.3, 3.6 Hz), 7.55-7.40 (8H, m), 7.34 (2H, t, *J* = 7.4 Hz), 6.05 (1H, d, *J* = 6.7 Hz), 4.50 (2H, d, *J* = 6.5 Hz), 4.28 (1H, t, *J* = 6.8 Hz), 3.93-3.74 (4H, m), 3.69 (1H, dd, *J* = 10.4, 4.5 Hz), 3.31 (1H, br), 2.05 (1H, br), 1.19 (9H, s), 1.13 (3H, d, *J* = 6.7 Hz); $^{13}$C NMR (100 MHz, $CDCl_3$) δ 157.4, 144.1, 141.4, 135.7, 132.9, 130.0, 127.9, 127.7, 127.1, 125.2, 120.0, 66.9, 66.0, 64.6, 56.7, 47.4, 35.7, 27.0, 19.2, 15.3. IR ($CH_2Cl_2$) n ($cm^{-1}$) 3402, 3067, 2928, 1701, 1508, 1450, 1327, 1227, 1111, 1042. HRMS (ESI, TOF): Exact mass calcd for $C_{36}H_{42}NO_4Si$ $[M+H]^+$ 580.2883. Found 580.2874.

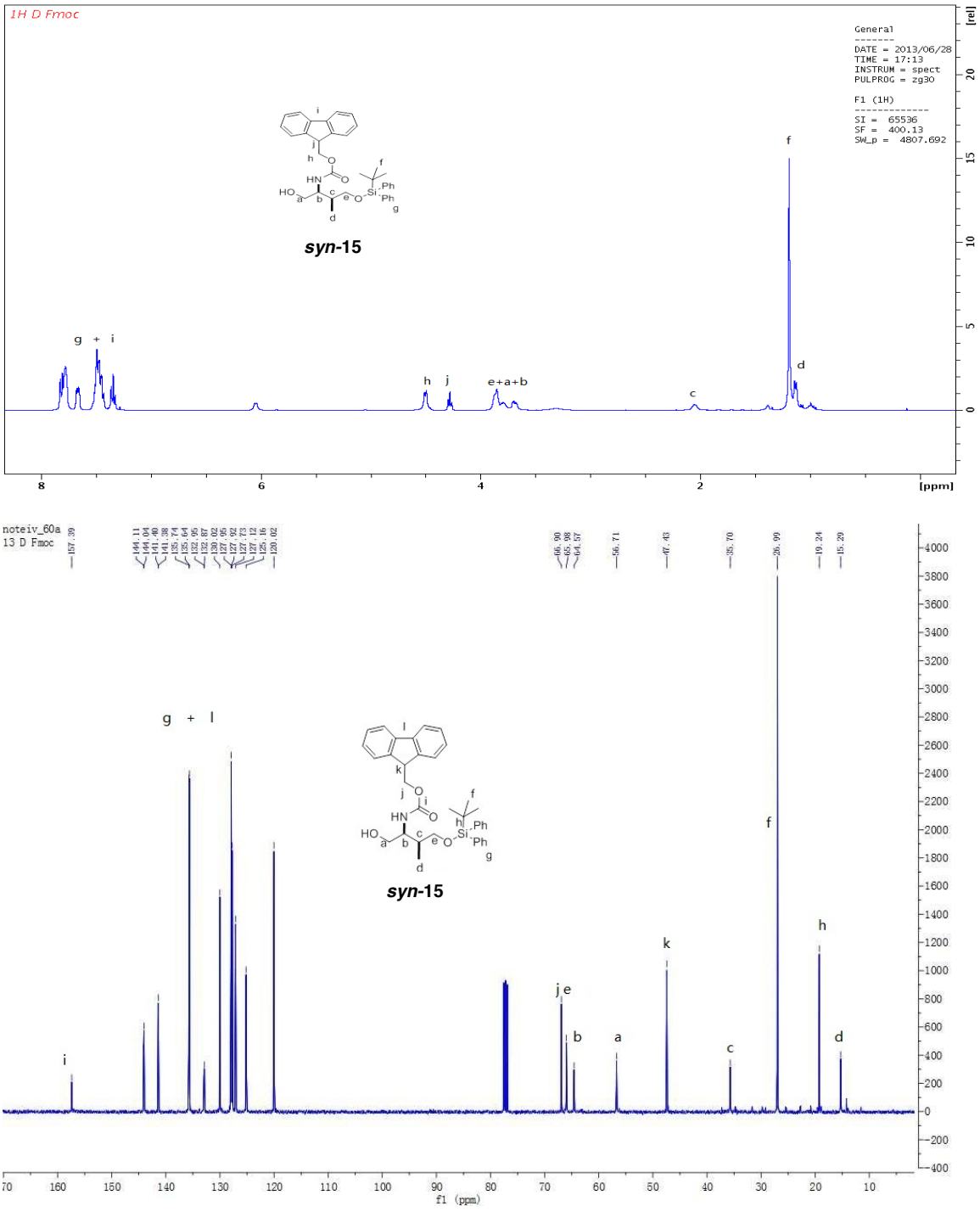


**(9*H*-Fluoren-9-yl)methyl ((2*R*,3*S*)-4-((*tert*-Butyldiphenylsilyl)oxy)-1-hydroxy-3-methylbutan-2-yl)carbamate (*anti*-15).**

Purification by flash chromatography afforded *anti*-**15** as a white foamy solid (1.24 g, 2.14 mmol, 95 % yield in two steps). $^{1}$H NMR (500 MHz, $CDCl_3$) δ 7.84-7.77 (2H, m), 7.74 (4H, dd, *J* = 7.7, 6.7 Hz), 7.64 (2H, d, *J* = 7.4 Hz), 7.55-7.39 (8H, m), 7.33 (2H, td, *J* = 7.5, 1.0 Hz), 5.85 (1H, d, *J* = 8.3 Hz), 4.51-4.43 (2H, m), 4.26 (1H, t, *J* = 6.9 Hz), 3.90 (1H, dd, *J* = 11.2, 4.2 Hz), 3.83-3.80 (1H, m), 3.78-3.69 (2H, m), 3.63 (1H, dd, *J* = 10.7, 7.2 Hz), 3.34 (1H, br), 2.11-2.10 (1H, m), 1.15 (9H, s), 0.97 (3H, d, *J* = 7.2 Hz); $^{13}$C NMR (125 MHz, $CDCl_3$) δ 156.9, 144.0, 141.4, 135.7, 132.8, 130.1, 127.9, 127.7, 127.1, 125.1, 120.0, 66.8, 66.1, 63.0, 56.3, 47.4, 37.2, 27.0, 19.2, 14.1. IR ($CH_2Cl_2$) n ($cm^{-1}$) 3368, 3067, 2928, 1701, 1512, 1450, 1242, 1111. HRMS (ESI, TOF): Exact mass calcd for $C_{36}H_{42}NO_4Si$ $[M+H]^+$ 580.2883. Found 580.2865.

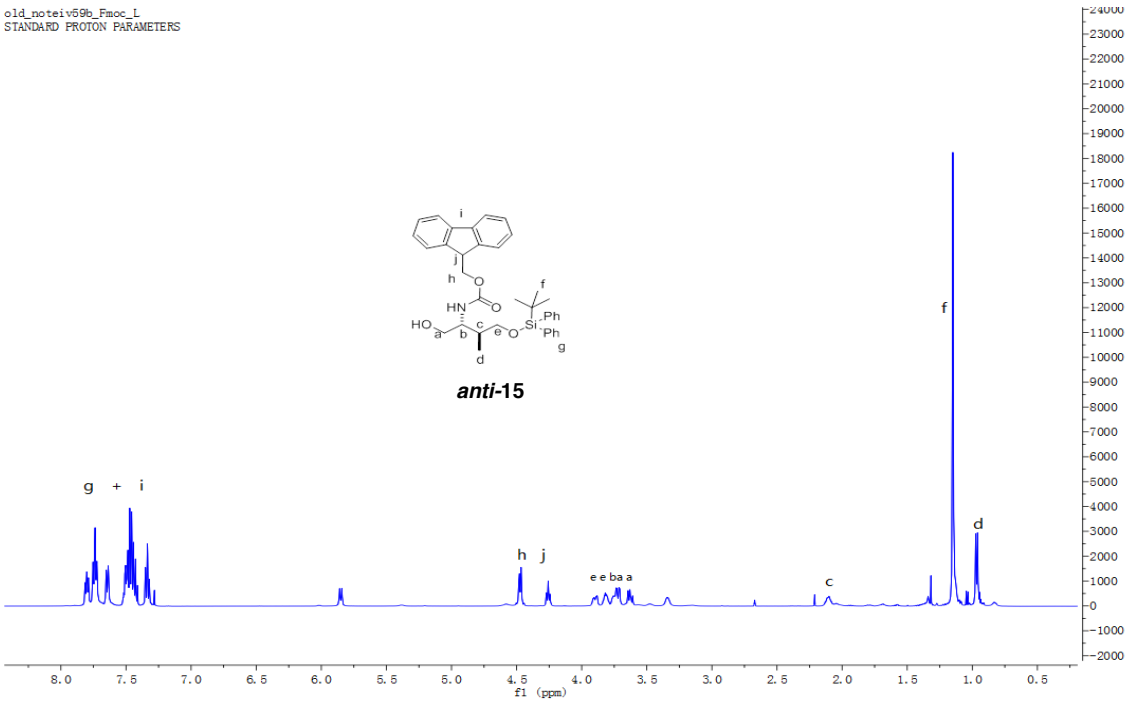

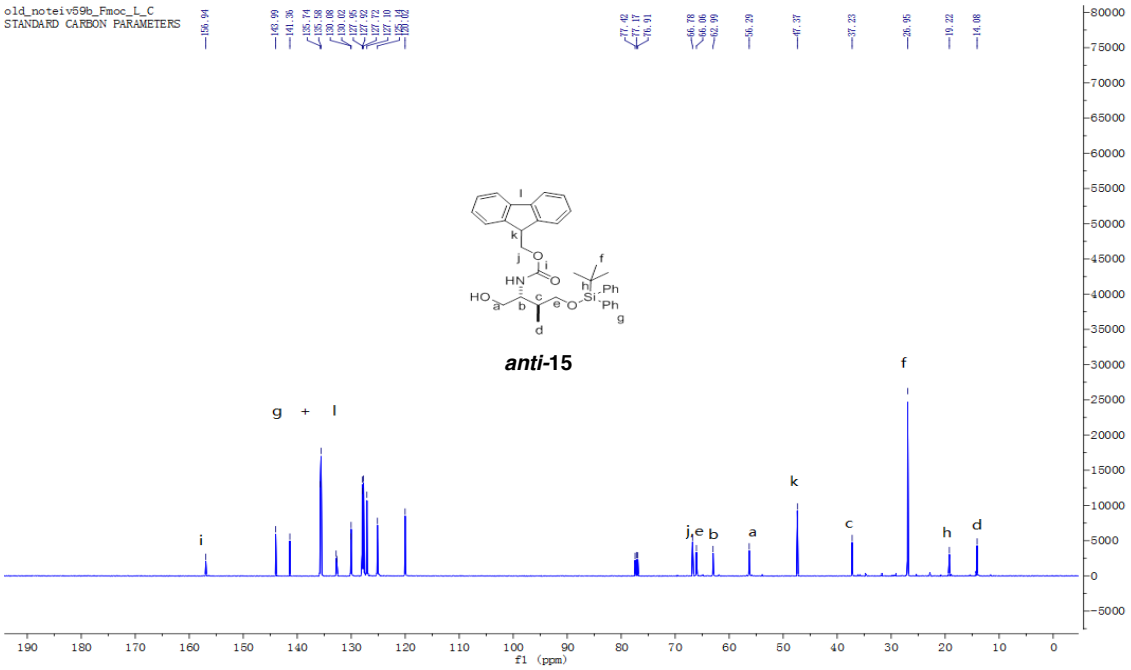


**(2*S*,3*S*)-2-((((9*H*-Fluoren-9-yl)methoxy)carbonyl)amino)-4-((*tert*-butyldiphenyl-silyl)oxy)-3-methylbutanoic acid (*syn*-16).**

Purification by flash chromatography afforded *syn*-**16** as a white foamy solid (0.42 g, 0.70 mmol, 49% yield). $^{1}$H NMR (400 MHz, $CDCl_3$) δ 7.89-7.60 (8H, m), 7.55-7.29 (10H, m), 6.41 (1H, d, $J$ = 8.4 Hz), 4.61-4.51 (7H, m), 4.34 (1H, t, $J$ = 6.9 Hz), 3.88 (1H, d, $J$ = 8.5 Hz), 3.62 (1H, dd, $J$ = 10.7, 5.1 Hz), 2.49 (1H, m), 1.25-1.09 (12H, m); $^{13}$C NMR (100 MHz, $CDCl_3$) δ 177.1, 156.9, 143.9, 141.3, 135.7, 132.6, 130.0, 127.9, 127.7, 127.1, 125.3, 120.0, 67.4, 66.1, 58.1, 47.1, 36.4, 26.9, 19.2, 14.7. IR ($CH_2Cl_2$) n (cm$^{-1}$) 3399, 3067, 2928, 1717, 1508, 1450, 1427, 1219, 1111, 1034. HRMS (ESI, TOF): Exact mass calcd for $C_{36}H_{39}NaNO_5Si$ $[M+Na]^+$ 616.2495. Found 616.2552.

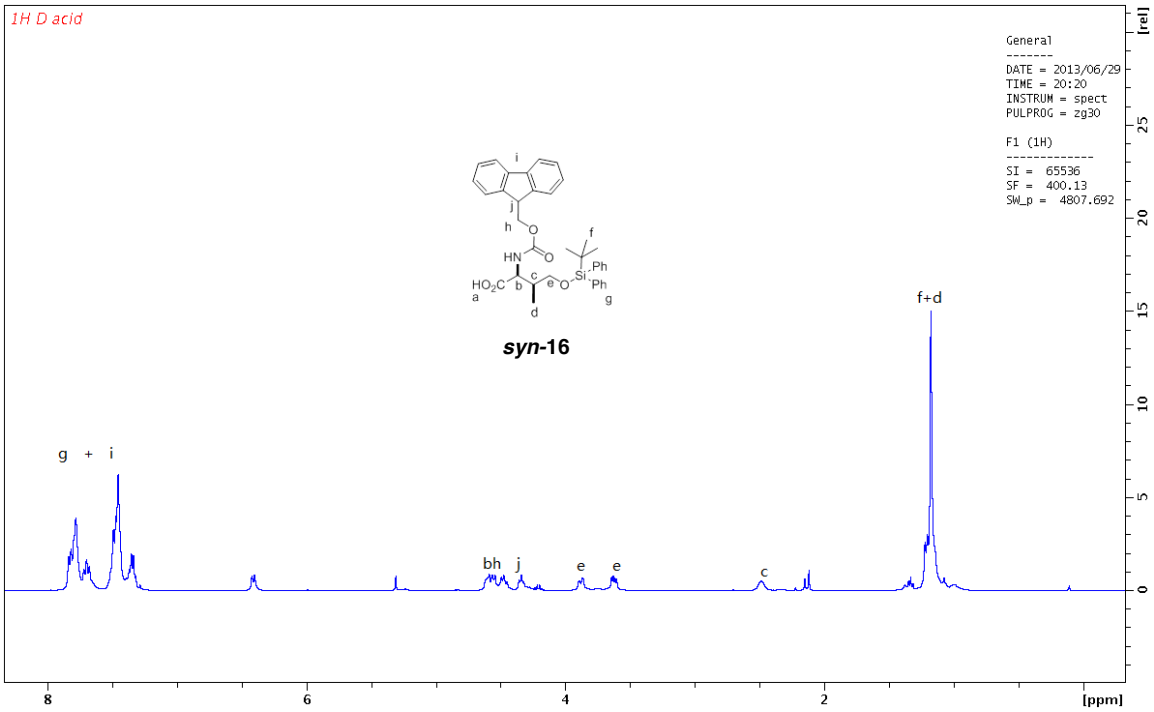
1H D acid
General
DATE = 2013/06/29
TIME = 20:20
INSTRUM = spect
PULPROG = zg30
F1 (1H)
SI = 65536
SF = 400.13
SW_p = 4807.692
[rel]
f+d
g + i
bh
j
e
e
c
[ppm]

*syn*-16

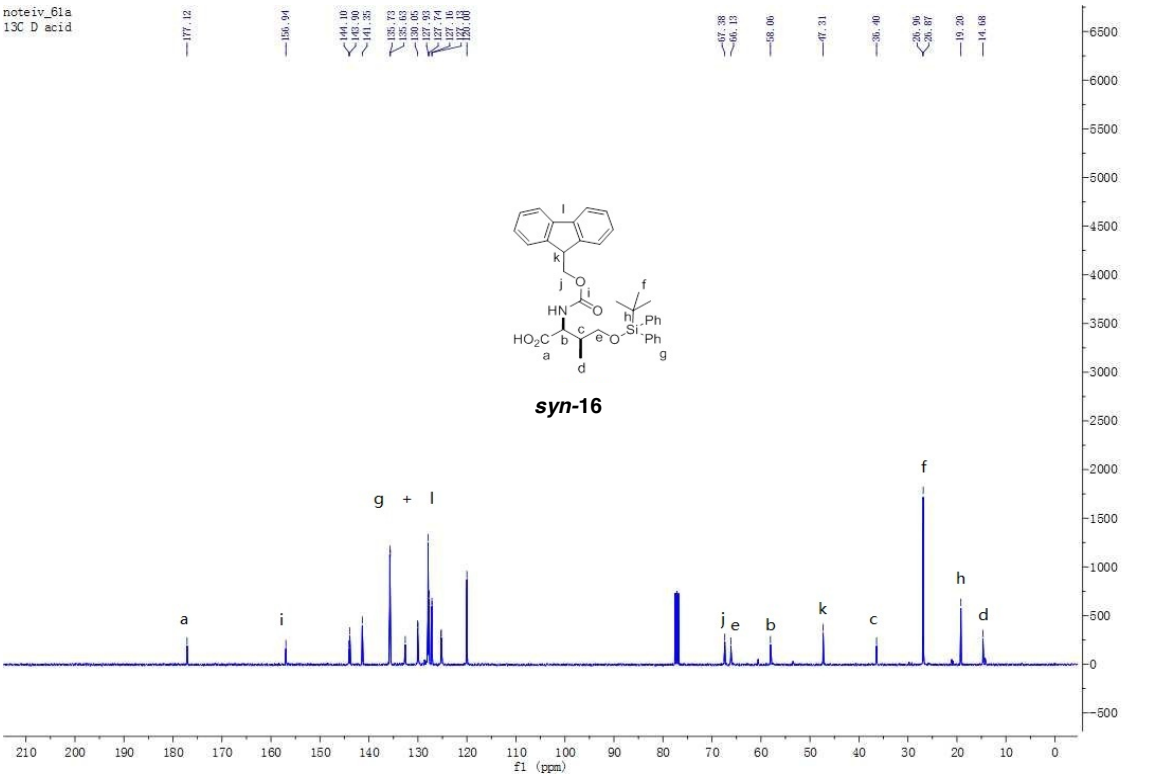
noteiv_61a
13C D acid
g + l
f
h
a
i
j
e
b
k
c
d
f1 (ppm)

*syn*-16

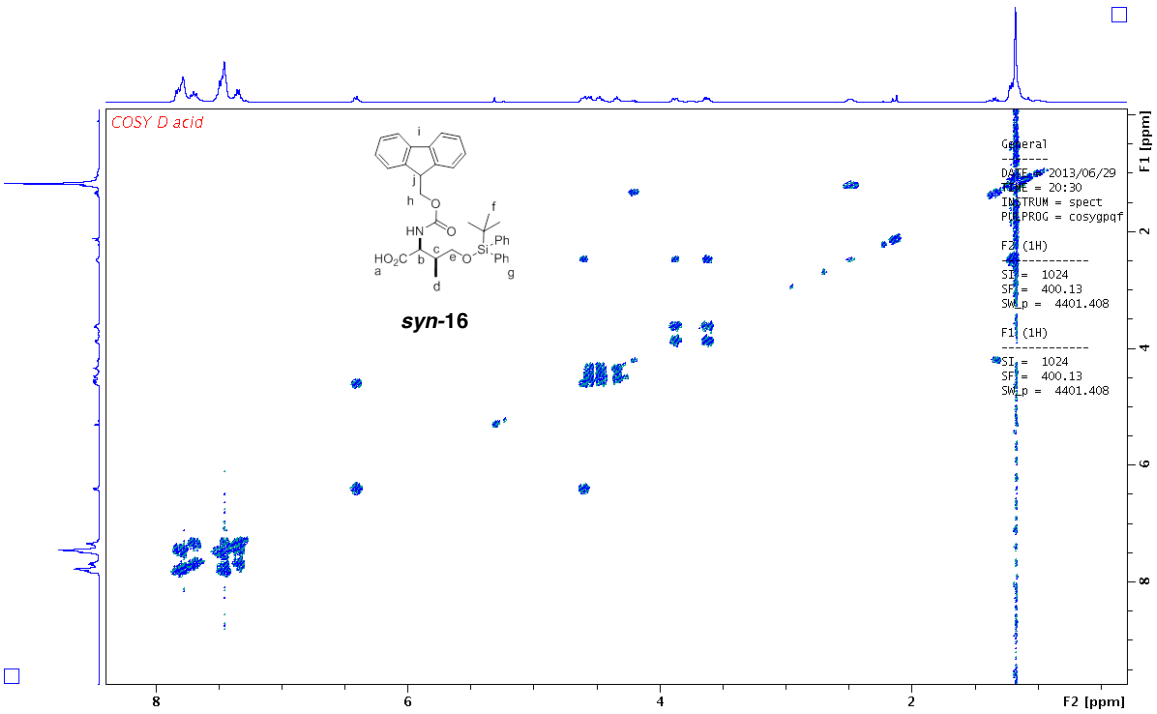
COSY D acid
General
DATE = 2013/06/29
TIME = 20:30
INSTRUM = spect
PULPROG = cosygpqf
F2 (1H)
SI = 1024
SF = 400.13
SW_p = 4401.408
F1 (1H)
SI = 1024
SF = 400.13
SW_p = 4401.408
F1 [ppm]
F2 [ppm]
syn-16

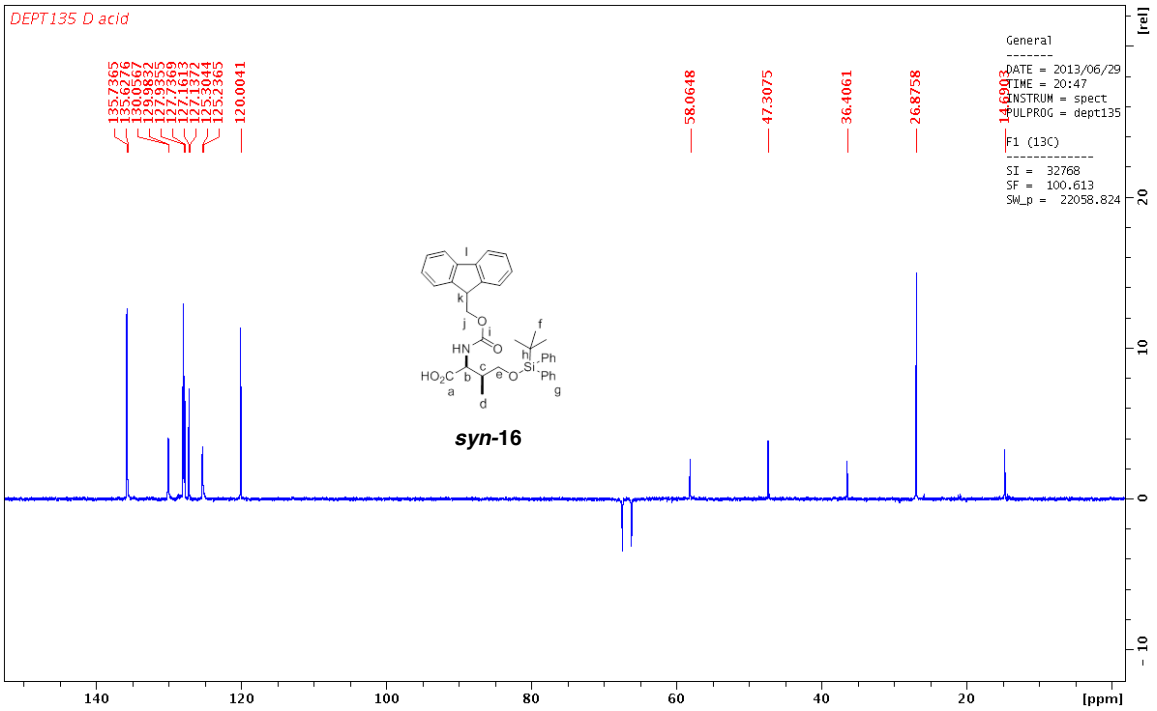
DEPT135 D acid
135.7365
135.6776
130.0567
129.9832
127.9355
127.7369
127.6143
127.1913
125.3044
125.2365
120.0041
58.0648
47.3075
36.4061
26.8758
14.6903
General
DATE = 2013/06/29
TIME = 20:47
INSTRUM = spect
PULPROG = dept135
F1 (13C)
SI = 32768
SF = 100.613
SW_p = 22058.824
[rel]
[ppm]
syn-16

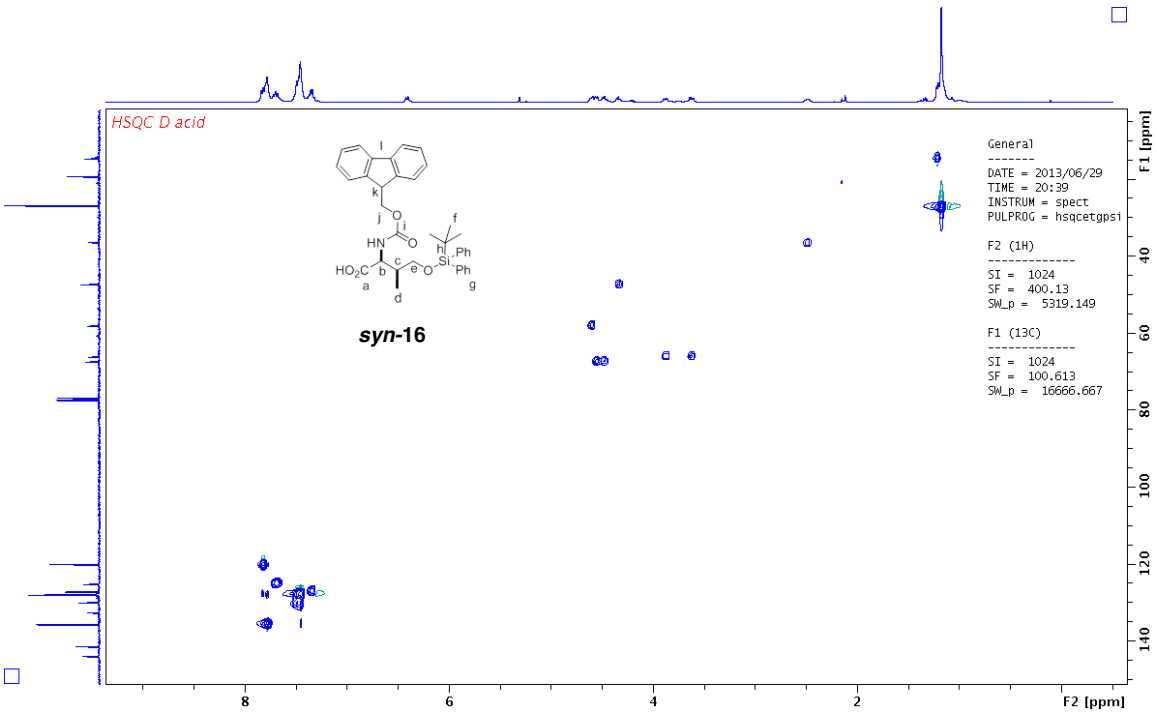


**(2*R*,3*S*)-2-((((9*H*-Fluoren-9-yl)methoxy)carbonyl)amino)-4-((*tert*-butyldiphenyl-silyl)oxy)-3-methylbutanoic acid (*anti*-16).**

Purification by flash chromatography afforded *anti*-**16** as a white foamy solid (0.34 g, 0.56 mmol, 40% yield). $^{1}$H NMR (400 MHz, $CDCl_3$) δ 7.81-7.56 (8H, m), 7.49-7.27 (10H, m), 5.90 (1H, d, *J* = 8.2 Hz), 4.69 (2H, d, *J* = 6.2 Hz), 4.51-4.34 (2H, m), 4.24 (1H, t, *J* = 6.5 Hz), 3.70-3.57 (2H, m), 2.43 (1H, br), 1.09 (9H, s), 0.95 (3H, d, *J* = 6.7 Hz); $^{13}$C NMR (100 MHz, $CDCl_3$) δ 156.4, 143.8, 141.3, 135.6, 133.0, 129.8, 127.8, 127.7, 127.1, 125.1, 119.9, 67.3, 66.1, 56.1, 47.2, 37.9, 29.7, 26.8, 19.1. HRMS (ESI, TOF): Exact mass calcd for $C_{36}H_{40}NO_5Si$ $[M+H]^+$ 594.2676. Found 594.2752.

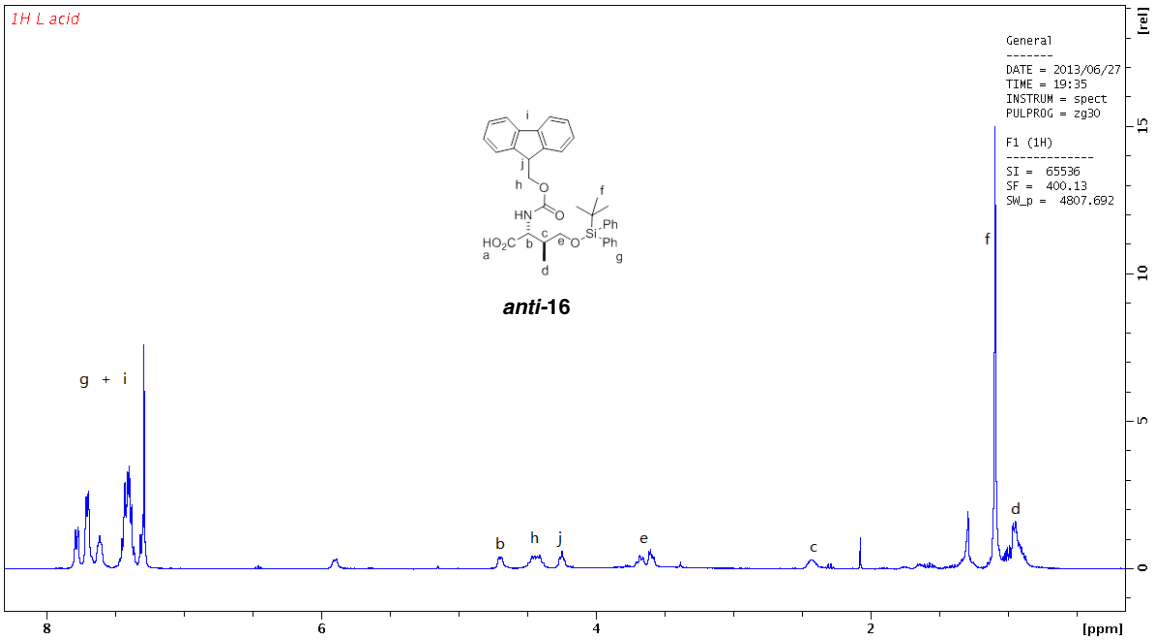
1H L acid
General
DATE = 2013/06/27
TIME = 19:35
INSTRUM = spect
PULPROG = zg30
F1 (1H)
SI = 65536
SF = 400.13
SW_p = 4807.692
anti-16
g + i
b
h
j
e
c
f
d
[ppm]
[rel]

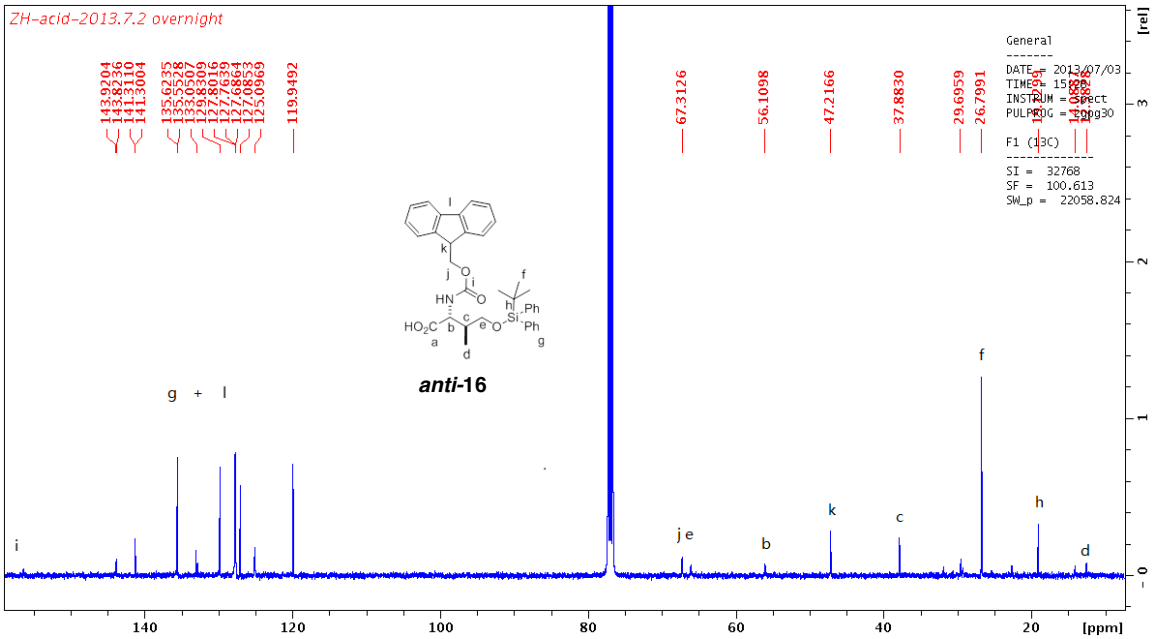
ZH-acid-2013.7.2 overnight
143.9204
143.8236
141.3110
141.3004
135.6235
135.5528
133.0507
129.8309
127.8016
127.7634
127.6629
127.0853
125.0969
119.9492
67.3126
56.1098
47.2166
37.8830
29.6959
26.7991
General
DATE = 2013/07/03
TIME = 15:28
INSTRUM = spect
PULPROG = zgpg30
F1 (13C)
SI = 32768
SF = 100.613
SW_p = 22058.824
anti-16
g + l
i
j e
b
k
c
f
h
d
[ppm]
[rel]

# APPENDIX D

# EXPERIMENTAL FOR CHAPTER IV

## A. Preparation of Compounds 17

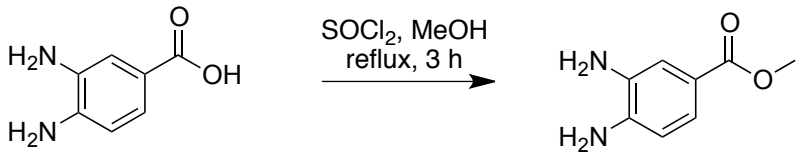


**17**

4.0 g, 98 %

**Methyl 3,4-diaminobenzoate (17).**

To a solution of 3,4-diaminobenzoic acid (3.6 g, 24 mmol) in dry MeOH (60 mL) was added $SO_2Cl$ (2.8 mL, 38 mmol) in 10 minutes at 23 °C. The solution was then refluxed for 3 h. Half of the solvent was removed under reduced pressure, and ethyl acetate (100 mL) was added. The resulting solution was washed with saturated aqueous $NaHCO_3$. The aqueous layers were extracted with ethyl acetate (2 × 50 mL). The combined organic layers were dried and evaporated to dryness, yielding a brown solid (4.0 g, 23 mmol, 98%) which was used for the next reaction without further purification. $^1$H NMR (400 MHz, $CDCl_3$) δ 7.49 (1H, dd, $J$ = 8.1, 1.9 Hz), 7.43 (1H, d, $J$ = 1.9 Hz), 6.69 (1H, d, $J$ = 8.1 Hz), 3.87 (3H, s), 3.82 (2H, br), 3.36 (2H, br); $^{13}$C NMR (100 MHz, $CDCl_3$) δ 167.3, 140.4, 133.1, 123.3, 121.2, 118.4, 114.9, 51.6.

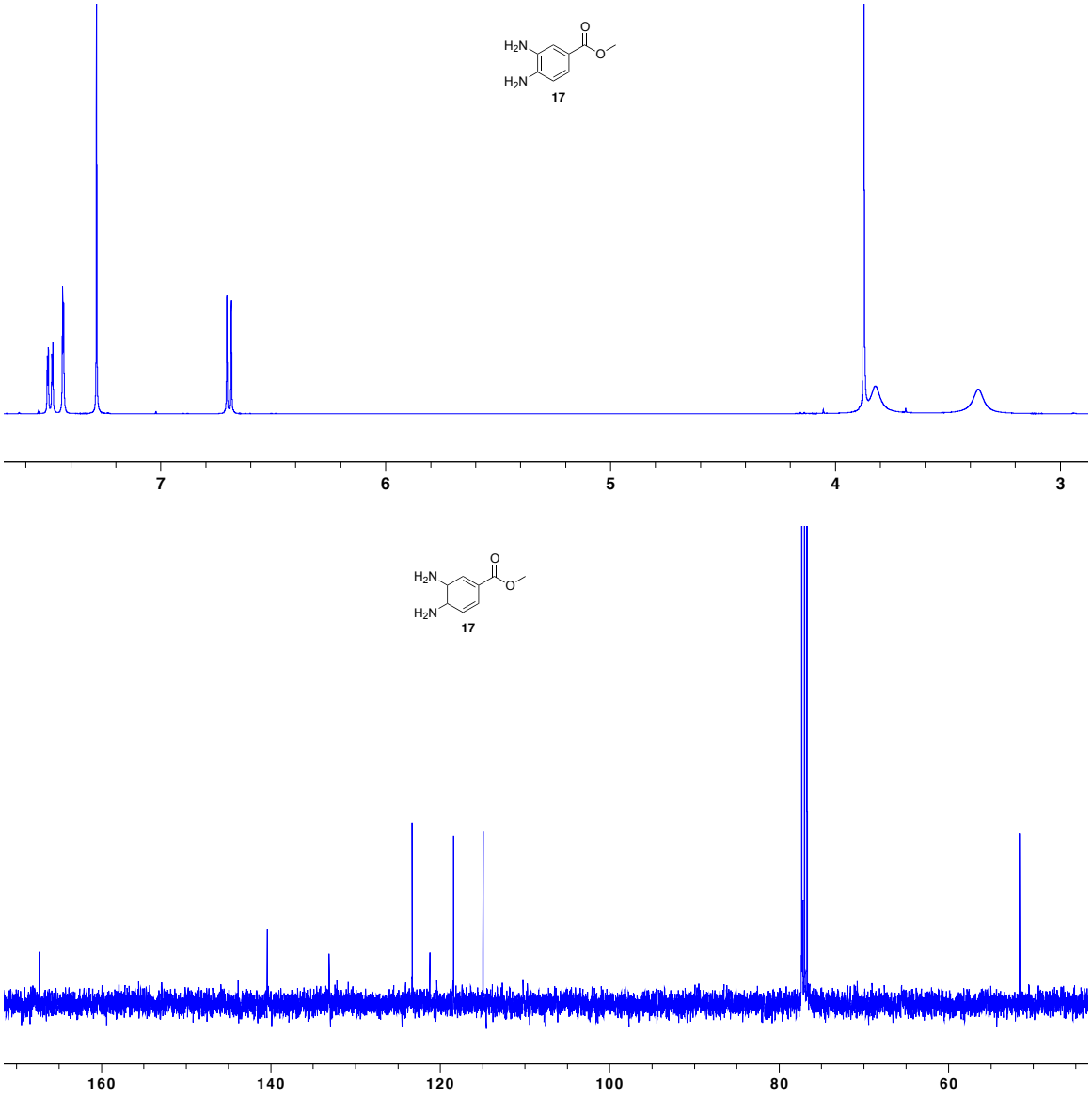


**B. Typical Procedure for Amide Coupling On The Linker**

Boc-protected amino acid (1.1 equiv), **17** (2.22 g, 13.3 mmol, 1 equiv), and HOBt (2.44 g, 16.0 mmol) were dissolved in anhydrous $CH_2Cl_2$ under Ar. The mixture was stirred for 2 min and then cooled to 0 ºC. Triethylamine (4.64 mL, 33.2 mmol) and EDCI (3.06 g, 16.0 mmol) were added to the solution at 0 ºC. The solution was then stirred at the room temperature for 12 h. Pure product precipitated out as white solid

without purification. A small amount of diethyl ether was added to the reaction mixture to allow more product precipitation.

**(*S*)-methyl 4-amino-3-(2-((tert-butoxycarbonyl)amino)propanamido)benzoate (18).**

**18** was isolated as white solid (2.7 g, 8.0 mmol, 60% yield). $^1$H NMR (400 MHz, MeOD) δ 7.76-7.64 (2H, m), 6.79 (1H, d, *J* = 8.4 Hz), 4.17 (1H, q, *J* = 7.0 Hz), 3.84 (3H, s), 1.48 (9H, s), 1.45 (3H, d, *J* = 7.2 Hz).

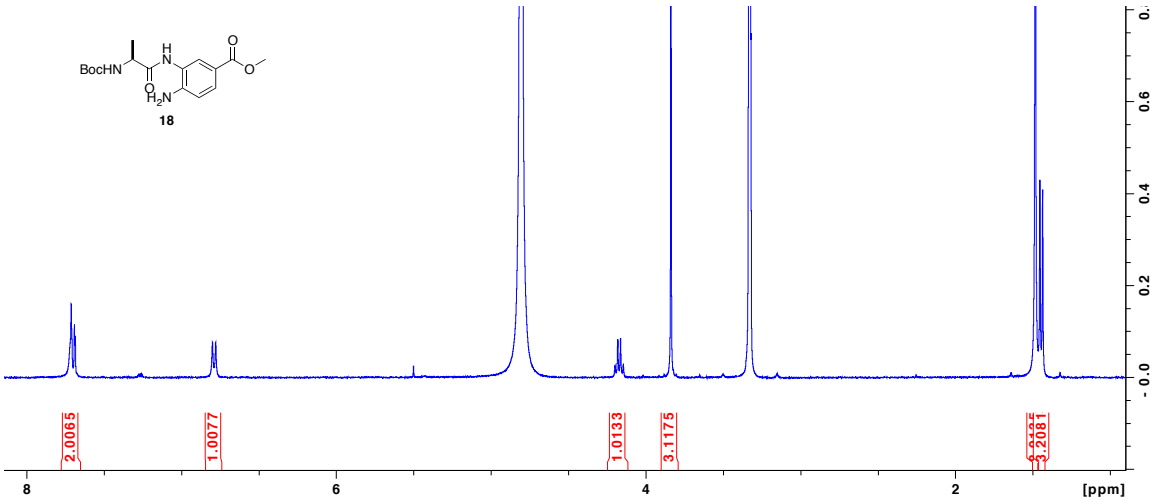


**(*S*)-methyl 4-amino-3-(2-((tert-butoxycarbonyl)amino)-3-methylbutanamido)benzoate (32).**

**32** was isolated as white solid (3.0 g, 8.2 mmol, 62% yield). $^1$H NMR (400 MHz, $CDCl_3$) δ 7.82 (1H, s), 7.77 (2H, dd, *J* = 8.5, 1.8 Hz), 6.73 (1H, d, *J* = 8.4 Hz), 3.99 (1H, t, *J* = 7.2 Hz), 3.87 (3H, s), 2.28 (1H, dq, *J* = 13.7, 6.8 Hz), 1.09 (6H, dd, *J* = 16.4, 6.8 Hz).

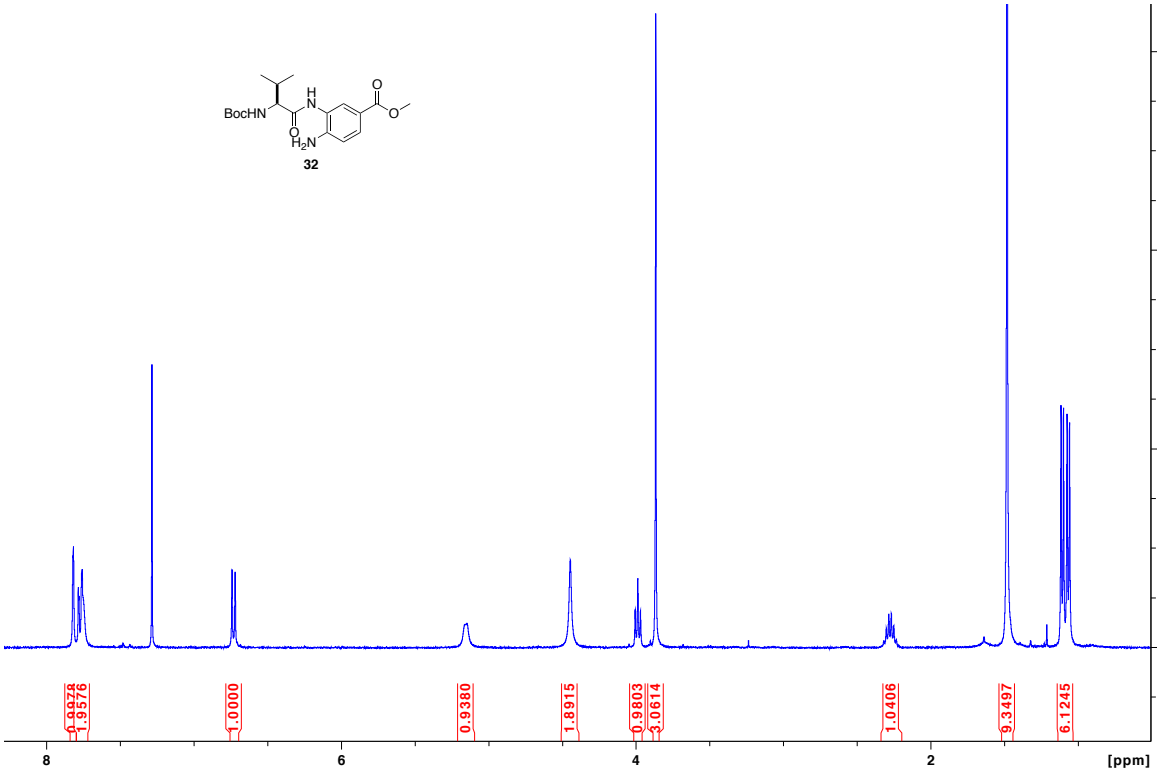


**C. Typical Procedure for Amide Coupling On Amine Intermediates.**

Boc-protected amino acid (6.60 mmol, 1.1 equiv), hydrochloride salt of amine intermediate (6.00 mmol, 1 equiv), and HOBt (1.10 g, 7.20 mmol) were dissolved in anhydrous $CH_2Cl_2$ under Ar. The mixture was stirred for 2 min and then cooled to 0 ºC. Triethylamine (4.19 mL, 30.0 mmol) and EDCI (1.38 g, 7.20 mmol) were added to the solution at 0 ºC. The solution was then stirred at the room temperature for 12 h. Pure product then precipitated out as white solid without purification. A small amount of diethyl ether was added to the reaction mixture to allow more product precipitation. If no precipitation occurred, wash the organic mixture with 0.2M $KHSO_4$ aqueous solution followed by sat. $NaHCO_3$ solution. The organic layer was dried by sat. NaCl solution and $MgSO_4$. Half of dichloromethane was removed under vacuum and diethyl ether was added to allow product precipitation.

**Methyl 4-amino-3-((*S*)-2-((*S*)-2-((tert-butoxycarbonyl)amino)propanamido) propanemido)benzoate (19).**

**19** was isolated as white solid (2.0 g, 4.9 mmol, 80% yield). $^{1}$H NMR (400 MHz, MeOD) δ 7.73 (1H, s), 7.69 (1H, dd, *J* = 8.5, 2.0 Hz), 6.79 (1H, d, *J* = 8.5 Hz), 4.45 (1H, q, *J* = 7.1 Hz), 4.09 (1H, q, *J* = 7.2 Hz), 3.84 (3H, s), 1.51 (3H, d, *J* = 7.2 Hz), 1.43 (9H, s), 1.35 (3H, d, *J* = 7.2 Hz).

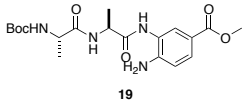


19

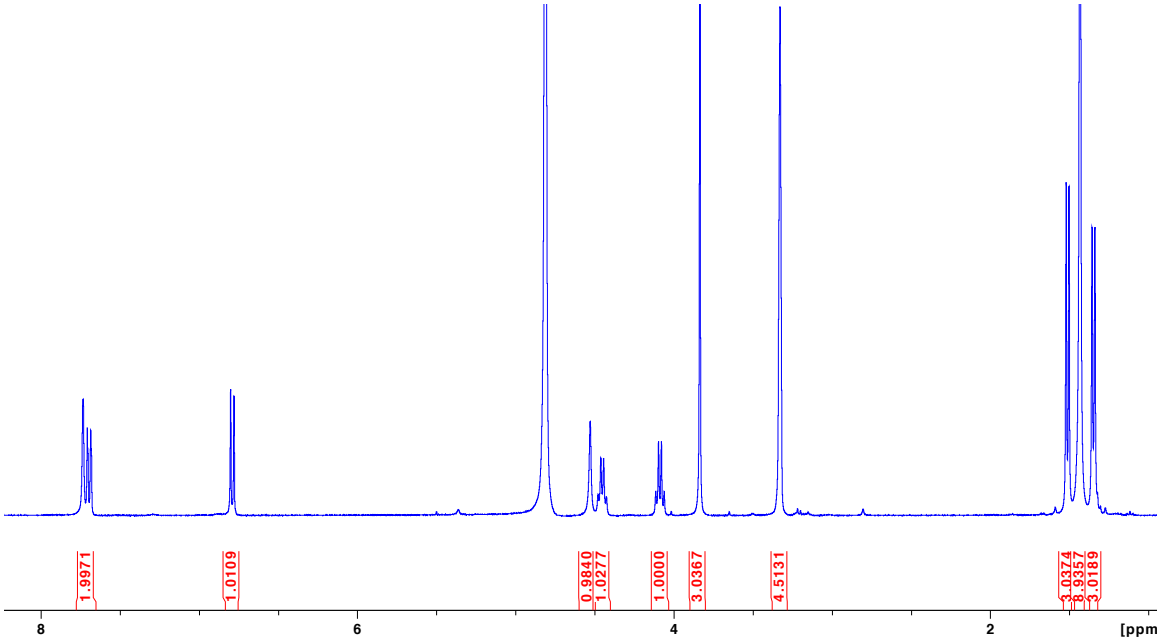

**Methyl 4-amino-3-((6*S*,9*S*,12*S*)-6-benzyl-2,2,9,12-tetramethyl-4,7,10-trioxo-3-oxa-5,8,11-triazatridecanamido)benzoate (20).**

**20** was isolated as off-white solid (1.2 g, 2.2 mmol, 85% yield). $^{1}$H NMR (400 MHz, MeOD) δ 7.76 (1H, d, *J* = 2.0 Hz), 7.70 (1H, dd, *J* = 8.5, 2.0 Hz), 7.32-7.19 (6H, m), 6.80 (1H, d, *J* = 8.5 Hz), 4.43 (1H, q, *J* = 7.2 Hz), 4.38-4.28 (2H, m), 3.83 (3H, s), 2.85 (1H, dd, *J* = 13.7, 9.8 Hz), 2.70-2.60 (1H, m), 1.51 (3H, d, *J* = 7.2 Hz), 1.39 (12H, m).

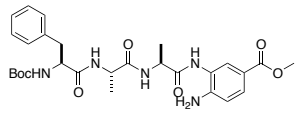


20

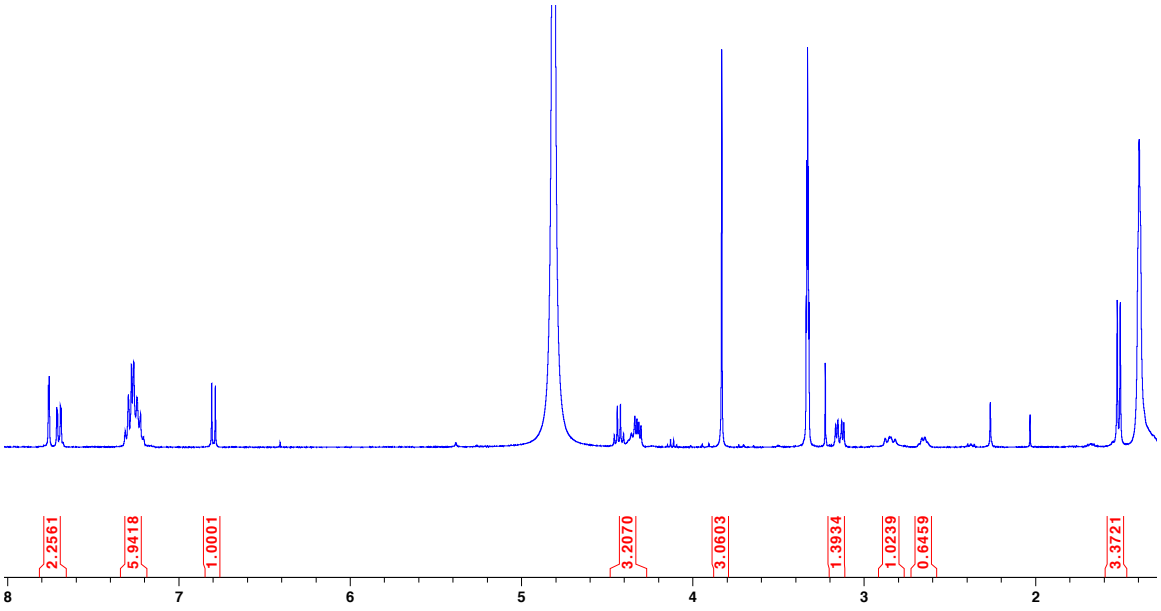

**Methyl 4-amino-3-((6*S*,9*S*,12*S*,15*S*)-9-benzyl-6-(tert-butoxymethyl)-2,2,12,15-tetramethyl-4,7,10,13-tetraoxo-3-oxa-5,8,11,14-tetraazahexadecanamido)benzoate (21).**

**21** was isolated as a foamy solid (0.90 g, 1.3 mmol, 79% yield). $^1$H NMR (400 MHz, $CDCl_3$) δ 8.17 (1H, s), 7.96 (1H, d, *J* = 1.9 Hz), 7.76 (1H, dd, *J* = 8.4, 2.0 Hz), 7.44-7.29 (6H, m), 7.20-7.14 (2H, m), 6.71 (1H, d, *J* = 8.4 Hz), 6.56 (1H, s), 5.34 (1H, d, *J* = 2.8 Hz), 4.60-4.47 (4H, m), 4.43-4.33 (1H, m), 3.95 (1H, q, *J* = 4.1 Hz), 3.85 (3H, s), 3.56 (2H, d, *J* = 4.3 Hz), 3.19 (1H, dd, *J* = 14.4, 4.8 Hz), 3.06 (1H, dd, *J* = 14.4, 7.7 Hz), 1.59 (3H, d, *J* = 7.3 Hz), 1.45 (3H, d, *J* = 7.4 Hz), 1.40 (9H, s), 1.10 (9H, s).

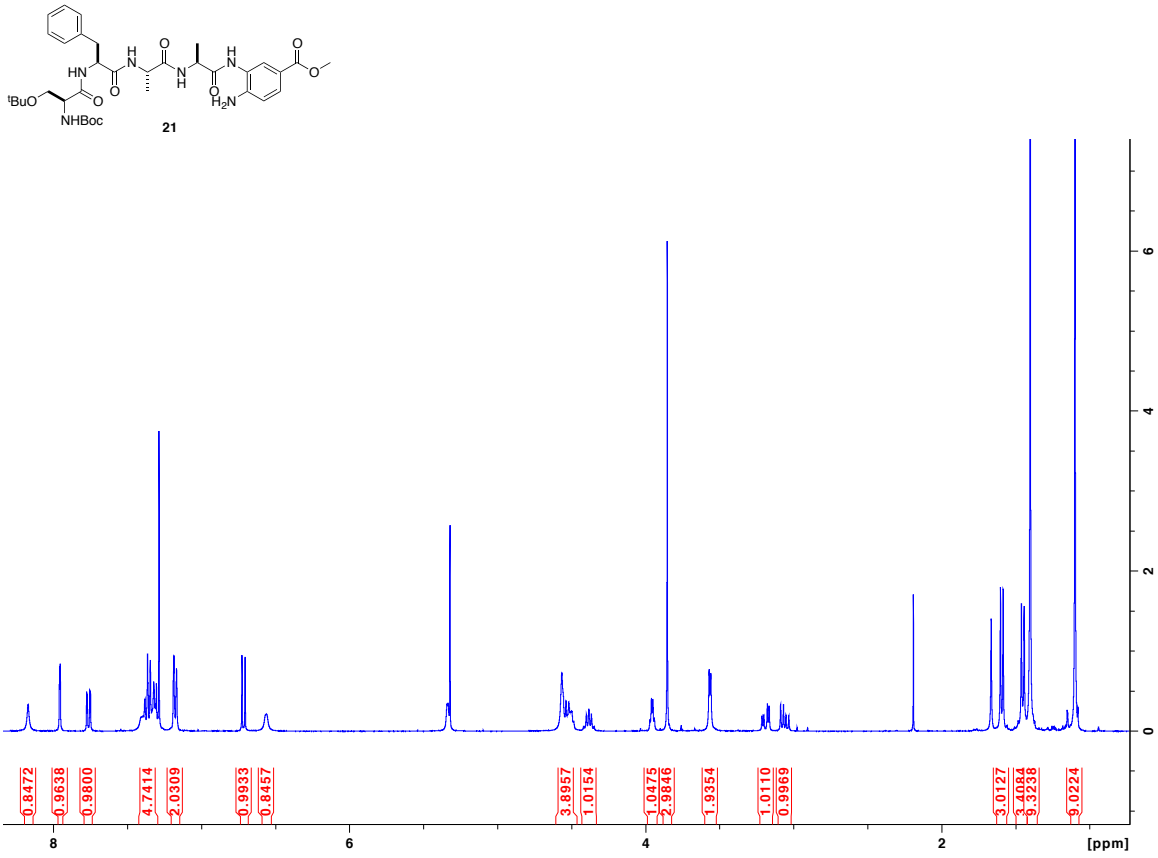

**Methyl 4-amino-3-((*R*)-2-((*S*)-3-(4-(benzyloxy)phenyl)-2-((tert-butoxycarbonyl) amino)propanamido)propanamido)benzoate (33).**

**33** was isolated as white solid (2.1 g, 4.6 mmol, 82% yield). $^{1}$H NMR (400 MHz, $CDCl_3$) δ 8.48 (1H, s), 7.86 (1H, d, *J* = 1.2 Hz), 7.71 (1H, dd, *J* = 8.4, 1.8 Hz), 7.48-7.29 (6H, m), 7.08 (2H, d, *J* = 8.5 Hz), 6.88 (3H, d, *J* = 8.5 Hz), 6.66 (1H, t, *J* = 9.3 Hz), 5.00 (2H, s), 4.60-4.47 (1H, m), 4.26 (1H, dd, *J* = 13.7, 6.7 Hz), 3.81 (3H, s), 2.98 (2H, qd, *J* = 13.8, 7.2 Hz), 1.33 (12H, m).

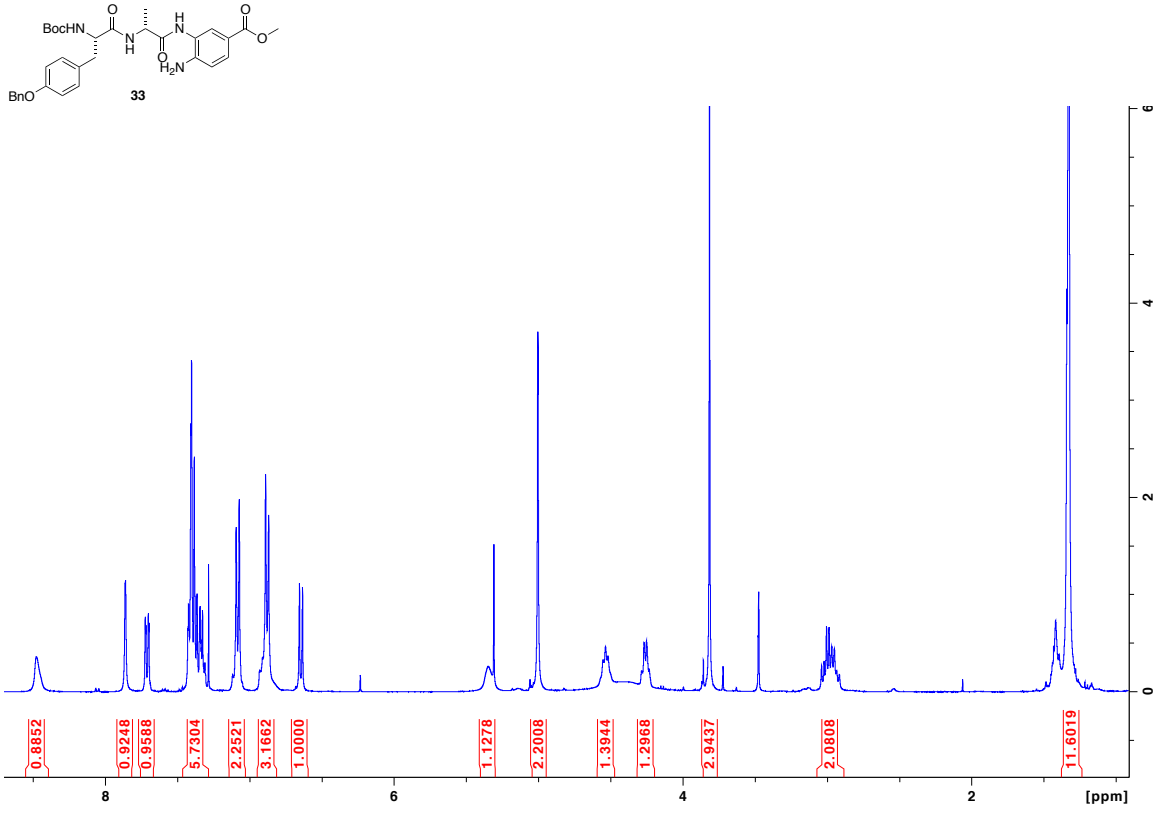

**Methyl 4-amino-3-((6*S*,9*R*,12*S*,15*R*)-9-benzyl-12-(4-(benzyloxy)benzyl)-6-(tert-butoxymethyl)-2,2,15-trimethyl-4,7,10,13-tetraoxo-3-oxa-5,8,11,14-tetraazahexadecanamido)benzoate (29).**

**29** was isolated as white foamy solid (0.76 g, 0.86 mmol, 78% yield). $^1$H NMR (400 MHz, $CDCl_3$) δ 7.88 (1H, s), 7.67 (1H, d, *J* = 8.4), 7.41-7.12 (11H, m), 6.99 (2H, d, *J* = 7.8 Hz), 6.84 (2H, d, *J* = 8.4 Hz), 6.64 (1H, d, *J* = 8.5 Hz), 4.95 (2H, s), 4.81 (2H, m), 4.60 (1H, m), 4.16 (1H, m), 3.81 (3H, s), 3.23 (2H, m), 3.16-3.03 (1H, m), 3.02-2.82 (3H, m), 1.39 (9H, s), 1.31 (3H, d, *J* = 6.7 Hz), 1.09-0.94 (9H, s).

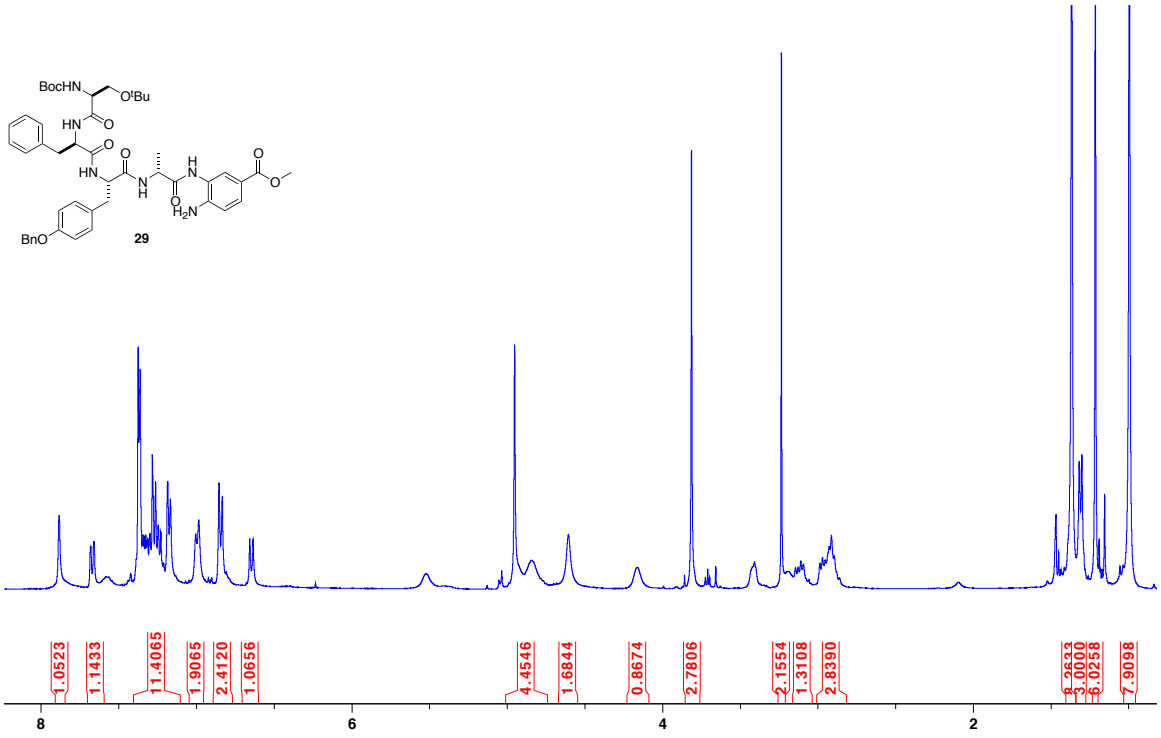

**Methyl 4-amino-3-((*S*)-2-((*S*)-2-((tert-butoxycarbonyl)amino)propanamido)-3-methylbutanamido)benzoate (35).**

**35** was isolated as white solid (2.1 g, 4.8 mmol, 75% yield). $^1$H NMR (400 MHz, $CDCl_3$) δ 8.34 (1H, br), 7.82 (1H, d, *J* = 1.7 Hz), 7.73 (1H, d, *J* = 8.4 Hz), 7.01 (1H, br), 6.67 (1H, d, *J* = 8.4 Hz), 5.20 (1H, br), 4.46 (2H, s), 4.38 (1H, t, *J* = 6.7 Hz), 4.23-4.11 (1H, m), 3.89-3.82 (3H, s), 2.42-2.29 (1H, m), 1.44-1.31 (12H, m), 1.07 (6H, dd, *J* = 16.8, 6.8 Hz).

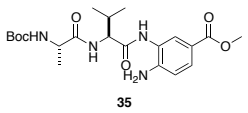


35

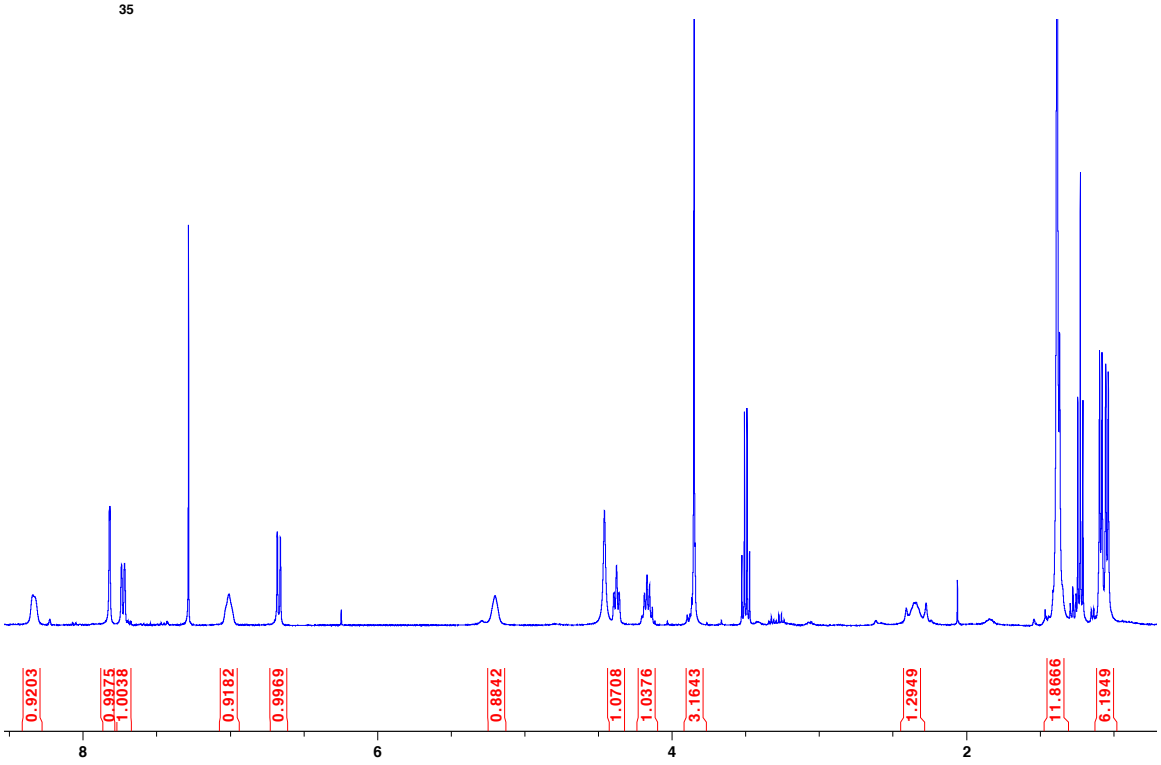

**Methyl 4-amino-3-((6*S*,9*S*,12*S*)-6-(4-(benzyloxy)benzyl)-12-isopropyl-2,2,9-trimethyl -4,7,10-trioxo-3-oxa-5,8,11-triazatridecanamido)benzoate (36).**

**36** was isolated as white foamy product (1.5 g, 2.1 mmol, 82% yield). $^{1}$H NMR (400 MHz, MeOD) δ 7.81-7.64 (2H, m), 7.36 (5H, m), 7.12 (2H, d, *J* = 7.9 Hz), 6.92 (2H, d, *J* = 8.2 Hz), 6.79 (1H, d, *J* = 8.6 Hz), 5.04 (2H, s), 4.34 (1H, d, *J* = 6.8 Hz), 4.27-4.11 (2H, m), 3.82 (3H, s), 2.92 (2H, m), 2.29 (1H, m), 1.39 (9H, s), 1.19 (3H, d, *J* = 6.1 Hz), 1.09 (6H, t, *J* = 6.5 Hz).

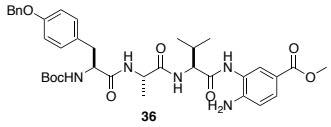

36

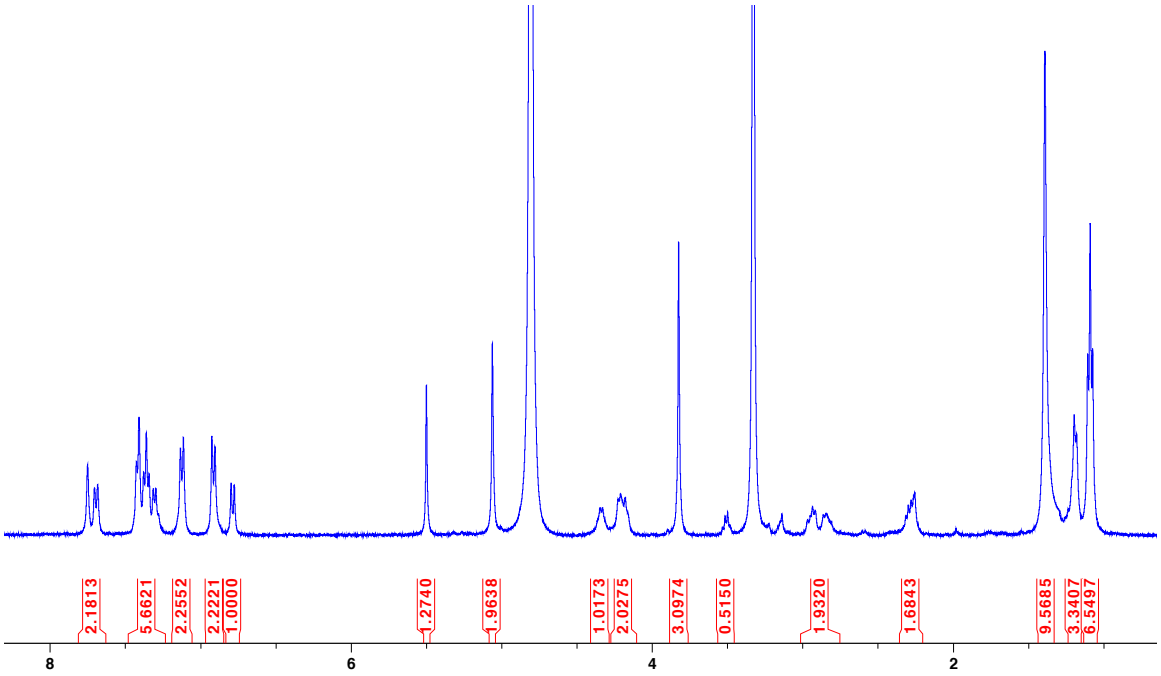

**Methyl 4-amino-3-((6*S*,9*S*,12*S*,15*S*)-9-(4-(benzyloxy)benzyl)-6-(tert-butoxymethyl)-15-isopropyl-2,2,12-trimethyl-4,7,10,13-tetraoxo-3-oxa-5,8,11,14-tetraazahexadecanamido)benzoate (30).**

**30** was isolated as white foamy solid (1.1 g, 1.3 mmol, 76% yield). $^1$H NMR (400 MHz, $CDCl_3$) δ 9.11 (1H, s), 7.90 (1H, s), 7.82 (1H, s), 7.60 (2H, m), 7.35 (5H, m), 7.09 (2H, d, *J* = 8.2 Hz), 6.87 (2H, d, *J* = 8.2 Hz), 6.58 (1H, d, *J* = 8.4 Hz), 5.41 (1H, s), 4.99 (3H, m), 4.61 (4H, m), 4.17 (1H, s), 3.79 (3H, s), 3.50 (1H, dd, *J* = 13.6, 6.8 Hz), 3.14 (1H, d, *J* = 38.3 Hz), 3.02 (2H, d, *J* = 5.3 Hz), 2.20 (1H, d, *J* = 5.7 Hz), 1.36 (9H, s), 1.23 (3H, d, *J* = 4.0 Hz), 1.10 (6H, dd, *J* = 19.1, 6.6 Hz), 1.00 (9H, s).

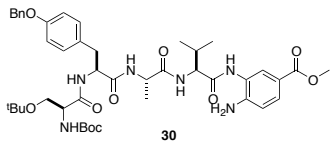

30

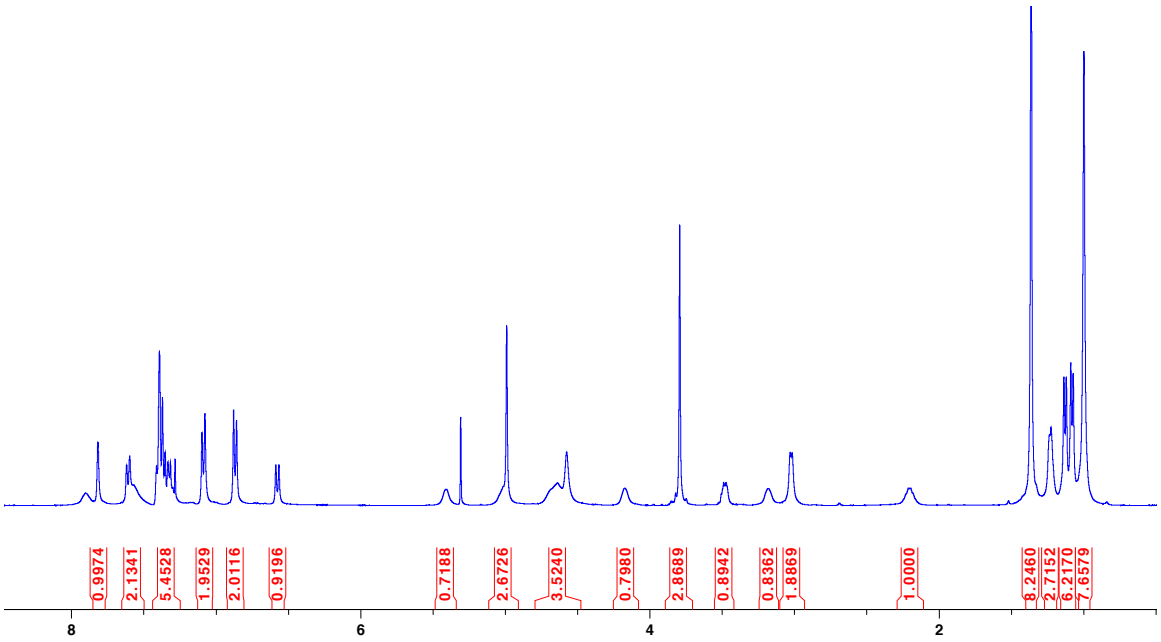

**Methyl 4-amino-3-((*R*)-2-((*S*)-2-((tert-butoxycarbonyl)amino)-3-phenylpropanamido)propanamido)benzoate (37).**

**37** was isolated as off-white foamy solid (1.7 g, 3.5 mmol, 85% yield). , $^{1}$H NMR (400 MHz, $CDCl_3$) δ 8.36 (1H, s), 7.85 (1H, s), 7.73 (1H, dd, *J* = 8.4, 1.8 Hz), 7.36-7.22 (5H, m), 7.19 (2H, d, *J* = 6.7 Hz), 6.68 (1H, d, *J* = 7.4 Hz), 6.57 (1H, s), 5.23 (1H, d, *J* = 5.9 Hz), 4.57-4.38 (3H, m), 4.26 (1H, q, *J* = 7.1 Hz), 3.84 (3H, s), 3.14-2.98 (2H, m), 1.33 (12H, m).

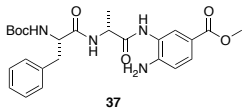


37

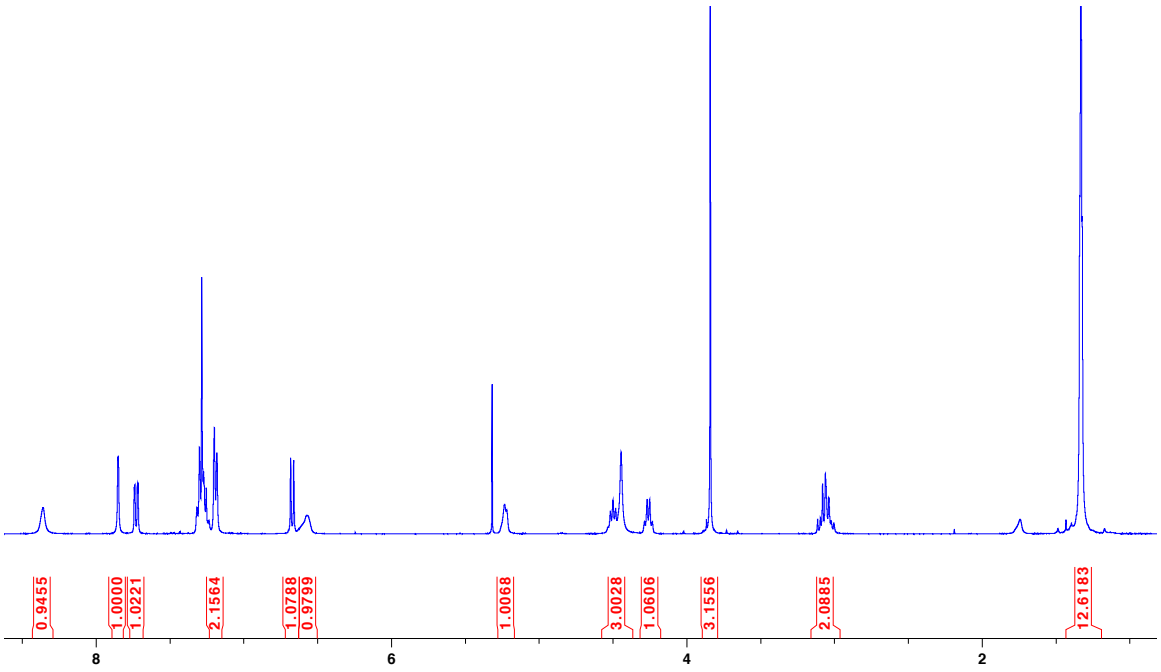

**Methyl 4-amino-3-((6*R*,9*S*,12*R*)-9-(4-(benzyloxy)benzyl)-6-isopropyl-2,2,12-trimethyl-4,7,10-trioxo-3-oxa-5,8,11-triazatridecanamido)benzoate (38).**

**38** was isolated as white solid (0.90 g, 1.5 mmol, 78% yield). $^{1}$H NMR (400 MHz, MeOD) δ 7.75 (1H, d, *J* = 2.0 Hz), 7.69 (1H, dd, *J* = 8.5, 2.0 Hz), 7.35-7.20 (5H, m), 6.79 (1H, d, *J* = 8.5 Hz), 4.48 (1H, t, *J* = 7.8 Hz), 4.31 (1H, q, *J* = 7.2 Hz), 3.88-3.81 (4H, m), 3.15-3.01 (2H, m), 1.95 (1H, dd, *J* = 12.9, 7.1 Hz), 1.43 (9H, s), 1.27 (3H, d, *J* = 7.3 Hz), 0.88 (6H, dd, *J* = 18.3, 6.7 Hz).

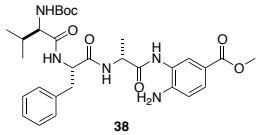

38

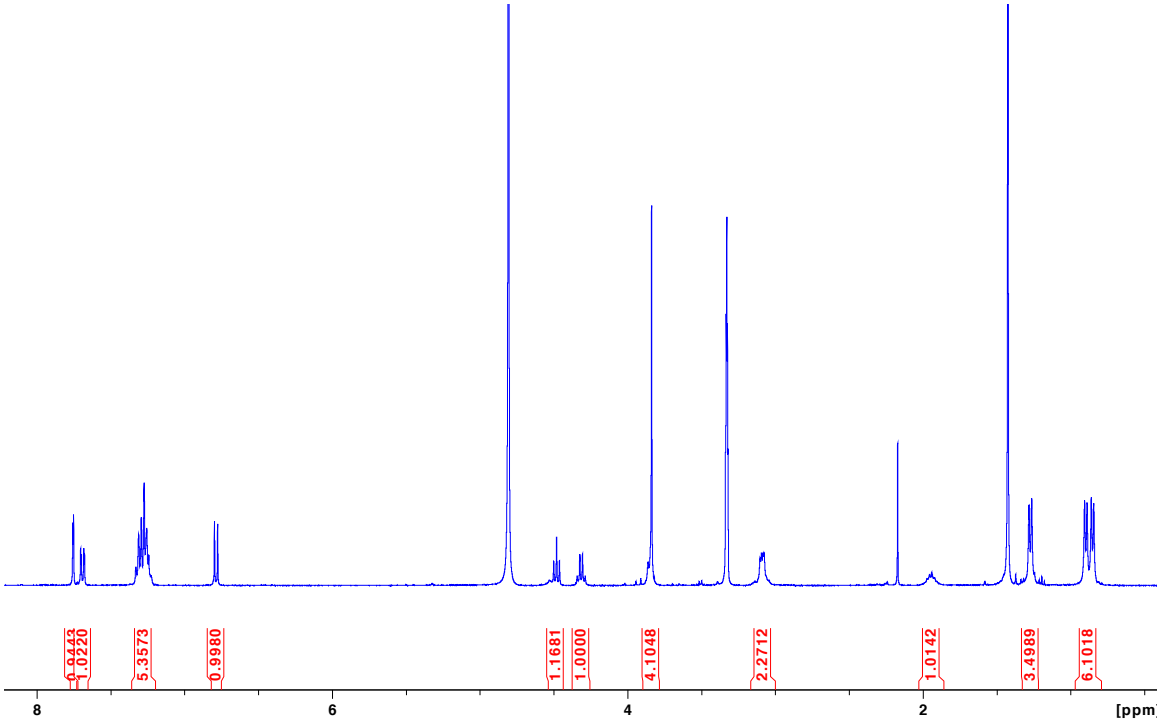

**Methyl 4-amino-3-((6*S*,9*R*,12*S*,15*R*)-12-benzyl-6-(tert-butoxymethyl)-9-isopropyl-2,2,15-trimethyl-4,7,10,13-tetraoxo-3-oxa-5,8,11,14-tetraazahexadecanamido) benzoate (31).**

**31** was isolated as white solid (0.42 g, 0.58 mmol, 77 % yield). $^{1}$H NMR (400 MHz, DMSO) δ 9.27 (1H, s), 8.38 (1H, t, *J* = 17.3 Hz), 8.24 (1H, t, *J* = 18.4 Hz), 7.54 (1H, d, *J* = 8.5 Hz), 7.31-7.09 (5H, m), 6.75 (1H, d, *J* = 8.5 Hz), 6.49 (1H, d, *J* = 8.1 Hz), 5.78 (1H, m), 4.54 (1H, s), 4.41 (1H, m), 4.16-4.00 (3H, m), 3.75 (3H, s), 2.87 (2H, ddd, *J* = 32.9, 19.8, 9.2 Hz), 1.70 (1H, m), 1.37 (9H, s), 1.30 (3H, d, *J* = 7.0 Hz), 1.08 (9H, s), 0.59 (6H, dd, *J* = 21.0, 6.7 Hz).

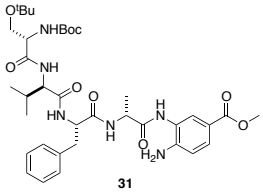


31

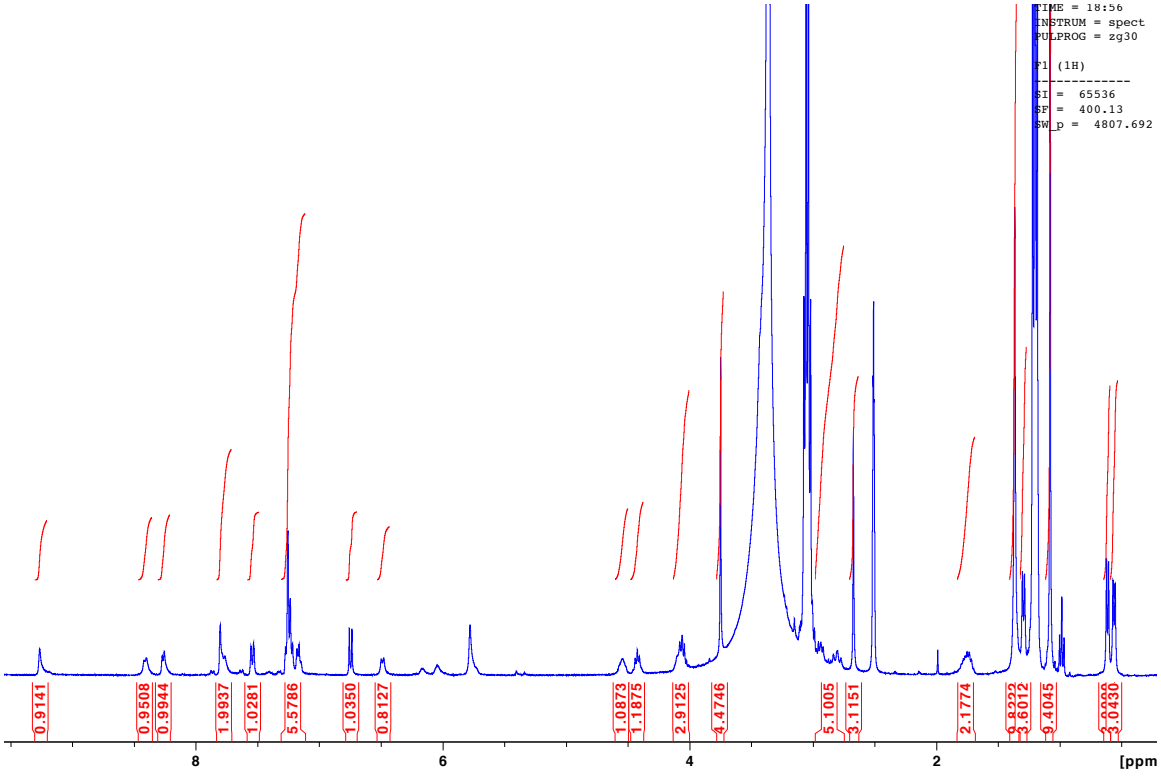

**Methyl 4-amino-3-((*R*)-2-((2*S*,3*S*)-2-((tert-butoxycarbonyl)amino)-3-methylpentanamido)propanamido)benzoate (39).**

**39** was isolated as white foamy solid (1.8 g, 3.9 mmol, 86% yield). $^{1}$H NMR (400 MHz, $CDCl_3$) δ 8.76 (1H, s), 7.78 (1H, m), 7.64-7.53 (2H, m), 6.57 (1H, d, *J* = 8.5 Hz), 5.61 (1H, d, *J* = 6.7 Hz), 4.71-4.60 (1H, m), 4.58 (2H, br), 3.93 (1H, dd, *J* = 14.9, 7.3 Hz), 3.77 (3H, s), 1.76 (1H, d, *J* = 6.1 Hz), 1.53-1.23 (13H, m), 1.12-0.97 (1H, m), 0.92-0.71 (7H, m); $^{13}$C NMR (101 MHz, $CDCl_3$) δ 173.1, 171.9, 166.9, 156.2, 146.7, 129.4, 128.7, 121.3, 118.9, 115.3, 80.1, 77.44 77.1, 76.8, 59.7, 51.5, 49.6, 36.9, 30.82, 28.2, 28.2, 24.9, 17.7, 15.5, 15.4, 11.1, 11.0.

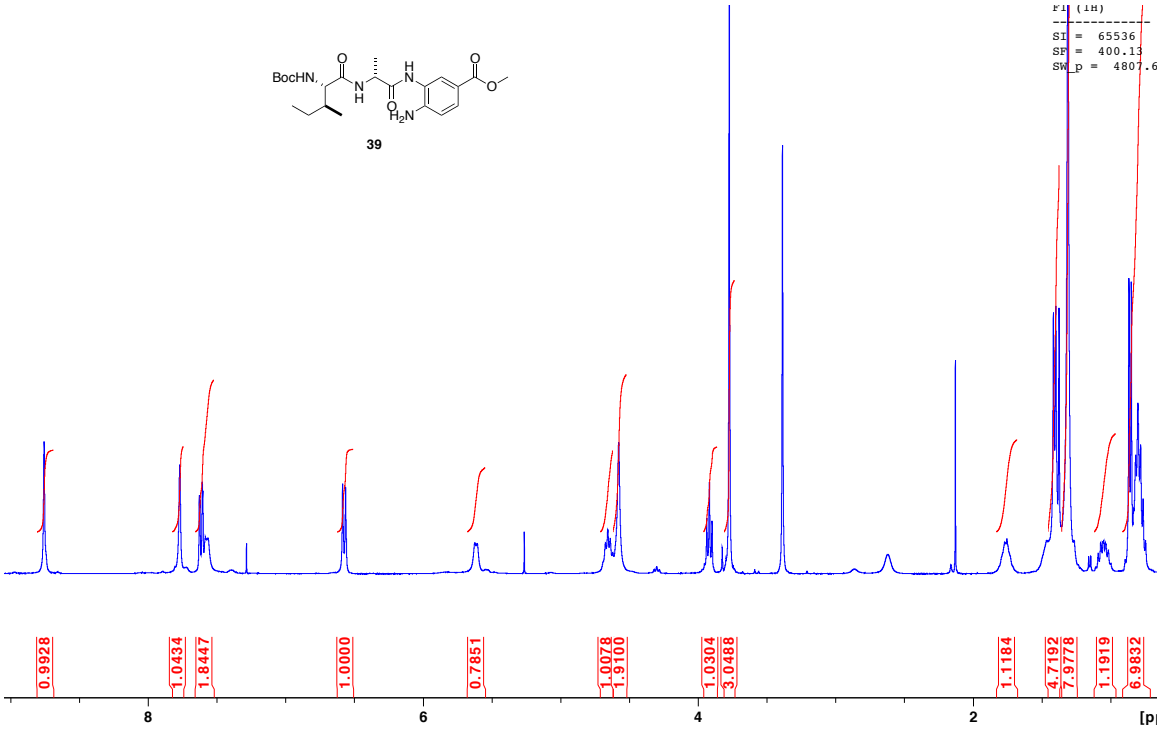

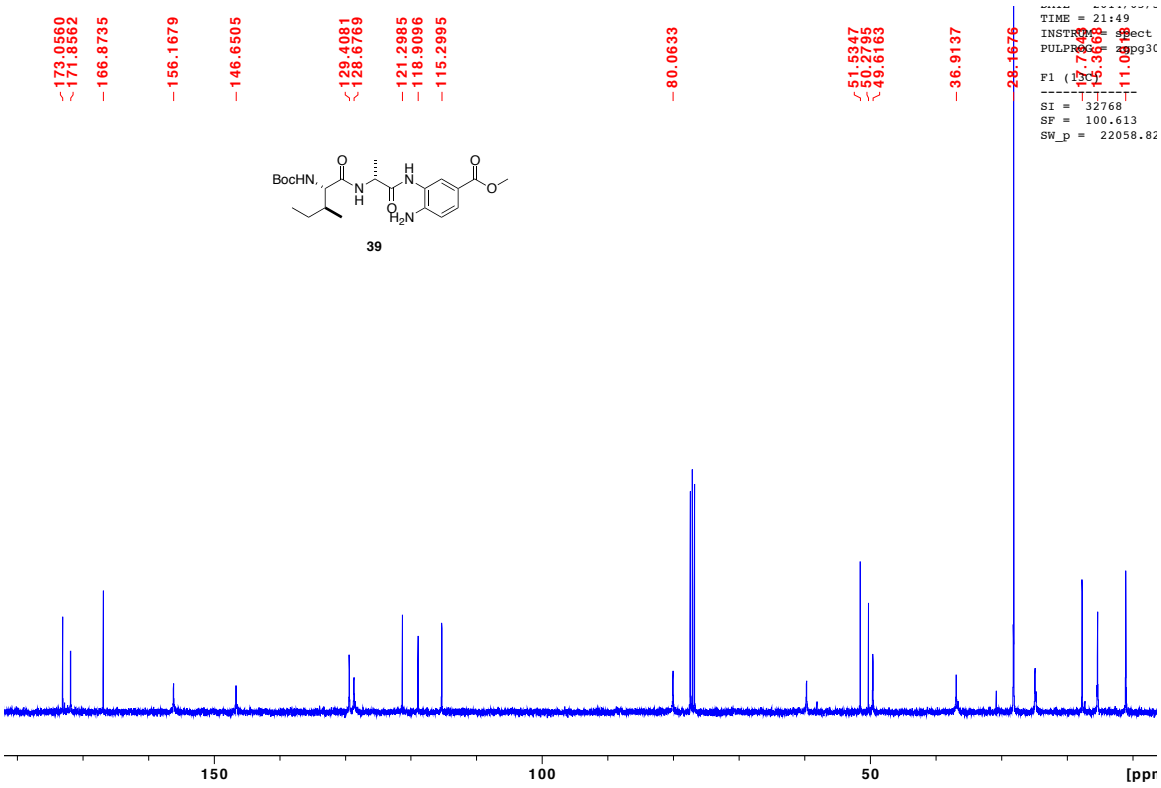
173.0560
171.8562
166.8735
156.1679
146.6505
129.4081
128.6769
121.2985
118.9096
115.2995
80.0633
51.5347
50.2795
49.6163
36.9137
28.1676
TIME = 21:49
INSTRUM = spect
PULPROG = zgpg30
F1 (13C)
SI = 32768
SF = 100.613
SW_p = 22058.82
BocHN
O
N
H
H
N
O
O
O
H2N
39
150
100
50
[ppm

**D. Typical Procedure for Boc Deprotection**

To a solution of Boc-protected intermediate in methanol (50 equiv) was added acetyl chloride (10 equiv) in 5 min at 0 ºC. The mixture was stirred at 23 ºC for 15 min. Solvent was removed under vacuum and the crude product was stirred in diethyl ether until white solid precipitated. The product was filtered and used for the next step without further purification.

**Methyl 4-amino-3-((*S*)-2-((*S*)-2-((*S*)-2-amino-3-phenylpropanamido)propanamido) propanamido)benzoate (42).** $^1$H NMR (400 MHz, DMSO) δ 9.51 (1H, s), 8.85 (1H, d, *J* = 7.4 Hz), 8.34 (2H, br), 7.86 (1H, d, *J* = 1.9 Hz), 7.37-7.21 (5H, m), 6.80 (1H, d, *J* = 8.5 Hz), 4.43 (2H, dp, *J* = 21.3, 6.9 Hz), 4.14-4.04 (1H, m), 3.75 (3H, s), 3.22-3.12 (1H, m), 3.08-2.97 (1H, m), 1.37 (3H, d, *J* = 7.1 Hz), 1.28 (3H, d, *J* = 7.0 Hz).

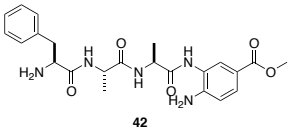


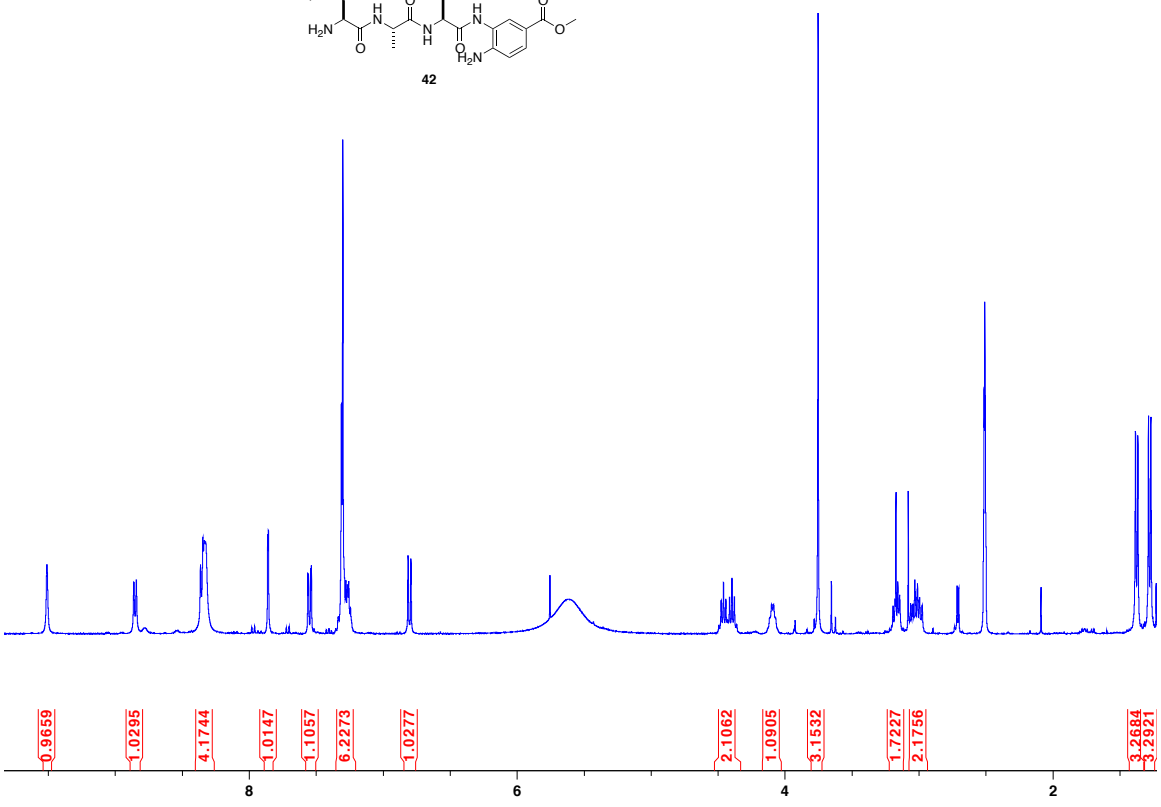

**(*S*)-methyl 4-amino-3-(2-amino-3-methylbutanamido)benzoate (43).** $^{1}$H NMR (400 MHz, MeOD) δ 8.02 (1H, s), 7.96 (1H, d, *J* = 8.4), 7.36 (1H, t, *J* = 7.0 Hz), 4.05 (1H, d, *J* = 5.7 Hz), 3.92 (3H, s), 2.42 (1H, dp, *J* = 13.4, 6.7 Hz), 1.19 (6H, dd, *J* = 17.8, 6.9 Hz).

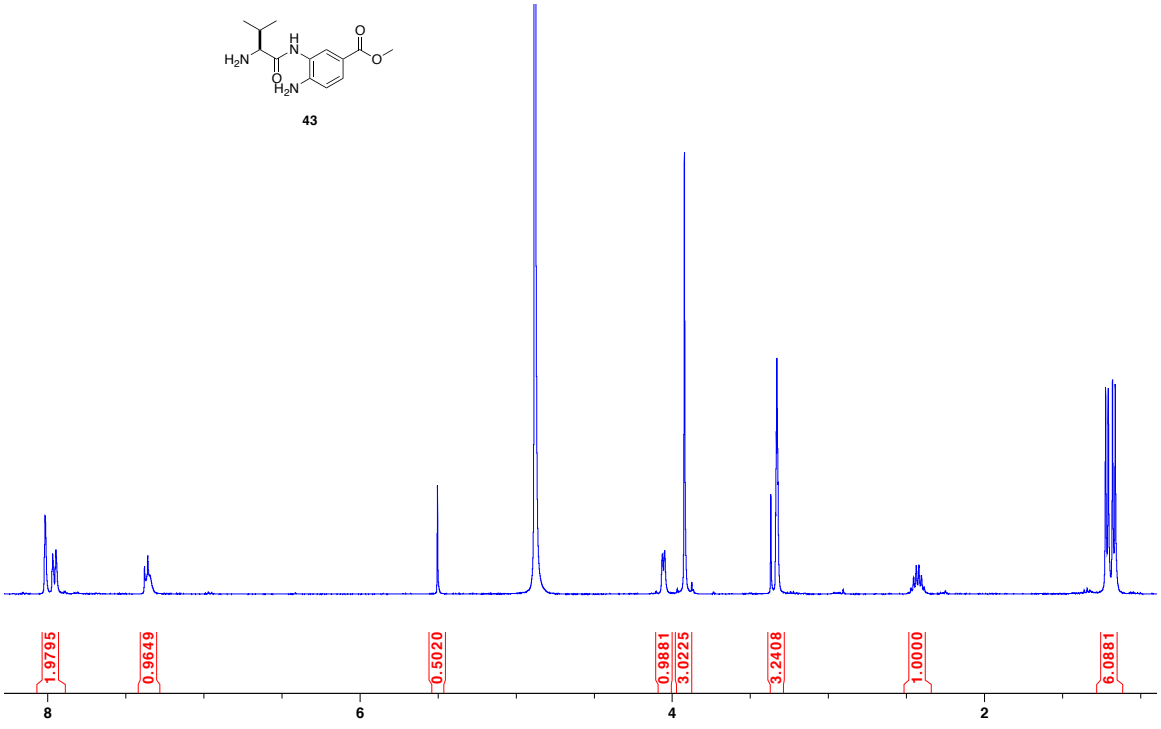

**Methyl 4-amino-3-((*S*)-2-((*S*)-2-((*S*)-2-amino-3-(4-(benzyloxy)phenyl)propanamido) propanamido)-3-methylbutanamido)benzoate (44).** $^{1}$H NMR (400 MHz, MeOD) δ 7.92 (1H, d, *J* = 1.9 Hz), 7.88 (1H, dd, *J* = 8.4, 1.9 Hz), 7.47-7.27 (5H, m), 7.25-7.16 (3H, m), 7.00 (2H, d, *J* = 8.6 Hz), 5.11 (2H, s), 4.44-4.30 (2H, m), 4.07 (1H, t, *J* = 7.5 Hz), 3.91 (3H, s), 2.32 (1H, dq, *J* = 13.6, 6.8 Hz), 1.26 (3H, d, *J* = 7.1 Hz), 1.10 (6H, dd, *J* = 6.8, 3.7 Hz).

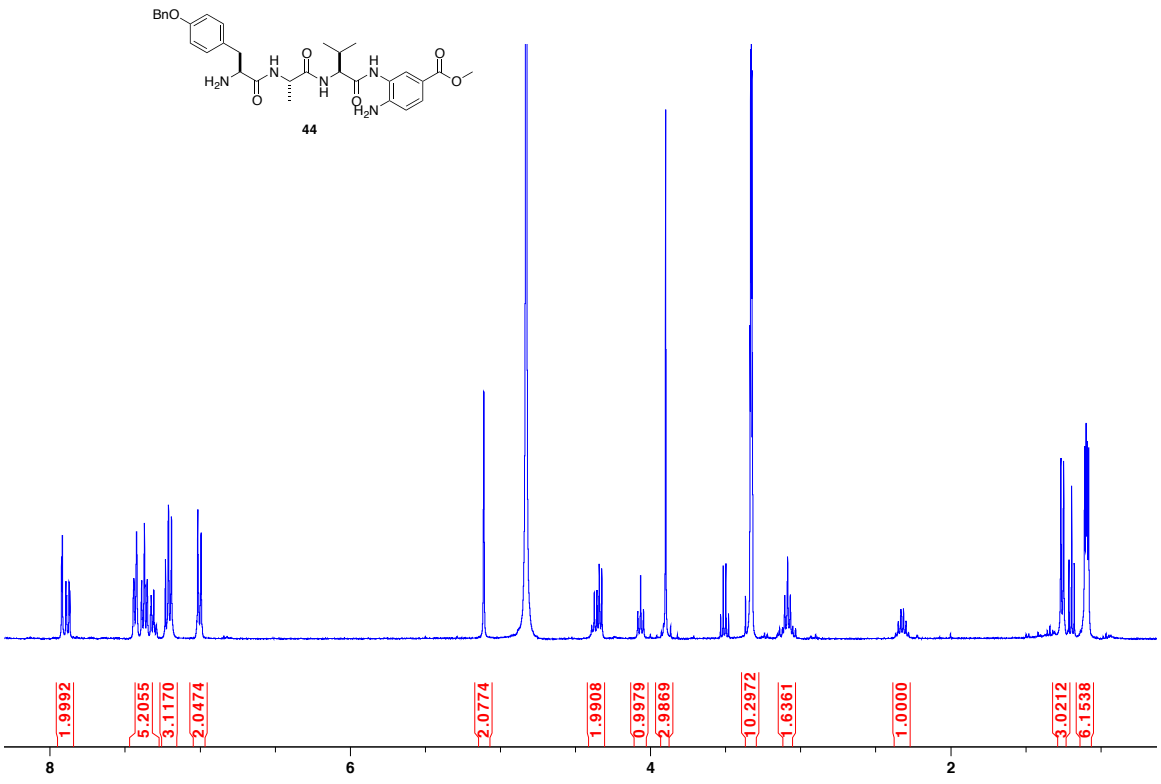

**E. Typical Procedure For Linear Tetrapeptidyl Acetal Preparation**

To a solution of linear tetrapeptide intermediate (0.60 mmol, 1.0 equiv) in 12 mL dichloromethane and 36 mL THF was added *p*-nitrochloroformate (160 mg, 1.3 equiv) and sodium bicarbonate (100 mg, 2 equiv) at room temperature. The solution was stirred for 1 h and then DIPEA (0.2 mL, 1.5 equiv) was added. The solution was stirred for another 20 minutes. Then 2-(dimethoxymethyl)phenol (1.2 mmol, 2.0 equiv) and sodium carbonate (6 mmol, 10 equiv) were added to the mixture, which was allowed to stirred for 16 h. The reaction mixture was filtered on celite and the solvent was removed under vacuo. Purification by column chromatography afforded the desired acetal as a foamy solid.

**(6*S*,9*S*,12*S*,15*S*)-2-(dimethoxymethyl)phenyl 9-benzyl-6-(*tert*-butoxymethyl)-2,2,12, 15-tetramethyl-4,7,10,13-tetraoxo-3-oxa-5,8,11,14-tetraazahexadecan-16-oate (50).** **50** was isolated as white foamy solid (0.43 g, 0.61 mmol, 75% yield). $^1$H NMR (400 MHz, $CDCl_3$) δ 8.13-8.06 (1H, m), 7.61 (1H, d, *J* = 7.7), 7.40-7.22 (6H, m), 7.21-7.15 (2H, m), 7.09 (3H, dt, *J* = 8.0, 2.0 Hz), 6.96-6.89 (1H, m), 6.73 (1H, br), 5.50 (1H, s), 5.34 (1H, d, *J* = 4.2 Hz), 4.76 (1H, t, *J* = 7.2 Hz), 4.70-4.56 (2H, m), 4.03 (1H, q, *J* = 4.8 Hz), 3.93 (1H, dd, *J* = 8.3, 5.5 Hz), 3.64 (1H, dd, *J* = 9.3, 4.7 Hz), 3.50 (1H, dd, *J* = 8.9, 5.8 Hz), 3.33-3.20 (7H, m), 3.08 (1H, dd, *J* = 14.1, 5.7 Hz), 1.62 (3H, d, *J* = 7.2 Hz), 1.44-1.33 (12H, m), 1.14 (9H, s).

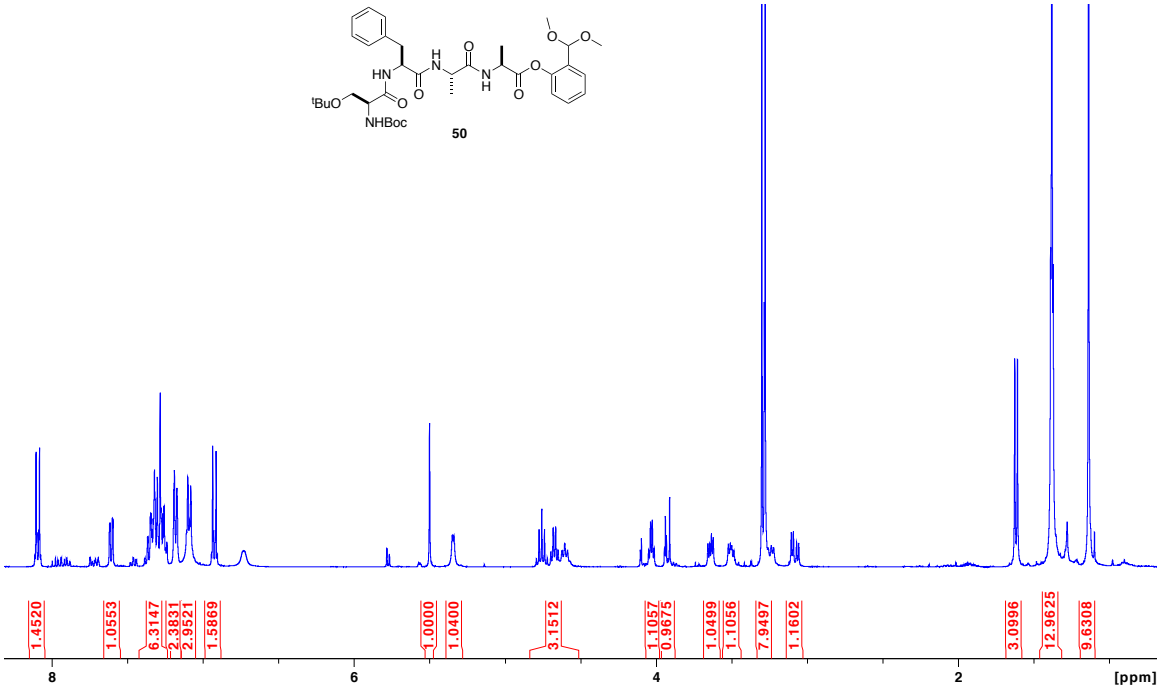


## F. Results Of EKO Analysis On CTPs

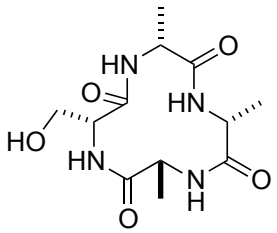


DserDDD

1abj structure of the hirulog 3-thrombin complex and nature of the s' subsites of substrates and inhibitors
1dwb crystallographic analysis at 3.0-angstroms resolution of the binding to human thrombin of four active site-directed inhibitors
1jgy hotosynthetic Reaction Center
1m57 Structure of cytochrome c oxidase from Rhodobacter sphaeroides (EQ(I-286) mutant))
1mkx the co-crystal structure of unliganded bovine alpha-thrombin and prethrombin-2: movement of the yppw segment and active site residues upon ligand binding
1y8q sumo e1 activating enzyme sae1-sae2-mg-atp complex
2agl Crystal structure of the phenylhydrazine adduct of aromatic amine dehydrogenase from Alcaligenes faecalis
2ah0 Crystal structure of the carbinolamine intermediate in the reductive half-reaction of aromatic amine dehydrogenase (AADH) with tryptamine. Monoclinic form
2ah1 Crystal structure of aromatic amine dehydrogenase (AADH) from Alcaligenes faecalis
2cw0 Crystal structure of Thermus thermophilus RNA polymerase holoenzyme at 3.3 angstroms resolution
2h3x Crystal Structure of an Electron Transfer Complex Between Aromatic Amine Dehydrogenase and Azurin from Alcaligenes Faecalis (Form 3)
2hj4 Crystal structure of Alcaligenes faecalis AADH complex with p-nitrobenzylamine
2hjb Crystal structure of Alcaligenes faecalis AADH in complex with p-methoxybenzylamine
2hkm Crystal structure of the Schiff base intermediate in the reductive half-reaction of aromatic amine dehydrogenase (AADH) with phenylethylamine.
2hkr Structures of the carbinolamine and schiff-base intermediates in the reductive half-reaction of aromatic amine dehydrogenase (AADH) with p-methoxyphenylethylamine
2hxc Crystal structure of the benzylamine complex of aromatic amine dehydrogenase in N-semiquinone form
2i0r Crystal structure of aromatic amine dehydrogenase TTQ-formamide adduct
2i0s Crystal structure of aromatic amine dehydrogenase TTQ-phenylacetaldehyde adduct
2i0t Crystal structure of phenylacetaldehyde derived R-carbinolamine adduct of aromatic amine dehydrogenase
2iaa Crystal Structure of an Electron Transfer Complex Between Aromatic Amine

Dephydrogenase and Azurin from Alcaligenes Faecalis (Form 2)
2ind Mn(II) Reconstituted Toluene/o-xylene Monooxygenase Hydroxylase X-ray Crystal Structure
2iup crystal structure of dithionite-reduced aromatic amine dehydrogenase (aadh) from alcaligenes faecalis
2iur crystal structure of n-quinol form of aromatic amine dehydrogenase (aadh) from alcaligenes faecalis, form a cocrystal
2iuv crystal structure of n-quinol form of aromatic amine dehydrogenase (aadh) from alcaligenes faecalis, form b
2j57 x-ray reduced paraccocus denitrificans methylamine dehydrogenase n-quinol in complex with amicyanin
2oiz Crystal Structure of the Tryptamine-Derived (Indol-3-Acetamide)-TTQ Adduct of Aromatic Amine Dehydrogenase
2ojy Crystal structure of indol-3-acetaldehyde derived TTQ-amide adduct of aromatic amine dehydrogenase
2ok4 Crystal structure of aromatic amine dehydrogenase TTQ-phenylacetaldehyde adduct oxidized with ferricyanide
2ok6 Crystal structure of aromatic amine dehydrogenase TTQ-formamide adduct oxidized with ferricyanide.
2q7q Crystal structure of Alcaligenes faecalis AADH in complex with p-chlorobenzylamine.
2rdb X-ray Crystal Structure of Toluene/o-Xylene Monooxygenase Hydroxylase I100W Mutant
2uuf Thrombin-hirugen binary complex at 1.26A resolution
2w3r crystal structure of xanthine dehydrogenase (desulfo form) from rhodobacter capsulatus in complex with hypoxanthine
2w54 crystal structure of xanthine dehydrogenase from rhodobacter capsulatus in complex with bound inhibitor pterin-6-aldehyde
2w55 crystal structure of xanthine dehydrogenase (e232q variant) from rhodobacter capsulatus in complex with hypoxanthine
3c9a High Resolution Crystal Structure of Argos bound to the EGF domain of Spitz
3dts E(L212)A, D(L213)A, R(M233)L triple mutant structure of photosynthetic reaction center from Rhodobacter sphaeroides
3jwn Complex of FimC, FimF, FimG and FimH
3og4 The crystal structure of human interferon lambda 1 complexed with its high affinity receptor in space group P21212
3puf Crystal structure of human RNase H2 complex
3puz Crystal Structure of a pre-translocation state MBP-Maltose transporter complex bound to AMP- PNP
3qt1 RNA polymerase II variant containing A Chimeric RPB9-C11 subunit
3s1m RNA Polymerase II Initiation Complex
3tu7 Human alpha-thrombin complexed with N-(methylsulfonyl)-D-phenylalanyl-N-((1-carbamimidoyl-4- piperidinyl)methyl)-l-prolinamide (BMS-189664)

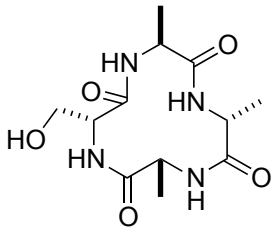


DserDDL

1a9x carbamoyl phosphate
1bpl glycosyltransferase a alpha-1,4-glucan-4-glucanohydrolase
1bxr structure of carbamoyl phosphate synthetase complexed with the atp analog amppnp
1c30 crystal structure of carbamoyl phosphate synthetase: small subunit mutation c269s ac carbamoyl
1c3o crystal structure of the carbamoyl phosphate synthetase: small subunit mutant c269s with bound
1cc1 crystal structure of a reduced, active form of the ni-fe-se hydrogenase from desulfomicrobium baculatum
1ce8 carbamoyl phosphate synthetase from escherichis coli with complexed with the allosteric ligand imp
1cs0 Crystal structure of carbamoyl phosphate synthetase complexed at CYS269 in the small subunit with the
1dtw human branched-chain alpha-keto acid dehydrogenase
1efv three-dimensional structure of human electron transfer flavoprotein to 2.1 a resolution
1ikv k103n mutant hiv-1 reverse transcriptase in complex with efivarenz
1iwa rubisco from galdieria partita
1jdb carbamoyl phosphate synthetase from escherichia coli
1jju structure of a quinohemoprotein amine dehydrogenase
1jkh crystal structure of y181c mutant hiv-1 reverse transcriptase in complex with dmp-266(efavirenz)
1jyo Structure of the Salmonella Virulence Effector SptP in Complex with its Secretion Chaperone SicP
1kee Inactivation of the Antibiotic Acivicin
1lvc Crystal structure of the adenylyl cyclase domain of anthrax edema factor (EF)
1m6v Crystal Structure of the G359F
1ni4 human pyruvate dehydrogenase
1nmb the structure of a complex between the nc10 antibody
1occ structure of bovine heart cytochrome c oxidase at the fully oxidized stat
Oco bovine heart cytochrome c oxidase in carbon monoxide-bound state
1ocr bovine heart cytochrome c oxidase in the fully reduced STATE
1olx roles of his291-alpha and his146-beta' in the reductive acylation

1pby Structure of the Phenylhydrazine Adduct of the Quinohemoprotein Amine Dehydrogenase
1pk0 Crystal Structure of the EF3-CaM complexed with PMEApp
1qge new crystal form of pseudomonas glumae (formerly chromobacterium viscosum atcc 6918) lipase
1rt4 hiv-1 reverse transcriptase
1s26 Structure of Anthrax Edema Factor-Calmodulin-alpha,beta-methyleneadenosine
1t36 Crystal structure of E. coli carbamoylphosphate synthetase small subunit mutant C248D
1t9g Structure of the human MCAD:ETF complex
1tco ternary complex of a calcineurin a fragment, calcineurin b, fkbp12
1tv6 hiv-1 reverse transcriptase
1u5b crystal structure of the human mitochondrial branched-chain alpha-ketoacid dehydrogenase
1v11 crosstalk between cofactor binding and the phosphorylation loop conformation in the bckd machine
1v1r crosstalk between cofactor binding and the phosphorylation loop conformation in the bckd machine
1v54 Bovine heart cytochrome c oxidase at the fully oxidized state
1v55 Bovine heart cytochrome c oxidase at the fully reduced state
1vrq complex with Folinic Acid
1wci molecular switch
1wyw Crystal Structure of SUMO1-conjugated thymine DNA glycosylase
1x31 Crystal Structure of Heterotetrameric Sarcosine Oxidase from Corynebacterium sp. U-96
1x7w Crystal structure of the human mitochondria
1x7x Crystal structure of the human mitochondria
1xct Complex HCV core-Fab 19D9D6-Protein L mutant
1yst structure of the photochemical reaction center of a spheroidene
1zud Structure of ThiS-ThiF protein complex
1zyr Structure of Thermus thermophilus RNA polymerase holoenzyme
2a45 Crystal structure of the complex between thrombin and the central "E" region of fibrin
2beu modulation of human branched-chain alpha-ketoacid dehydrogenase
2bev modulation of human branched-chain alpha-ketoacid dehydrogenase
2bew modulation of human branched-chain alpha-ketoacid dehydrogenase
2bfb modulation of human branched-chain alpha-ketoacid dehydrogenase
2d07 Crystal Structure of SUMO-3-modified Thymine-DNA Glycosylase
2d2c Crystal Structure Of Cytochrome B6F Complex with DBMIB From M. Laminosus
2dyr Bovine heart cytochrome C oxidase at the fully oxidized state
2efc Ara7-GDP/AtVps9a
2eho Crystal structure of human GINS complex
2eik Cadmium ion binding structure of bovine heart cytochrome C oxidase in the fully reduced state

2gag Heteroteterameric sarcosine: structure of a diflavin metaloenzyme at 1.85 a resolution
2gah Structure of the Neisseria gonorrhoeae Type IV pilus filament from x-ray crystallography and electron cryomicroscop
2iaj Crystal Structure of K103N/Y181C Mutant HIV-1 Reverse Transcriptase (RT) in Complex with ATP
2ie3 Structure of the Protein Phosphatase 2A Core Enzyme Bound to Tumor-inducing Toxins
2j9f human branched-chain alpha-ketoacid dehydrogenase-decarboxylase e1b
2koz Solution structure of nasonin-1
2nvx RNA polymerase II elongation complex in 5 mM Mg+2 with 2'-dUTP
2nyl Crystal structure of Protein Phosphatase 2A (PP2A) holoenzyme with the catalytic subunit carboxyl terminus truncated
2occ bovine heart cytochrome c oxidase at the fully oxidized state
2osl crystal structure of rituximab fab in complex with an epitope peptide
2ozl human pyruvate dehydrogenase s264e variant
2uv8 crystal structure of yeast fatty acid synthase with stalled acyl carrier protein at 3.1 angstrom resolution
2v52 structure of mal-rpel2 complexed to g-actin
2vgo crystal structure of aurora b kinase in complex with reversine inhibitor
2wpn structure of the oxidised, as-isolated nifese hydrogenase from d. Vulgaris hildenborough
2xsj structure of desulforubidin from desulfomicrobium norvegicum
2y69 Bovine heart cytochrome c oxidase re-refined with molecular oxygen
2zhf Exploring thrombin S3 pocket
2zxw Bovine heart cytochrome c oxidase at the fully oxidized state (1-s X-ray exposure dataset)
3ad7 Heterotetrameric Sarcosine Oxidase from Corynebacterium sp. U-96 in complex with methylthio acetate
3ag2 Bovine Heart Cytochrome c Oxidase
3alq Crystal structure of TNF-TNFR2 complex
3arc Crystal structure of oxygen-evolving Photosystem II at 1.9 angstrom resolution
3asn Bovine heart cytochrome C oxidase in the fully oxidized state measured at 1.7470 angstrom wavelength
3c5w Complex between PP2A-specific methylesterase PME-1 and PP2A core enzyme
3clr Crystal structure of the R236A ETF mutant from M. methylotrophus
3dol Crystal structure of L100I mutant HIV-1 reverse transcriptase in complex with GW695634.
3duf Snapshots of catalysis in the E1 subunit of the pyruvate dehydrogenase multi-enzyme complex
3dw8 Structure of a Protein Phosphatase 2A Holoenzyme with B55 subunit
3gtj Backtracked RNA polymerase II complex with 13mer RNA
3gtk Backtracked RNA polymerase II complex with 18mer RNA
3gto Backtracked RNA polymerase II complex with 15mer RNA

3h0g RNA Polymerase II from Schizosaccharomyces pombe
3h42 Crystal structure of PCSK9 in complex with Fab from LDLR competitive antibody
3h9r Crystal structure of the kinase domain of type I activin receptor (ACVR1) in complex with FKBP12 and dorsomorphin
3jvz E2~Ubiquitin-HECT
3kcg Crystal structure of the antithrombin-factor IXa-pentasaccharide complex
3kjv HIV-1 reverse transcriptase in complex with DNA
3kow Crystal Structure of ornithine 4,5 aminomutase backsoaked complex
3koy Crystal Structure of ornithine 4,5 aminomutase in complex with ornithine (Aerobic)
3m8q HIV-1 RT with AMINOPYRIMIDINE NNRTI
3mm5 Dissimilatory sulfite reductase in complex with the substrate sulfite
3mtu Structure of the Tropomyosin Overlap Complex from Chicken Smooth Muscle
3oc3 Crystal structure of the Mot1 N-terminal domain in complex with TBP
3sn6 Crystal structure of the beta2 adrenergic receptor-Gs protein complex
3uyf Crystal structure analysis of ribosomal decoding. this entry contains the 30s ribosomal subunit of the first 70s molecule in the asymmetric unit for the near-cognate trna-leu complex
3vcm Crystal structure of human prorenin
3ztx Aurora kinase selective inhibitors identified using a Taxol-induced checkpoint sensitivity screen.
4a49 Structure of phosphoTyr371-c-Cbl-UbcH5B complex
4ap4 Rnf4 - ubch5a - ubiquitin heterotrimeric complex
4ddg Crystal structure of human OTUB1/UbcH5b~Ub/Ub
4dg1 Crystal structure of HIV-1 reverse transcriptase (RT) with polymorphism mutation K172A and K173A
4erp Crystal structure of a gemcitabine-diphosphate inhibited E. coli class Ia ribonucleotide reductase complex
4gaq Allosteric control of the ribosome by small-molecule antibiotics

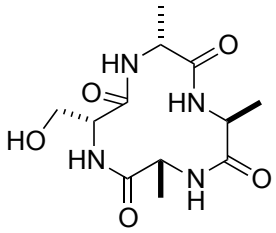


DserDLD

1ava amy2/basi protein-protein complex from barley seed
1awf novel covalent thrombin inhibitor from plant extract
1bhx x-ray structure of the complex of human alpha thrombin WITH THE INHIBITOR SDZ 229-357
1br1 smooth muscle myosin motor domain-essential light chain complex with mgadp.alf4 bound at the active site
1e6y methyl-coenzyme m reductase from methanosarcina barkeri
1eoc crystal structure of acinetobacter sp. Adp1 protocatechuate 3,4-dioxygenase in complex with 4-nitrocatechol
1f3m crystal structure of human serine/threonine kinase pak1
1fin cyclin a-cyclin-dependent kinase 2 complex
1ghv methyl-coenzyme m reductase enzyme product complex
1i3q rna polymerase ii crystal form i at 3.1 a resolution
1icf crystal structure of mhc class ii associated p41 ii fragment in complex with cathepsin l
1k8k Crystal Structure of Arp2/3 Complex
1mmf Crystal structure of substrate free form of glycerol dehydrates
1o2g Elaborate Manifold of Short Hydrogen Bond Arrays Mediating Binding of Active Site-Directed Serine Protease Inhibitors
1okv cyclin a binding groove inhibitor h-arg-arg-leu-ile-phe-nh2
1qhr novel covalent active site thrombin inhibitors
1tbg beta-gamma dimer of the heterotrimeric g-protein transducin
1tyg Structure of the thiazole synthase/ThiS complex
1u2v Crystal structure of Arp2/3 complex with bound ADP and calcium
1uc5 Structure of diol dehydratase complexed with (R)-1,2-propanediol
1xf6 High resolution crystal structure of phycoerythrin 545 from the marine cryptophyte rhodomonas CS24
2c5o differential binding of inhibitors to active and inactive cdk2 provides insights for drug design
2cf4 pyrococcus horikoshii tet1 peptidase can assemble into a tetrahedron or a large octahedral shel
2e2i RNA polymerase II elongation complex in 5 mM Mg+2 with 2'-dGTP
70S T.Th. ribosome functional complex with mRNA and E- and P-site tRNAs at 4.5A. This entry contains 50S ribosomal subunit. The 30S ribosomal subunit can be found in PDB entry

2i40 Cdk2/Cyclin A complexed with a thiophene carboxamide inhibitor
2icw Crystal structure of a complete ternary complex between TCR, superantigen, and peptide-MHC class II molecule
2jkr ap2 clathrin adaptor core with Dileucine peptide RM(phosphoS)QIKRLLSE
2jkt ap2 clathrin adaptor core with CD4 Dileucine peptide RM(phosphoS) EIKRLLSE Q to E mutant
2p9k Crystal Structure of bovine Arp2/3 complex
2pt7 phosducin/transducin
2uze crystal structure of human cdk2 complexed with a thiazolidinone inhibitor
2uzl crystal structure of human cdk2 complexed with a thiazolidinone inhibitor
2wfy truncation and optimisation of peptide inhibitors of cdk2, cyclin a through structure guided design
2wxv structure of cdk2-cyclin a with a pyrazolo(4,3-h) quinazoline-3-carboxamide inhibitor
2xqy crystal structure of pseudorabies core fragment of glycoprotein h in complex with fab d6.3
3dw8 Structure of a Protein Phosphatase 2A Holoenzyme with B55 subunit
3dxk Structure of Bos Taurus Arp2/3 Complex with Bound Inhibitor CK0944636
3dxm Structure of Bos taurus Arp2/3 Complex with Bound Inhibitor CK0993548
3ej1 CDK2/CyclinA complexed with a pyrazolopyridazine inhibitor
3euk Crystal structure of MukE-MukF(residues 292-443)-MukB(head domain)-ATPgammaS complex, asymmetric dimer
3gto Backtracked RNA polymerase II complex with 15mer RN
3gyx Crystal structure of adenylylsulfate reductase from Desulfovibrio gigas
3hiz Crystal structure of p110alpha H1047R mutant in complex with niSH2 of p85alpha
3k7a Crystal Structure of an RNA polymerase II-TFIIB complex
3kow Crystal Structure of ornithine 4,5 aminomutase backsoaked complex
3m1v Structural Insight into Methyl-Coenzyme M Reductase Chemistry using Coenzyme B Analogues
3m2v Structural Insight into Methyl-Coenzyme M Reductase Chemistry using Coenzyme B Analogues
3nbz Crystal structure of the HIV-1 Rev NES-CRM1-RanGTP nuclear export complex (crystal I)
3nc1 Crystal structure of the CRM1-RanGTP complex
3o4x Crystal structure of complex between amino and carboxy terminal fragments of mDia1
3oe7 Structure of four mutant forms of yeast f1 ATPase: gamma-I270T
3phf Crystal Structure of the Epstein-Barr virus gH and gL complex
3q3o Toluene 4 monooxygenase HD complex with phenol
3r66 RNA Polymerase II Initiation Complex
3sdl Crystal structure of human ISG15 in complex with NS1 N-terminal region from influenza B virus, Northeast Structural Genomics Consortium Target IDs HX6481, HR2873, and OR2
3sf5 Crystal Structure of Helicobacter pylori Urease Accessory Protein UreF/H complex

3sqg Crystal structure of a methyl-coenzyme M reductase purified from Black Sea mats
3u9s Crystal structure of P. aeruginosa 3-methylcrotonyl-CoA carboxylase (MCC) 750 kD holoenzyme, CoA complex
4a0c structure of the cand1-cul4b-rbx1 complex
4ds7 Crystal structure of yeast calmodulin bound to the C-terminal fragment of spindle pole body protein Spc110
4g5r Structure of LGN GL4/Galphai3 complex
4gq2 S. pombe Nup120-Nup37 complex

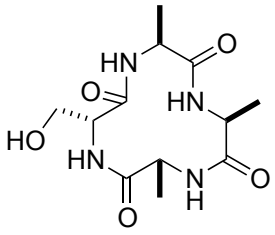

DserDLL

1a14 complex between nc10 anti-influenza virus neuraminidase single chain antibody
1a5k k217e variant of klebsiella aerogenes urease
1a5l k217c variant of klebsiella aerogenes urease
1a5m k217a variant of klebsiella aerogenes urease
1a9x carbamoyl phosphate synthetase: caught in the act of glutamine hydrolysis
1bpl glycosyltransferase
1c30 crystal structure of carbamoyl phosphate synthetase: small subunit mutation c269s
1c3o crystal structure of the carbamoyl phosphate synthetase: small subunit mutant c269s with bound glutamine
1cc1 crystal structure of a reduced, active form of the ni-fe-se hydrogenase from desulfomicrobium baculatum
1ce8 carbamoyl phosphate synthetase from escherichis coli with complexed with the allosteric ligand imp
1cn4 erythropoietin complexed with extracellular domains of erythropoietin receptor
1cs0 Crystal structure of carbamoyl phosphate synthetase complexed at CYS269 in the small subunit with the tetrahedral mimic l-glutamate gamma-semialdehyde
1dtw human branched-chain alpha-keto acid dehydrogenase
1ef2 crystal structure of manganese-substituted klebsiella aerogenes urease
1efv three-dimensional structure of human electron transfer flavoprotein to 2.1 a resolution
1ejs rystal Structure of the H219N Variant of Klebsiella Aerogenes Urease
1f2u Crystal Structure of RAD50 ABC-ATPASE

1fwa klebsiella aerogenes
1fwc klebsiella aerogenes
1g8k crystal structure analysis of arsenite oxidase from alcaligenes faecalis
1h0d crystal structure of human angiogenin in complex with fab fragment of its monoclonal antibody mab 26-2f
1iwa rubisco from galdieria partita
1jdb carbamoyl phosphate synthetase from escherichia coli
1jju structure of a quinohemoprotein amine dehydrogenase with a unique redox cofactor and highly unusual crosslinking
1jkh crystal structure of y181c mutant hiv-1 reverse transcriptase in complex with dmp-266(efavirenz)
1jrh complex (antibody/antigen)
1jw9 Structure of the Native MoeB-MoaD Protein Complex
1jwa Structure of the ATP-bound MoeB-MoaD Protein Complex
1kee Amidotransferase Activity of Carbamoyl Phosphate Synthetase by the Antibiotic Acivicin
1krb crystal structure of klebsiella aerogenes urease, its apoenzyme and two active site mutants
1krc crystal structure of klebsiella aerogenes urease, its apoenzyme and two active site mutants
1lvc crystal structure of the adenylyl cyclase domain of anthrax edema factor (ef) in complex with calmodulin and 2' deoxy, 3' anthraniloyl atp
1m6v crystal structure of the g359f (small subunit) point mutant of carbamoyl phosphate synthetase
1mlc monoclonal antibody fab d44.1 raised against chicken egg-white lysozyme complexed with lysozyme
1ni4 human pyruvate dehydrogenase
1nmb comparison with the overlapping binding site of the nc41 antibody
1nmc complex between nc10 anti-influenza virus neuraminidase single chain antibody with a 15 residue linker and influenza virus neuraminidase
1occ structure of bovine heart cytochrome c oxidase at the fully oxidized state
1oco bovine heart cytochrome c oxidase in carbon monoxide-bound state
1ols roles of his291-alpha and his146-beta' in the reductive acylation reaction catalyzed by human branched-chain alpha-ketoacid dehydrogenase
1pby Structure of the Phenylhydrazine Adduct of the Quinohemoprotein Amine Dehydrogenase from Paracoccus denitrificans at 1.7 A Resolution
1pk0 Crystal Structure of the EF3-CaM complexed with PMEApp
1qge new crystal form of pseudomonas glumae (formerly chromobacterium viscosum atcc 6918) lipase
1rt4 hiv-1 reverse transcriptase complexed with uc781
1rti high resolution structures of hiv-1 rt from four rt-inhibitor complexes
1s26 Structure of Anthrax Edema Factor-Calmodulin-alpha,beta-methyleneadenosine 5'-triphosphate Complex Reveals an Alternative Mode of ATP Binding to the Catalytic Site
1t36 Crystal structure of E. coli carbamoyl phosphate synthetase small subunit mutant

C248D complexed with uridine 5'-monophosphate
1t9g Structure of the human MCAD:ETF complex
1tco ternary complex of a calcineurin a fragment, calcineurin b, fkbp12 and the immunosuppressant drug fk506 (tacrolimus)
1u5b crystal structure of the human mitochondrial branched-chain alpha-ketoacid dehydrogenase
1v11 crosstalk between cofactor binding and the phosphorylation loop conformation in the bckd machine
1v16 crosstalk between cofactor binding and the phosphorylation loop conformation in the bckd machine
1v1m crosstalk between cofactor binding and the phosphorylation loop conformation in the bckd machine
1v54 bovine heart cytochrome c oxidase at the fully oxidized state
1vrq crystal structure of heterotetrameric sarcosine oxidase from corynebacterium sp. U-96 in complex with folinic acid
1wci reactivity modulation of human molecular switch
1wyw Crystal Structure of SUMO1-conjugated thymine DNA glycosylase
1x31 Crystal Structure of Heterotetrameric Sarcosine Oxidase from Corynebacterium sp. U-96
1xct Complex HCV core-Fab 19D9D6-Protein L mutant
1yau Structure of Archeabacterial 20S proteasome-
1yst structure of the photochemical reaction center of a spheroidene containing purple bacterium, rhodobacter sphaeroides y, at 3 angstroms resolution
1zud Structure of ThiS-ThiF protein complex
1zyr Structure of Thermus thermophilus RNA polymerase holoenzyme in complex with the antibiotic streptolydigin
2b4j Structural basis for the recognition between HIV-1 integrase and LEDGF/p75
2bfx mechanism of aurora-b activation by incenp and inhibition by hesperidin.
2d07 Crystal Structure of SUMO-3-modified Thymine-DNA Glycosylase
2d3c Crystal Structure of the Maize Glutamine Synthetase complexed with ADP and Phosphinothricin Phosphate
2d6f Crystal structure of Glu-tRNA(Gln) amidotransferase in the complex with tRNA(Gln)
2dd5 Thiocyanate hydrolase (SCNase) from Thiobacillus thioparus native holo-enzyme
2dyr Bovine heart cytochrome C oxidase at the fully oxidized state
2dys Bovine heart cytochrome C oxidase modified by DCCD
2efc Ara7-GDP/AtVps9a
2eho Crystal structure of human GINS complex
2eij Bovine heart cytochrome C oxidase in the fully reduced state
2eik Cadmium ion binding structure of bovine heart cytochrome C oxidase in the fully reduced state
2fyn Crystal Structure Analysis of the double mutant Rhodobacter Sphaeroides bc1 complex
2gag Heteroteteramеric sarcosine: structure of a diflavin metaloenzyme at 1.85 a

resolution
2gah Heterotetrameric sarcosine: structure of a diflavin metaloenzyme at 1.85 a resolution
2h1l The Structure of the Oncoprotein SV40 Large T Antigen and p53 Tumor Suppressor Complex
2hjf Potassium channel kcsa-fab complex with tetrabutylammonium (TBA)
2hwl Crystal structure of thrombin in complex with fibrinogen gamma' peptide
2iaj Crystal Structure of K103N/Y181C Mutant HIV-1 Reverse Transcriptase (RT) in Complex with ATP
2ie3 Structure of the Protein Phosphatase 2A Core Enzyme Bound to Tumor-inducing Toxins
2ivf Ethylbenzene dehydrogenase from aromatoleum aromaticum
2j9f human branched-chain alpha-ketoacid dehydrogenase-decarboxylase e1b
2npp Structure of the Protein Phosphatase 2A Holoenzyme
2nvx RNA polymerase II elongation complex in 5 mM Mg+2 with 2'-dUTP
2nyl Crystal structure of Protein Phosphatase 2A (PP2A) holoenzyme with the catalytic subunit carboxyl terminus truncated
2ozl Human pyruvate dehydrogenase S264E variant
2r17 Functional architecture of the retromer cargo-recognition complex
2v4j the crystal structure of desulfovibrio vulgaris dissimilatory sulfite reductase bound to dsrc provides novel insights into the mechanism of sulfate respiration
2vg6 crystal structures of hiv-1 reverse transcriptase complexes with thiocarbamate non-nucleoside inhibitors
2vxq crystal structure of the major grass pollen allergen phl p 2 in complex with its specific ige-fab
2vxt human il-18 complexed to murine reference antibody 125-2h fab
2wbl structure of a binary rop-prone complex
2wom crystal structure of uk-453061 bound to hiv-1 reverse transcriptase (k103n).
2won crystal structure of uk-453061 bound to hiv-1 reverse transcriptase (wild-type).
2wpn structure of the oxidised, as-isolated nifese hydrogenase from d. Vulgaris hildenborough
2xsj structure of desulforubidin from desulfomicrobium norvegicum
2xt9 crystal structure of mycobacterium smegmatis alpha-ketoglutarate decarboxylase in complex with gara.
2y10 the crystal structure of ef-tu and trp-trna-trp bound to a cognate codon on the 70s ribosome.
2y18 ef-tu and trp-trna-trp bound to a cognate codon on the 70s ribosome.
2zt9 Crystal Structure of the Cytochrome b6f Complex from Nostoc sp. PCC 7120
3alq Crystal structure of TNF-TNFR2
3arc Crystal structure of oxygen-evolving Photosystem II at 1.9 angstrom resolution
3b9k Crystal structure of CD8alpha-beta in complex with YTS 156.7 FAB
3bpn Crystal structure of the IL4-IL4R-IL13Ra ternary complex
3c5w Complex between PP2A-specific methylesterase PME-1 and PP2A core enzyme
3clr Crystal structure of the R236A ETF mutant from M. methylotrophus

3clt Crystal structure of the R236E mutant of Methylophilus methylotrophus ETF
3dbh Structural Dissection of a Gating Mechanism Preventing Misactivation of Ubiquitin by NEDD8's E1 (APPBP1-UBA3Arg190Ala-NEDD8Ala72Arg)
3duf Snapshots of catalysis in the E1 subunit of the pyruvate dehydrogenase multi-enzyme complex
3ei3 Structure of the hsDDB1-drDDB2 complex
3exe Crystal structure of the pyruvate dehydrogenase (E1p) component of human pyruvate
3exf Crystal structure of the pyruvate dehydrogenase (E1p) component of human pyruvate dehydrogenase complex
3f5w KcsA Potassium channel in the open-inactivated state with 32 A opening at T112
3gtg Backtracked RNA polymerase II complex with 12mer RNA
3gyx Crystal structure of adenylylsulfate reductase from Desulfovibrio gigas
3h42 Crystal structure of PCSK9 in complex with Fab from LDLR competitive antibody
3h9r Crystal structure of the kinase domain of type I activin receptor (ACVR1) in complex with FKBP12 and dorsomorphin
3he6 Crystal structure of mouse CD1d-alpha-galactosylceramide with mouse Valpha14-Vbeta8.2 NKT TCR
3hpl KcsA E71H-F103A mutant in the closed state
3i1q Crystal structure of the E. coli 70S ribosome in an intermediate state of ratcheting
3jsm K65R mutant HIV-1 reverse transcriptase cross-linked to DS-DNA and complexed with tenofovir- diphosphate as the incoming nucleotide substrate
3jvz E2~Ubiquitin-HECT
3kow Crystal Structure of ornithine 4,5 aminomutase backsoaked complex
3koy Crystal Structure of ornithine 4,5 aminomutase in complex with ornithine (Aerobic)
3mm6 Dissimilatory sulfite reductase cyanide complex
3mtu Structure of the Tropomyosin Overlap Complex from Chicken Smooth Muscle
3oc3 Crystal structure of the Mot1 N-terminal domain in complex with TBP
3oc6 Crystal structure of 6-phosphogluconolactonase from mycobacterium smegmatis, apo form
3qa3 Crystal Structure of A-domain in complex with antibody
3rzd RNA Polymerase II Initiation Complex with a 5-nt RNA
3sn6 Crystal structure of the beta2 adrenergic receptor-Gs protein complex
3uyf Crystal structure analysis of ribosomal decoding. this entry contains the 30s ribosomal subunit of the first 70s molecule in the asymmetric unit for the near-cognate trna-leu complex
3v4y first Nuclear PP1 holoenzyme
3vq2 Crystal structure of mouse TLR4/MD-2/LPS complex
3ztx Aurora kinase selective inhibitors identified using a Taxol-induced checkpoint sensitivity screen.
4a08 TRUCTURE OF HSDDB1-DRDDB2 BOUND TO A 13 BP CPD-DUPLEX (PURINE AT D-1 POSITION) AT 3.0 A
4a1s Crystallographic structure of the Pins:Insc complex

4a3c RNA polymerase ii initial transcribing complex with a 5nt DNA-RNA HYBRID
4a3l RNA polymerase ii initial transcribing complex with a 7nt dna-rna hybrid and soaked with ampcpp
4a4b Structure of modified phosphoTyr371-c-Cbl-UbcH5B-ZAP-70 complex
4al8 Structure of Dengue virus DIII in complex with Fab 2H12
4ala Structure of Dengue virus DIII in complex with Fab 2H12
4ap4 Rnf4 - ubch5a - ubiquitin heterotrimeric complex
4ddg Crystal structure of human OTUB1/UbcH5b~Ub/Ub
4erp Crystal structure of a gemcitabine-diphosphate inhibited E. coli class Ia ribonucleotide reductase complex
4g8a Crystal structure of human TLR4 polymorphic variant D299G and T399I in complex with MD-2 and LPS

## APPENDIX E

## EXPERIMENTAL FOR CHAPTER V

### A. EKO Results For Oxopiperazine Dimers

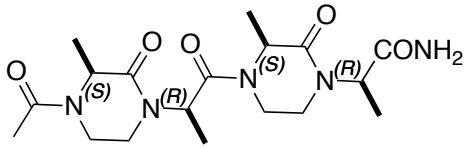

DDL

| PDB ID | RMSD | Protein |
|---|---|---|
| 1hyr | 0.20 ~0.30 | crystal structure of human mica in complex with natural killer cell receptor nkg2d |
| 1nu1 | 0.20 ~0.30 | Crystal Structure of Mitochondrial Cytochrome bc1 Complexed with 2-nonyl-4-hydroxyquinoline N-oxide (NQNO) |
| 1nw9 | 0.20 ~0.30 | structure of caspase-9 in an inhibitory complex with xiap-bir3 |
| 1s63 | 0.20 ~0.30 | Human protein farnesyltransferase complexed with L-778,123 and FPP |
| 2h6i | 0.20 ~0.30 | W102T/Y365F Protein Farnesyltransferase Double Mutant Complexed with a Geranylgeranylated DDPTASACVLS Peptide Product at 3.0A |
| 3gcx | 0.20 ~0.30 | PCSK9:EGFA |
| 3gtq | 0.20 ~0.30 | Backtracked RNA polymerase II complex induced by damage |
| 3ksq | 0.20 ~0.30 | Discovery of C-Imidazole Azaheptapyridine FPT Inhibitors |
| 3orv | 0.20 ~0.30 | Crystal Structure of the Y294H-MauG/pre-Methylamine Dehydrogenase Complex |
| 3s1q | 0.20 ~0.30 | RNA Polymerase II Initiation Complex with a 5-nt 3'-deoxy RNA soaked with ATP |
| 4gms | 0.20 ~0.30 | Crystal structure of heterosubtypic Fab S139/1 in complex with influenza A H3 hemagglutinin |

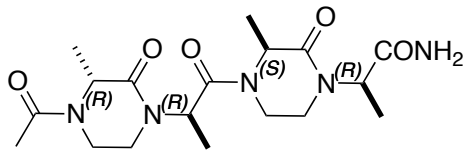

DDD

| PDB ID | RMSD | Protein |
|---|---|---|
| 1acm | 0.20~0.30 | arginine 54 in the active site of escherichia coli aspartate transcarbamoylase is critical for catalysis: a site-specific mutagenesis, nmr and x-ray crystallography study |
| 1at1 | 0.20~0.30 | crystal structures of phosphonoacetamide ligated t and phosphonoacetamide and malonate ligated r states of aspartate carbamoyltransferase at 2.8-angstroms resolution and neutral p*h |
| 1bhx | 0.20~0.30 | x-ray structure of the complex of human alpha thrombin with the inhibitor sdz 229-357 |
| 1bj1 | 0.20~0.30 | vascular endothelial growth factor in complex with a neutralizing antibody |
| 1dwb | 0.20~0.30 | crystallographic analysis at 3.0-angstroms resolution of the binding to human thrombin of four active site-directed inhibitors |
| 1efv | 0.20~0.30 | three-dimensional structure of human electron transfer flavoprotein to 2.1 a resolution |
| 1fzm | 0.20~0.30 | mhc class i natural mutant h-2kbm8 heavy chain complexed with beta-2 microglobulin and vesicular stomatitis virus nucleoprotein |
| 1g20 | 0.20~0.30 | mgatp-bound and nucleotide-free structures of a nitrogenase protein complex between leu127del-fe protein and the mofe protein |
| 1g21 | 0.20~0.30 | mgatp-bound and nucleotide-free structures of a nitrogenase protein complex between leu127del-fe protein and the mofe protein |
| 1hhh | 0.20~0.30 | the antigenic identity of peptide(slash)mhc complexes: a comparison of the conformation of five peptides presented by hla-a2 |
| 1hlt | 0.20~0.30 | the structure of a nonadecapeptide of the fifth egf domain of thrombomodulin complexed with thrombin |
| 1hsb | 0.20~0.30 | different length peptides bind to hla-aw68 similarly at their ends but bulge out in the middle |
| 1htl | 0.20~0.30 | mutation of a buried residue causes lack of activity but no conformational change: crystal structure of e. coli heat-labile enterotoxin mutant val 97--> lys |
| 1i3q | 0.20~0.30 | RNA polymerase ii crystal form i at 3.1 a resolution |
| 1i6h | 0.20~0.30 | RNA polymerase ii elongation complex |
| 1jnr | 0.20~0.30 | Structure of adenylylsulfate reductase from the hyperthermophilic Archaeoglobus fulgidus at 1.6 resolution |
| 1jnz | 0.20~0.30 | Structure of adenylylsulfate reductase from the hyperthermophilic |

| | | |
|---|---|---|
| | | Archaeoglobus fulgidus at 1.6 resolution |
| 1jpf | 0.20~0.30 | Crystal Structure Of The LCMV Peptidic Epitope Gp276 In Complex With The Murine Class I Mhc Molecule H-2Db |
| 1k8k | 0.20~0.30 | Crystal Structure of Arp2/3 Complex |
| 1kpu | 0.20~0.30 | High resolution crystal structure of the MHC class I complex H-2Kb/VSV8 |
| 1lta | 0.20~0.30 | 2.2 angstroms crystal structure of e. coli heat-labile enterotoxin (lt) with bound galactose |
| 1n0w | 0.20~0.30 | Crystal structure of a RAD51-BRCA2 BRC repeat complex |
| 1n2c | 0.20~0.30 | nitrogenase complex from azotobacter vinelandii stabilized by adp-tetrafluoroaluminate |
| 1ocr | 0.20~0.30 | bovine heart cytochrome c oxidase in the fully reduced state |
| 1ocz | 0.20~0.30 | bovine heart cytochrome c oxidase in azide-bound state |
| 1r0b | 0.20~0.30 | Aspartate Transcarbamylase (ATCase) of Escherichia coli: A New Crystalline R State Bound to PALA, or to Product Analogues Phosphate and Citrate |
| 1s7s | 0.20~0.30 | Crystal structures of the murine class I major histocompatibility complex H-2Kb in complex with LCMV-derived gp33 index peptide and three of its escape variants |
| 1tmb | 0.20~0.30 | molecular basis for the inhibition of human alpha-thrombin by the macrocyclic peptide cyclotheonamide a |
| 1twc | 0.20~0.30 | RNA polymerase II complexed with GTP |
| 1twh | 0.199 | RNA polymerase II complexed with 2'dATP |
| 1u3h | 0.20~0.30 | Crystal structure of mouse TCR 172.10 complexed with MHC class II I-Au molecule at 2.4 A |
| 1v55 | 0.20~0.30 | Bovine heart cytochrome c oxidase at the fully reduced state |
| 1wby | 0.20~0.30 | crystal structures of murine mhc class i h-2 db and kb molecules in complex with ctl epitopes from influenza a virus: implications for tcr repertoire selection and immunodominance |
| 1ya7 | 0.20~0.30 | Implications for interactions of proteasome with PAN and PA700 from the 1.9 A structure of a proteasome-11S activator complex |
| 1yar | 0.20~0.30 | Structure of Archeabacterial 20S proteasome mutant D9S- PA26 complex |
| 1yau | 0.20~0.30 | Structure of Archeabacterial 20S proteasome- PA26 complex |
| 1yn6 | 0.20~0.30 | Crystal structure of a mouse MHC class I protein, H2-Db, in complex with a peptide from the influenza A acid polymerase |
| 1yn7 | 0.20~0.30 | Crystal structure of a mouse MHC class I protein, H2-Db, in complex with a mutated peptide (R7A) of the influenza A acid polymerase |
| 1zrt | 0.20~0.30 | Rhodobacter capsulatus cytochrome bc1 complex with stigmatellin bound |
| 2a06 | 0.20~0.30 | Bovine cytochrome bc1 complex with stigmatellin bound |
| 2b8k | 0.20~0.30 | 12-subunit RNA Polymerase II |
| 2bto | 0.20~0.30 | structure of btuba from prosthecobacter dejongeii |

| | | |
|---|---|---|
| 2dyp | 0.20~0.30 | Crystal Structure of LILRB2(LIR2/ILT4/CD85d) complexed with HLA-G |
| 2dys | 0.20~0.30 | Bovine heart cytochrome C oxidase modified by DCCD |
| 2e2i | 0.200 | RNA polymerase II elongation complex in 5 mM Mg+2 with 2'-dGTP |
| 2e2j | 0.20~0.30 | RNA polymerase II elongation complex in 5 mM Mg+2 with GMPCPP |
| 2eij | 0.20~0.30 | Bovine heart cytochrome C oxidase in the fully reduced state |
| 2eim | 0.20~0.30 | Zinc ion binding structure of bovine heart cytochrome C oxidase in the fully reduced state |
| 2esv | 0.20~0.30 | Structure of the HLA-E-VMAPRTLIL/KK50.4 TCR complex |
| 2fja | 0.20~0.30 | adenosine 5'-phosphosulfate reductase in complex with substrate |
| 2fjb | 0.20~0.30 | Adenosine-5'-phosphosulfate reductase im complex with products |
| 2fje | 0.20~0.30 | adenosine-5-phosphosulfate reductase oxidized state |
| 2fo4 | 0.186 | Enhanced MHC class I binding and immune responses through anchor modification of the non-canonical tumor associated MUC1-8 peptide |
| 2fp4 | 0.20~0.30 | Crystal structure of pig GTP-specific succinyl-CoA synthetase in complex with GTP |
| 2fpi | 0.20~0.30 | Crystal structure of pig GTP-specific succinyl-CoA synthetase from polyethylene glycol |
| 2hsn | 0.20~0.30 | Structural basis of yeast aminoacyl-tRNA synthetase complex formation revealed by crystal structures of two binary sub-complexes |
| 2j01 | 0.20~0.30 | structure of the thermus thermophilus 70s ribosome complexed with mrna, trna and paromomycin (part 2 of 4). this file contains the 50s subunit from molecule i. |
| 2j03 | 0.20~0.30 | structure of the thermus thermophilus 70s ribosome complexed with mrna, trna and paromomycin (part 4 of 4). this file contains the 50s subunit from molecule ii. |
| 2j0s | 0.20~0.30 | the crystal structure of the exon junction complex at 2.2 a resolution |
| 2j3t | 0.20~0.30 | the crystal structure of the bet3-trs33-bet5-trs23 complex. |
| 2ja5 | 0.20~0.30 | CPD lesion containing RNA Polymerase II elongation complex A |
| 2ja6 | 0.20~0.30 | CPD lesion containing RNA Polymerase II elongation complex B |
| 2nvq | 0.20~0.30 | RNA Polymerase II Elongation Complex in 150 mM Mg+2 with 2'dUTP |
| 2nvt | 0.20~0.30 | RNA Polymerase II Elongation Complex in 150 mM Mg+2 with GMPCPP |
| 2nvx | 0.20~0.30 | RNA polymerase II elongation complex in 5 mM Mg+2 with 2'-dUTP |
| 2nxy | 0.20~0.30 | HIV-1 gp120 Envelope Glycoprotein(S334A) Complexed with CD4 and Antibody 17b |
| 2ny4 | 0.20~0.30 | HIV-1 gp120 Envelope Glycoprotein (K231C, T257S, E268C, S334A, S375W) Complexed with CD4 and Antibody 17b |

| | | |
|---|---|---|
| 2p5e | 0.20~0.30 | Crystal Structures of High Affinity Human T-Cell Receptors Bound to pMHC Reveal Native Diagonal Binding Geometry |
| 2p9p | 0.20~0.30 | Crystal Structure of bovine Arp2/3 complex co-crystallized with ADP |
| 2qqn | 0.20~0.30 | Neuropilin-1 b1 Domain in Complex with a VEGF-Blocking Fab |
| 2r29 | 0.20~0.30 | Neutralization of dengue virus by a serotype cross-reactive antibody elucidated by cryoelectron microscopy and x-ray crystallography |
| 2r7z | 0.20~0.30 | Cisplatin lesion containing RNA polymerase II elongation complex |
| 2r92 | 0.20~0.30 | Elongation complex of RNA polymerase II with artificial RdRP scaffold |
| 2rd5 | 0.20~0.30 | Structural basis for the regulation of N-acetylglutamate kinase by PII in Arabidopsis thaliana |
| 2uv8 | 0.20~0.30 | crystal structure of yeast fatty acid synthase with stalled acyl carrier protein at 3.1 angstrom resolution |
| 2wdl | 0.142 | structure of the thermus thermophilus 70s ribosome in complex with mrna, paromomycin, acylated a- and p-site trnas, and e-site trna. this file contains the 50s subunit for molecule i. |
| 2wdn | 0.143 | structure of the thermus thermophilus 70s ribosome in complex with mrna, paromomycin, acylated a- and p-site trnas, and e-site trna. this file contains the 50s subunit for molecule ii. |
| 3aec | 0.20~0.30 | Crystal structure of porcine heart mitochondrial complex II bound with 2-Iodo-N-(1-methylethyl)-benzamid |
| 3c5z | 0.20~0.30 | Crystal structure of mouse MHC class II I-Ab/3K peptide complexed with mouse TCR B3K506 |
| 3d39 | 0.20~0.30 | The complex between TCR A6 and human Class I MHC HLA-A2 with the modified HTLV-1 TAX (Y5(4-fluoroPhenylalanine)) peptide |
| 3dxm | 0.20~0.30 | Structure of Bos taurus Arp2/3 Complex with Bound Inhibitor CK0993548 |
| 3euh | 0.20~0.30 | Crystal Structure of the MukE-MukF Complex |
| 3fol | 0.20~0.30 | Crystal structure of the Class I MHC Molecule H-2Kwm7 with a Single Self Peptide VNDIFERI |
| 3fqr | 0.20~0.30 | Phosphorylation of self-peptides alters Human Leukocyte Antigen Class I-restricted antigen presentation and generates tumor specific epitopes |
| 3g43 | 0.20~0.30 | Crystal structure of the calmodulin-bound Cav1.2 C-terminal regulatory domain dimer |
| 3g5o | 0.20~0.30 | The crystal structure of the toxin-antitoxin complex RelBE2 (Rv2865-2866) from Mycobacterium tuberculosis |
| 3gso | 0.20~0.30 | Crystal structure of the binary complex between HLA-A2 and HCMV NLV peptide |
| 3gtl | 0.20~0.30 | Backtracked RNA polymerase II complex with 13mer with G<>U mismatch |

| | | |
|---|---|---|
| 3gtq | 0.20~0.30 | Backtracked RNA polymerase II complex induced by damage |
| 3how | 0.20~0.30 | Complete RNA polymerase II elongation complex III with a T-U mismatch and a frayed RNA 3'-uridine |
| 3hoy | 0.20~0.30 | Complete RNA polymerase II elongation complex VI |
| 3i4m | 0.20~0.30 | 8-oxoguanine containing RNA polymerase II elongation complex D |
| 3jse | 0.20~0.30 | Crystal structure of archaeal 20S proteasome in complex with mutated P26 activator |
| 3jvt | 0.20~0.30 | Calcium-bound Scallop Myosin Regulatory Domain (Lever Arm) with Reconstituted Complete Light Chains |
| 3k7a | 0.20~0.30 | Crystal Structure of an RNA polymerase II-TFIIB complex |
| 3kir | 0.137 | Structure of RelE nuclease bound to the 70S ribosome (precleavage state; Part 2 of 4) |
| 3kit | 0.137 | Structure of RelE nuclease bound to the 70S ribosome (precleavage state; Part 4 of 4) |
| 3kiy | 0.177 | Structure of RelE nuclease bound to the 70S ribosome (postcleavage state; Part 4 of 4) |
| 3kno | 0.20~0.30 | The structures of capreomycin bound to the 70S ribosome. THIS FILE CONTAINS THE 50S SUBUNIT FOR MOLECULE II |
| 3l4m | 0.204 | Crystal Structure of the MauG/pre-Methylamine Dehydrogenase Complex. |
| 3l4o | 0.20~0.30 | Crystal Structure of the MauG/pre-Methylamine Dehydrogenase Complex After Treatment with Hydrogen Peroxide |
| 3loh | 0.20~0.30 | Structure of the insulin receptor ectodomain, including ct peptide |
| 3m3y | 0.20~0.30 | RNA polymerase II elongation complex C |
| 3m4o | 0.20~0.30 | RNA polymerase II elongation complex B |
| 3mrf | 0.189 | Crystal Structure of MHC class I HLA-A2 molecule complexed with EBV bmlf1-280-288 nonapeptide T4P variant |
| 3mrn | 0.20~0.30 | Crystal Structure of MHC class I HLA-A2 molecule complexed with HCV NS4b-1807-1816 decapeptide |
| 3n40 | 0.20~0.30 | Crystal structure of the immature envelope glycoprotein complex of Chikungunya virus. |
| 3n44 | 0.20~0.30 | Crystal structure of the mature envelope glycoprotein complex (trypsin cleavage; Osmium soak) of Chikungunya virus. |
| 3ndy | 0.20~0.30 | The structure of the catalytic and carbohydrate binding domain of endoglucanase D from Clostridium cellulovorans |
| 3ndz | 0.20~0.30 | The structure of the catalytic and carbohydrate binding domain of endoglucanase D from Clostridium cellulovorans bound to cellotriose |
| 3oat | 0.20~0.30 | Crystal structure of the E. coli ribosome bound to telithromycin. This file contains the 50S subunit of the first 70S ribosome with telithromycin bound. |
| 3oh5 | 0.20~0.30 | Structure of the Thermus Thermophilus 70S ribosome complexed with chloramphenicol. This file contains the 50S subunit of one 70S ribosome. The entire crystal structure contains two 70S |

| | | |
|---|---|---|
| | | ribosomes. |
| 3ora | 0.20~0.30 | Crystal structure of the E. coli ribosome bound to CEM-101. This file contains the 30S subunit of the second 70S ribosome. |
| 3po3 | 0.20~0.30 | Arrested RNA Polymerase II reactivation intermediate |
| 3pxs | 0.20~0.30 | Crystal Structure of Diferrous MauG in Complex with Pre-Methylamine Dehydrogenase: |
| 3pxt | 0.20~0.30 | Crystal Structure of Ferrous CO Adduct of MauG in Complex with Pre-Methylamine Dehydrogenase |
| 3pxw | 0.20~0.30 | Crystal Structure of Ferrous NO Adduct of MauG in Complex with Pre-Methylamine Dehydrogenase |
| 3q7f | 0.20~0.30 | Cryptococcus neoformans protein farnesyltransferase in complex with FPP and ethylenediamine inhibitor 1 |
| 3qt1 | 0.20~0.30 | RNA polymerase II variant containing A Chimeric RPB9-C11 subunit |
| 3rae | 0.20~0.30 | Quinolone(Levofloxacin)-DNA cleavage complex of type IV topoisomerase from S. pneumoniae |
| 3raf | 0.20~0.30 | Quinazolinedione-DNA cleavage complex of type IV topoisomerase from S. pneumoniae |
| 3rfr | 0.20~0.30 | Crystal Structure of particulate methane monooxygenase (pMMO) from Methylocystis sp. strain M |
| 3rgb | 0.20~0.30 | Crystal structure of particulate methane monooxygenase from Methylococcus capsulatus (Bath) |
| 3rlm | 0.20~0.30 | Structure of the W199F MauG/pre-Methylamine Dehydrogenase complex after treatment with hydrogen peroxide |
| 3rmz | 0.20~0.30 | Crystal Structure of the W199F-MauG/pre-Methylamine Dehydrogenase Complex |
| 3rn0 | 0.20~0.30 | Crystal Structure of the W199K-MauG/pre-Methylamine Dehydrogenase Complex |
| 3rn1 | 0.20~0.30 | Crystal Structure of the W199E-MauG/pre-Methylamine Dehydrogenase Complex |
| 3rzd | 0.20~0.30 | RNA Polymerase II Initiation Complex with a 5-nt RNA |
| 3rzo | 0.20~0.30 | RNA Polymerase II Initiation Complex with a 4-nt RNA |
| 3s15 | 0.194 | RNA Polymerase II Initiation Complex with a 7-nt RNA |
| 3s16 | 0.20~0.30 | RNA Polymerase II Initiation Complex with an 8-nt RNA |
| 3s17 | 0.20~0.30 | RNA Polymerase II Initiation Complex with a 9-nt RNA |
| 3s1n | 0.20~0.30 | RNA Polymerase II Initiation Complex with a 5-nt RNA (variant 2) |
| 3s1q | 0.20~0.30 | RNA Polymerase II Initiation Complex with a 5-nt 3'-deoxy RNA soaked with ATP |
| 3s1r | 0.20~0.30 | RNA Polymerase II Initiation Complex with a 5-nt 3'-deoxy RNA soaked with GTP |
| 3s2d | 0.195 | RNA Polymerase II Initiation Complex with a 5-nt RNA containing a 5Br-U |
| 3sic | 0.20~0.30 | MOLECULAR RECOGNITION AT THE ACTIVE SITE OF subtilisin bpn': crystallographic studies using genetically |

| | | |
|---|---|---|
| | | engineered proteinaceous inhibitor ssi (streptomyces subtilisin inhibitor) |
| 3sjl | 0.20~0.30 | Crystal Structure of the P107S-MauG/pre-Methylamine Dehydrogenase Complex |
| 3svw | 0.20~0.30 | Crystal Structure of the P107V-MauG/pre-Methylamine Dehydrogenase Complex |
| 3sws | 0.20~0.30 | Crystal Structure of the Quinone Form of Methylamine Dehydrogenase in Complex with the Diferric Form of MauG |
| 3sxt | 0.20~0.30 | Crystal Structure of the Quinol Form of Methylamine Dehydrogenase in Complex with the Diferrous Form of MauG |
| 3u9s | 0.20~0.30 | Crystal structure of P. aeruginosa 3-methylcrotonyl-CoA carboxylase (MCC) 750 kD holoenzyme, CoA complex |
| 3utq | 0.20~0.30 | Human HLA-A*0201-ALWGPDPAAA |
| 3vh5 | 0.20~0.30 | Crystal structure of the chicken CENP-T histone fold/CENP-W/CENP-S/CENP-X heterotetrameric complex, crystal form I |
| 3vj6 | 0.20~0.30 | Structure of the MHC class Ib molecule Qa-1b |
| 3zvk | 0.20~0.30 | Crystal structure of VapBC2 from Rickettsia felis bound to a DNA fragment from their promoter |
| 4a3e | 0.20~0.30 | RNA polymerase ii initial transcribing complex with a 5nt dna-rna hybrid and soaked with ampcpp |
| 4a3f | 0.20~0.30 | RNA polymerase ii initial transcribing complex with a 6nt dna-rna hybrid and soaked with ampcpp |
| 4a3g | 0.20~0.30 | RNA Polymerase II initial transcribing complex with a 2nt DNA-RNA hybrid |
| 4a3i | 0.20~0.30 | RNA Polymerase II binary complex with DNA |
| 4a3m | 0.20~0.30 | RNA polymerase ii initial transcribing complex with a 4nt dna-rna hybrid and soaked with ampcpp |
| 4b1o | 0.20~0.30 | Archaeal RNAP-DNA binary complex at 4.32Ang |
| 4b1p | 0.20~0.30 | Archaeal RNAP-DNA binary complex at 4.32Ang |
| 4ba1 | 0.20~0.30 | Archaeal exosome (Rrp4-Rrp41(D182A)-Rrp42) bound to inorganic phosphate |
| 4ba2 | 0.20~0.30 | Archaeal exosome (Rrp4-Rrp41(D182A)-Rrp42) bound to inorganic phosphate |
| 4dgl | 0.20~0.30 | Crystal Structure of the CK2 Tetrameric Holoenzyme |
| 4div | 0.127 | The structure of a 1.8 MDa viral genome injection device suggests alternative infection mechanisms |
| 4elz | 0.20~0.30 | CCDBVFI:GYRA14VFI |
| 4fxe | 0.20~0.30 | Crystal structure of the intact E. coli RelBE toxin-antitoxin complex |
| 4fxk | 0.20~0.30 | Human complement C4 |
| 8atc | 0.20~0.30 | complex of n-phosphonacetyl-l-aspartate with aspartate carbamoyltransferase. x-ray refinement, analysis of conformational changes and catalytic and allosteric mechanisms |

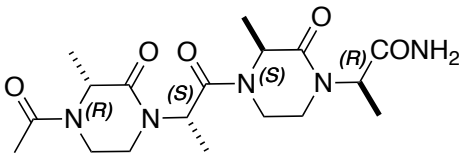

DLD

| PDB ID | RMSD | Protein |
|---|---|---|
| 1eiy | 0.186 | the crystal structure of phenylalanyl-trna synthetase from thermus thermophilus complexed with cognate trnaphe |
| 1g20 | 0.20~0.27 | mgatp-bound and nucleotide-free structures of a nitrogenase protein complex between leu127del-fe protein and the mofe protein |
| 1jmu | 0.20~0.27 | Crystal Structure of the Reovirus mu1/sigma3 Complex |
| 1m1j | 0.20~0.27 | Crystal structure of native chicken fibrinogen with two different bound ligands |
| 1o7g | 0.20~0.27 | naphthalene 1,2-dioxygenase with naphthalene bound in the active site. |
| 1oco | 0.20~0.27 | bovine heart cytochrome c oxidase in carbon monoxide-bound state |
| 1ocr | 0.20~0.27 | bovine heart cytochrome c oxidase in the fully reduced state |
| 1ocz | 0.20~0.27 | bovine heart cytochrome c oxidase in azide-bound state |
| 1qlb | 0.20~0.27 | respiratory complex II-like fumarate reductase from Wolinella succinogenes |
| 1s9k | 0.20~0.27 | Crystal Structure of Human NFAT1 and Fos-Jun on the IL-2 ARRE1 Site |
| 1sqb | 0.20~0.27 | Crystal Structure Analysis of Bovine Bc1 with Azoxystrobin |
| 1sqq | 0.20~0.27 | Crystal Structure Analysis of Bovine Bc1 with Methoxy Acrylate Stilbene (MOAS) |
| 1sqv | 0.20~0.27 | Crystal Structure Analysis of Bovine Bc1 with UHDBT |
| 1unn | 0.20~0.27 | complex of beta-clamp processivity factor and little finger domain of poliv |
| 1ynj | 0.20~0.27 | Taq RNA polymerase-Sorangicin complex |
| 1zvy | 0.20~0.27 | Crystal structure of the VHH D3-L11 in complex with hen egg white lysozyme |
| 2afh | 0.20~0.27 | Crystal Structure of Nucleotide-Free Av2-Av1 Complex |
| 2bs2 | 0.20~0.27 | quinol:fumarate reductase from wolinella succinogenes |
| 2bs3 | 0.20~0.27 | glu c180 -> gln variant quinol:fumarate reductase from wolinella succinogenes |
| 2bs4 | 0.20~0.27 | glu c180 -> ile variant quinol:fumarate reductase from wolinella succinogenes |
| 2eim | 0.20~0.27 | Zinc ion binding structure of bovine heart cytochrome C oxidase in the fully reduced state |
| 2gaf | 0.20~0.27 | Crystal Structure of the Vaccinia Polyadenylate Polymerase |

| | | |
|---|---|---|
| | | Heterodimer (apo form) |
| 2ja5 | 0.20~0.27 | CPD lesion containing RNA Polymerase II elongation complex A |
| 2ja8 | 0.20~0.27 | cpd lesion containing rna polymerase ii elongation complex d |
| 2pjr | 0.150 | helicase product complex |
| 2qov | 0.20~0.27 | Crystal structure of the bacterial ribosome from Escherichia coli in complex with spectinomycin. This file contains the 50S subunit of the first 70S ribosome. The entire crystal structure contains two 70S ribosomes. |
| 2qox | 0.20~0.27 | Crystal structure of the bacterial ribosome from Escherichia coli in complex with spectinomycin. This file contains the 50S subunit of the second 70S ribosome. The entire crystal structure contains two 70S ribosomes. |
| 2r92 | 0.20~0.27 | Elongation complex of RNA polymerase II with artificial RdRP scaffold |
| 2vpy | 0.20~0.27 | polysulfide reductase with bound quinone inhibitor, pentachlorophenol (pcp) |
| 2waq | 0.20~0.27 | the complete structure of the archaeal 13-subunit dna-directed rna polymerase |
| 2wvr | 0.20~0.27 | human cdt1:geminin complex |
| 2xsj | 0.20~0.27 | structure of desulforubidin from desulfomicrobium norvegicum |
| 3gtg | 0.20~0.27 | Backtracked RNA polymerase II complex with 12mer RNA |
| 3gtm | 0.20~0.27 | Co-complex of Backtracked RNA polymerase II with TFIIS |
| 3hov | 0.20~0.27 | Complete RNA polymerase II elongation complex II |
| 3hox | 0.200 | Complete RNA polymerase II elongation complex V |
| 3hoy | 0.20~0.27 | Complete RNA polymerase II elongation complex VI |
| 3po2 | 0.20~0.27 | Arrested RNA Polymerase II elongation complex |
| 3qjr | 0.20~0.27 | The structure of and photolytic induced changes of carbon monoxide binding to the cytochrome ba3-oxidase from Thermus thermophilus |
| 3rzd | 0.20~0.27 | RNA Polymerase II Initiation Complex with a 5-nt RNA |
| 3s15 | 0.20~0.27 | RNA Polymerase II Initiation Complex with a 7-nt RNA |
| 3s17 | 0.20~0.27 | RNA Polymerase II Initiation Complex with a 9-nt RNA |
| 3s1m | 0.20~0.27 | RNA Polymerase II Initiation Complex with a 5-nt RNA (variant 1) |
| 3s3d | 0.20~0.27 | Structure of Thermus thermophilus cytochrome ba3 oxidase 480s after Xe depressurization |
| 3s6n | 0.20~0.27 | Crystal Structure of the Gemin2-binding domain of SMN, Gemin2 in Complex with SmD1/D2/F/E/G from Human |
| 3thm | 0.194 | Crystal structure of Fas receptor extracellular domain in complex with Fab EP6b_B01 |
| 3tje | 0.20~0.27 | Crystal structure of Fas receptor extracellular domain in complex with Fab E09 |
| 3uzv | 0.140 | Crystal structure of the dengue virus serotype 2 envelope protein domain III in complex with the variable domains of Mab 4E11 |

| | | |
|---|---|---|
| 4a3c | 0.20~0.27 | RNA polymerase ii initial transcribing complex with a 5nt dna-rna hybrid |
| 4a3g | 0.20~0.27 | RNA Polymerase II initial transcribing complex with a 2nt DNA-RNA hybrid |
| 4a3i | 0.20~0.27 | RNA Polymerase II binary complex with DNA |
| 4a3j | 0.20~0.27 | rna polymerase ii initial transcribing complex with a 2nt dna-rna hybrid and soaked with gmpcpp |
| 4a3k | 0.20~0.27 | RNA polymerase ii initial transcribing complex with a 7nt dna-rna hybrid |
| 4a3l | 0.20~0.27 | RNA polymerase ii initial transcribing complex with a 7nt dna-rna hybrid and soaked with ampcpp |
| 4a3m | 0.20~0.27 | RNA polymerase ii initial transcribing complex with a 4nt dna-rna hybrid and soaked with ampcpp |

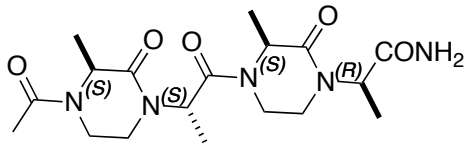


DLL

| PDB ID | RMSD | Protein |
|---|---|---|
| 1bmf | 0.163 | bovine mitochondrial f1-atpase |
| 1cow | 0.140 | bovine mitochondrial f1-atpase complexed with aurovertin b |
| 1e1q | 0.153 | bovine mitochondrial f1-atpase at 100k |
| 1e1r | 0.20~0.21 | bovine mitochondrial f1-atpase inhibited by mg2+adp and aluminium fluoride |
| 1efr | 0.154 | bovine mitochondrial f1-atpase complexed with the peptide antibiotic efrapeptin |
| 1g21 | 0.20~0.21 | mgatp-bound and nucleotide-free structures of a nitrogenase protein complex between leu127del-fe protein and the mofe protein |
| 1h8e | 0.144 | (adp.alf4)2(adp.so4) bovine f1-atpase (all three catalytic sites occupied) |
| 1h8h | 0.142 | Bovine mitochondrial F1-Atpase at 100K |
| 1i3q | 0.166 | rna polymerase ii crystal form i at 3.1 a resolution |
| 1i9r | 0.128 | structure of cd40l in complex with the fab fragment of humanized 5c8 antibody |
| 1jyo | 0.20~0.21 | Structure of the Salmonella Virulence Effector SptP in Complex with its Secretion Chaperone SicP |
| 1k83 | 0.20~0.21 | Crystal Structure of Yeast RNA Polymerase II Complexed with the Inhibitor Alpha Amanitin |
| 1ncd | 0.20~0.21 | refined crystal structure of the influenza virus n9 neuraminidase-nc41 fab complex |

| | | |
|---|---|---|
| 1oco | 0.20~0.21 | bovine heart cytochrome c oxidase in carbon monoxide-bound state |
| 1ocr | 0.20~0.21 | bovine heart cytochrome c oxidase in the fully reduced state |
| 1ocz | 0.20~0.21 | bovine heart cytochrome c oxidase in azide-bound state |
| 1ohh | 0.20~0.21 | bovine mitochondrial f1-atpase complexed with the inhibitor protein if1 |
| 1ol5 | 0.193 | structure of aurora-a 122-403, phosphorylated on thr287, thr288 and bound to tpx2 1-43 |
| 1otc | 0.20~0.21 | the o. nova telomere end binding protein complexed with single strand dna |
| 1ph5 | 0.20~0.21 | crystal structure of the oxytricha nova telomere end-binding protein complexed with noncognate ssdna ggggttttg(3dr)gg |
| 1pss | 0.20~0.21 | crystallographic analyses of site-directed mutants of the photosynthetic reaction center from rhodobacter sphaeroides |
| 1qlb | 0.20~0.21 | respiratory complex II-like fumarate reductase from Wolinella succinogenes |
| 1tb6 | 0.20~0.21 | 2.5A Crystal Structure of the Antithrombin-Thrombin-Heparin Ternary Complex |
| 1tfk | 0.20~0.21 | Ribonuclease from Escherichia coli complexed with its inhibtor protein |
| 1tfo | 0.20~0.21 | Ribonuclease from Escherichia coli complexed with its inhibitor protein |
| 1tzh | 0.20~0.21 | Crystal Structure of the Fab YADS1 Complexed with h-VEGF |
| 1v55 | 0.20~0.21 | Bovine heart cytochrome c oxidase at the fully reduced state |
| 1v74 | 0.20~0.21 | ribonuclease-inhibitor complex |
| 1w0j | 0.186 | Beryllium fluoride inhibited bovine F1-ATPase |
| 1xx9 | 0.20~0.21 | Crystal Structure of the FXIa Catalytic Domain in Complex with EcotinM84R |
| 1xxd | 0.20~0.21 | Crystal Structure of the FXIa Catalytic Domain in Complex with mutated Ecotin |
| 1xxf | 0.20~0.21 | Crystal Structure of the FXIa Catalytic Domain in Complex with Ecotin Mutant (EcotinP) |
| 1yq4 | 0.20~0.21 | Avian respiratory complex ii with 3-nitropropionate and ubiquinone |
| 2a0l | 0.20~0.21 | Crystal structure of KvAP-33H1 Fv complex |
| 2aep | 0.20~0.21 | An epidemiologically significant epitope of a 1998 influenza virus neuraminidase forms a highly hydrated interface in the NA-antibody complex. |
| 2aeq | 0.20~0.21 | An epidemiologically significant epitope of a 1998 influenza virus neuraminidase forms a highly hydrated interface in the NA-antibody complex. |
| 2b1x | 0.20~0.21 | Crystal structure of naphthalene 1,2-dioxygenase from Rhodococcus sp. |
| 2bki | 0.20~0.21 | myosin vi nucleotide-free (mdinsert2-iq) crystal structure |
| 2bs2 | 0.193 | quinol:fumarate reductase from wolinella succinogenes |

| | | |
|---|---|---|
| 2bs3 | 0.196 | glu c180 -> gln variant quinol:fumarate reductase from wolinella succinogenes |
| 2bs4 | 0.20~0.21 | glu c180 -> ile variant quinol:fumarate reductase from wolinella succinogenes |
| 2ck3 | 0.20~0.21 | Azide inhibited bovine F1-ATPase |
| 2e2h | 0.20~0.21 | RNA polymerase II elongation complex at 5 mM Mg2+ with GTP |
| 2e2j | 0.20~0.21 | RNA polymerase II elongation complex in 5 mM Mg+2 with GMPCPP |
| 2eil | 0.20~0.21 | Cadmium ion binding structure of bovine heart cytochrome C oxidase in the fully oxidized state |
| 2eim | 0.20~0.21 | Zinc ion binding structure of bovine heart cytochrome C oxidase in the fully reduced state |
| 2ein | 0.199 | Zinc ion binding structure of bovine heart cytochrome C oxidase in the fully oxidized state |
| 2hh1 | 0.20~0.21 | Reaction centre from Rhodobacter sphaeroides strain R-26.1 complexed with dibrominated phosphatidylcholine |
| 2hit | 0.20~0.21 | Reaction centre from Rhodobacter sphaeroides strain R-26.1 complexed with dibrominated phosphatidylethanolamine |
| 2iou | 0.20~0.21 | Major Tropism Determinant P1 (Mtd-P1) Variant Complexed with Bordetella brochiseptica Virulence Factor Pertactin extracellular domain (Prn-E). |
| 2ja5 | 0.20~0.21 | CPD lesion containing RNA Polymerase II elongation complex A |
| 2jdi | 0.20~0.21 | ground state structure of f1-atpase from bovine heart mitochondria (bovine f1-atpase crystallised in the absence of azide) |
| 2nvt | 0.20~0.21 | RNA Polymerase II Elongation Complex in 150 mM Mg+2 with GMPCPP |
| 2nvz | 0.20~0.21 | RNA Polymerase II elongation complex with UTP, updated 11/2006 |
| 2o8m | 0.20~0.21 | Crystal structure of the S139A mutant of Hepatitis C Virus NS3/4A protease |
| 2ooy | 0.20~0.21 | Crystal structure of the adenylate sensor from AMP-activated protein kinase complexed with ATP |
| 2pjy | 0.20~0.21 | Structural basis for cooperative assembly of the TGF-beta signaling complex |
| 2qjb | 0.20~0.21 | Crystal structure analysis of BMP-2 in complex with BMPR-IA variant IA/IB |
| 2qy0 | 0.20~0.21 | Active dimeric structure of the catalytic domain of C1r reveals enzyme-product like contacts |
| 2r6g | 0.20~0.21 | The Crystal Structure of the E. coli Maltose Transporter |
| 2v4j | 0.20~0.21 | the crystal structure of desulfovibrio vulgaris dissimilatory sulfite reductase bound to dsrc provides novel insights into the mechanism of sulfate respiration |
| 2v7q | 0.20~0.21 | the structure of f1-atpase inhibited by i1-60his, a monomeric |

| | | |
|---|---|---|
| | | form of the inhibitor protein, if1. |
| 2w6h | 0.163 | low resolution structures of bovine mitochondrial f1-atpase during controlled dehydration: hydration state 4a. |
| 2w6i | 0.162 | low resolution structures of bovine mitochondrial f1-atpase during controlled dehydration: hydration state 4b. |
| 2wbl | 0.20~0.21 | three-dimensional structure of a binary rop-prone complex |
| 2wwx | 0.20~0.21 | crystal structure of the sidm/drra(gef/gdf domain)-rab1 (gtpase domain) complex |
| 2xnd | 0.20~0.21 | crystal structure of bovine f1-c8 sub-complex of atp synthase |
| 2xok | 0.20~0.21 | refined structure of yeast f1c10 atpase complex to 3 a resolution |
| 2xsj | 0.181 | structure of desulforubidin from desulfomicrobium norvegicum |
| 3arc | 0.20~0.21 | Crystal structure of oxygen-evolving Photosystem II at 1.9 angstrom resolution |
| 3ayh | 0.20~0.21 | Crystal structure of the C17/25 subcomplex from S. pombe RNA Polymerase III |
| 3b1j | 0.20~0.21 | Crystal structure of Glyceraldehyde-3-Phosphate Dehydrogenase complexed with CP12 in the presence of copper from Synechococcus elongatus |
| 3d0g | 0.20~0.21 | Crystal structure of spike protein receptor-binding domain from the 2002-2003 SARS coronavirus human strain complexed with human-civet chimeric receptor ACE2 |
| 3dta | 0.20~0.21 | E(L212)Q, N(M44)D double mutant structure of photosynthetic reaction center from Rhodobacter sphaeroides |
| 3dtr | 0.20~0.21 | E(L212)Q, L(L227)F double mutant structure of photosynthetic reaction center from Rhodobacter sphaeroides |
| 3e5a | 0.20~0.21 | Crystal structure of Aurora A in complex with VX-680 and TPX2 |
| 3ehb | 0.20~0.21 | A D-Pathway Mutation Decouples the Paracoccus Denitrificans Cytochrome c Oxidase by Altering the side chain orientation of a distant, conserved Glutamate |
| 3fki | 0.20~0.21 | 12-Subunit RNA Polymerase II Refined with Zn-SAD data |
| 3grw | 0.141 | FGFR3 in complex with a Fab |
| 3how | 0.20~0.21 | Complete RNA polymerase II elongation complex III with a T-U mismatch and a frayed RNA 3'-uridine |
| 3hox | 0.20~0.21 | Complete RNA polymerase II elongation complex V |
| 3hoz | 0.20~0.21 | Complete RNA polymerase II elongation complex IV with a T-U mismatch and a frayed RNA 3'-guanine |
| 3jza | 0.20~0.21 | Crystal structure of human Rab1b in complex with the GEF domain of DrrA/SidM from Legionella pneumophila |
| 3kcg | 0.20~0.21 | Crystal structure of the antithrombin-factor IXa-pentasaccharide complex |
| 3knl | 0.20~0.21 | The structures of Capreomycin bound to the 70S ribosome. THIS FILE CONTAINS THE 30S SUBUNIT FOR MOLECULE I |
| 3m32 | 0.20~0.21 | Structural Insight into Methyl-Coenzyme M Reductase Chemistry using Coenzyme B Analogues |
| 3m4o | 0.20~0.21 | RNA polymerase II elongation complex B |

| | | |
|---|---|---|
| 3ogk | 0.20~0.21 | Structure of COI1-ASK1 in complex with coronatine and an incomplete JAZ1 degron |
| 3or2 | 0.194 | Crystal structure of dissimilatory sulfite reductase II (DsrII) |
| 3po2 | 0.20~0.21 | Arrested RNA Polymerase II elongation complex |
| 3puv | 0.20~0.21 | Crystal Structure of an outward-facing MBP-Maltose transporter complex bound to ADP-VO4 |
| 3pux | 0.20~0.21 | Crystal Structure of an outward-facing MBP-Maltose transporter complex bound to ADP-BeF3 |
| 3puz | 0.20~0.21 | Crystal Structure of a pre-translocation state MBP-Maltose transporter complex bound to AMP-PNP |
| 3raf | 0.20~0.21 | Quinazolinedione-DNA cleavage complex of type IV topoisomerase from S. pneumoniae |
| 3rfr | 0.20~0.21 | Crystal Structure of particulate methane monooxygenase (pMMO) from Methylocystis sp. strain M |
| 3ryc | 0.20~0.21 | Tubulin: RB3 stathmin-like domain complex |
| 3ryf | 0.20~0.21 | GTP-Tubulin: RB3 Stathmin-like domain complex |
| 3rzo | 0.20~0.21 | RNA Polymerase II Initiation Complex with a 4-nt RNA |
| 3s1r | 0.20~0.21 | RNA Polymerase II Initiation Complex with a 5-nt 3'-deoxy RNA soaked with GTP |
| 3s2h | 0.20~0.21 | RNA Polymerase II Initiation Complex with a 6-nt RNA containing a 2[prime]-iodo ATP |
| 3s3x | 0.20~0.21 | Structure of chicken acid-sensing ion channel 1 AT 3.0 A resolution in complex with psalmotoxin |
| 3tdh | 0.20~0.21 | Structure of the regulatory fragment of sccharomyces cerevisiae AMPK in complex with AMP |
| 3thm | 0.20~0.21 | Crystal structure of Fas receptor extracellular domain in complex with Fab EP6b_B01 |
| 3tje | 0.20~0.21 | Crystal structure of Fas receptor extracellular domain in complex with Fab E09 |
| 4a3g | 0.20~0.21 | RNA Polymerase II initial transcribing complex with a 2nt DNA-RNA hybrid |
| 4a3i | 0.20~0.21 | RNA Polymerase II binary complex with DNA |
| 4a3k | 0.20~0.21 | RNA polymerase ii initial transcribing complex with a 7nt dna-rna hybrid |
| 4a3l | 0.20~0.21 | RNA polymerase ii initial transcribing complex with a 7nt dna-rna hybrid and soaked with ampcpp |
| 4asu | 0.155 | F1-ATPase in which all three catalytic sites contain bound nucleotide, with magnesium ion released in the Empty site |
| 4ayb | 0.20~0.21 | RNAP at 3.2Ang |
| 4b1o | 0.20~0.21 | Archaeal RNAP-DNA binary complex at 4.32Ang |
| 4b1p | 0.20~0.21 | Archaeal RNAP-DNA binary complex at 4.32Ang |
| 4efa | 0.20~0.21 | Crystal Structure of the Heterotrimeric EGChead Peripheral Stalk Complex of the Yeast Vacuolar ATPase - second conformation |
| 4f61 | 0.20~0.21 | Tubulin:Stathmin-like domain complex |

| | | |
|---|---|---|
| 4fhm | 0.20~0.21 | Nup37-Nup120(aa1-961) complex from Schizosaccharomyces pombe |
| 4gms | 0.20~0.21 | Crystal structure of heterosubtypic Fab S139/1 in complex with influenza A H3 hemagglutinin |

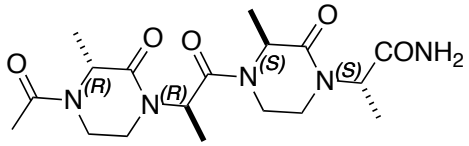

LDD

| PDB ID | RMSD | Protein |
|---|---|---|
| 1aa1 | 0.20~0.30 | activated spinach rubisco in complex with the product 3-phosphoglycerate |
| 2djg | 0.20~0.30 | Re-determination of the native structure of human dipeptidyl peptidase I (cathepsin C) |
| 2qjb | 0.20~0.30 | Crystal structure analysis of BMP-2 in complex with BMPR-IA variant IA/IB |
| 3r8s | 0.20~0.30 | Structures of the bacterial ribosome in classical and hybrid states of tRNA binding |

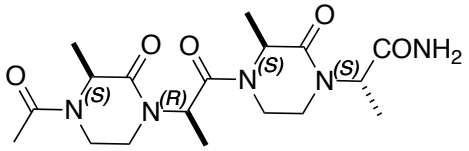

LDL

| PDB ID | RMSD | Protein |
|---|---|---|
| 1hys | 0.20~0.30 | crystal structure of hiv-1 reverse transcriptase in complex with a polypurine tract rna:dna |
| 1ocr | 0.20~0.30 | bovine heart cytochrome c oxidase in the fully reduced state |
| 1ott | 0.20~0.30 | Structure of the Escherichia coli ClC Chloride channel E148A mutant and Fab Complex |
| 1otu | 0.20~0.30 | Structure of the Escherichia coli ClC Chloride channel E148Q mutant and Fab Complex |
| 1rjl | 0.20~0.30 | Structure of the complex between OspB-CT and bactericidal Fab-H6831 |
| 1tzi | 0.20~0.30 | Crystal Structure of the Fab YADS2 Complexed with h-VEGF |
| 1uj3 | 0.20~0.30 | Crystal structure of a humanized Fab fragment of anti-tissue-factor antibody in complex with tissue factor |
| 2e2i | 0.20~0.30 | RNA polymerase II elongation complex in 5 mM Mg+2 with 2'- |

| | | |
|---|---|---|
| | | dGTP |
| 2exy | 0.20~0.30 | Crystal structure of the E148Q Mutant of EcClC, Fab complexed in absence of bound ions |
| 2ez0 | 0.20~0.30 | Crystal structure of the S107A/E148Q/Y445A mutant of EcClC, in complex with a FaB fragment |
| 2gmr | 0.20~0.30 | Photosynthetic reaction center mutant from Rhodobacter sphaeroides with Asp L210 replaced with Asn |
| 2hit | 0.197 | Reaction centre from Rhodobacter sphaeroides strain R-26.1 complexed with dibrominated phosphatidylethanolamine |
| 2htk | 0.20~0.30 | Structure of the Escherichia coli ClC chloride channel Y445A mutant and Fab complex |
| 2nvx | 0.20~0.30 | RNA polymerase II elongation complex in 5 mM Mg+2 with 2'-dUTP |
| 2nxz | 0.20~0.30 | HIV-1 gp120 Envelope Glycoprotein (T257S, S334A, S375W) Complexed with CD4 and Antibody 17b |
| 2ny0 | 0.20~0.30 | HIV-1 gp120 Envelope Glycoprotein (M95W, W96C, T257S, V275C, S334A, S375W, A433M) Complexed with CD4 and Antibody 17b |
| 2ny2 | 0.20~0.30 | HIV-1 gp120 Envelope Glycoprotein (T123C, T257S, S334A, S375W, G431C) Complexed with CD4 and Antibody 17b |
| 2ny4 | 0.20~0.30 | HIV-1 gp120 Envelope Glycoprotein (K231C, T257S, E268C, S334A, S375W) Complexed with CD4 and Antibody 17b |
| 2qqn | 0.20~0.30 | Neuropilin-1 b1 Domain in Complex with a VEGF-Blocking Fab |
| 2r0l | 0.20~0.30 | Short Form HGFA with Inhibitory Fab75 |
| 2xtj | 0.20~0.30 | THE CRYSTAL STRUCTURE OF PCSK9 IN COMPLEX WITH 1D05 FAB |
| 2xwt | 0.20~0.30 | crystal structure of the tsh receptor in complex with a blocking type tshr autoantibody |
| 3du3 | 0.175 | E(L212)A, D(L213)A, A(M249)Y triple mutant structure of photosynthetic reaction center |
| 3grw | 0.20~0.30 | FGFR3 in complex with a Fab |
| 3h3v | 0.20~0.30 | Yeast RNAP II containing poly(A)-signal sequence in the active site |
| 3h42 | 0.20~0.30 | Crystal structure of PCSK9 in complex with Fab from LDLR competitive antibody |
| 3hox | 0.20~0.30 | Complete RNA polymerase II elongation complex V |
| 3hoy | 0.20~0.30 | Complete RNA polymerase II elongation complex VI |
| 3kr3 | 0.20~0.30 | Crystal structure of IGF-II antibody complex |
| 3l4m | 0.126 | Crystal Structure of the MauG/pre-Methylamine Dehydrogenase Complex. |
| 3m7n | 0.20~0.30 | archaeoglobus fulgidus exosome with RNA bound to the active site |
| 3ma9 | 0.20~0.30 | Crystal structure of gp41 derived protein complexed with fab 8066 |
| 3mac | 0.20~0.30 | crystal structure of GP41-derived protein complexed with fab 8062 |

| | | |
|---|---|---|
| 3mxw | 0.20~0.30 | Crystal structure Sonic hedgehog bound to the 5E1 fab fragment |
| 3nps | 0.20~0.30 | Crystal structure of membrane-type serine protease 1 (MT-SP1) in complex with the Fab Inhibitor S4 |
| 3o2d | 0.20~0.30 | Crystal structure of HIV-1 primary receptor CD4 in complex with a potent antiviral antibody |
| 3o4o | 0.20~0.30 | Crystal structure of an Interleukin-1 receptor complex |
| 3orv | 0.122 | Crystal Structure of the Y294H-MauG/pre-Methylamine Dehydrogenase Complex |
| 3pxs | 0.081 | Crystal Structure of Diferrous MauG in Complex with Pre-Methylamine Dehydrogenase: |
| 3pxt | 0.108 | Crystal Structure of Ferrous CO Adduct of MauG in Complex with Pre-Methylamine Dehydrogenase |
| 3pxw | 0.072 | Crystal Structure of Ferrous NO Adduct of MauG in Complex with Pre-Methylamine Dehydrogenase |
| 3r1g | 0.20~0.30 | Structure Basis of Allosteric Inhibition of BACE1 by an Exosite-Binding Antibody |
| 3rlm | 0.096 | Structure of the W199F MauG/pre-Methylamine Dehydrogenase complex after treatment with hydrogen peroxide |
| 3s3x | 0.20~0.30 | Structure of chicken acid-sensing ion channel 1 AT 3.0 A resolution in complex with psalmotoxin |
| 3sle | 0.096 | Crystal Structure of the P107C-MauG/pre-Methylamine Dehydrogenase Complex |
| 3thm | 0.20~0.30 | Crystal structure of Fas receptor extracellular domain in complex with Fab EP6b_B01 |
| 3ulu | 0.20~0.30 | Structure of quaternary complex of human TLR3ecd with three Fabs (Form1) |
| 3v65 | 0.20~0.30 | Crystal structure of agrin and LRP4 complex |
| 4a3e | 0.20~0.30 | RNA Polymerase ii initial transcribing complex with a 5nt dna-rna hybrid and soaked with ampcpp |
| 4a3i | 0.20~0.30 | RNA Polymerase II binary complex with DNA |
| 4a3k | 0.190 | RNA polymerase ii initial transcribing complex with a 7nt dna-rna hybrid |
| 4dn4 | 0.20~0.30 | Crystal structure of the complex between cnto888 fab and mcp-1 mutant p8a |
| 4fxe | 0.20~0.30 | Crystal structure of the intact E. coli RelBE toxin-antitoxin complex |

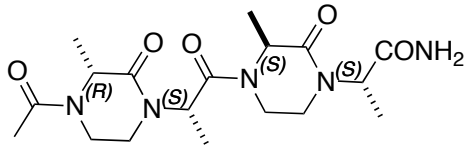


LLD

| PDB ID | RMSD | Protein |
|---|---|---|
| 1ccw | 0.20~0.30 | structure of the coenzyme b12 dependent enzyme glutamate mutase from clostridium cochlearium |
| 1fns | 0.20~0.30 | crystal structure of the von willebrand factor (vwf) a1 domain i546v mutant in complex with the function blocking fab nmc4 |
| 1fyz | 0.20~0.30 | methane monooxygenase hydroxylase, form ii reduced by soaking |
| 1fz0 | 0.163 | methane monooxygenase hydroxylase, form ii mixed-valent grown anaerobically |
| 1fz1 | 0.164 | methane monooxygenase hydroxylase, form iii oxidized |
| 1fz2 | 0.171 | methane monooxygenase hydroxylase, form ii mixed-valent generated by crystal soaking |
| 1fz3 | 0.20~0.30 | methane monooxygenase hydroxylase, form iii soak at ph 6.2 (0.1 m pipes) |
| 1fz6 | 0.162 | methane monooxygenase hydroxylase, form ii soaked in 1 m methanol |
| 1fz7 | 0.20~0.30 | methane monooxygenase hydroxylase, form iii soaked in 0.9 m ethanol |
| 1fz8 | 0.20~0.30 | methane monooxygenase hydroxylase, form ii cocrystallized with dibromomethane |
| 1fz9 | 0.164 | methane monooxygenase hydroxylase, form ii cocrystallized with iodoethane |
| 1fzh | 0.155 | methane monooxygenase hydroxylase, form ii pressurized with xenon gas |
| 1fzi | 0.20~0.30 | methane monooxygenase hydroxylase, form i pressurized with xenon gas |
| 1g20 | 0.20~0.30 | mgatp-bound and nucleotide-free structures of a nitrogenase protein complex between leu127del-fe protein and the mofe protein |
| 1i6h | 0.20~0.30 | RNA polymerase ii elongation complex |
| 1j8h | 0.20~0.30 | Crystal Structure of a Complex of a Human alpha/beta-T cell Receptor, Influenza HA Antigen Peptide, and MHC Class II Molecule, HLA-DR4 |
| 1jeq | 0.20~0.30 | Crystal Structure of the Ku Heterodimer |
| 1k83 | 0.20~0.30 | Crystal Structure of Yeast RNA Polymerase II Complexed with the Inhibitor Alpha Amanitin |
| 1ken | 0.20~0.30 | Influenza virus hemagglutinin complexed with an antibody that prevents the hemagglutinin low ph fusogenic transition |

| | | |
|---|---|---|
| 1kg0 | 0.20~0.30 | Structure of the Epstein-Barr Virus gp42 Protein Bound to the MHC class II Receptor HLA-DR1 |
| 1klg | 0.20~0.30 | Crystal structure of HLA-DR1/TPI(23-37, Thr28-->Ile mutant) complexed with staphylococcal enterotoxin C3 variant 3B2 (SEC3-3B2) |
| 1klu | 0.20~0.30 | Crystal structure of HLA-DR1/TPI(23-37) complexed with staphylococcal enterotoxin C3 variant 3B2 (SEC3-3B2) |
| 1ktz | 0.20~0.30 | Crystal Structure of the Human TGF-beta Type II Receptor Extracellular Domain in Complex with TGF-beta3 |
| 1kyi | 0.20~0.30 | HslUV (H. influenzae)-NLVS Vinyl Sulfone Inhibitor Complex |
| 1lo5 | 0.20~0.30 | Crystal structure of the D227A variant of Staphylococcal enterotoxin A in complex with human MHC class II |
| 1mty | 0.20~0.30 | methane monooxygenase hydroxylase from methylococcus capsulatus (bath) |
| 1n8z | 0.20~0.30 | Crystal structure of extracellular domain of human HER2 complexed with Herceptin Fab |
| 1o97 | 0.20~0.30 | structure of electron transferring flavoprotein from methylophilus methylotrophus, recognition loop removed by limited proteolysis |
| 1occ | 0.20~0.30 | structure of bovine heart cytochrome c oxidase at the fully oxidized state |
| 1oco | 0.20~0.30 | bovine heart cytochrome c oxidase in carbon monoxide-bound state |
| 1ocr | 0.196 | bovine heart cytochrome c oxidase in the fully reduced state |
| 1ocz | 0.20~0.30 | bovine heart cytochrome c oxidase in azide-bound state |
| 1pyw | 0.20~0.30 | Human class II MHC protein HLA-DR1 bound to a designed peptide related to influenza virus hemagglutinin, FVKQNA(MAA)AL, in complex with staphylococcal enterotoxin C3 variant 3B2 (SEC3-3B2) |
| 1s9k | 0.20~0.30 | Crystal Structure of Human NFAT1 and Fos-Jun on the IL-2 ARRE1 Site |
| 1sje | 0.20~0.30 | HLA-DR1 complexed with a 16 residue HIV capsid peptide bound in a hairpin conformation |
| 1sqx | 0.20~0.30 | Crystal Structure Analysis of Bovine Bc1 with Stigmatellin A |
| 1sr5 | 0.20~0.30 | antithrombin-anhydrothrombin-heparin ternary complex structure |
| 1t5x | 0.20~0.30 | HLA-DR1 in complex with a synthetic peptide (AAYSDQATPLLLSPR) and the superantigen SEC3-3B2 |
| 1ub4 | 0.20~0.30 | crystal structure of MazEF complex |
| 1v54 | 0.20~0.30 | Bovine heart cytochrome c oxidase at the fully oxidized state |
| 1xkb | 0.20~0.30 | factor xa complexed with a synthetic inhibitor fx-2212a,(2s)-(3'-amidino-3-biphenylyl)-5-(4-pyridylamino)pentanoic acid |
| 1xmg | 0.20~0.30 | Crystal structure of apo methane monooxygenase hydroxylase from M. capsulatus (Bath) |
| 1xmh | 0.173 | Structure of Co(II) reconstituted methane monooxygenase hydroxylase from M. capsulatus (Bath) |
| 1xu3 | 0.190 | Soluble methane monooxygenase hydroxylase-soaked with |

| | | |
|---|---|---|
| | | bromophenol |
| 1xu5 | 0.171 | Soluble methane monooxygenase hydroxylase-phenol soaked |
| 1xvb | 0.167 | soluble methane monooxygenase hydroxylase: 6-bromohexanol soaked structure |
| 1xvc | 0.173 | soluble methane monooxygenase hydroxylase: 8-bromooctanol soaked structure |
| 1xvd | 0.20~0.30 | Soluble methane monooxygenase hydroxylase: 4-fluorophenol soaked structure |
| 1xve | 0.180 | soluble methane monooxygenase hydroxylase: 3-bromo-3-butenol soaked structure |
| 1xvf | 0.20~0.30 | soluble methane monooxygenase hydroxylase: chloropropanol soaked structure |
| 1xvg | 0.20~0.30 | soluble methane monooxygenase hydroxylase: bromoethanol soaked structure |
| 1za1 | 0.20~0.30 | Structure of wild-type E. coli Aspartate Transcarbamoylase in the presence of CTP at 2.20 A resolution |
| 2dyr | 0.20~0.30 | Bovine heart cytochrome C oxidase at the fully oxidized state |
| 2fzg | 0.20~0.30 | The Structure of Wild-Type E. Coli Aspartate Transcarbamoylase in Complex with Novel T State Inhibitors at 2.25 Resolution |
| 2fzk | 0.20~0.30 | The Structure of Wild-Type E. Coli Aspartate Transcarbamoylase in Complex with Novel T State Inhibitors at 2.50 Resolution |
| 2i07 | 0.20~0.30 | Human Complement Component C3b |
| 2iam | 0.20~0.30 | Structural basis for recognition of mutant self by a tumor-specific, MHC class II-restricted TCR |
| 2omt | 0.20~0.30 | Crystal structure of InlA G194S+S/hEC1 complex |
| 2pjy | 0.20~0.30 | Structural basis for cooperative assembly of the TGF-beta signaling complex |
| 2pm9 | 0.20~0.30 | Crystal structure of yeast Sec13/31 vertex element of the COPII vesicular coat |
| 2v4j | 0.20~0.30 | the crystal structure of desulfovibrio vulgaris dissimilatory sulfite reductase bound to dsrc provides novel insights into the mechanism of sulfate respiration |
| 2vaa | 0.20~0.30 | mhc class i h-2kb heavy chain complexed with beta-2 microglobulin and vesicular stomatitis virus nucleoprotein |
| 2vab | 0.20~0.30 | mhc class i h-2kb heavy chain complexed with beta-2 microglobulin and sendai virus nucleoprotein |
| 2vgl | 0.20~0.30 | ap2 clathrin adaptor core |
| 2vhm | 0.20~0.30 | structure of pdf binding helix in complex with the ribosome (part 1 of 4) |
| 2x5u | 0.20~0.30 | 80 microsecond laue diffraction snapshot from crystals of a photosynthetic reaction centre without illumination. |
| 2xn9 | 0.20~0.30 | crystal structure of the ternary complex between human t cell receptor, staphylococcal enterotoxin h and human major histocompatibility complex class ii |
| 2xts | 0.179 | crystal structure of the sulfane dehydrogenase soxcd from |

| | | |
|---|---|---|
| | | paracoccus pantotrophus |
| 2yu9 | 0.20~0.30 | RNA polymerase II elongation complex in 150 mm MG+2 with UTP |
| 3ayx | 0.20~0.30 | Membrane-bound respiratory [NiFe] hydrogenase from Hydrogenovibrio marinus in an H2-reduced condition |
| 3cqz | 0.20~0.30 | Crystal structure of 10 subunit RNA polymerase II in complex with the inhibitor alpha-amanitin |
| 3gtp | 0.20~0.30 | Backtracked RNA polymerase II complex with 24mer RNA |
| 3k7a | 0.20~0.30 | Crystal Structure of an RNA polymerase II-TFIIB complex |
| 3lq5 | 0.20~0.30 | Structure of CDK9/CyclinT in complex with S-CR8 |
| 3mhs | 0.20~0.30 | Structure of the SAGA Ubp8/Sgf11/Sus1/Sgf73 DUB module bound to ubiquitin aldehyde |
| 3mi9 | 0.20~0.30 | Crystal structure of HIV-1 Tat complexed with human P-TEFb |
| 3oat | 0.20~0.30 | Crystal structure of the E. coli ribosome bound to telithromycin. This file contains the 50S subunit of the first 70S ribosome with telithromycin bound. |
| 3ogk | 0.20~0.30 | Structure of COI1-ASK1 in complex with coronatine and an incomplete JAZ1 degron |
| 3rzd | 0.20~0.30 | RNA Polymerase II Initiation Complex with a 5-nt RNA |
| 3s14 | 0.20~0.30 | RNA Polymerase II Initiation Complex with a 6-nt RNA |
| 3s1m | 0.20~0.30 | RNA Polymerase II Initiation Complex with a 5-nt RNA (variant 1) |
| 3s1n | 0.20~0.30 | RNA Polymerase II Initiation Complex with a 5-nt RNA (variant 2) |
| 3s1q | 0.20~0.30 | RNA Polymerase II Initiation Complex with a 5-nt 3'-deoxy RNA soaked with ATP |
| 3s2d | 0.20~0.30 | RNA Polymerase II Initiation Complex with a 5-nt RNA containing a 5Br-U |
| 3sri | 0.20~0.30 | Crystal structure of Plasmodium falciparum AMA1 in complex with a 29aa PfRON2 peptide |
| 3tnh | 0.20~0.30 | CDK9/cyclin T in complex with CAN508 |
| 3tni | 0.20~0.30 | structure of CDK9/cyclin T F241L |
| 4a3d | 0.20~0.30 | RNA polymerase ii initial transcribing complex with a 6nt dna-rna hybrid |
| 4a3g | 0.20~0.30 | RNA polymerase ii initial transcribing complex with a 2nt dna-rna hybrid |
| 4a3k | 0.20~0.30 | RNA polymerase ii initial transcribing complex with a 7nt dna-rna hybrid |
| 4ec9 | 0.20~0.30 | Crystal structure of full-length cdk9 in complex with cyclin t |
| 5prc | 0.20~0.30 | photosynthetic reaction center from rhodopseudomonas viridis (atrazine complex) |
| 6prc | 0.169 | photosynthetic reaction center from rhodopseudomonas viridis (dg-420314 (triazine) complex) |
| 7prc | 0.20~0.30 | photosynthetic reaction center from rhodopseudomonas viridis (dg-420315 (triazine) complex) |

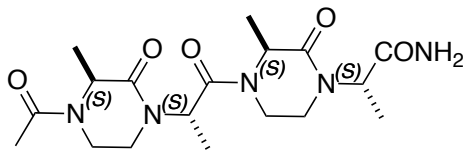

LLL

| PDB ID | RMSD | Protein |
|---|---|---|
| 1bcp | 0.20~0.30 | binary complex of pertussis toxin and atp |
| 1e6v | 0.20~0.30 | methyl-coenzyme m reductase from methanopyrus kandleri |
| 1eex | 0.20~0.30 | crystal structure of the diol dehydratase-adeninylpentylcobalamin complex from klebsiella oxytoca |
| 1egv | 0.20~0.30 | crystal structure of the diol dehydratase-adeninylpentylcobalamin complex from klebsella oxytoca under the illuminated condition. |
| 1fzi | 0.20~0.30 | methane monooxygenase hydroxylase, form i pressurized with xenon gas |
| 1hap | 0.20~0.30 | complex of human alpha-thrombin with a 15mer oligonucleotide ggttggtgtggttgg (based on x-ray model of dna) |
| 1hbm | 0.20~0.30 | methyl-coenzyme m reductase enzyme product complex |
| 1hbn | 0.20~0.30 | methyl-coenzyme m reductase |
| 1hbo | 0.20~0.30 | methyl-coenzyme m reductase mcr-red1-silent |
| 1hbu | 0.20~0.30 | methyl-coenzyme m reductase in the mcr-red1-silent state in complex with coenzyme m |
| 1i50 | 0.20~0.30 | RNA polymerase ii crystal form ii at 2.8 a resolution |
| 1iwp | 0.20~0.30 | Glycerol Dehydratase-cyanocobalamin Complex of Klebsiella pneumoniae |
| 1jmu | 0.199 | Crystal Structure of the Reovirus mu1/sigma3 Complex |
| 1jnr | 0.20~0.30 | Structure of adenylylsulfate reductase from the hyperthermophilic Archaeoglobus fulgidus at 1.6 resolution |
| 1jnz | 0.20~0.30 | Structure of adenylylsulfate reductase from the hyperthermophilic Archaeoglobus fulgidus at 1.6 resolution |
| 1mhy | 0.20~0.30 | methane monooxygenase hydroxylase |
| 1mro | 0.20~0.30 | methyl-coenzyme m reductase |
| 1mty | 0.20~0.30 | methane monooxygenase hydroxylase from methylococcus capsulatus (bath) |
| 1oco | 0.20~0.30 | bovine heart cytochrome c oxidase in carbon monoxide-bound state |
| 1ocr | 0.20~0.30 | bovine heart cytochrome c oxidase in the fully reduced state |
| 1qlb | 0.20~0.30 | respiratory complex II-like fumarate reductase from Wolinella succinogenes |
| 1rjc | 0.193 | Crystal structure of the camelid single domain antibody cAb- |

| | | |
|---|---|---|
| | | Lys2 in complex with hen egg white lysozyme |
| 1rld | 0.20~0.30 | solid-state phase transition in the crystal structure of ribulose 1,5-biphosphate carboxylase(slash)oxygenase |
| 1sqp | 0.20~0.30 | Crystal Structure Analysis of Bovine Bc1 with Myxothiazol |
| 1sqq | 0.20~0.30 | Crystal Structure Analysis of Bovine Bc1 with Methoxy Acrylate Stilbene (MOAS) |
| 1t36 | 0.20~0.30 | Crystal structure of E. coli carbamoyl phosphate synthetase small subunit mutant C248D complexed with uridine 5'-monophosphate |
| 1tbg | 0.20~0.30 | beta-gamma dimer of the heterotrimeric g-protein transducin |
| 1twg | 0.20~0.30 | RNA polymerase II complexed with CTP |
| 1uc4 | 0.20~0.30 | Structure of diol dehydratase complexed with (S)-1,2-propanediol |
| 1uc5 | 0.20~0.30 | Structure of diol dehydratase complexed with (R)-1,2-propanediol |
| 1vsy | 0.178 | Proteasome Activator Complex |
| 1xve | 0.20~0.30 | soluble methane monooxygenase hydroxylase: 3-bromo-3-butenol soaked structure |
| 1ynn | 0.20~0.30 | Taq RNA polymerase-rifampicin complex |
| 1z7q | 0.20~0.30 | Crystal structure of the 20s proteasome from yeast in complex with the proteasome activator PA26 from Trypanosome brucei at 3.2 angstroms resolution |
| 2d5r | 0.20~0.30 | Crystal Structure of a Tob-hCaf1 Complex |
| 2eim | 0.20~0.30 | Zinc ion binding structure of bovine heart cytochrome C oxidase in the fully reduced state |
| 2f2a | 0.20~0.30 | Structure of tRNA-Dependent Amidotransferase GatCAB complexed with Gln |
| 2fja | 0.20~0.30 | adenosine 5'-phosphosulfate reductase in complex with substrate |
| 2fjb | 0.20~0.30 | Adenosine-5'-phosphosulfate reductase im complex with products |
| 2fjd | 0.20~0.30 | adenosine-5-phosphosulfate reductase in complex with sulfite (covalent adduct) |
| 2fje | 0.20~0.30 | adenosine-5-phosphosulfate reductase oxidized state |
| 2h4m | 0.20~0.30 | Karyopherin Beta2/Transportin-M9NLS |
| 2h89 | 0.20~0.30 | Avian Respiratory Complex II with Malonate Bound |
| 2i0q | 0.20~0.30 | Crystal structure of a telomere single-strand DNA-protein complex from O. nova with full-length alpha and beta telomere proteins |
| 2j8s | 0.20~0.30 | drug export pathway of multidrug exporter acrb revealed by darpin inhibitors |
| 2r6g | 0.20~0.30 | the crystal structure of the e. coli maltose transporter |
| 2uxl | 0.20~0.30 | x-ray high resolution structure of the photosynthetic reaction center from rb. sphaeroides at ph 10 in the neutral state, 2nd dataset |

| | | |
|---|---|---|
| 2v4j | 0.20~0.30 | the crystal structure of desulfovibrio vulgaris dissimilatory sulfite reductase bound to dsrc provides novel insights into the mechanism of sulfate respiration |
| 2v67 | 0.20~0.30 | crystal structure of chlamydomonas reinhardtii rubisco with a large-subunit supressor mutation t342i |
| 2v68 | 0.20~0.30 | crystal structure of chlamydomonas reinhardtii rubisco with large-subunit mutations v331a, t342i |
| 2v69 | 0.20~0.30 | crystal structure of chlamydomonas reinhardtii rubisco with a large-subunit mutation d473e |
| 2vdh | 0.20~0.30 | crystal structure of chlamydomonas reinhardtii rubisco with a large-subunit c172s mutation |
| 2vdi | 0.20~0.30 | crystal structure of chlamydomonas reinhardtii rubisco with a large-subunit c192s mutation |
| 2vpy | 0.20~0.30 | polysulfide reductase with bound quinone inhibitor, pentachlorophenol (pcp) |
| 2wjm | 0.20~0.30 | lipidic sponge phase crystal structure of the photosynthetic reaction centre from blastochloris viridis (low dose) |
| 2xsj | 0.191 | structure of desulforubidin from desulfomicrobium norvegicum |
| 2xts | 0.20~0.30 | crystal structure of the sulfane dehydrogenase soxcd from paracoccus pantotrophus |
| 2y10 | 0.20~0.30 | the crystal structure of ef-tu and trp-trna-trp bound to a cognate codon on the 70s ribosome. |
| 2zmz | 0.20~0.30 | The 1.37-A crystal structure of the hydroxylamine-induced deoxy-form of the copper-bound tyrosinase in complex with a caddie protein from Streptomyces castaneoglobisporus |
| 3aad | 0.20~0.30 | Structure of the histone chaperone CIA/ASF1-double bromodomain complex linking histone modifications and site-specific histone eviction |
| 3ae1 | 0.20~0.30 | Crystal structure of porcine heart mitochondrial complex II bound with N-Phenyl-2-(trifluoromethyl)-benzamide |
| 3ae4 | 0.20~0.30 | Crystal structure of porcine heart mitochondrial complex II bound with 2-Iodo-N-methyl-benzamide |
| 3ae5 | 0.20~0.30 | Crystal structure of porcine heart mitochondrial complex II bound with 2-Methyl-N-(3-isopropoxy-phenyl)-benzamide |
| 3ae8 | 0.20~0.30 | Crystal structure of porcine heart mitochondrial complex II bound with N-(3-Isopropoxy-phenyl)-2-trifluoromethylbenzamide |
| 3ae9 | 0.20~0.30 | Crystal structure of porcine heart mitochondrial complex II bound with N-(3-Pentafluorophenyloxy-phenyl)-2-trifluoromethyl-benzamide |
| 3aea | 0.20~0.30 | Crystal structure of porcine heart mitochondrial complex II bound with N-(3-Dimethylaminomethyl-phenyl)-2-trifluoromethyl-benzamide |
| 3aec | 0.20~0.30 | Crystal structure of porcine heart mitochondrial complex II bound with 2-Iodo-N-(1-methylethyl)-benzamid |

| | | |
|---|---|---|
| 3aeg | 0.20~0.30 | Crystal structure of porcine heart mitochondrial complex II bound with N-Biphenyl-3-yl-2-iodo-benzamide |
| 3arc | 0.20~0.30 | Crystal structure of oxygen-evolving Photosystem II at 1.9 angstrom resolution |
| 3auj | 0.20~0.30 | Structure of diol dehydratase complexed with glycerol |
| 3dmj | 0.20~0.30 | crystal structure of hiv-1 v106a and y181c mutant reverse transcriptase in complex with gw564511. |
| 3euh | 0.20~0.30 | Crystal Structure of the MukE-MukF Complex |
| 3gtm | 0.20~0.30 | Co-complex of Backtracked RNA polymerase II with TFIIS |
| 3gyx | 0.20~0.30 | Crystal structure of adenylylsulfate reductase from Desulfovibrio gigas |
| 3hox | 0.20~0.30 | Complete RNA polymerase II elongation complex V |
| 3hoy | 0.20~0.30 | Complete RNA polymerase II elongation complex VI |
| 3i3t | 0.198 | Crystal structure of covalent ubiquitin-USP21 complex |
| 3kno | 0.20~0.30 | The structures of capreomycin bound to the 70S ribosome. this file contains the 50s subunit for molecule ii |
| 3koy | 0.20~0.30 | Crystal Structure of ornithine 4,5 aminomutase in complex with ornithine (Aerobic) |
| 3l5q | 0.179 | Proteasome Activator Complex |
| 3m1v | 0.20~0.30 | Structural Insight into Methyl-Coenzyme M Reductase Chemistry using Coenzyme B Analogues |
| 3m2r | 0.20~0.30 | Structural Insight into Methyl-Coenzyme M Reductase Chemistry using Coenzyme B Analogues |
| 3m2u | 0.20~0.30 | Structural Insight into Methyl-Coenzyme M Reductase Chemistry using Coenzyme B Analogues |
| 3m2v | 0.20~0.30 | Structural Insight into Methyl-Coenzyme M Reductase Chemistry using Coenzyme B Analogues |
| 3m30 | 0.20~0.30 | Structural Insight into Methyl-Coenzyme M Reductase Chemistry using Coenzyme B Analogues |
| 3m32 | 0.20~0.30 | Structural Insight into Methyl-Coenzyme M Reductase Chemistry using Coenzyme B Analogues |
| 3mm5 | 0.20~0.30 | Dissimilatory sulfite reductase in complex with the substrate sulfite |
| 3mm7 | 0.20~0.30 | Dissimilatory sulfite reductase carbon monoxide complex |
| 3mm9 | 0.20~0.30 | Dissimilatory sulfite reductase nitrite complex |
| 3noc | 0.20~0.30 | Designed ankyrin repeat protein (DARPin) binders to AcrB: Plasticity of the Interface |
| 3or2 | 0.20~0.30 | Crystal structure of dissimilatory sulfite reductase II (DsrII) |
| 3pmk | 0.20~0.30 | Crystal structure of the Vesicular Stomatitis Virus RNA free nucleoprotein/phosphoprotein complex |
| 3pot | 0.20~0.30 | Structural analysis of a Ni(III)-methyl species in methyl-coenzyme M reductase from Methanothermobacter marburgensis |
| 3pux | 0.20~0.30 | Crystal Structure of an outward-facing MBP-Maltose transporter complex bound to ADP-BeF3 |

| | | |
|---|---|---|
| 3rg6 | 0.20~0.30 | Crystal structure of a chaperone-bound assembly intermediate of form I Rubisco |
| 3s17 | 0.20~0.30 | RNA Polymerase II Initiation Complex with a 9-nt RNA |
| 3s2d | 0.20~0.30 | RNA Polymerase II Initiation Complex with a 5-nt RNA containing a 5Br-U |
| 3t6e | 0.20~0.30 | Crystal Structure of the Reaction Centre from Blastochloris viridis strain DSM 133 (ATCC 19567) substrain-94 |
| 3thm | 0.146 | Crystal structure of Fas receptor extracellular domain in complex with Fab EP6b_B01 |
| 3u44 | 0.20~0.30 | Crystal structure of AddAB-DNA complex |
| 3uzv | 0.20~0.30 | Crystal structure of the dengue virus serotype 2 envelope protein domain III in complex with the variable domains of Mab 4E11 |
| 3vhl | 0.20~0.30 | Crystal structure of the DHR-2 domain of DOCK8 in complex with Cdc42 (T17N mutant) |
| 4a3c | 0.20~0.30 | RNA polymerase ii initial transcribing complex with a 5nt dna-rna hybrid |
| 4a3j | 0.20~0.30 | RNA polymerase ii initial transcribing complex with a 2nt dna-rna hybrid and soaked with gmpcpp |
| 4a8j | 0.20~0.30 | Crystal Structure of the Elongator subcomplex Elp456 |
| 4akr | 0.20~0.30 | Crystal Structure of the cytoplasmic actin capping protein Cap32_34 from Dictyostelium discoideum |
| 4dcn | 0.20~0.30 | Crystal Structure Analysis of the Arfaptin2 BAR domain in Complex with ARL1 |
| 4dx7 | 0.20~0.30 | Transport of drugs by the multidrug transporter AcrB involves an access and a deep binding pocket that are separated by a switch-loop |
| 4eb6 | 0.20~0.30 | Tubulin-Vinblastine: Stathmin-like complex |
| 4ely | 0.20~0.30 | CCDBVFI:GYRA14EC |
| 4fe1 | 0.20~0.30 | Improving the Accuracy of Macromolecular Structure Refinement at 7 A Resolution |
| 4g4s | 0.20~0.30 | Structure of Proteasome-Pba1-Pba2 Complex |
| 8ruc | 0.20~0.30 | activated spinach rubisco complexed with 2-carboxyarabinitol bisphosphate |